Development of CMOS sensors for a future neutron eleetronie personal dosemeter

Ying Zhang

UNIVERSITÉ DE STRASBOURG

N° d'ordre: xxxx

École Doctorale de Physique et Chimie-Physique de l'Université de Strasbourg

UDS

THÈSE

présentée pour obtenir le grade de

Docteur de l'Université de Strasbourg

Discipline: Électronique, Électrotechnique et Automatique

Spécialité : Instrumentation et Microélectronique

par

Ying ZHANG

Development of CMOS Sensors for a Future Neutron Electronic Personal Dosemeter

soutenue publiquement le 19 septembre 2012 devant le jury:

Directeurs de thèse:	M. Yann HU	Pr. UDS, Strasbourg
	M. Daniel HUSSON	MC. UDS, Strasbourg
Rapporteurs externes:	M. Denis DAUVERGNE	DR IPN, Lyon
	M. Eric LIATARD	Pr. LPSC, Grenoble
Examinateurs:	M. Jean-Marc BORDY	DR CEA/LNHB, Gif-sur-Yvette
	M. Luc HEBRARD	Pr. InESS, Strasbourg

Acknowledgments

It is a pleasure to thank those who made this thesis possible. First of all, I would like to express my gratitude to my supervisors Prof. Yann Hu and Dr. Daniel Husson for giving me the opportunity to work on such exciting project and for their invaluable support, guidance and encouragement during my research. I sincerely appreciate Dr. Daniel Husson for his assistance in preparations of my manuscript by offering corrections and suggestions for improvements. I would also like to thank Dr. Christine Hu-Guo, the leader of microelectronics group, for her helpful discussions and suggestions during the prototype design.

I would like to show my gratitude to Prof. Abdel-Mjid Nourreddine, the leader of RaMsEs group for his support and for providing the proper environment for the physical experiments in this thesis.

I owe my gratitude to Anthony Bozier and Hung Pham for their fruitful discussions in the circuit design. I would like to thank Andrei Dorokhov and Min Fu for their help on device simulations. I appreciate Stéphane Higueret for his technical support during the tests and for his work in the neutron irradiation in Cadarache. I am grateful to Thê-Duc Le for his work in the test board design and his kind help at the beginning of the tests. I extend my gratitude to Khalil Amgarou for his valuable suggestions in the neutron measurements. Thanks also to Marie Vanstalle for her advice on experiments and data analysis.

I am grateful to all the other colleagues in PICSEL group: Marc Winter, Wojciech Dulinski, Abdelkader Himmi, Claude Colledani, Guy Doziere, Frédéric Morel, Gregory Bertolone, Isabelle Valin, Jérôm Nanni, Christian Illinger, Sylviane Molinet for their kind help, suggestions, and technical support during this thesis.

Many thanks to all the friends I met during my stay in France for the fun we shared together and for making my life here much easier.

I should not forget to thank China Scholarship Council (CSC) for their financial support.

Last but not least, I would also like to thank my parents for their love, understanding, and constant support that enabled me to complete this work.

Contents

List of Figures

List of Tables

Résumé en Français

Les radiations ionisantes sont bien connues pour causer des dommages aux cellules vivantes et aux dispositifs électroniques à base de silicium. Au total, ce sont 63000 travailleurs en Europe qui sont exposés à ces rayonnements, dans les installations nucléaires ainsi que, de plus en plus, en milieu médical. La mesure quantitative des doses absorbées est réalisée par différents types de dosimètres, selon le type de radiation (X, β, γ, n). Les neutrons présentent les plus grandes difficultés de mesure au niveau des doses, car, électriquement neutres, ils ne sont pas directement détectables, mais seulement au travers des particules secondaires qu'ils créent par réactions nucléaires ou simple diffusion. De plus, on les trouve sur une gamme d'énergie extrêmement étendue, qui va du meV au GeV, avec des effets biologiques très fortement dépendants de leur énergie. Il est donc essentiel pour un dosimètre de distinguer les neutrons de basse énergie des neutrons rapides (>100 keV). En dernier lieu, les neutrons apparaissent toujours en champs mixtes n-γ, la tâche d'un bon dosimètre est alors d'opérer une claire distinction entre les deux.

A l'heure actuelle, seuls les dosimètres passifs, qui intègrent la dose, sont considérés comme fiables pour la mesure de neutron, les dosimètres opérationnels ne donnant pas de résultats satisfaisants, alors qu'une telle mesure est obligatoire pour tous les travailleurs du nucléaire depuis 1995 (circulaire IEC1323).

Au sein de l'IPHC (Institut Pluridisciplinaire Hubert Curien) le groupe RaMsEs a donc proposé une solution en propre, basée sur la technologie des capteurs CMOS (« Complementary Metal Oxyde ») pour lesquels le laboratoire possède une expertise de niveau mondial. Une décennie de développements, motivée par la physique des particules (projet ILC) a fait émerger d'autres applications possibles. En particulier, ces capteurs présentent des caractéristiques intéressantes pour la détection efficace des neutrons : faible consommation électrique, bas coût, portabilité, volume limité (d'où une sensibilité aux photons presque nulle) ainsi qu'une possibilité d'intégration complète de l'électronique de traitement. Une étude préliminaire a déjà été conduite au RaMsEs, avec un vrai capteur à pixels, le MIMOSA-V (« Minimum Ionising particle MOS sensor ») développé pour la trajectographie des particules de haute énergie. Il a été démontré qu'une coupure adéquate rendait bien le capteur transparent aux γ, sans perte de signal. L'efficacité de détection aux neutrons rapides, de l'ordre de 10^{-3}, est celle attendue par simulation, et quasiment identique à l'efficacité aux neutrons lents (convertisseur au bore), résultats qui laissent présager une réponse constante sur toute la gamme des énergies. Malgré

ces résultats prometteurs pour la dosimétrie neutron, le MIMOSA-V ne saurait être la solution pour un dosimètre, à cause de l'encombrement actuel du système complet (qui doit devenir un vrai système intégré) et au vu de l'énorme flux de données généré sur une courte période par un quart de million de pixels.

Cette thèse présente donc le développement d'un système miniaturisé pour la dosimétrie neutron sur la base des acquis en capteurs à pixels. Un circuit dédié, AlphaRad-2, a été conçu et implémenté en technologie AMS 0.35 (Austria MicroSystems), circuit CMOS à très faible consommation et alimenté en 2.5 V.

La thèse est organisée selon le plan suivant:

Chapitre 1 : présentation de la physique de l'interaction rayonnement-matière, et problèmes généraux de détection. Nous discutons aussi les interactions photons ainsi que des particules secondaires. Dans une seconde partie, nous présentons les grandeurs associées à la mesure des doses définies par l'ICRP (International Commission on Radiological Protection), ainsi que les méthodes spécifiques de détection des neutrons.

Chapitre 2 : les principes de base de détection de particules ionisantes dans un détecteur silicium sont passés en revue. Après un résumé de la décennie de développement des capteurs pixels (CPS) pour la physique des particules (détecteurs de vertex), on exposera les résultats du MIMOSA-5 aux neutrons, ainsi que les faiblesses du système.

Chapitre 3 : l'idée originale d'une architecture en « mono-pixel » est explicitée dans un premier temps. Une étude complète de simulation avec la suite Sentaurus-TCAD a été conduite pour comprendre le processus de collection de charge (efficacité et temps caractéristique). Nous détaillons ces résultats, essentiels pour fixer les paramètres du capteur (taille de la micro-diode élémentaire, espacement). S'en suit l'analyse des différents étages de traitement électronique, incluant une discussion des architectures « tension » ou « courant ».

Chapitre 4 : un circuit dédié, AlphaRad-2, pour un futur dosimètre électronique personnel de neutrons est proposé. Ce chapitre se penche sur l'étude théorique complète de l'électronique de lecture, présentée avec les résultats de tests électroniques.

Chapitre 5 : ce chapitre est consacré à des tests de notre prototype sous différents types de rayonnement, avec en première partie la réponse à une source alpha pour l'étalonnage du taux de comptage. Nous présentons également une mesure de la sensibilité aux électrons, aux neutrons rapides ainsi que la procédure pour distinguer photons et neutrons. En tout dernier lieu, nous abordons l'influence de l'épaisseur de convertisseur polyéthylène et la réponse du capteur en fonction de la distance.

Pour finir, le dernier chapitre présente les conclusions générales de ce développement, avant d'introduire une perspective de grand intérêt : en 2012, nous avons transposé l'architecture de l'AlphaRad-2 dans un « process » de fabrication nouveau (XO035 de X-FAB), qui doit permettre de décliner la plage à neutrons lents de manière telle à éviter, dans le futur, de devoir amincir le capteur.

Introduction

It is universally acknowledged that radiation causes damage, which can range from a subtle cell mutation in a living organism to the bulk damage in a silicon detector. About 63000 workers in Europe are exposed to the risk posed by these harmful radiation, mainly in nuclear power plans and in medical therapy facilities. Quantitative measurement of the dose absorbed by an organism is provided by dosemeters. There are different types of dosemeters according to the detected radiation (γ, β, X, n,...). Neutrons, are well-known to be an even more troublesome particle species with respect to dosimetry. Firstly, they are electrically neutral, so that they are not affected by electromagnetic forces and unable to directly ionize matter. In fact, detection of neutrons is only possible through the secondary charged particles released from their nuclear interactions in a given material. Moreover, neutrons exist over a wide energy range from meV to GeV, and their biological effects on life beings are different according to their energies. It is therefore essential for a dosemeter to be able to differentiate low energy neutrons from fast neutrons (E_n >100 keV). Finally, neutrons are always accompanied by γ radiation, leading to n-γ mixed fields. A neutron dosemeter has to recognize neutrons in the presence of photon and electron radiations. Currently, only the passive dosemeters, providing an integral on the dose to an individual over the wearing period, are considered reliable in neutron dosimetry. Active dosemeters (giving the dose information "online") exist, but do not yet give results as satisfactory as passive devices. Their use, however, became mandatory for workers in addition to the passive dosimetry since 1995 (IEC 1323).

Therefore, the *RaMsEs* group in the laboratory IPHC (*Institut Pluridisciplinaire Hubert Curien*, *UMR 7178*) proposed its own solution to active neutron dosemeters, based on a new technology in the field of dosimetry: CMOS (Complementary Metal Oxide Semiconductor) technology, in which IPHC has a world-class expertise. More than a decade has passed since the first CMOS sensor was developed for charged particle tracking, motivated by the linear collider project. Numerous other applications have emerged since then. These sensors present attractive characteristics for neutron dosimetry: low power consumption, low cost, portability, a thin sensitive volume which implies a low sensitivity to photons and the full integration of the read-out electronics on the same substrate as the sensing elements. To investigate the feasibility of CMOS technology for the application in neutron dosimetry, a previous study had been done by the *RaMsEs* group. Extensive experiments had been performed with a true pixelated CMOS

sensor, MIMOSA-5, (Minimum Ionizing particle MOS Active pixel sensor), originally designed for particle tracking. It has been demonstrated that by applying an appropriate threshold the sensor can be considered as γ-transparent. The measured efficiency to fast neutrons is of the same order of magnitude (10^{-3}) as that to thermal neutrons obtained using a natural boron converter. These results are encouraging to obtain a constant response of the detector with the energy of the incident neutrons. The study with the MIMOSA-5 sensor provided experimental evidence that CMOS sensors offer promising characteristics in the application to neutron dosimetry. However, the MIMOSA-5 sensor can not be used directly for a personal dosemeter due to a major drawback: its pixelation makes the data stream too large to develop a portable integrated system (system-on-chip) where data is directly processed.

The work presented in this thesis addresses the development and characterization of an efficient and miniaturized system based on a dedicated CMOS sensor for a future neutron personal dosemeter. Based on the results obtained with the MIMOSA-5, a new dedicated sensor AlphaRad-2, with very low power consumption, has been implemented in the AMS (Austriamicrosystems AG) 0.35 μm CMOS technology with a 2.5 V power supply.

This thesis is organized as follows:

- In chapter 1, the physics of the interactions of radiation with matter, which the detection of particles is based on, will be presented. We make an overview of interactions of photons and the secondary charged particles that were encountered during this work. The second part of the chapter focuses on the radiation dosimetry in general by introducing a series of dosimetric quantities defined by the International Commission on Radiological Protection (ICRP). Finally, the methods currently used in neutron dosimetry will be described.
- In chapter 2, basic physics principles governing charge generation and collection in silicon detectors after a passage of an ionizing particle will be presented. Development of CMOS Pixel Sensor (CPS) for vertex detectors at IPHC in the past more than ten years will be the second part of this chapter. The third part presents the experimental measurements of the MIMOSA-5 sensor with fast and thermal neutrons. The possibilities and the weak points of the sensor are identified.
- In chapter 3, the idea of using an equivalent "mono-pixel" architecture as the sensing part for dosimetric applications is described in the beginning. Device physics simulations by means of the Sentaurus-TCAD (Technology Computer-Aided Design) tool targeting on the study of charge collection in micro-diodes will be given. We detail the simulation results in order to set the sensor parameters (size of the micro-diode, inter-diode distance). The charge collection simulation is followed by the analysis and design of the two different signal processing architectures, including the voltage mode and the current mode.
- In chapter 4, a dedicated CMOS sensor, AlphaRad-2, for a future neutron personal dosemeter is proposed. The design of a low-noise, low-power consumption readout circuit is presented for both its theoretical analysis and electrical test results.
- In chapter 5, the detailed experiments for the AlphaRad-2 prototype with radiative sources

are presented. The first part shows the results of measurements made to test the sensor in detection efficiency by the exposure to α particles. It also summarizes the results of experiments performed to determine the sensor sensitivity to photons and fast neutrons as well as a n/γ discrimination threshold. The last part of this chapter covers the study on the influence of the thickness of polyethylene converters and the sensor response as a function of distance.

- In the conclusion, the results obtained in this thesis will be summarized and the main conclusions will be presented. At the end, the perspectives for using CMOS sensors in neutron dosimetry are addressed. To improve the detection performance and exploit the possibility of detecting thermal neutrons without thinning down the standard sensor, we present a reproduction of the AlphaRad-2 in a specialized process for optoelectronic applications (XO035 technology, X-FAB).

Chapter 1

Neutron interactions and dosimetry

The detection of neutrons requires not only to know the interaction probability with matter but also the knowledge of the interactions of the related particles with matter, i.e. the secondary charged particles (α, protons) generated by neutrons along their paths. In addition, we need a good knowledge of the particles that make up the physical background of the signal (i.e. photons, in our case). We start this chapter with the review of the interaction mechanisms of the related particles.

1.1 Interactions of particles with matter

Particles and radiation can be detected only through their interactions with matter. The way particles interact with matter depends not only on the types of incident and target particles but also on their properties, such as energy and momentum. There are two main kinds of processes by which a particle going through matter can lose energy. In the first kind the energy loss is gradual, which is the case for charged particles. In the second kind the energy loss happens as single event; for instance, a photon moves without any interaction at all through the material until, most of the time in a single collision, it loses all its energy. The neutron itself is an intermediate case, able to lose energy in several collisions before undergoing a single inelastic event. In this section, we will start by considering the interaction of heavy charged particles with matter, and then proceed to look at the interaction of electrons and photons.

1.1.1 Interaction of heavy charged particles

The moving charged particles exert electromagnetic forces on atomic electrons and impart energy to them. A heavy charged particle travels with an almost straight path through matter, losing its energy gradually.

1.1.1.1 Energy loss

The main interactions of heavy charged particles with matter are ionization and excitation. The mean rate of energy loss (or stopping power) by moderately relativistic charged heavy particles is well-described by the Bethe-Bloch equation

$$-\frac{dE}{dx} = Kz^2\frac{Z}{A}\frac{1}{\beta^2}[\frac{1}{2}\ln\frac{2m_ec^2\beta^2\gamma^2T_{max}}{I^2} - \beta^2 - \frac{\delta(\beta\gamma)}{2}] \tag{1.1}$$

where

z – charge of the incident particle in units of the elementary charge;
Z, A – atomic number and mass of the absorber;
m_e – electron mass, $m_ec^2 = 0.510$ MeV;
r_e – classical electron radius, $r_e = 2.817 \times 10^{-15}$ m;
N_A – Avogadro's number, $N_A = 6.022 \times 10^{23}$ mol^{-1};
I – mean excitation energy in units of eV;
β – velocity of the particle in units of speed of light, $\beta = \nu/c$;
γ – the Lorentz factor, $\gamma = \frac{1}{\sqrt{1-\beta^2}}$;
$\delta(\beta\gamma)$ – density effect correction to ionization energy loss;

$K/A = 4\pi N_A r_e^2 m_e c^2/A = 0.307$ MeV g^{-1}cm^2 for $A = 1$ g mol^{-1}.

T_{max} is the maximum kinetic energy which can be imparted to a free electron in a single collision and given by

$$T_{max} = \frac{2m_ec^2\beta^2\gamma^2}{1 + 2\gamma m_e/M + (m_e/M)^2} \tag{1.2}$$

where M is the mass of the incident particle.

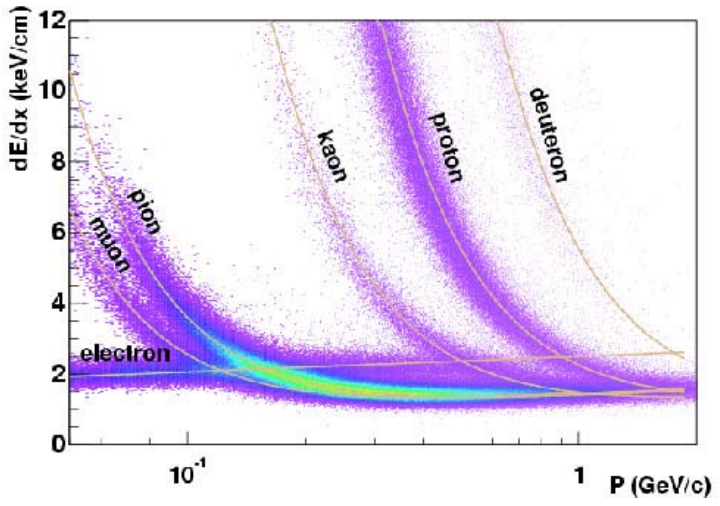

Figure 1.1: Energy loss for electron, muon, pion, kaon, proton, and deuteron in air as a function of their momentum [1].

Equation (1.1) describes the mean rate of energy loss in the region $0.1 \lesssim \beta\gamma \lesssim 1000$ for intermediate-Z materials with an accuracy of a few percent. At the upper limit, radiation losses begin to be important, at at lower energies, the projectile velocity becomes comparable to atomic electron "velocities" [2]. Both limits are Z dependent. In the region of Bethe-Bloch, the energy loss is decreasing as $1/\beta^2$ until it reaches the minimum at $\beta\gamma \approx 3$. Particles with this minimum amount of energy loss are referred to as Minimum Ionizing Particles (MIPs). Figure 1.1 shows the ionization energy loss for electrons, muons, pions, kaons, protons and deuterons in air. As their energy loss curves are well separated, these particles can be discriminated according to their deposited energy. However, this discrimination is no longer achievable for $\beta\gamma$ values above 3.

As the particle energy increased, its electric field flattens and extends, so that the distant-collision contribution to Bethe-Bloch equation increased as $\ln \beta\gamma$. Another effect responsible for the relativistic rise originates from the $\beta^2\gamma^2$ growth of T_{max}, which is due to (rare) large energy transfers to a few electrons. When these events are excluded, the energy deposit in an absorbing layer approaches a constant value [3].

For energy loss at low energies shell corrections must be included in the square bracket of Eq. (1.1) to correct for atomic binding. A detailed discussion of low-energy corrections to the Bethe formula can be found in [4]. When the correction are properly included, the Bethe treatment is accurate to about 1% down to $\beta \approx 0.05$, or about 1 MeV for protons.

For $0.01 < \beta < 0.05$, there is no satisfactory theory. For protons, one usually relies on the phenomenological fitting formulae developed by Andersen and Ziegler [4, 5].

The energy loss is a stochastic process because of two sources of variations: the transferred energy in a single collision and the actual number of collisions. The fluctuation of the number of collisions can be described by the Poisson law. The quantity $(dE/dx)\delta x$ represents the mean energy loss via interactions with electrons in a layer of thickness δx. For finite thickness, strong fluctuations around the average energy loss exist. The energy-loss distribution is strongly asymmetric, skewed towards high values. For detectors of moderate thickness x, the energy loss probability distribution is firstly described by the Landau distribution [6]. The Landau distribution is not an accurate description of the energy loss in thin absorbers, such as silicon detectors (i.e. CMOS sensors). While the most probable energy loss can be calculated adequately, its distribution becomes significantly wider than the Landau width [2]. Thinner absorbing layers exhibit a larger deviation from the Landau distribution, and the most general model to be applied is the Vavilov theory. Figure 1.2 presents the energy loss distributions for 500 MeV pions incident on thin silicon detectors. The position of the peak in the distribution defines the most probable energy loss. The mean energy loss is shifted to a higher energy.

In reality, detectors only measure the energy which is actually deposited in their sensitive volume rather than the total energy loss by the impinging particle. Some of the energy lost by an impinging particle is carried away by knock-on electrons (δ-rays) or by fluorescence photons or in a much less extent by Cherenkov radiation and Bremsstrahlung.

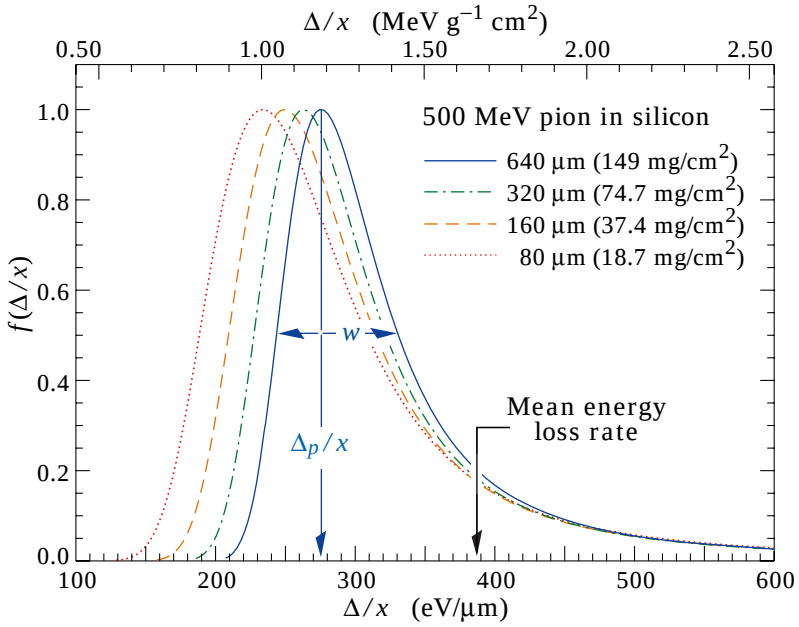

Figure 1.2: Straggling functions in silicon for 500 MeV pions, normalized to unity at the most probable value δ/x. The width w is the full width at half maximum [2].

1.1.1.2 Energy-range relation

The range $R(E)$ of a charged particle of kinetic energy E_0 is the integral of the stopping power over the full energy spectrum of the incident particle

$$R(E) = \int_0^{E_0} \frac{dE}{-dE/dx} \tag{1.3}$$

Because of the fluctuations of the energy loss and the multiple Coulomb scattering in the material, the range of charged particles in matter shows statistical fluctuations around a mean value, termed as *range straggling*. Equation (1.1) may be integrated to find the total (or partial) CSDA (Continuous Slowing Down Approximation) range R for a particle which loses energy only through ionization and atomic excitation. However, since the energy loss is a complicated function of the energy, in most cases approximations of this integral are used. Experimentally, some empirical and semi-empirical formulae have been proposed for certain particle species in the given energy ranges.

Range of α-particles Several empirical and semi-empirical formulae have been given to calculate the range of α-particles in air. For example [7]

$$R_\alpha^{air} = \begin{cases} 0.56E_\alpha & \text{for } E_\alpha < 4 \text{ MeV} \\ 1.24E_\alpha - 2.62 & \text{for } 4 \text{ MeV} \leq E_\alpha \leq 8 \text{ MeV} \end{cases} \tag{1.4}$$

where the kinetic energy E_α is in MeV, and the R_α^{air} is in cm.

The range of α-particles in other materials obeying scale law can be roughly estimated by

$$R_\alpha = 3.37 \times 10^{-4} R_\alpha^{air} \frac{\sqrt{A}}{\rho} \tag{1.5}$$

where A (g/mol) is the atomic weight, and ρ (g/cm^3) is the density of the material, respectively.

Range of protons In air the range (in cm) of protons having energy E_p can be described by Eq. (1.6) [8]

$$R_p^{air} = 100 \cdot (\frac{E_p}{9.3})^{1.8} \quad 0.6 \text{ MeV} \leq E_p \leq 20 \text{ MeV}, \tag{1.6}$$

while for aluminum, one can use Eq. (1.7) [9]

$$R_p^{Al} = \begin{cases} 3.837 E_p^{1.5874} & \text{for } 1.13 \text{ MeV} < E_p \leq 2.677 \text{ MeV} \\ \frac{2.837 E_p^2}{0.68 + \log E_p} & \text{for } 2.677 \text{ MeV} \leq E_p \leq 18 \text{ MeV}, \end{cases} \tag{1.7}$$

where the R_p^{Al} is given in mg/cm^2.

1.1.2 Interaction of electrons

There is a significant difference between electron and heavy charged particle behaviors when passing through matter. The way an electron interacts with matter depends, to a large extent, on its energy. At low to moderate energies, the primary types of interaction are: ionization, Moeller scattering, and Bhabha scattering. At higher energies the Bremsstrahlung process dominates the energy loss.

1.1.2.1 Energy loss

Ionization energy loss by electrons differs from loss by heavy particles because in the case of electrons the mass of the incident particle and the target electron are the same. Apart from this interaction process, the incident electron interacts with the nucleus of the absorber atom via Bremsstrahlung resulting in abrupt changes in the electron direction. Hence the stopping power for electrons consists of two components, collisional and radiative

$$(\frac{dE}{dx})_{tot} = (\frac{dE}{dx})_{coll} + (\frac{dE}{dx})_{rad} \tag{1.8}$$

where *coll* denotes the collisional term due to ionization and excitation, and *rad* denotes the radiative term due to electromagnetic radiation. The collisional energy loss rate rises logarithmically with energy, while bremsstrahlung losses rise nearly linearly, and dominate above a few tens of MeV in most materials.

1.1.2.2 Passage of electrons

The trajectory of an electron is often erratic and winding, due to the fact that it will experience multiple scattering and will suffer Bremsstrahlung in the absorber. The mean free path is then defined as the thickness of a material which reduces the intensity of a monoenergetic beam of electrons to half. To estimate the value of this path, there is no analytical formula but only empirical formulas. For example, the expression is given by Katz and Penfold [10]

$$R_{max} = \begin{cases} 0.412 E_e^{1.265-0.0954\ln(E_e)} & \text{for 10 keV} \leq E_e \leq 2.5 \text{ MeV} \\ 0.530 E_e - 0.106 & \text{for 2.5 MeV} \leq E_e \leq 20 \text{ MeV} \end{cases} \tag{1.9}$$

where the maximum range R_{max} is in g/cm^2, and the energy E_e is in MeV.

1.1.2.3 Radiation length

High energy electrons predominantly lose energy by Bremsstrahlung. The energy loss by Bremsstrahlung can be described by

$$E = E_0 e^{-x/X_0} \tag{1.10}$$

where E_0 is the energy of the incident electron, and x/X_0 is the thickness of the scattering medium, measured in units of radiation length X_0. The radiation length X_0 is defined as the mean distance over which a high-energy electron loses $1 - \frac{1}{e}$ of its energy by Bremsstrahlung. The radiation length X_0, usually measured in g/cm^2, is a property of the material. A good approximation is given by Dahl [11]

$$X_0 = \frac{716.4 \cdot A}{Z(Z+1)\ln(287/\sqrt{Z})} \tag{1.11}$$

where A, Z are the atomic weight and atomic number of the medium, respectively.

1.1.3 Interaction of photons

Photons are detected indirectly via interactions with the medium of the detector. In our energy range of interest, photons interact with matter by mainly three processes: photoelectric effect, Compton effect and pair production. These interaction processes have different energy thresholds and high cross-sections regions for different materials. The relative importance of these three interactions is a function of the energy of incident photon and of the atomic number of the detector material, as shown in Fig. 1.3. In every photon interaction, the photon is either completely absorbed or scattered. In the following, we describe with more details these different processes.

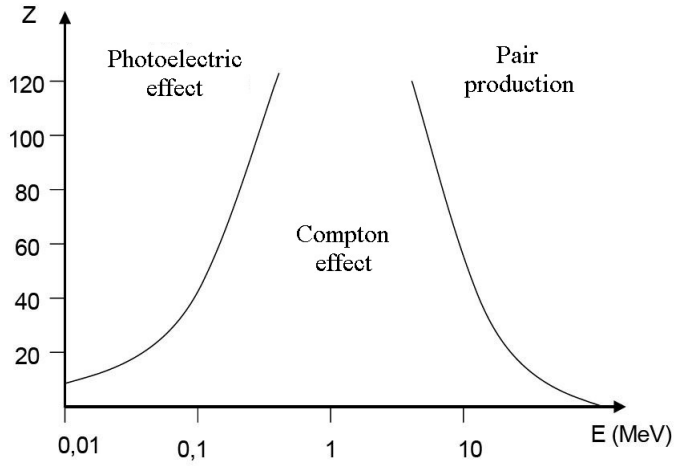

Figure 1.3: Regions where the photoelectric effect, Compton effect and pair production dominate as a function of the photon energy and the atomic number Z of the absorber.

1.1.3.1 Photoelectric effect

This effect predominates for photons of energy below 100 keV (or 300 keV for heavy material). In the photoelectric interaction, the photon is absorbed by the atom, generating photoelectron. Since an atom is much more massive than an electron, the ejected electron takes practically all the energy and momentum of the photon. The kinetic energy of the ejected electron (E_{pe}) is determined by the electron binding energy (E_B), as described by Eq. (1.12).

$$E_{pe} = h\nu - E_B \tag{1.12}$$

where $h\nu$ is the kinetic energy of the incident photon. If the resulting photoelectron has sufficient kinetic energy, following secondary ionization may occur along its trajectory. The vacancy created by the emission of the photoelectron is immediately filled by another atomic electron, emitting then either a characteristic X-ray or an Auger electron. If these radiations are stopped within the detector material, then the deposited energy corresponds to the full energy of the incident photon. This feature of the photoelectric effect allows to calibrate the gain of the detector with its readout system if the required energy for creating a single electron-hole pair is known. The mass attenuation coefficient for photoelectric absorbtion decreases with the increase of the photon energy. For a given value of energy, the attenuation coefficient increases with the atomic number Z of the material. The relevant cross section σ_{pe} can be approximated by

$$\sigma_{pe} \propto \frac{Z^{4.35}}{(h\nu)^n} \tag{1.13}$$

where n is roughly 3 for $h\nu <$ 0.5 MeV, and $n \simeq 1$ for $h\nu \simeq 2MeV$.

1.1.3.2 Compton effect

Compton effect becomes significant for photons of energy between 100 keV and 5 MeV(or 10 MeV for light materials). The Compton effect is the scattering of photons off quasi-free atomic electrons. Part of the energy of the photon ($h\nu$) is transferred to the emitted electron, and its direction is changed. The energy of the scattered photon $E'_\gamma = h\nu'$ is given by

$$E'_\gamma = \frac{h\nu}{1 + \eta(1 - \cos\theta)} \tag{1.14}$$

where $\eta = h\nu/m_e c^2$ with $m_e c^2 = 511$ keV, and θ is the scattering angle of the photon. The secondary electron is ejected with an angle φ with respect to the direction of the incident photon, and its kinetic energy E_e given by Eq. (1.15).

$$E_e = \frac{\eta(1 - \cos\theta)}{1 + \eta(1 - \cos\theta)} h\nu \tag{1.15}$$

with a simple relationship between the angles θ and φ: $\cos\varphi = (1 + \theta)\tan(\theta/2)$.

1.1.3.3 Pair production

If the photon energy reaches more than 1.022 MeV, the production of electron-positron pairs in the Coulomb field of a nucleus or an electron is possible. The threshold energy is given by the rest masses of two electrons plus the energy transferred to the nucleus or electron. Consequently, the effective threshold is about $2m_e c^2$ (1.022 MeV) or $4m_e c^2$ (2.044 MeV) for the interaction with a nucleus or an electron, respectively.

1.1.3.4 Attenuation of photons

When a monoenergetic beam of photons with intensity I_0 strikes the detector material of thickness x, the intensity of photons, $I(x)$, penetrating without any interaction is given by

$$I(x) = I_0 e^{-\mu_l x} \tag{1.16}$$

where μ_l (in m^{-1} or cm^{-1}) is the linear attenuation coefficient, describing the probability of interaction per unit distance. A more useful quantity, the mass attenuation coefficient μ_m is defined as μ_l/ρ (with ρ is the density of the material). μ_m is related to the cross section for the various interaction processes of photons according to

$$\mu_m = \frac{N_A}{A} \sum_i \sigma_i. \tag{1.17}$$

where σ_i is the atomic cross section for the process i, A is the atomic weight and N_A is the Avogadro number. The mass attenuation coefficient depends strongly on the photon energy, in

fact like the various cross sections.

1.1.4 Interaction of neutrons

Neutrons, being uncharged, undergo extremely weak electromagnetic interactions, therefore pass through matter largely unimpeded, only interacting with atomic nuclei. As they are highly penetrating and can induce secondary deep body ionizing radiation doses, the health risk associated with neutrons is significant.

1.1.4.1 Classification of neutrons

Neutron reactions can take place at any energy, and the interaction type strongly depends on neutron energy. Neutrons are usually classified on the basis of their kinetic energies but without clear established limits. Table 1.1 summarizes the main categories that are commonly used in neutron dosimetry:

Type of neutrons	Energy
Ultra-cold	< 100 neV
Cold	< 25 meV
Thermal	25 meV – 1 eV
Intermediate	1 eV – 100 keV
Fast	100 keV – 20 MeV
Relativistic	20 MeV – 1 GeV
Ultra-relativistic	1 GeV – 10 TeV

Table 1.1: Classification of neutrons based on their energies.

1.1.4.2 Cross sections of neutrons

The probability of a particular reaction occurring between a neutron and an individual particle or nucleus is defined through its microscopic cross section (σ). It is dependent not only on the kind of nucleus involved, but also on the energy of the neutron. Another cross section, known as the macroscopic cross section (Σ), is defined to describe the probability per unit path length that a particular type of interaction will occur. The macroscopic cross section (Σ) is related to the microscopic cross section (σ) by

$$\Sigma = N\sigma \tag{1.18}$$

where N is the atom density of the material (atoms/cm^3). All process can be combined to calculate the total probability per unit path length that any type of interaction will occur by

the Eq. (1.19).

$$\Sigma_{tot} = \Sigma_{sca} + \Sigma_{abs} \tag{1.19}$$

where Σ_{sca}, Σ_{abs} represent the macroscopic cross section for scattering and absorption, respectively.

1.1.4.3 Different types of interactions

This section introduces five reactions that can occur when a neutron interacts with a nucleus. In the first two, known as scattering reactions, a neutron emerges from the reaction. In the remaining reactions, known as absorption reactions, the incoming neutron is absorbed by the nucleus with the emission of secondary particles. For fast and thermal neutrons, scattering and absorption reactions are prominent, respectively.

Elastic scattering (n,n) Elastic scattering, being the principle mode of interaction of neutrons with atomic nuclei, occurs at all neutron energies. A neutron collides with a nucleus, transfers some energy to it, and bounces off in a different direction. The amount of kinetic energy transferred to the target strongly depends on the nucleus mass and the angle of impact. Elastic scattering is the most likely interaction between fast neutrons and low mass absorbers. For an elastic collision by conservation of the momentum and the kinetic energy, the kinetic energy of the recoil nucleus E_r is given by

$$E_r = E_n \cdot \frac{4A}{(1+A)^2}(\cos^2\theta) \tag{1.20}$$

where E_n is the energy of the incident neutron, θ is the angle between the recoil and the target nucleus in the laboratory system, and A is the ratio of the mass of the target nucleus to the neutron mass. Fast neutron detectors take advantage of the fact that a fraction of the neutron's kinetic energy can be transferred to the target nucleus producing an energetic recoil nucleus. When a hydrogen absorber (A = 1) is used, the transferred energy to the recoil proton increases to $E_p = E_n \cos^2\theta$. This indicates that the fast neutrons could transfer all their energy in a single interaction with the hydrogen nucleus (proton). This reaction is the main process used for the fast neutron detection in Chapter 5 of this work.

Inelastic scattering (n,n') Inelastic scattering is similar to elastic scattering except that the nucleus undergoes an internal rearrangement into an excited state from which it subsequently emits γ-rays. The total kinetic energy of the outgoing neutron and nucleus is much less than the kinetic energy of the incoming neutron, because part of the original kinetic energy is used to excite the compound nucleus. The emitted neutron may or may not be the incoming one. The average energy loss depends on the energy levels of the target nucleus. The inelastic scattering can occur only if the energy of the incoming neutron reaches the required energy for exciting the

target nucleus. This threshold energy depends on the type of nucleus. In particular, the inelastic scattering with hydrogen is impossible since the hydrogen nucleus does not have excited states.

Radiative capture (n,γ) In this process, the nucleus is excited but the level of excitation is insufficient to eject a neutron. All the energy of the incoming neutron is transferred to the nucleus as kinetic energy and excitation energy. To return to a stable state, the excited nucleus emits γ-rays. The incoming neutron remains in the nucleus, leading to the creation of a heavier isotope of the original element. Many of these may be radioactive and decay over time in different ways. As neutrons reach thermal or near thermal energies, their probability to be captured by an absorber nucleus increases. In this energy range, the cross section of many nuclei has been found to be inversely proportional to the velocity of the neutron.

Nuclear transmutation (n,p), (n,α) In a nuclear transmutation (charged particle reaction), the incident neutron enters the target nucleus forming a compound nucleus. The newly formed compound nucleus is in an excited state and ejects a new particle, while the incident neutron remains in the nucleus. In this process the total number of protons in the target nucleus is reduced by one for proton emission and by two for α-particle emission. The original element is thus changed or transmuted into a different element. After the new particle is emitted, the remaining nucleus may or may not stay in an excited state depending upon the mass-energy balance of the reaction. This reaction is important in neutron dosimetry. As the Q-values for most of these reactions are negative, the processes are usually endoenergetic. However, the nuclear transmutation reaction could be exoenergetic for some specific nuclei. Some of them can be used to detect neutrons of low energy with respect to their high cross sections, including reactions: ^{3}He(n,p)^{3}H, ^{6}Li(n,α)^{3}H, and ^{10}B(n,α)^{7}Li (see Fig. 1.4). The latter reaction is shown below:

$$\begin{aligned} {}^{1}_{0}\mathrm{n} + {}^{10}_{5}\mathrm{B} &\rightarrow {}^{4}_{2}\mathrm{He}\ (1.78\ \mathrm{MeV}) + {}^{7}_{3}\mathrm{Li}\ (1.02\ \mathrm{MeV}) \qquad (6\%) \\ &\rightarrow {}^{4}_{2}\mathrm{He}\ (1.47\ \mathrm{MeV}) + {}^{7}_{3}\mathrm{Li}\ (0.84\ \mathrm{MeV}) + \gamma\ (0.48\ \mathrm{MeV}) \qquad (94\ \%) \end{aligned}$$

Neutron producing reaction (n,xn) This reaction is observed with high energy neutrons. It occurs if the target nucleus gets excited into an unstable state as with the inelastic scattering, but in this case two or three neutrons instead one are emitted. This is an uncommon reaction occurring in only a few isotopes.

Fission (n,f) In the fission reaction the incident neutron enters the heavy nucleus target ($Z > 90$), forming a compound nucleus that is excited to such a high energy level (excitation energy $E_{exc} >$ critical energy E_{crit}) that the compound nucleus splits into two (or more) fragments. The fission process is always accompanied by prompt emission of one or more neutrons that

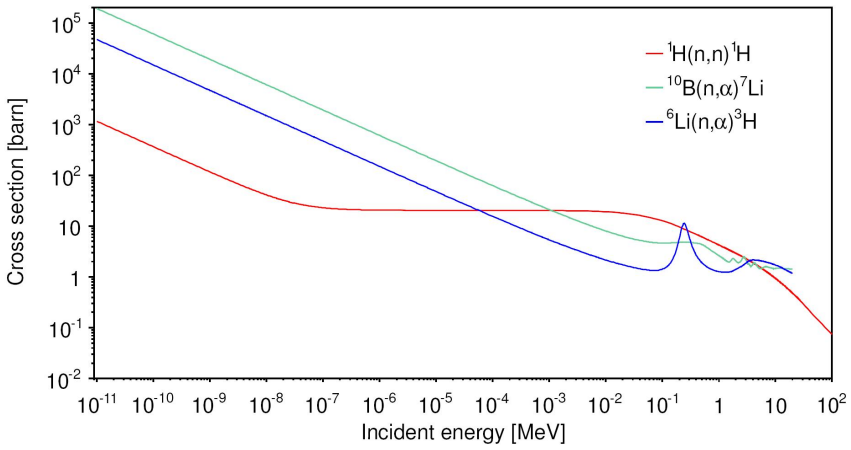

Figure 1.4: Cross sections of the main reactions used for the detection of low-energy neutrons [12].

may lead to further fission of other nuclei leading to a chain reaction. This reaction are likely for several isotopes of thorium, uranium, neptunium, plutonium, and higher mass actinides.

1.1.4.4 Neutron sources in workplaces

Neutron radiation fields can be produced by natural or induced phenomena, with radionuclide sources or by nuclear reactions [13]. A great variety of neutron fields can be found in the nuclear industry, the research laboratories, the medical facilities, the places where radionuclide sources are used for testing and process control, and in the cosmic-rays. These different types of neutron sources involve neutron energies from 1 meV to hundreds of MeV and up to 10^{18} eV in cosmic environment. Photons emission from most of the neutron's nuclear interactions with nuclei of the materials, results in n/γ mixed fields. Neutron fields can be classified considering their different application areas.

Neutrons in nuclear energy production and fuel cycle Neutrons could be found at power production, at the production, reprocessing and transportation of nuclear fuel. These neutrons are created by neutron-induced reactions and spontaneous fission of heavy nuclei. Their spectra commonly exhibit three regions, a fast component up to a few MeV, an intermediate component and a thermal contribution. The shape of these three components, their amplitude, the mean energy of the high energy peak as well as the directionality of the field depend on the shielding and surrounding structures [13].

Neutron sources for industrial uses Neutron sources provided by radionuclide sealed sources or by particle accelerators or by (α, n) reactions are used for various industrial applications, such as radiography, material activation analysis, mineral resource exploration, in-

strument calibration in radiation protection, quality control of neutron absorber materials and moisture gauging. Sources of ^{252}Cf, ^{241}Am-Be and ^{238}Pu-Be are commonly used in industry. ^{252}Cf is preferably used for applications in reprocessing plant [13]. Its spontaneous fission decay emits neutrons at the rate of about 2.30×10^{12} s^{-1} per gram. Compared to the neutron sources created by (α, n) reactions, the encapsulated sources of ^{252}Cf have much smaller dimensions. The main drawback of ^{252}Cf for some applications may be its high cost and relatively short half-life (2.65 years), but its well defined spectrum shape is a real advantage over other sources.

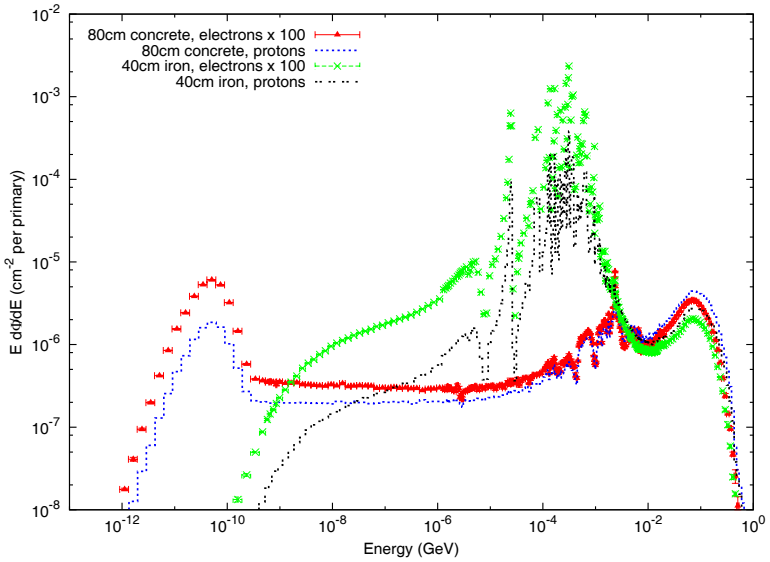

Figure 1.5: Neutron energy spectra from 25 GeV proton and electron beams on a thick copper target. Spectra are evaluated at 90° to the beam direction behind 80 cm of concrete or 40 cm of iron. All spectra are normalized per beam particle. For readability, spectra for electron beam are multiplied by a factor of 100 [2].

Neutron sources at nuclear research laboratories Neutrons, either as primary beams or as secondary particles (considered as parasite radiations) are widely produced in both fundamental and applied research laboratories. These neutrons are preliminarily generated by accelerators or research nuclear reactors. The energy of the neutrons, depending on the production process, varies from several eV up to hundreds of MeV. We can mention the AMANDE (Accelerator for metrology and neutron applications for external dosimetry) facility, providing monoenergetic neutron fields between 2 keV and 20 MeV. Neutrons dominate the particle environment outside thick shielding ($>$ 1 m of concrete) for high energy ($>$ a few hundred MeV) electron and hadron accelerators [2]. For instance, at electron accelerators, neutrons are generated via photonuclear reactions from bremsstrahlung photons. Typical neutron energy spectra outside of concrete (80 cm thick, 2.35 g/cm^3) shows a low-energy peak at around 1 MeV and a high-energy shoulder at

around 70-80 MeV as well as a pronounced peak at the thermal neutron energies (see Fig. 1.5). At proton accelerators, neutron yields emitted per incident proton by different target materials are roughly independent of proton energy between 20 MeV and 1 GeV. Typical neutron energy spectra outside of concrete and iron shielding are presented in Fig. 1.5. A special mention should be made to the ITER (International Thermonuclear Experimental Reactor), which may produce excessive neutron fluxes with energies around 2.5 MeV from the deuterium-deuterium discharge reaction and around 14 MeV from the triton-deuterium reaction [14].

Neutron sources in medical facilities Neutron therapy is well known to be especially efficient for the treatment of salivary and prostate tumors, as well as sarcomas [15]. Neutron beams are produced by high energy protons or deuterons impinging thick or semi-thick beryllium targets through ^{9}Be(p,n)^{9}B or ^{9}Be(d,n)^{10}B reactions [13]. The protons or deuterons are accelerated with linear accelerators or cyclotrons. As cyclotron technology has been improved significantly since 1980s, cyclotrons dedicated to the production of the standard PET (Positron Emission Tomography) radioisotopes are now installed in many hospitals. Around PET cyclotrons, neutrons are produced as secondary particles and may be scattered with the PET cyclotron vault. As a consequence, thermal neutrons could also exist accompanying MeV neutrons. In the case of LINACs (LINear electron ACcelerators), neutrons can be generated either by (e^{-},n) or (γ,n) reactions, when the energy of primary electron beams are more than 7-8 MeV. In the LINAC treatment rooms, neutron spectra exhibit from thermal to a few MeV. Neutrons are also unavoidably present in hadron and ion therapy facilities, and these therapies are now much preferred over direct neutron irradiation.

Cosmic-ray induced neutrons in the atmosphere Cosmic radiation may originate from Galactic Cosmic Radiation (GCR) or Solar Particle Event (SPE). The galactic cosmic radiation consists of about 86% protons, 11% alpha particles, 2% electrons and 1% heavy nuclei. The energy of the nuclei can reach up to 10^{21} eV. When they penetrate the magnetic fields of the earth, they interact with atoms of the atmosphere and produce secondary particles, such as neutrons, protons, pions, photons, electrons and muons [16]. The cosmic-ray induced neutron field is complex and isotropic. It varies with altitude, geomagnetic latitude and solar activity. In general, cosmic neutron fields in atmosphere exhibit two high energy peaks, around 1 MeV and 100 MeV. The peak at around 1 MeV corresponds to the evaporation process. While the peak at 100 MeV is attributed to the neutrons produced by the pre-equilibrium and intranuclear cascade processes. The thermal component can be only found at ground level, as it is attributed to the Earth's albedo neutrons.

1.2 Radiological protection quantities

Radiological protection is concerned with controlling exposures to ionizing radiation in order to prevent acute damage and to limit the risk of long term health effects to acceptable level. To quantify the extent of exposure to ionizing radiation from both whole and partial body external irradiation and from intakes of radionuclides, specific protection quantities have been developed for dosimetric and radiological protection by the ICRP (International Commission on Radiation Protection) [17, 18].

1.2.1 Primary standard quantities

1.2.1.1 Activity

The activity A is the expectation value of the number of nuclear decays occurring in a given quantity of material per unit time. It is given by

$$A = \frac{dN}{dt} \tag{1.21}$$

The SI unit of activity is s^{-1}, with the specific name becquerel (Bq, 1 Bq = 1 s^{-1}).

1.2.1.2 Fluence

Radiation field quantities are defined at any point in a radiation field. The quantity fluence, Φ, is defined as the number of particles dN incident upon a small sphere of cross sectional area dS, given by

$$\Phi = \frac{dN}{dS} \tag{1.22}$$

In dosimetric calculations, fluence is frequently expressed in terms of the lengths of the particle trajectories through a small volume dV, thus Φ is given by

$$\Phi = \frac{dl}{dV} \tag{1.23}$$

where dl is the sum of the lengths of trajectories through the volume dV.

As fluence always needs the additional specification of the particle and the particle energy as well as directional distributions, it is not really practicable for general use in radiological protection and the definition of safety limits. Its correlation with the radiation detriment is also complex.

1.2.1.3 Absorbed dose

The absorbed dose, D, is the fundamental physical quantity in radiological protection, and is used for all types of ionizing radiation and any irradiation geometry. It is defined as the quotient

of the mean energy $d\bar{\varepsilon}$ imparted by ionizing radiation in a volume element of a specified material, and the mass dm

$$D = \frac{d\bar{\varepsilon}}{dm} \tag{1.24}$$

The SI unit of the absorbed dose is the Gray (J/kg). The definition of the absorbed dose takes account of the radiation fields as well as of all of its interactions with matter inside and outside the specified volume. It does not take account of the atomic structure of the matter and of the stochastic nature of the interactions. Absorbed dose is defined at any point in matter and is a measurable quantity.

1.2.1.4 Linear energy transfer

The Linear Energy Transfer (LET) is the mean energy dE transferred to materials by a charged particle owing to collisions with electrons in crossing a distance dl in matter. It is given by

$$LET = \frac{dE}{dl} \tag{1.25}$$

At a given absorbed dose, the imparted energy ε in a small tissue volume, e.g., in a cell, is given by the sum of the deposited energies of all individual events in that volume. The fluctuations of ε are caused by the variation in the number of events and in the deposited energy of each event. For low-LET radiations (photons and electrons) the energy imparted in each event is relatively low. At low doses, the number of cells encountering of energy deposition events is higher than in the case of high-LET radiation (neutrons and heavy charged particles). Therefore, the fluctuation in the energy deposited on the cells is smaller for low-LET than for high-LET radiations.

1.2.1.5 kerma

Kerma is the sum of the initial kinetic energies, $\sum dE_{tr}$, of all charged particles liberated by indirectly ionizing radiation (X, γ, neutrons) in a volume element of the specified material divided by the mass dm of this volume element. It is given by

$$K = \frac{\sum dE_{tr}}{dm} \tag{1.26}$$

The SI unit of kerma is the Gray.

1.2.2 Protection quantities

Protection quantities are dose quantities developed for radiological protection. They allow quantification of the extent of exposure to ionizing radiation from both whole and partial body external irradiation and from intakes of radionuclides. They are based on evaluation of the energy imparted to organs and tissues of the body.

1.2.2.1 Mean absorbed dose

The definition of the protection quantities is based on the mean absorbed dose, $D_{T,R}$, due to radiation of type R and averaged over the volume of a specified organ or tissue T. $D_{T,R}$ is defined by

$$D_{T,R} = \frac{\int_T D_R(x,y,z)\rho(x,y,z)dV}{\int_T \rho(x,y,z)dV} \tag{1.27}$$

where V is the volume of the organ or tissue region, $D_R(x,y,z)$ the absorbed dose at a point (x,y,z) in the region and $\rho(x,y,z)$ the mass density at this point.

$D_{T,R}$ depends on the type of organ or tissue and on the radiation type. It is not able to estimate the radiation risk due to induced stochastic health effects. For this reason, additional quantities have been defined to take into account the differences in biological effectiveness of different radiations and the differences in sensitivities of organs and tissues to stochastic health effects.

1.2.2.2 Equivalent dose

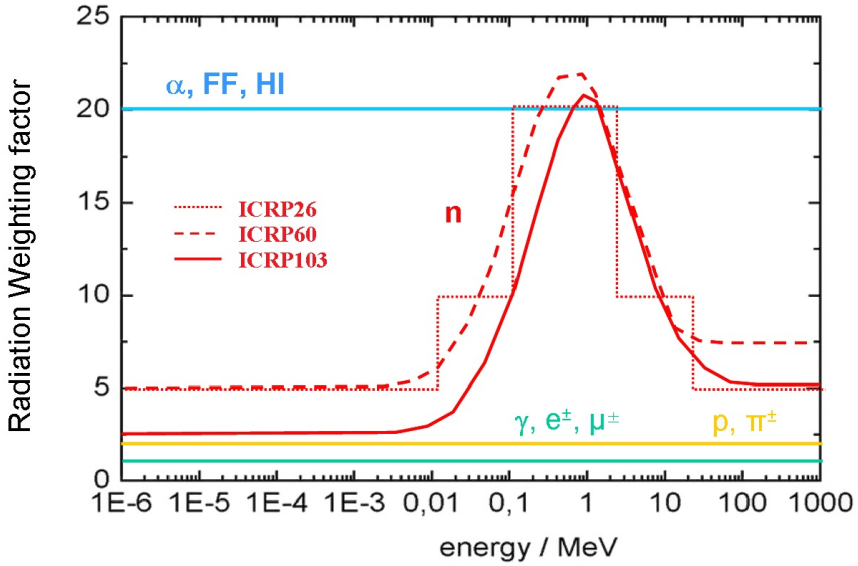

Figure 1.6: Radiation weighting factors w_R for different types of radiations from ICRP26 [19], ICRP60 [17], ICRP103 [18].

The equivalent dose H_T in an organ or tissue T is equal to the sum of the mean absorbed doses $D_{T,R}$ in the organ or tissue caused by different radiation types R weighted with its radiation weighting factor w_R. It is defined by

$$H_T = \sum_R w_R D_{T,R} \tag{1.28}$$

The SI unit of equivalent dose is J/kg and has the specific name Sievert (Sv). H_T expresses long-term risks (primarily cancer and leukemia) from low-level chronic exposure. The values of w_R are mainly based upon experimental values of the Relative Biological Effectiveness (RBE) for various types of radiations compared to the effects of x- and γ-rays at low doses. A set of w_R values recommended by ICRP Publication 103 (ICRP103) are given in Table 1.2. Figure 1.6 presents w_R values as a function of neutron energy defined in ICRP103 compared to those defined in ICRP26 and ICRP60.

Radiation type		w_R
photons, electrons and muons		1
protons and charged pions		2
alpha particles, fission fragments, heavy ions		20
neutrons	$E_n < 1$ MeV	$2.5 + 18.2 \exp[-(\ln E_n)^2/6]$
	1 MeV $\leq E_n \leq$ 50 MeV	$5.0 + 17.0 \exp[-(\ln(2E_n))^2/6]$
	$E_n >$ 50 MeV	$2.5 + 3.25 \exp[-(\ln(0.04E_n))^2/6]$

Table 1.2: Radiation weighting factors w_R from ICRP103 [18].

1.2.2.3 Effective dose

The equivalent dose can be used for one tissue type only as it does not address the sensitiveness of tissue types to the same type of radiation. ICRP60 introduced the notion of effective dose E, which is defined by the weighted sum of tissue equivalent dose as

$$E = \sum_T w_T H_T = \sum_T w_T \sum_R w_R D_{T,R} \tag{1.29}$$

where w_T is the tissue weighting factor for tissue T with $\sum_T w_T = 1$. The sum is performed over all organs and tissues of the human body considered. The w_T values are chosen to represent the contributions of individual organs and tissues to overall radiation detriment from stochastic effects. The unit of effective dose is the Sievert (Sv). Based on the last epidemiological data for cancer induction, new w_T values for different organs and tissues recommended by ICRP103, are shown in Table 1.3.

1.2.3 Operational quantities

The body-related protection quantities, equivalent dose H_T and effective dose E, are not measurable in a straightforward manner. On the other hand, effective dose is not appropriate in area monitoring, because in a non-isotropic radiation field its value depends on the orientation of the human body. Furthermore, instruments for radiation monitoring need to be calibrated in terms of a measurable quantity for which calibration standards exist. Therefore, operational

Tissue	w_T	$\sum_T w_T$
Bone-marrow (red), colon, lung, stomach		
breast, remainder tissues	0.12	0.72
Gonads	0.08	0.08
Bladder, oesophagus, liver, thyroid	0.04	0.16
Bone-surface, brain, salivary glands, skin	0.01	0.04
Total		1.00

Table 1.3: Tissue weighting factors w_T from ICRP103 [18].

quantities are defined to provide a conservative estimate or upper limit for the value of the protection quantity related to an exposure or potential exposure of persons under most irradiation conditions.

The quantity dose equivalent, H, is defined by

$$H = Q \cdot D \tag{1.30}$$

where D is the absorbed dose at the point of interest in tissues, and Q the corresponding quality factor at this point. The value of Q is determined by the type and energy of charged particles passing a small volume element at this point. It is well known that the biological effectiveness of a radiation is related to the ionization density along the track of charged particles in tissue. Therefore, Q is defined as a function of the unrestricted linear energy transfer, L_∞ (often denoted as L or LET), of charged particles in water. The quality factor function $Q(L)$ was given in ICRP60

$$Q(L) = \begin{cases} 1 & \text{if} \quad L < 10 \text{ keV/µm} \\ 0.32L - 2.2 & \text{if} \quad 10 \leq L \leq 100 \text{ keV/µm} \\ 300/\sqrt{L} & \text{if} \quad L > 100 \text{ keV/µm} \end{cases} \tag{1.31}$$

This function takes into account various results of radiobiological investigations on cellular and molecular systems as well as results of animal experiments. The quality factor Q at a point in tissue is then given by

$$Q = \frac{1}{D} \int_{L=0}^{\infty} Q(L) D_L dL \tag{1.32}$$

where $D_L = \frac{dD}{dL}$ is the distribution of the absorbed dose in the linear energy transfer for the charged particles contributing to the absorbed dose at the point of interest. This function is particularly important for neutrons because various types of secondary charged particles are produced in organic tissues by the neutron interactions.

Different operational dose quantities are required for the different tasks in radiological protection, including area monitoring for controlling the radiation in workplaces and for defining controlled or restricted areas, as well as individual monitoring for the control and limitation of in-

dividual exposures. For the different tasks of monitoring of external exposure different quantities are defined.

1.2.3.1 Operational quantities for area monitoring

For all types of radiation, the operational quantities for area monitoring are defined on the basis of a dose equivalent value at a point in a simple phantom, the ICRU (International Commission on Radiation Units and measurements) sphere. It is a sphere of tissue-equivalent material that adequately approximates the human body concerning the scattering and attenuation of the radiation fields under consideration. It has a diameter of 30 cm, a density of 1 g/cm^3, as well as a mass composition of 76.2% oxygen, 11.1% carbon, 10.1% hydrogen and 2.6% nitrogen.

Ambient dose equivalent The ambient dose equivalent $H^*(d)$ at a point in a radiation field is the dose equivalent that would be produced by the corresponding expanded and aligned field in a ICRU sphere at a depth of d (mm) on the radius vector opposed to the direction of the aligned field.

The quantity ambient dose equivalent is mainly used for strongly penetrating radiation, e.g., photons (above about 12 keV) and neutrons. The recommended depth is 10 mm, then $H^*(d)$ is written as $H^*(10)$.

Directional dose equivalent The directional dose equivalent $H'(d,\Omega)$ at a point in a radiation field, is the dose equivalent that would be produced by the corresponding expanded field in the ICRU sphere at a depth d, on a radius in a specified direction Ω. It is suitable for weakly penetrating radiation, e.g., α- and β-particles. The recommended depth is 0.07 mm, in which case the directional dose equivalent must be $H'(0.07,\Omega)$.

In practice, $H'(0.07,\Omega)$ is almost exclusively used in area monitoring. For unidirectional radiation incidence the quantity may be written as $H'(0.07,\alpha)$, where α is the angle between the direction Ω and direction opposite to radiation incidence. In radiological protection practice, the direction Ω is often not specified, because the maximum value of $H'(0.07,\Omega)$ at the point of interest is mostly important. It is usually obtained by rotating the dose rate monitor during the measurement and looking for the maximum.

1.2.3.2 Operational quantities for individual monitoring

Individual monitoring of external exposure is usually performed with individual dosemeters (or personal dosemeters) worn on the body, and the operational quantity for individual monitoring takes into account this situation. The true value of the operational quantity is determined by the irradiation situation near the point where the dosemeter is worn. The operational quantity for individual monitoring is the personal dose equivalent, $H_p(d)$. It is the dose equivalent in

ICRU tissue at a depth d in a human body below the position where a personal dosemeter is worn.

As already stated, for penetrating radiation a depth of 10 mm and for weakly penetrating radiation a depth of 0.07 mm is recommended. In special cases of monitoring the dose to the lens of the eye a depth of 3 mm had been proposed to be appropriate. In practice, however, $H_p(3)$ has never been used and no instruments exist for this quantity. Because monitoring of the skin of the head is, in general, considered sufficient for the protection of the eye. Furthermore, $H_p(0.07)$ is also used for monitoring the doses to the extremities from all ionizing radiations.

Task	Operational quantities for Area monitoring	Individual monitoring
Control of effective dose	Ambient dose equivalent $H^*(10)$	Personal dose equivalent $H_p(10)$
Control of skin dose,	Directional dose equivalent $H'(0.07, \Omega)$	Personal dose equivalent $H_p(0.07)$

Table 1.4: Operational quantities for different radiation protection tasks.

Table 1.4 summarizes the operational quantities defined for the different tasks of monitoring of external exposure. In some situations, individual monitoring is not used and area monitoring or computational methods are applied to assess individual exposures. These situations include the assessment of doses to aircraft, prospective dose assessments, assessment of doses in workplaces and the natural environment, and also accidental cases.

1.3 Neutron dosimetry

Neutrons interact with mater through different processes for different energy ranges, leading to a strong dependence of the conversion coefficient of fluence to dose equivalent on energy. Additionally, the particular problems in neutron dosimetry are the large energy range (meV to GeV) in which an event can occur and the variation of the energy ranges due to the absorbed dose. Another problem comes from the fact that neutron fields always contain photon contributions, and in many cases this contribution will be dominant in the dose equivalent. Therefore, discrimination against photons has always been a serious concern in the development of neutron dosemeters, and it is of central importance in this development.

Neutron dosemeters are used both for area monitoring and for individual monitoring. A number of general considerations for the design of neutron dosemeters are stated in ICRU Report 66 [20]. The neutron area dosemeters (neutron area monitors) are intended to determine the ambient dose equivalent $H^*(10)$. The energy dependence of their fluence response should match as closely as possible that of the fluence-to-ambient dose equivalent conversion coefficient. To

measure $H^*(10)$ under all conditions of irradiation, e.g. independence of the direction distribution of the neutron field, the instrument should have a fluence response independent of the angle of the incidence of neutrons. Although $H^*(10)$ is defined in a 'receptor' (the ICRU sphere), its values are assigned to a point in the radiation field without a receptor. This implies that the area dosemeters are used for free-in-air measurements of the external field.

Neutron personal dosemeters are worn on the body and are intended to determine the personal dose equivalent, $H_p(10)$. The energy and angle dependence of their fluence response should match as closely as possible that of the fluence-to-personal dose equivalent conversion coefficient. $H_p(10)$ is defined in the body of the wearer of the personal dosemeter. However, dosemeters are type-tested and routinely calibrated in terms of $H_p(10)$ defined in, and calculated for, a phantom of ICRU tissue of the same size and shape as that on which the dosemeter is fixed for testing. It implies that the response characteristics determined in terms of the phantom quantity are adequately similar to those in terms of the body quantity that would have pertained if the dosemeter had been tested on the body.

Each of the presently available methods for neutron monitoring has advantages and disadvantages. The best choice depends on the specific application. The factors that influence the choice of a monitoring method include [20]:

- operational quantity to be measured (ambient dose equivalent for area and environmental monitoring; personal dose equivalent for individual monitoring);
- neutron and gamma ray field characteristics (energy and direction distribution, dose rate);
- detection limit required;
- dose equivalent range;
- need for immediate reading;
- length of monitoring period;
- environmental conditions (temperature, humidity, vibration, shock);
- size and weight of the device;
- ease of use;
- cost.

1.3.1 Area dosemeter

The area dosemeter includes portable survey meters as well as installed area monitors, and it generally applies to monitoring within facilities.

1.3.1.1 Rem-meters

The most common type of portable neutron area monitor uses a thermal-neutron detector surrounded by a hydrogenous moderator (generally polyethylene), and is commonly referred to as a 'Rem meters'. They are generally hand-held instruments having a mass of 8-10 kg, and provide a reading approximately proportional to the ambient dose equivalent $H^*(10)$. Several

types of detector can serve as the central neutron detector. Spherical survey meters varying in diameter between about 20 cm and 25 cm have been used as commercial survey instruments. Cylindrical neutron survey meters are also commercially used. They typically consist of a circular cylindrical polyethylene moderator, with an inner perforated sleeve of boron-loaded plastic and a central BF_3 proportional counter [21]. When a rem-meter is used as an integrating monitor, gold foils or TLD (Thermoluminescent detectors) chips may also serve as the central detector.

Moderator-based survey instruments are sufficiently sensitive to neutrons and have intrinsically good discrimination against gamma rays. However, all presently available moderator-based survey instruments suffer from a poor energy dependence of dose equivalent response. They typically show a large over-response in the eV and keV region and a under-response in the 10 MeV region, compared to their response at 1 MeV.

Finally, it is to be noted that the official unit of personal dose is no more the rem ("rontgen equivalent in men") but the sievert.

1.3.1.2 Tissue-equivalent proportional counter (TEPC)

A tissue-equivalent proportional counter (TEPC) is a spherical or cylindrical cavity chamber detector constructed with walls of tissue-equivalent plastic and filled with tissue-equivalent gas. It is much smaller and lighter than the moderator-based instruments. This type of instrument allows the simultaneous determination of the absorbed dose to tissue and of the spectrum of pulse heights. In addition, the TEPC is able to provide a simultaneous determination of neutron and gamma ray doses, or dose equivalents, using a single detector. However, its low sensitivity leads to slow response times at low dose rates.

TEPCs have been used as reference standard instruments for calibrating personal dosemeters and providing field correction factors for personal dosemeters [22]. They have also been used for measurements in commercial nuclear power reactors [23] and in calibration facilities [24]. TEPCs can also be used as a reference instrument in high-energy neutron (> 20 MeV) fields. The first TEPC-based ambient monitors for in-flight and space shuttle applications had been developed by Braby et al. [25]. A commercially available hand-held TEPC monitor (REM-500) was tested in high-energy neutron fields by Aroua et al. [26].

1.3.1.3 Superheated emulsions

Superheated-emulsion neutron detectors are often referred to as superheated-drop or bubble detectors. They are based on the superheated droplets dispersed in a firm medium such as a polymer [27]. The suspended droplets consist of over-expanded halocarbon and/or hydrocarbon, which vaporizes upon exposure to the high-LET recoils from neutron interactions. A small vapour bubble is formed and begins to expand by vaporising adjoining liquid. If sufficient energy has deposited in the liquid, the seed bubble grow into larger (i.e., visible) bubble that is trapped by the surrounding gel. Neutron detectors based on superheated emulsions differ primarily in the

way in which the bubbles are detected, which depends on the viscosity of the host medium [20].

Superheated emulsions are particularly suited for neutron dosimetry in mixed fields with a large photon component and high neutron dose rate. Both passive and active superheated-emulsion dosemeters had been developed for area monitoring. The passive devices are need to be removed for reading, repress-urisation or replacement and therefore are not convenient for routine or long-term area monitoring. The active detectors used for area monitoring (installed or portable) have the advantages of alarm capability, easy reading, light weight, and the possibility of remote readout. However, many influence factors, including the storage time, the temperature before irradiation, and the time between sensitization and irradiation as well as the number of re-uses, may effect the reading of superheated-emulsion monitors. In particulary, the use of the active instrument in the industrial environment faces the major challenge of discrimination between acoustic waves produced by bubble formation and external noise or vibration. Furthermore, their relatively low sensitivity leads to a slow response at low dose rates, making the superheated emulsions detectors inconvenient to be used as dose rate survey meters [20].

1.3.1.4 Recombination chambers

High-pressure tissue-equivalent ionization chambers, called recombination chambers, are designed to work in such a way that their ion collection efficiency is governed by the initial recombination of ions. The degree of the initial recombination in the gas cavity of an ionization chamber depends on the local ionization density, which can be related to LET. This mechanism is utilized in recombination chambers to provide information on radiation quality. The dose equivalent response of the chamber can be obtained by comparing the ionization currents collected at two different collecting voltages applied to the chamber. The precise definition and reproducibility of the recombination conditions are established by calibration in a reference gamma radiation field. For instance, the REM-2 chamber designed by Zielczyński et al. was calibrated in a ^{137}Cs reference field [28]. Tests of REM-2 performed in a mixed neutron-gamma radiation source of ^{241}Am-Be indicated that it can be operated in a large dynamical range at ambient dose equivalent $H^*(10)$ rate from 1 µSv/h up to about 1 Sv/h.

Recombination chambers are accurate to within a few percent accuracy for neutron radiation fields with low gamma contributions and within about 50% for the most complex radiation fields. They are usually recommended for a fast estimation of the ambient dose equivalent in a mixed radiation field.

1.3.2 Individual dosemeter

Individual dosemeter may be passive, capable of measuring long-term exposure and implying a later evaluation of the measurement results; or active, with immediate readout for regular short-term evaluation or warning in case of elevated radiation levels.

1.3.2.1 Passive dosemeter

Thermoluminescence detectors (TLDs) Their operating principle is based on that energy from ionising radiation is absorbed in a thermoluminescent (TL) material, and a portion of the energy causes electrons to become trapped, subsequently escape from the traps and return to a lower energy state, accompanied by the visible light release. They are widely used in albedo dosemeters. TLD materials consisting of ^{6}Li or ^{10}B can be used to detect slow neutrons due to the large cross-section reactions ^{6}Li(n, α)^{3}H or ^{10}B(n, α)^{7}Li. The most often used materials for slow neutrons are enriched lithium fluoride (^{6}LiF) and enriched lithium borate ($^{6}Li_2{}^{10}B_4O_7$:Mn). Since TLDs are sensitive to photons, the measurement for neutrons is usually carried out by reading the difference between a ^{6}LiF detector (sensitive to neutrons and photons) and a ^{7}LiF detector (with similar photon sensitivity but almost no sensitivity to neutrons). If the neutron-photon dose rate ratio is low in the field of interest, the relative difference of readings in the two detectors will be small and lead to a large statistical uncertainty.

TLDs offer a number of advantages for personal dosemeters including simplicity, low cost, ease of automated reading, durability, linearity of responses, and low detection limit. Their main disadvantages are strong energy dependence and high photon sensitivity.

Solid state nuclear track detectors (SSNTDs) The solid state nuclear track detectors are able to register the damages created along the trajectories of the charged particles in the materials. These particle tracks can be rendered visible under an optical microscope by chemical or electrochemical etching. Since they are insensitive to gamma radiation, the neutron/gamma discrimination can be achieved in a straightforward manner. The materials most commonly used for neutron detection are polycarbonate, cellulose nitrate and PADC (Poly Allyl Diglycol Carbonate). PADC detector, (known with its trade name CR-39), has become popular for neutron measurement since it was first introduced as track detector in 1978 [29]. PADC can detect charged particles over a very wide range of energies. Combined with a thermal to a few keV detection convertors, PADC detectors are suitable for most neutron workplace fields. However, they are inaccurate for neutrons above 10 MeV. To improve their sensitivity for high energy neutrons above 10 MeV, many types of radiators have been designed, for instance, the two-layer structured radiator [30] and the Multi-layer radiator [31].

SSNTDs have some advantages compared to other neutron detectors, such as long time stability, insensitivity to gamma radiation, small size, light weight, etc. Nevertheless, their accuracy over a sufficiently wide energy range still needs to be improved, and the pre- and post-processing procedures imply considerable sources of inaccuracy.

Bubble dosemeters The mechanism of these detectors has been already explained in § 1.3.1.3. In the passive type of bubble detectors, the displacement volume of the bubbles may serve as a measure for neutron fluence or dose. The important features of passive bubble detectors are

their independence on dose-rate and insensitivity to gamma radiation, making them suitable for mapping mixed neutron-photon fields over short exposure times and useful at high neutron dose rates and in the presence of high photon fields. However, they are sensitive to the environment temperature, have a high cost and a short lifetime. They are currently excluded from the regulatory dosimetry because they are not exploited by an authorized laboratory.

1.3.2.2 Active dosemeter

The main advantage of the Active Personal Dosemeter (APD) is to provide an immediate indication of neutron dose at the workplaces. In fact, the ratio of photon to neutron dose in the nuclear industry has changed due to the increasing shielding of the photon component. Changes in fuel burn up and new fuel types result in an increasing risk of neutron exposure. Work on the refurbishment of decommissioning plant will also increase neutron dose rate, and for these workplaces there may be sudden dose rate fluctuations in space or time [32]. In such cases, APD can serve as a warning tool for any unexpected high radiation level.

Neutron active personal dosemeters are generally based on the semiconductor detectors, which work on the same principle as most passive dosemeters: detect the charged particles generated by the incident neutrons in the detector itself or the charged particles created in the converter coupled with the detector. To measure the neutrons of energy up to 10 keV, ^{6}LiF or ^{10}B can be used as the convertor and mounted close to charged particle detectors, such as photodiodes, surface barrier detectors or PIPS (Passivated Implanted Planar Silicon) detectors. For neutrons of energies above several tens of keV, hydrogenous converters can be used to generate recoil protons, which will be detected by the semiconductor detectors. The main weakness of these dosemeters is their sensitivity to photons, which prevents from the detection of neutrons with energy below 800 keV. In consequence, their dose equivalent response presents strong energy dependence. The possible approaches to n/γ discrimination include reduction of the sensitive area, use of electronic threshold to cut off photon-induced signals, and use of several detectors to subtract the photon component.

Passive personal dosemeters are commonly employed for neutron dosimetry, while in the year 2000 some active dosemeters became commercially available for neutron dosimetry [33,34]. APD systems were proposed as a more convenient method for individual dosimetry than passive personal dosemeters, the question was therefore whether the active devices could compete with the passive ones in terms of performance. An investigation project, EVIDOS (EValuation of Individual DOSimetry), aiming at the improvement of individual monitoring in mixed neutron-photon radiation fields, had been performed over a period from November 2001 to October 2005. This project involved the collaboration of seven European institutes: PTB, IRSN, HPA-RPD, DIMNP, PSI, SSI and SCK-CEN [35,36]. The main objective was to establish whether innovative electronic dosemeters allow an improved determination of personal dose. Within the project, the following tasks were carried out:

- determination of the energy and direction distribution of the neutron fluence;
- derivation of the (conventionally true) values of radiation protection quantities;
- determination of the readings of routine and innovative personal dosemeters and of area monitors;
- comparison between dosemeter readings and values of the radiation protection quantities.

Figure 1.7: Electronic neutron personal dosemeters investigated in the EVIDOS survey.

Measurements were performed at different environments, such as SCK-CEN (Belgium), IRSN (France), etc. In every workplace field, all available personal neutron dosemeters were exposed. The electronic personal neutron dosemeters used in the EVIDOS project included both commercial types (EPD-N, EPD-N2 etc.), and laboratory prototype (DOS-2002), shown in Fig. 1.7. In addition, dosemeters with an (almost) immediate readout (DIS-N) was used along with passive dosemeters. Their main characteristics are given in Table 1.5.

Name	Short description	Commercial(c) /prototype (p)
Siemens EPD-N	$(\gamma + \mathrm{n}_{thermal})$ dosemeter with 3 silicon detectors	c
Siemens EPD-N2	$(\gamma + \mathrm{n})$ dosemeter with 3 silicon detectors	c
Saphymo, Saphydose-N	neutron dosemeter using a segmented silicon diode	c
Aloka, PDM-313	neutron dosemeter with 1 silicon detector	c
MGP, DMC 2000 GN	$(\gamma + \mathrm{n})$ dosemeter with 1 silicon diode	c
DOS-2002	$(\gamma + \mathrm{n})$ dosemeter with 1 silicon detector	p
DIS-N (PSI, RADOS)	$(\gamma + \mathrm{n})$ dosemeter based on direct ion storage	p

Table 1.5: Characteristics of the electronic neutron personal dosemeters tested in the EVIDOS survey.

Figure 1.8 shows the $H_p(10)$ response as a function of neutron energy for the two dosemeters, Saphydose-N and EPD-N2 dosemeters, which are considered as the most reliable ones in this

investigation. On their response functions, we notice a significant fluctuation around the value 1 ($H_p(10)$). This illustrates one of the difficulties for the development of neutron active personal dosemeters: how to obtain a constant response function over a large energy range. Additionally, the lack of monoenergetic neutron sources below several tens of keV increases the difficulty to determine the response of a neutron dosemeter. In those energy ranges the responses are determined by simulations.

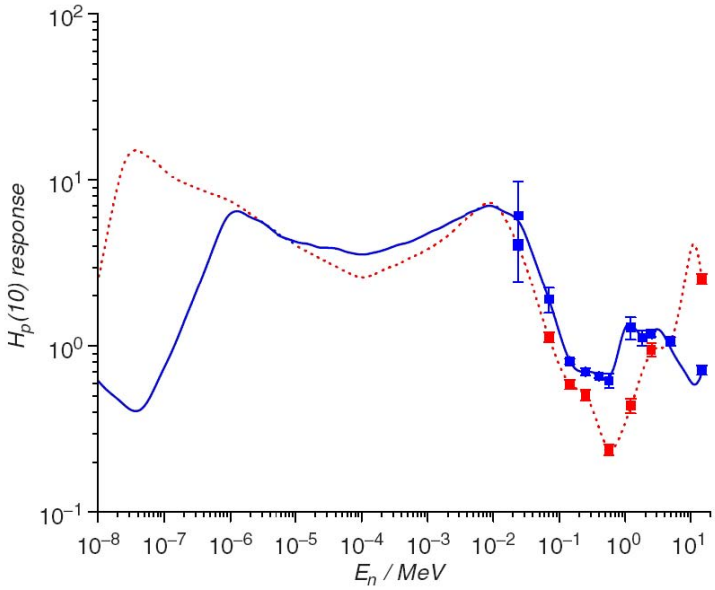

Figure 1.8: Experimental (square symbols) and simulated (lines) response functions for the Saphydose-N (in blue) and the EPD-N2 (in red) [37].

The project EVIDOS indicated that the neutron active (electronic) personal dosemeters (APDs) do not generally give better results than the passive ones in terms of the spread of response, at least for the investigated workplaces. However, APDs provide a much lower detection limit, for instance, 20 µSv can be achieved with a statistical uncertainty of 10% with most APDs in reactor fields [36].

1.4 Conclusion

It is clear that the development of a practical active personal dosemeter is difficult. Effort has been devoted by many research and development groups without complete success. More attempts are needed to enable the APDs to compete with the passive ones. The IPHC has a world-class expertise in CMOS Pixel Sensor (CPS) for charged particle tracking. The developments on CPS during more than a decade have led to promising applications for dosimetry. Therefore, the RaMsEs group of IPHC proposed a new solution for active neutron dosimetry by using a new technology in the field of dosimetry: CMOS technology. Their advantages and feasibility for neutron dosimetry have been demonstrated by our group in previous studies, which

will be described in detail in the next chapter.

Bibliography

[1] S. Eidelman *et al.*, "Particle Data Group: Review of Particle Properties," *Phys. Lett. B*, vol. 592, pp. 1–5, 2004.

[2] K. Nakamura *et al.*, "Particle Data Group: Review of Particle Physics," *J. Phys. G*, vol. 37, 2010. [Online]. Available: http://pdg.lbl.gov

[3] W. M. Yao *et al.*, "Particle Data Group: Review of Particle Properties," *J. Phys. G*, vol. 33, pp. 1–1232, 2006.

[4] ICRU, "Stopping powers and ranges for protons and alpha particles," ICRU, International Commission on Radiation Units and Measurements, Technical report, 1993, Bethesda, MD, US.

[5] H. H. Andersen, *Hydrogen Stopping Powers and Ranges in All Elements (The Stopping and Ranges of Ions in Matter, Vol. 3)*, J. F. Ziegler, Ed. Pergamon Press, 1977.

[6] L. Landau, "On the energy loss of fast particles by ionization," *J. Phs. (USSR)*, vol. 8, p. 201, 1994.

[7] N. Tsoulfanidis, *Measurement and Detection of Radiation*. Hemisphere Publishing Corp., 1983.

[8] C. Grupen, B. Shwartz, and H. Spieler, *Particle Detectors*, ser. Cambridge Monographs on Particle Physics, Nuclear Physics, and Cosmology. Cambridge University Press, 2008.

[9] H. Bichsel, "Experimental Range of Protons in Al," *Phys. Rev.*, vol. 112, pp. 1089–1091, Nov 1958. [Online]. Available: http://link.aps.org/doi/10.1103/PhysRev.112.1089

[10] L. Katz and A. S. Penfold, "Range-energy relations for electrons and the determination of beta-ray end-point energies by absorption," *Rev. Mod. Phys.*, vol. 24, pp. 28–44, Jan 1952. [Online]. Available: http://link.aps.org/doi/10.1103/RevModPhys.24.28

[11] K. Hagiwara *et al.*, "Particle Data Group: Review of Particle Physics," *J. Phys. D*, vol. 66, 2002.

[12] M. Vanstalle, "Dosimétrie électronique et métrologie neutrons par capteur CMOS a pixels actifs," Ph.D. dissertation, Université de Strasbourg, Strasbourg, France, 2011.

[13] V. Lacoste, "Review of radiation sources, calibration facilities and simulated workplace fields," *Radiation Measurements*, vol. 45, no. 10, pp. 1083–1089, 2010, proceedings of the 11th symposium on neutron and ion dosimetry. [Online]. Available: http://www.sciencedirect.com/science/article/pii/S1350448710001873

[14] M. J. Garcia, "Neutron spectrometry in complex n-γ fields: Application to LINAC and PET facilities," Ph.D. dissertation, Universitat Autónoma de Barcelona, 2010.

[15] G. Noel, L. Feuvret, R. Ferrand, and J.-J. Mazeron, "Treatment with neutrons: hadrontherapy part ii: physical basis and clinical experience," *Cancer/Radiothérapie*, vol. 7, no. 5, pp. 340–352, 2003. [Online]. Available: http://www.sciencedirect.com/science/article/pii/S1278321803001136

[16] D. T. Bartlett, "Radiation protection aspects of the cosmic radiation exposure of aircraft crew," *Radiation Protection Dosimetry*, vol. 109, no. 4, pp. 349–355, 2004.

[17] ICRP, "ICRP publication 60: Recommendations of the International Commission on Radiological Protection," ICRP, International Commission on Radiological Protection, Technical Report Annals of the ICRP Volume 21 (1-3), 1990, Oxford, Pergamon Press.

[18] ICRP103, "ICRP publication 103: Recommendations of the International Commission on Radiological Protection," ICRP, International Commission on Radiological Protection, Technical Report Annals of the ICRP Volume 37 (2-4), 2007, Elsevier.

[19] ICRP, "ICRP publication 26: Recommendations of the International Commission on Radiological Protection," ICRP, International Commission on Radiological Protection, Technical Report Annals of the ICRP Volume 1(3), 1977, Oxford, Pergamon Press.

[20] ICRU, "ICRU report 66: Determination of Operational Dose Equivalent Quantities for Neutrons," ICRU, International Commission on Radiation Units and Measurements, Technical report, 2001, Bethesda, MD, US.

[21] I. O. Andersson and J. Braun, "A neutron rem counter," *Nukleonika*, vol. 6, pp. 237–241, 1964.

[22] L. Brackenbush, J. McDonald, G. Endres, and W. Quam, "Mixed field dose equivalent measuring instruments," *Radiation Protection Dosimetry*, vol. 10, no. 1-4, pp. 307–318, 1985.

[23] A. Waker, "Microdosimetric radiation field characterisation and dosimetry in a heavy water moderated reactor environment," *Radiation Protection Dosimetry*, vol. 52, no. 1-4, pp. 415–418, 1994.

[24] J. McDonald, F. Posny, S. Gerdung-List, J. Chartier, and J. Kurkdjian, "Dosimetric measurements in simulated practical neutron fields using several dosemeter systems," *Radiation Protection Dosimetry*, vol. 62, no. 4, pp. 197–202, 1995.

[25] L. Braby, C. Ratcliffe, and N. Metting, "A portable microdosimetric system," in *Fifth Symposium on Neutron Dosimetry, Neuherberg 1984*, vol. I. EUR9762, 1985, pp. 321–329.

[26] A. Aroua, M. H ofert, and A. Sannikov, "On the use of tissue-equivalent proportional counters in high energy stray radiation fields," *Radiation Protection Dosimetry*, vol. 59, no. 1, pp. 49–53, 1995.

[27] H. Ing and H. Birnboim, "A bubble-damage polymer detector for neutrons," *Nuclear Tracks and Radiation Measurements (1982)*, vol. 8, no. 1-4, pp. 285–288, 1984, Special Volume: Solid State Nuclear Track Detectors. [Online]. Available: http://www.sciencedirect.com/science/article/pii/0735245X84901066

[28] M. Zielczyński, N. Golnik, and Z. Rusinowski, "A computer controlled ambient dose equivalent meter based on a recombination chamber," *Nuclear Instruments and Methods in Physics Research Section A: Accelerators, Spectrometers, Detectors and*

Associated Equipment, vol. 370, no. 2-3, pp. 563–567, 1996. [Online]. Available: http://www.sciencedirect.com/science/article/pii/0168900295010130

[29] B. Cartwright, E. Shirk, and P. Price, "A nuclear-track-recording polymer of unique sensitivity and resolution," *Nuclear Instruments and Methods*, vol. 153, no. 2-3, pp. 457–460, 1978. [Online]. Available: http://www.sciencedirect.com/science/article/pii/0029554X78909898

[30] K. Oda, Y. Imasaka, T. Yamauchi, Y. Nakane, A. Endo, H. Tawara, and Y. Yamaguchi, "Radiator design for detecting high-energy neutrons with a nuclear track detector," *Radiation Measurements*, vol. 40, no. 2-6, pp. 570–574, 2005, proceedings of the 22nd International Conference on Nuclear Tracks in Solids. [Online]. Available: http://www.sciencedirect.com/science/article/pii/S1350448705001071

[31] K. Shimada, T. Iimoto, and T. Kosako, "Design of a high energy neutron dosimeter using cr-39 with multi-layer radiator," *Radiation Measurements*, vol. 46, no. 12, pp. 1778–1781, 2011, proceedings of the 16th Solid State Dosimetry Conference , September 19-24 , Sydney , Australia. [Online]. Available: http://www.sciencedirect.com/science/article/pii/S1350448711004641

[32] D. Bartlett, R. Tanner, and D. Thomas, "Active Neutron Personal Dosemeters - A Review of Current Status," *Radiation Protection Dosimetry*, vol. 86, no. 2, pp. 107–122, 1999.

[33] F. d'Errico, M. Luszik-Bhadra, and T. Lahaye, "State of the art of electronic personal dosimeters for neutrons," *Nuclear Instruments and Methods in Physics Research Section A: Accelerators, Spectrometers, Detectors and Associated Equipment*, vol. 505, no. 1-2, pp. 411–414, 2003, proceedings of the tenth Symposium on Radiation Measurements and Applications. [Online]. Available: http://www.sciencedirect.com/science/article/pii/S0168900203011100

[34] M. Luszik-Bhadra, "Electronic personal dosemeters: the solution to problems of individual monitoring in mixed neutron/photon fields?" *Radiation Protection Dosimetry*, vol. 110, no. 1-4, pp. 747–752, 2004.

[35] F. d'Errico, D. Bartlett, T. Bolognese-Milsztajn, M. Boschung, M. Coeck, G. Curzio, A. Fiechtner, J.-E. Kyll onen, V. Lacoste, L. Lindborg, M. Luszik-Bhadra, M. Reginatto, H. Schuhmacher, R. Tanner, and F. Vanhavere, "Evaluation of individual dosimetry in mixed neutron and photon radiation fields (evidos). part i: scope and methods of the project," *Radiation Protection Dosimetry*, vol. 125, no. 1-4, pp. 275–280, 2007.

[36] H. Schuhmacher, D. Bartlett, T. Bolognese-Milsztajn, M. Boschung, M. Coeck, G. Curzio, F. d'Errico, A. Fiechtner, J.-E. Kyll onen, V. Lacoste, L. Lindborg, M. Luszik-Bhadra, M. Reginatto, R. Tanner, and F. Vanhavere, "Evaluation of individual dosimetry in mixed neutron and photon radiation fields (evidos). part ii: conclusions and recommendations," *Radiation Protection Dosimetry*, vol. 125, no. 1-4, pp. 281–284, 2007.

[37] M. Reginatto and M. Luszik-Bhadra, "Determination of the full response function of personal neutron dosemeters," *Radiation Protection Dosimetry*, vol. 125, no. 1-4, pp. 285–288, 2007.

Chapter 2

CMOS Pixel Sensors for radiation detection

2.1 Silicon detector physics

Silicon is a semiconductor material that is by far the most commonly used for radiation detection. Its energy band gap of 1.12 eV at room temperature is neither very low to avoid high leakage current from electron-hole pair generation, nor too high to allow abundant production of charge carriers by an ionizing particle. This feature and the fact that silicon has moderate intrinsic charge concentration and intrinsic resistivity make it well suitable for radiation detectors based on solid-state medium. Silicon detector offers good energy and excellent position resolution and is of particular interest for tracking. The other major advantage of using silicon in radiation detectors is the fact that the existing and advanced Integrated Circuit technologies based on silicon. This allows the integration of readout electronics and of the sensitive volume on the same substrate. This approach yields a monolithic, thin and compact radiation detector. CMOS Pixel Sensors (CPS) discussed in this work is an example of monolithic detectors originally developed for tracking detectors in high energy physics and firstly proposed to be used for neutron dosimetry by the *RaMsEs* group [1].

2.1.1 The p-n junction

A pure semiconductor, called intrinsic, contains approximately the same number of positive charge carriers (holes) and negative charge carriers (electrons). The conductivity of any semiconductor can be adjusted by doping, which is a process adding controlled amounts of impurities. Impurities replace silicon atoms in the crystal structure and create additional energy levels between valence and conduction bands. The locations of these levels in the band gap depend on the type of the impurity added. The impurity that creates energy levels near the conduction/valence band introducing additional negative/positive charges in the material is known

as *donor/acceptor*. In the semiconductor doping with donor impurity, the concentration of electrons exceeds the concentration of holes; such material is referred to as n-type semiconductor. As a result of acceptor impurity doping, holes are the major carriers resulting in a p-type semiconductor. For detector fabrication the doping levels are kept small to achieve high resistivity, which is important to suppress noise.

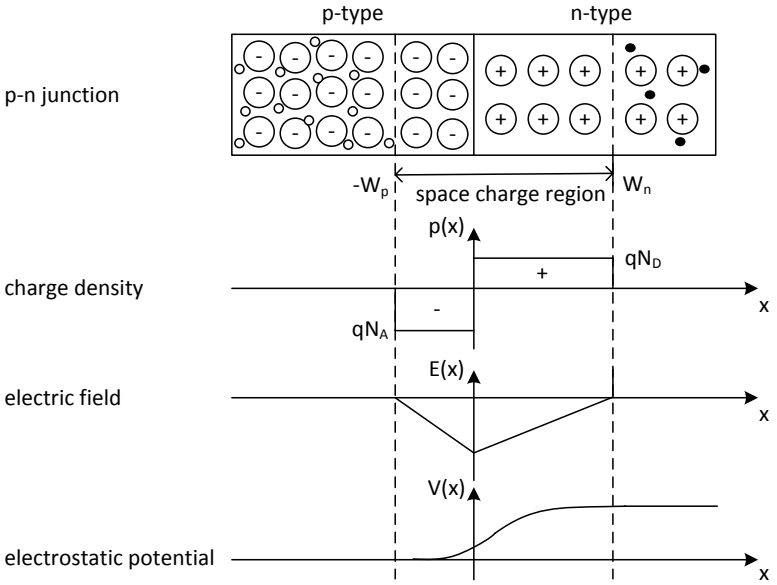

Figure 2.1: Approximation of an abrupt p-n junction: depletion region, space charge density, electric field distribution, and electrostatic potential distribution.

The p-type and n-type regions can be joined together to form a p-n junction (Fig. 2.1). These p-n junctions are extremely useful not only for building semiconductor electronics but also for radiation detector technology. When a p-type and n-type regions are brought together, holes from the p-side diffuse into the n-side and electrons from the n-side flow towards the p-side. As the holes and electrons move in opposite directions and combine together, a negative space charge leaves in the p-side and a positive space charge leaves in the n-side. An electric field builds up and prevents the further diffusion of electrons and holes. Thus a central region free of mobile carriers is created, called *depletion region* or *space-charge region*. The electrostatic potential difference across the depletion region at thermal equilibrium is referred to as the built-in potential (V_b). The width of the depletion region is the sum of the width of the depletion region on each side, given by

$$\begin{aligned} W &= x_n + x_p \\ &= \sqrt{\frac{2\varepsilon_{Si}\varepsilon_0 V_b}{q}\left(\frac{1}{N_A} + \frac{1}{N_D}\right)} \end{aligned} \tag{2.1}$$

where $q = 1.602\times10^{-19}$ C is the elementary charge, x_n and x_p are the widthes of the deple-

tion regions on n-side and p-side, N_A and N_D are the concentrations of acceptor and donor, respectively, ε_{Si} and ε_0 are the dielectric constant of silicon and the permittivity of vacuum, respectively, and q is the unit charge of electron. x_n or x_p is inversely proportional to the doping concentration. Usually in semiconductor detector diodes, the doping in one side is typically a few orders of magnitude higher so that the depth on the higher doped side can be safely ignored. It implies that the depletion region extends essentially only into the lightly doped region (bulk). In this case, the total depth of the diode junction W_j according to Eq. 2.1 becomes:

$$W_j = \sqrt{\frac{2\varepsilon_{Si}\varepsilon_0 V_b}{qN_b}} \tag{2.2}$$

where N_b is the concentration of bulk. The depletion region, in which the incident radiation creates electron-hole pairs, plays a central role in semiconductor radiation detectors. These charges move in opposite directions under the influence of the effective junction electric field and constitute an electrical current that can be measured. However, in this case the junction is too thin to be effectively used. The width of the depletion region can be increased by applying external reverse bias voltage. For a silicon bulk-diode made on a wafer of 300 µm thick, typically 60 to 100 volts are needed to significantly deplete the lightly doped bulk. The upper limit of the reverse bias voltage is the breakdown voltage of the junction. In the absence of incident radiation, except for a small leakage current, the depletion region of a p-n junction essentially acts as a parallel plate capacitor with a capacitance of:

$$C_j = \frac{\varepsilon_{Si}\varepsilon_0 A}{W_j} = A\sqrt{\frac{q\varepsilon_{Si}\varepsilon_0 N_b}{2(V_B - V_b)}} \tag{2.3}$$

where V_B is the reverse bias voltage, and A is the surface area of the junction. In the case of particle detectors, a large depleted volume leads to a large sensitive volume and decreased detector capacitance. This translates to increase in the signal-to-noise ratio (SNR).

2.1.2 Charge collection

The operation of a silicon detector is based on the collection of charged carriers on collecting electrodes. The charged carriers (electrons and holes) created by radiation in ionization processes are separated and constitute a current under the influence of the externally applied electric field. The current can be sensed and processed by the external circuit. Typically, a fully depleted detection volume is preferred since it reduces the probability of charge trapping and guides charge motion. This effect allows fast detector response and improves charge collection efficiency. However, in some detector technologies, high electric fields can not be employed because of the limited voltage range allowed by the fabrication processes. This is just the case of CPS, using standard CMOS process, discussed in this thesis. Consequently, CPS operate at partial depletion, and the electric field is present only in the vicinity of the electrodes. The charges from

the undepleted region is collected through thermal diffusion. They can contribute to the total signal only if they reach the depletion region, otherwise they are lost due to either recombination or trapping far away from the depletion zone.

The incident radiation produces electron-hole pairs along its track in the detector. These free carriers (electrons and holes) result in a inhomogeneous distribution, leading to a net movement of free carriers from high to low concentration. This process generates the diffusion current with direction opposite to the concentration gradient. In the presence of the electric field, the free carriers drift parallel to the field. The drift velocity of electrons, $\vec{v}_e$, and holes $\vec{v}_h$, depend on the electric field strength E. For low fields, the velocities increase almost linearly with $\vec{E}$, that is:

$$\vec{v}_e = \mu_e \vec{E}, \qquad \vec{v}_h = \mu_h \vec{E}, \tag{2.4}$$

where μ_e is the electron mobility and μ_h is the hole mobility. The mobility is constant for the electric field up to about 10^4 V/cm, but then decreases with the increase of electric filed. In silicon, at room temperature, μ_e and μ_h are 1350 $\mathrm{cm^2V^{-1}s^{-1}}$ and 480 $\mathrm{cm^2V^{-1}s^{-1}}$, respectively. At high field (above 10^5V/cm), the mobility is inversely proportional to E, and the drift velocity eventually saturates at about 10^7 cm/s. The time required for charge carriers originating at position x_0 to reach a point x can be calculated according to their velocities. The charge collection time is defined as the required time for the carriers to traverse 95% of the detector [2]. The determination of the collection time varies with the detector operation mechanism: for a fully depleted detector, the charge collection time depends on the electric field; for a partially depleted detector (the case of CPS), it depends only on the carrier mobility and doping concentration in the bulk material. For the latter case, typically, in a n-type silicon of 10 kΩ, the charge collection time is of the order of 30 ns and 90 ns for electrons and holes, respectively. Whereas for the same material in a fully depleted detector, the collection time is reduced by a factor of 3.

2.1.3 Signal current

The signal current is generated by the collected charge induced on the detector electrodes. This current is given by the Ramo-Shockley theorem [3, 4]:

$$I = -q\vec{v}\vec{E}_w \tag{2.5}$$

where $\vec{E}_w$ is the weighting field strength, and $\vec{v}$ is the velocity of charge carrier. The weighting field depends on the geometry of electrodes. The electric field and the weighting field are the same for two electrode configurations. The weighting field determines the coupling between the moving charge and the electrode. In general, if the moving charge does not terminate on the collecting electrode, the induced current changes sign and integrates to zero. The current cancellation on non-collecting electrodes relies on the motion of both electrons and holes.

In the case of CPS, usually the depletion regions of each charge collecting diode are very

shallow and separated on the same substrate. As a result, the electric fields due to each electrode are also separated, while the non-depleted region can be regarded as a constant potential volume. The weighting potential is strongly peaked near the collecting electrode, therefore, most of the signal is induced when the moving charge is near or terminates on the collecting electrode.

2.2 Development of CMOS pixel sensors at IPHC

Silicon devices have been used since the 60s for the detection of radiation. Since the early 1990's, rapid development of monolithic pixel sensors has been driven by visible radiation imaging [5]. These sensors are fabricated in standard CMOS VLSI technologies commonly used for modern integrated circuit manufacturing, referred to as CMOS image sensors, which are generally classified as passive and active sensors. In the case of Passive Pixel Sensors (PPS), a photodiode together with selection switches integrated in a pixel provide only charge collection capability. The collected charge of each pixel is transferred through the common read-out lines to the processing circuit placed on the periphery of the pixel array. Active Pixel Sensors (APS) feature a first stage amplifier integrated directly within each pixel. This structure is favored in most CMOS image sensors since it makes possible to perform several processing operations independently on each pixel before signals are transferred to the common processing blocks. CMOS detectors, competing with CCDs (Charge Coupled Devices), have found applications in numerous fields, ranging from consumer electronics to medical imaging and high-energy physics.

The development of CMOS pixel sensors for charged particle tracking was inspired by their use in visible light domain and initiated by the IReS-LEPSI [1] team in 1999 [6]. The proposed device is an APS fabricated on a single substrate, known as Monolithic Active Pixel Sensors (MAPS). As compared to other pixel technologies (i.e. Hybrid pixel detector, CCDs, Depleted P-channel FET Device), CMOS sensors are particularly attractive for position sensitive detectors because of the following prominent advantages:

- high granularity: a pixel size of 10×10 µm^2 or even smaller is possible, permitting a spatial resolution better than 3 µm even with a binary readout. Taking advantage of possible analog readout and natural charge spread between neighboring pixels, the spatial resolution can be improved to as high as $\sim$1 µm;
- low material budget: the device having a thin sensitive volume (typically around 10-15 µm) can be thinned, by a commercially available post-processing, to a few tens of µm without affecting the performance;
- signal processing on the same substrate: it allows easy integration of the readout microcircuits on the same substrate used for the sensor elements, which leads to many benefits such as miniaturization, high data throughput, flexibility, etc.;

1. Institut de Recherches Subatomiques and Laboratoire d'Electronique et Physique de Systèmes Instrumentaux, Strasbourg, France. In 2006 these units became a part of Département Recherches Subatomiques at Institut Pluridisciplinaire Hubert Curien (IPHC), Strasbourg

- low cost: since they are fabricated in a standard VLSI technology. The processes are easily available through multi-project and engineering runs that allow cost-effective and relatively fast design-to-verification cycle in sensor design;
- room temperature operation.

However, CPS suffer from a few apparent limitations. The first one is that the fabrication parameters (doping profile, number of metal layers, etc.) are not optimized for particle detection. The choice of industrial processes are often driven by epitaxial layer characteristics, at the expense of the signal processing circuitry parameters (feature size, number of metal layers). Moreover, the use of PMOS transistors inside the pixel array is restricted in most processes, thus limiting signal processing functionalities inside pixels. The second limitation originates from the almost undepleted sensitive volume, which impacts on radiation tolerance and charge collection speed.

CPS are being developed at IPHC for vertexing and tracking purposes in future particle physics experiments as well as in various other fields. A typical CPS chip is designed as an array of pixels with the readout and processing circuitry integrated in the periphery of the chip. A series of prototypes named MIMOSA (Minimum Ionizing particle MOS Active pixel sensor) has been designed and tested by the *PICSEL* (Physics with Integrated Cmos Sensors and Electron machines) group, proving the working principle.

2.2.1 Detection principle

The major difference between the CPS for charged particle detection from the classical detectors on a fully depleted, high resistivity substrate, is the charge collection achieved in a very thin lightly doped layer: the epitaxial layer (the sensitive volume). This layer is common in most modern CMOS processes, which feature twin tubes (p and n tube), grown on a highly doped substrate. The epitaxial layer defines some important characteristics of a sensor. Its thickness can notably affect the intensity of the signal and the sensitivity to photons. In fact, the thinner the sensitive layer is, the lower interacting probability the photons have, thus the lower sensitivity to low energy photons it has.

Since sub-micro technologies support bias voltages limited to a few volts, in CMOS sensors, the active volume can not be fully depleted. Hence, the collection mechanism relies on thermal diffusion instead of being enhanced by a strong electric field. The principle of operation for charged particle detection is illustrated in Fig. 2.2. The impinging charged particle produces electron-hole pairs along its track in the epitaxial layer. The electrons liberated diffuse thermally inside the epitaxial layer, which lies in between two highly doped regions: the p++ substrate and the p-well. The doping levels of the p-well and p++ substrate are three orders of magnitude higher than the epitaxial one, resulting in potential barriers at the region boundaries that act like mirrors and limit the diffusion of the electrons. The regularly implanted n-wells collect the electrons diffusing in their neighborhood. The distance between the two adjacent n-wells

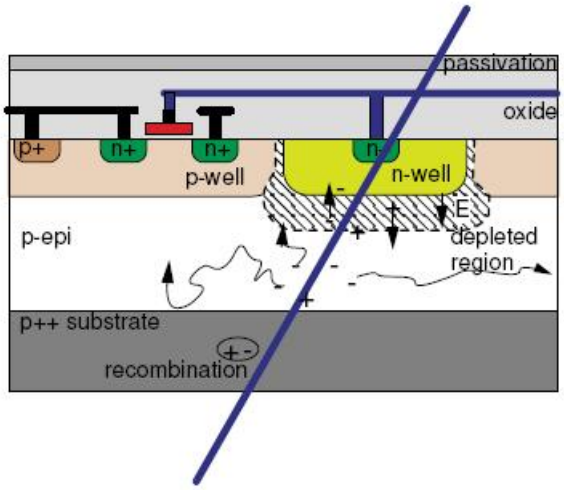

Figure 2.2: Principle operation of a typical CMOS pixel sensor for charged particle detection. The undepleted epitaxial layer (p-epi), common in modern CMOS technologies, forms the active volume of the sensor. The charge generated in this volume by an incident charged particle diffuses thermally and is collected on an n-well/p-epi diode. Typically, the thickness of the epitaxial layer is 10-15 µm [7].

defines the size of pixel, referred to as *pitch*. The diffusing charge is generally shared between the neighboring pixels which are closest to the particle impact point, and those pixels form a *cluster*. Device simulations at the physical level showed the collection time for a typical pixel pitch of 30 µm, to be less than 100 ns [2]. The current induced by the collected electrons is integrated on a collection diode, resulting in a voltage drop whose magnitude depends on the distance between the collection diode and the impact point. The total amount of charge generated by a single event mainly depends on the thickness of the epitaxial layer. The charge liberated in the highly doped substrate is mostly lost due to fast recombination of carriers. However, some fraction of this charge may reach the active layer.

2.2.2 Basic pixel architectures

In a twin-tub process, a PMOS transistor is placed in an n-well. Since n-well implantation areas are used for collecting diodes, any additional n-well in a pixel cell would limit the charge collection on the measured electrode. As a result, the pixel level readout electronics is placed in the p-well and limited to NMOS transistors.

2.2.2.1 Classical 3-transistor (3T) pixel

The basic single pixel readout architecture, consisting of three transistors and the charge collection diode, generally referred to as 3T-pixel [6], is schematically presented in Fig. 2.3(a), with the time diagram showing the principle of operation. The transistor M_1 resets the diode to the reverse bias, and the transistor M_2 operates as a source follower connected to a row selection

switch, the transistor M_3. Such a pixel integrates charge within the integration time separating two consecutive reset operations. The current source for the source follower and the column selection switch are placed outside the pixel. The signal generated by a particle is observed as a voltage drop on the floating n-well/p-substrate diode. The leakage current (typically of the order of fA at room temperature) introduces a signal offset which depends strongly on the integration time. This offset is referred to as pedestal, and varies from pixel to pixel due to the dispersion of process parameter. To correctly record the particle hits, this offset must be subtracted. The subtraction can be easily achieved in software, while hardware implementation is more problematic, because it requires a large memory to store the reference level for each pixel of the pixel array. Building such a memory would be complex, occupy a significant area of the chip, and increase considerably the power consumption.

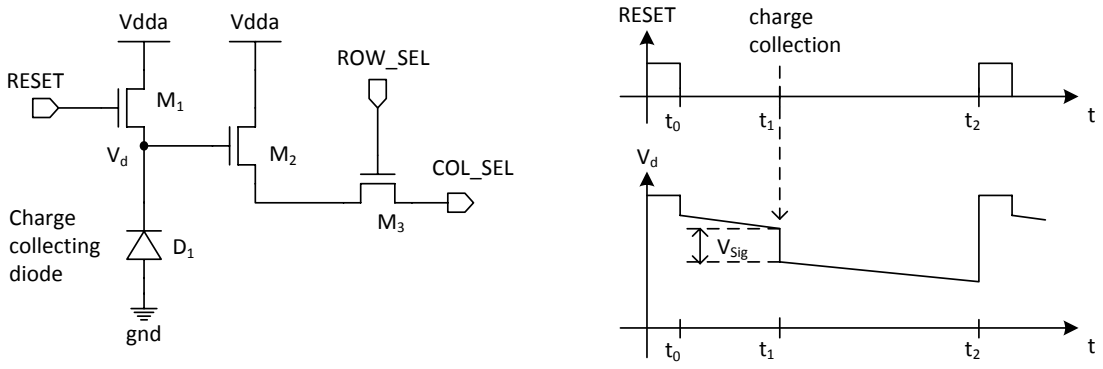

(a) (b)

Figure 2.3: The classical single pixel cell, consisting of three transistors and the charge collection diode (3T-pixel), (a) schematic, (b) timing diagram showing the operation and the signal shape.

2.2.2.2 Self-biased (SB) pixel

Another pixel architecture, based on two diodes connected together with cathode and anode nodes, was proposed for application of low signal intensities and low individual signal amplitudes [2]. The schematic of this architecture and its time diagram of operation are illustrated in Fig. 2.4. The charge collecting diode is also reverse biased as in the 3T-pixel, while the load diode is forward biased. A continuous reverse bias of the charge collecting diode is provided by the load diode, while the high resistance of the load diode allows for treating the n-well as a floating node. This structure is often referred to as a self-biased (SB) pixel. It is intrinsically a logarithmic pixel, characterized by a wide dynamic range of the pixel response [8]. Logarithmic response pixels do not integrate the charge, but their voltage responses V is logarithmically dependent on the physical signal instantaneous power P: $V = A \cdot \log P$. However, for small input signals, the response can be approximated with a linear behavior. Device simulations show the linearity of

the response up to approximately 3000 e^- [7]. When the reverse biased diode collects charge, the voltage on the diode drops and a slow discharging begins. The discharge time constant is defined by the equivalent resistance of the forward biased diode and the capacitance of the reverse biased diode. The equivalent resistance decreases with the increase of signals. Consequently, the signal read out after the integration time is not linear. Compared to the 3T-pixel, the SB-pixel is free from reset noise and signal offset. Nevertheless, a subtraction of the two samples, typically implemented by correlated double sampling (CDS), is required for extracting useful signals generated by impinging particles.

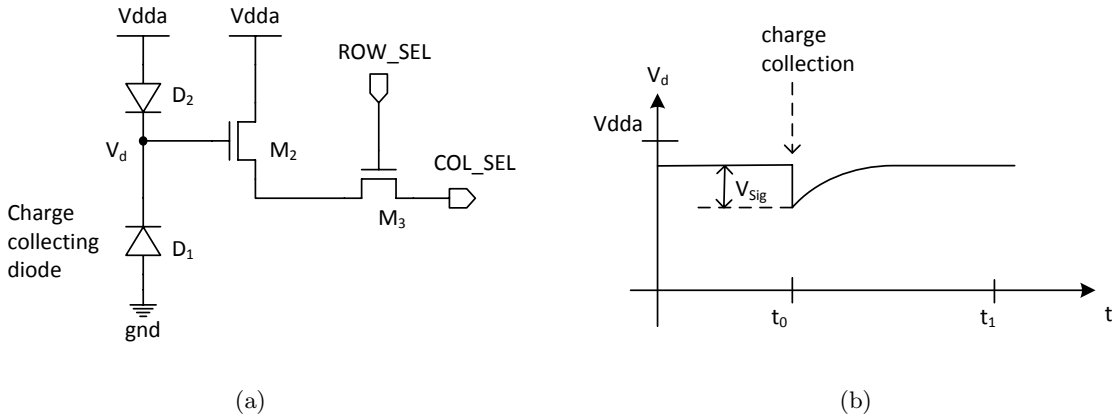

Figure 2.4: Self-biased pixel cell (SB-pixel), (a) schematic, (b) timing diagram showing the operation and the signal shape.

In both of 3T-pixel and SB-pixel, the voltage signal generated on the charge sensing node, typically being of the order of several mV, is then read out by a source follower with a gain factor of about 0.7-0.8. Such a weak signal can be easily affected by the electronic noise, which is usually generated by the charge collection diode, in-pixel electronics and the other parts of the readout circuitry. Thus the signal amplification in each pixel may be necessary to minimize the noise contribution of the readout chain and to increase the readout flexibility as well as on-chip processing capabilities. In the typically two-tube technology, basically only NMOS transistors can be used for in-pixel amplifications, which limits the number of possible amplifier structures. The two basic architectures employed in pixel are Common Source (CS) and cascode structure. The first verification of the feasibility and flexibility of the in-pixel amplification has been carried out in the MIMOSA-6 prototype [9]. Since then different in-pixel amplifier architectures have been studied and implemented in many MIMOSA prototypes developed for tracking application, and the detailed descriptions can be found in [7]. A further optimization of in-pixel amplifiers are addressed in [10].

A different way of improving the sensor performance, other than introducing a signal amplification into a pixel cell, is the implementation of CDS in-pixel. Using CDS is advantageous for rejecting low-frequency noise, i.e., the kTC noise (i.e. reset noise) and most of the flicker noise ($1/f$) in the pixel. Additionally, this technique is necessary for extracting useful signals in the

case of self-biased structure. The simple in-pixel amplifiers combined with in-pixel CDS circuitry are commonly used in the MIMOSA prototypes after MIMOSA-6. Different pixel architectures have been developed depending on the requirements of each application considered.

2.2.3 Readout of the pixel arrays

The individual pixels are arranged in the form of *pixel matrices*, where the readout of each pixel is achieved with an addressing logic. A typical CPS chip is designed as an array of pixels with the readout and processing electronics located at the periphery of the chip. The first MIMOSA prototypes are equipped with a serial analog readout requiring, apart of a few lines used to bias the circuitry, only two digital signals to operate. In the last decade, close to 20 different MIMOSA prototypes with analog output have been designed and tested, showing excellent performances. However, the readout frequency of reticule size sensors made of several 10^5 pixels is limited to $\sim$1 kHz without of any signal filtering. Numerous application domains require higher readout frequencies, which implies for instance grouping the pixels in columns read out in parallel and digitizing the signals on the chip [11].

2.2.3.1 Analog readout

An example of a typical CPS with analog readout architecture is schematically presented in Fig. 2.5. The addressing of the pixels is done with two shift registers, where one of them selects the column of the pixel addressed and the other one defines the corresponding row. The addressed pixel is connected to one common analog data bus. Typically, the output signal of the pixel matrix is buffered by an output amplifier and sent to the outside of the chip in form of a serial analog signal. Using shift registers leads to a continuous readout of one pixel per clock cycle. The time needed for one full readout cycle of all pixels in the matrix is referred to as the frame readout time. At the end of each frame, a synchronization signal is generated by the registers and a new frame readout starts autonomously. In the case of using the 3T-pixel architecture, a reset operation is required to set the potential of the collecting diodes to their original state. For this purpose, a reset of the system is forced from outside by a digital signal. Within the reset cycle, no pixel is connected with the current source. This results in a drop of the potential on the readout line. To overcome this problem, the dummy pixel was invented. This pixel not being meant to be a sensing element, it gets connected with the line within the reset period and delivers the charge required to hold the line potential on the expected value [12].

2.2.3.2 Digital readout

Integrating signal processing functionalities, such as CDS, ADC (Analogue to Digital Converter), data zero suppression circuitry are facing severe constraints from the pixel dimensions, readout speed and power consumption. The first attempt to build a CPS with on-chip digitization

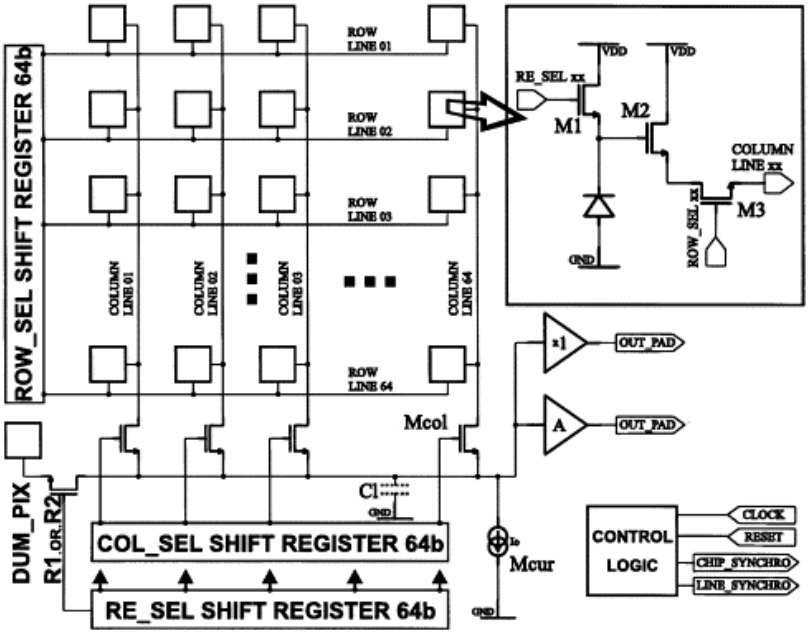

Figure 2.5: Block diagram of a typical CMOS pixel sensor with analog outputs. The column and row addressing shift registers sequentially select pixels for readout [2].

was MIMOSA-6, which featured in-pixel signal amplification and signal discrimination implemented at the column level [13]. The MIMOSA-6 chip did not allow testing the full functionality of the complete readout chain due to large pixel dispersion. A second prototype, MIMOSA-8, with a similar architecture was therefore implemented as an improved version [14]. The very encouraging performances exhibited by MIMOSA-8 led to the development of further prototypes. Then, two versions of MIMOSA-16 prototypes with improved pixels and in a CMOS process with thicker epitaxial layers (∼14 µm and ∼20 µm) had been developed to increase the performance of MIMOSA-8 [15]. A fast readout architecture prototype, MIMOSA-22, integrating on-chip data sparsification achieves the readout speed of 10 kframes/s [16]. Zero-suppression was investigated for the EUDET project [17] with the fully digital prototype, SUZE-01, which also incorporates the output memory buffers and is adapted to 128 columns read out in parallel [18].

2.2.4 Achieved performances for charged particle tracking

For high energy charged particle tracking application, CMOS sensors offer attractive balance between granularity, material budget, radiation tolerance, readout speed and power consumption. Motivated by the linear collider project, within the last 10 years more than 30 MIMOSA prototypes have been designed and fabricated. They have been tested both in the laboratory and on high energy beams (from several to 100 GeV). This section presents a short overview on their prominent achievements, because some of these improvements have inspired the application to dosimetry.

2.2.4.1 Detection performances

Analog output sensors Most of the MIMOSA prototypes with analog output were manufactured in a 0.35 µm OPTO process, featuring an epitaxial layer of ∼14 or 20 µm. The measured pixel noise is of the order of ∼10 e^- ENC (Equivalent Noise Charge) at room temperature, translating into a typical SNR of ∼20-30 (most probable value), depending essentially on the pixel pitch and the collection diode dimensions. Consequently, a detection efficiency $\gtrsim 99.8\%$ was achieved either with small prototypes or full scale sensors composed of several 10^5 pixels [11].

Due to the charge sharing between neighbouring pixels, one can calculate the center of gravity of the charge spread about different pixels through digitalization of the charge readout (12-bit ADC). The measured single point resolution varies for various pixel pitch (p) values, i.e. ∼1 µm for a 10 µm pitch, and $\lesssim$3 µm for a 40 µm pitch. The spatial resolution (σ) reached with this concept can be approximated by the relation $\sigma \approx 0.075p$ [12]. It is well below the binary resolution expected from the pixel pitch, as typically more than one pixel fires for one hit.

Digital output sensors To increase the readout speed, column-level discriminator and zero suppression logic are integrated on-chip (see § 2.2.3.2). The latest full reticle size sensor with digital output, the ULTIMATE sensor [19], has been fabricated in 2011. The sensor was fabricated with a substrate featuring a high resistivity (400 Ω·cm) epitaxial layer to guarantee its non-ionizing radiation tolerance. It consists of 928 × 960 pixels with 20.7 µm pitch, covering a sensitive area of ∼3.8 cm^2. Its main architecture is similar to those of MIMOSA-26 sensors, featuring column parallel readout with amplification and CDS inside each pixel [20]. The rolling shutter readout mode and the zero suppression process lead to a fast readout speed up to 185.6 μs/frame (200ns/row) with a power consumption of around 150 mW/cm^2. The good detection performances of ULTIMATE sensors had been demonstrated with a 120 GeV π^- beam test. Figure 2.6(a) presents the measured results of the thinned sensor (120 µm-thick) as a function of discriminator threshold. The performances achieved are a detection efficiency above 95% for an average fake hit rate below 10^{-4}, combined with a single point resolution in the 3.5-4.0 µm range (for a discriminator threshold in the range of 5-10 mV).

2.2.4.2 Radiation tolerance

Concerning the radiation tolerance of CMOS detectors, one has to distinguish between two types of radiation damage, the ionizing and the non-ionizing radiation damage. To investigate the radiation tolerance of MIMOSA sensors, various tests have been performed with 10 keV X-rays and ∼1 MeV neutron sources or beams. Ionizing radiation, which mainly damages the electronics, is produced by interactions between the radiation and the electrons of material. Ionizing radiation mainly increases the shot noise due to a leakage current growth. This effect was substantially alleviated by fine-tuning the layout of the collection diode as well as by choosing good running conditions (small integration time, low operation temperature). The CMOS sensors

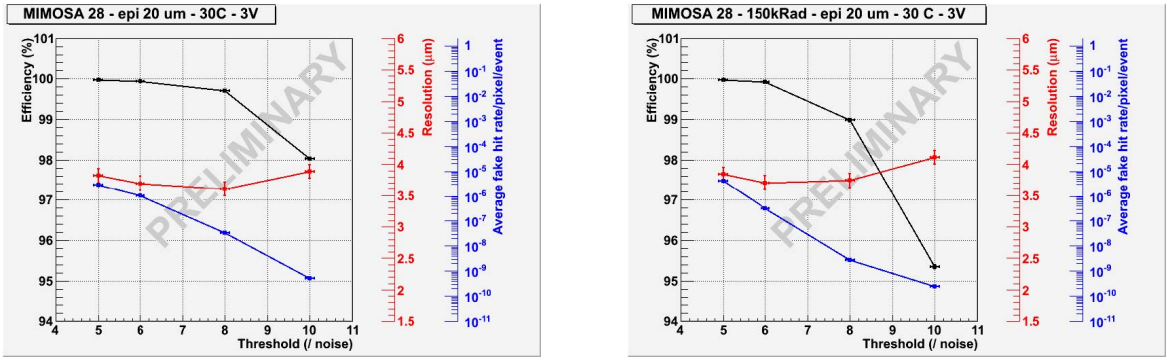

(a) (b)

Figure 2.6: Detection performances of the ULTIMATE sensor with a 20 µm thick epitaxial layer, measured at 30 ℃ and for a power supply of 3.0 V (a) before irradiation, (b) after exposure to integrated dose of 150 kRad with 10 keV X-rays [19].

with a simple in-pixel architecture (i.e. SB-pixel) and a serial analog readout are resistant to ionizing doses of 1 MRad [12]. However, the radiation tolerance is worse in the presence of in-pixel amplifiers required for fast sensors. After irradiation up to 300 kRad, the prototypes showed performance losses due to the increased temporal noise of above 15 e^-, showing that higher ionizing dose (e.g. 1 MRad) would be presumably unreachable [21]. Further improvement in ionizing radiation tolerance with in-pixel amplifications is therefore still necessary.

Non-ionizing radiation mainly reduces the charge collection efficiency, as it increases the probability of charge lost due to recombination. The magnitude of the effect depends on the pixel pitch and the sensing diode dimension. The measured non-ionizing radiation tolerance achieved $10^{13} n_{eq}/cm^2$ for sensors with 10 µm pitch, while it barely exceeds $2 \times 10^{12} n_{eq}/cm^2$ for a 20 µm pitch [22]. However, due to the fact that the smaller pixel pitch requires a higher number of pixels per surface unit, accordingly, a higher power consumption and/or a slower readout, reducing the pixel pitch is not satisfactory in terms of improving the non-ionizing radiation tolerance. The alternative and most natural way to minimize the probabilities of charges lost by recombination is to deplete the sensors. Most of the CMOS processes including an epitaxial layer feature it with low resistivity, typically of the order of 10 Ω·cm. Consequently, the depletion depth in such a standard resistivity epitaxial layer is limited to a fraction of micrometer. The recent advent of CMOS processes involving a dedicated high resistivity (10^2-10^3 Ω·cm) removes this obstacle for charge collection. A first exploratory prototype, called MIMOSA-25, had demonstrated that CPS can substantially improve their radiation tolerance with a high resistivity epitaxial layer (1 kΩ·cm) [23]. With a 20 µm pitch, the non-ionizing radiation tolerance of above $3 \times 10^{13} n_{eq}/cm^2$ was improved by more than one order of magnitude with respect to similar designs based on standard CMOS processes with low resistivity sensitive layer. The improved tolerance had also been demonstrated with a fast column parallel readout sensor MIMOSA-26 [20]. The use of high resistivity epitaxial layer provides substantial benefits in terms of CCE (Charge Collection Efficiency), which leads to a twice higher SNR than for the standard sensors. Fur-

thermore, unlike standard sensors, the CCE of the HR-sensor (high resistivity sensor) remains mostly stable after bulk damage consecutive to a fluence up to $3 \times 10^{13} n_{eq}/cm^2$ (see Fig. 2.7). During a beam test performed at 0 °C with ∼120 GeV/c pions, the HR-15 (with a high resistivity epitaxial layer of 15 µm) sensor irradiated with $10^{13} n_{eq}/cm^2$ demonstrated an efficiency above 99.9% in combination with a fake hit rate of 10^{-4}, which exceeds the performances of a non-irradiated standard sensor [24]. This good radiation tolerance is one of the primary interests for our dosimetry application.

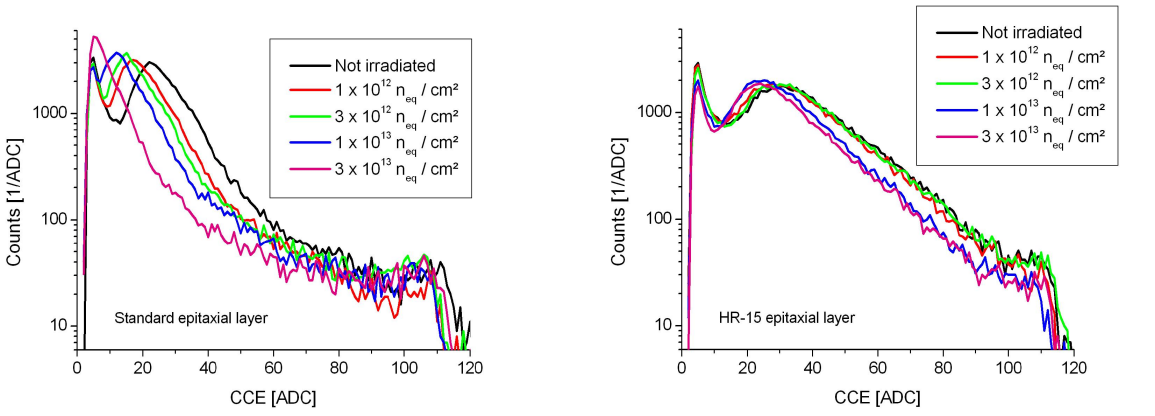

Figure 2.7: Charge collection spectra of MIMOSA-26 sensors with (a) standard, (b) HR-15 (which has a 15 µm thick high resistivity epitaxial layer) chips. Tests with an ^{55}Fe-source were performed before and after irradiation with fission neutrons [24].

2.2.5 Sensor thinning

Sensor thinning is mainly motivated by the requirement of low material budget (< 0.1% of radiation length per layer) for the vertex tracker, i.e. International Linear Collider (ILC). Since the sensitive volume of CPS is usually 10-20 µm thick, it is possible to remove most of the bulk silicon using a back-thinning process. For our application, sensor thinning may be also useful.

2.2.5.1 Decreasing substrate thickness

Thinning CMOS chips by reducing their substrate can be achieved by an industrial process. The first thinning attempts were made in 2003 with the MIMOSA-5 chips on a wafer scale (developed at IPHC), which has been thinned down to 120 µm without any loss of performance [25].

Other thinning experiences were also obtained from the study on back-thinning individual diced chips [26]. The thinning was performed with MIMOSA-5 chips to the thickness of 50 and 40 µm. During the thinning procedure, a proprietary hot wax formula is used to mount wafers or

dice to stainless steel grinding plates. Using wax as an adhesive facilitates dealing with thinner parts and leads to elimination of damages caused by electrostatic discharge (ESD). The back-thinning is based on a wet grind procedure with a rust inhibitor for cooling the chips, which keeps the grind wheel free of debris that could damage chips thinner than 100 µm. The grinding is followed by a polish process which minimizes the stress from the backside of the device and allows thinning below 50 µm. The measurements demonstrated that neither their noise nor their response to ionizing particles has been degraded by the thinning process.

2.2.5.2 Back illuminated devices

In a standard CMOS detector, the front side of the epitaxial layer is covered by a passive material made of several layers of metal and silicon oxide used for circuit electrical interconnection. This structure is well adapted to the detection of high energy particles (i.e., MIPs), but unsuitable for low energy particles (i.e., electrons with energies below 30 keV, α-particles with energies below 1.7 MeV, protons with energies below 550 keV). As the low energy particles cannot penetrate deeply into silicon, almost no particles would reach the epitaxial layer in a front illuminated device. Therefore, substrate removal and back illumination are required.

One application of backside illuminated CMOS devices was motivated by the development of a non-destructive beam monitoring in a hadron therapy center [27]. This requires the detection of low energy electrons (a few keV). For a standard CPS device, the sensitivity to such electrons can be obtained by reducing the passive entrance window of the device to be much less than 1 µm. A few wafers of MIMOSA-5 chips had been successfully thinned down to the epitaxial layer [28]. After thinning, a passive entrance window with a thickness of the order of 100 nm is created to protect the surface of the thinned chips. Another concern is then to restore the reflective electrostatic barrier, originally existing between the epitaxial layer and the highly doped substrate before thinning. The reason is that an electric potential profile, pushing the electrons from the interface into the epitaxial layer, is required to limit charge trapping and recombination on the interface. The entrance side of the back-thinned chip is left electrically floating [29].

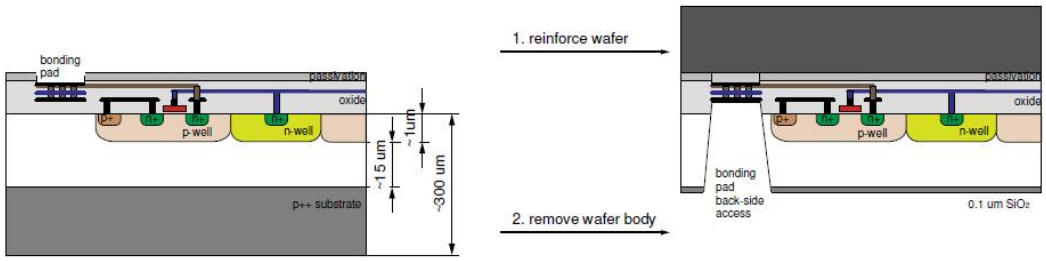

Figure 2.8: The substrate removal procedure includes the following steps: adding a new reinforcing wafer, removing the original wafer body, creating deep trenches to provide contacts to the original pads, and forming a thin SiO_2 entrance window [7].

The substrate removal procedure, leading to the back-side illuminated CMOS sensor is schematically depicted in Fig. 2.8. Before the thinning, the original front side of the chip is mechanically reinforced by adding a support wafer of several hundreds of microns. Then, the p++ substrate is removed and the exposure side of the sensor is passivated, resulting in a thin SiO_2 entrance window. The bonding pads of the original chip are now inaccessible, due to the presence of the reinforcing wafer. To allow electrical connections to the chip, a new access path for bonding wires is created from the opposite side by removing the silicon plugs underneath the bonding pads. The aluminum pads in deep trenches are reachable, allowing bonding the chip to the printed circuit board (PCB) support. The thinned sensor performed well in laboratory tests. However, a noticeable effect of back-thinning on charge collection efficiency was observed [27, 29]. The substantial decrease of the total collected charge was attributed to the reduction of the epitaxial layer and the electron recombination at the interface of the sensor and the epitaxial layer. Despite the deterioration of the charge collection efficiency weakened the detection efficiency of the sensor for MIPs, the thinned sensor demonstrated the feasibility of detecting low energy electrons (typically with energies of a few keV) with CPS. It opens the door to the applications on medicine (i.e. beam monitoring for hadron-therapy [30]), biology (i.e. beta marking with tritium [28]) and material science (i.e. electron microscopy [31]).

For our neutron dosimetry application, the possibility of using such a thinned, backside illuminated sensor in the detection of α-particles with energies below 1.7 MeV, as well as protons with energies below 550 keV, had been found to be promising. The *RaMsEs* group is currently exploring a new real-time neutron dosemeter based on CMOS sensor. The very first detection of neutron with a thinned MIMOSA-5 sensor was published in 2008, estimating the response of this kind of sensor to fast neutrons [1]. In the next section, we will discuss the latest experimental results of neutron detection with a thinned, back illuminated MIMOSA-5 sensor.

2.3 Neutron detection with MIMOSA-5 at IPHC

The MIMOSA chips developed in IPHC have demonstrated numerous advantages for high energy physics experiments. Concerned by neutron detection, these CMOS sensors present two additional features of primary interest: γ-transparency and portability. A study using the MIMOSA-5 detector for detection of fast and thermal neutrons has been done by Vanstalle [32] of *RaMsEs* group. The study not only provides experimental evidence that CMOS technology could be used for an electronic neutron dosemeter, but also determines the weakness of the MIMOSA-5 in the application on neutron dosimetry. The results from the study in [32] lead to the necessity of a dedicated CMOS sensor (the design within this thesis) and provide guidance for the development of a compact neutron active personal dosemeter based on CMOS technology.

2.3.1 Experimental setup

2.3.1.1 MIMOSA-5 Sensor

The MIMOSA-5 chip was the first full-reticle scale monolithic active pixel sensor prototype, designed for particle tracking. The MIMOSA-5 prototype, whose general architecture is shown in Fig. 2.9(a), had been designed and manufactured using a 0.6 µm CMOS process with 14 µm epitaxial layer. The chip dimensions are 19400× 17350 µm^2, while the effective active area is 17480×17350 µm^2 [28]. It is made of four matrices of 512×512 pixels, each one with a square pitch of 17 µm. Each array has a independent analog output. There are two digital control blocks, and each one is shared between two left (P2TOP and P2BOT) or two right (P1TOP and P1BOT) matrices. The readout and control electronics are placed at the bottom of the chip, occupying a band of 2000 µm width, including I/O pads. The internal architecture of a single matrix, the readout arrangement and the schematic diagram of a pixel are depicted in Fig. 2.9(b). The pixel design is based on the classical 3T-pixel scheme (see 2.2.2) with an n-well/p-epi diode used for charge collection. The photo of the MIMOSA-5 chip is shown in Fig. 2.10.

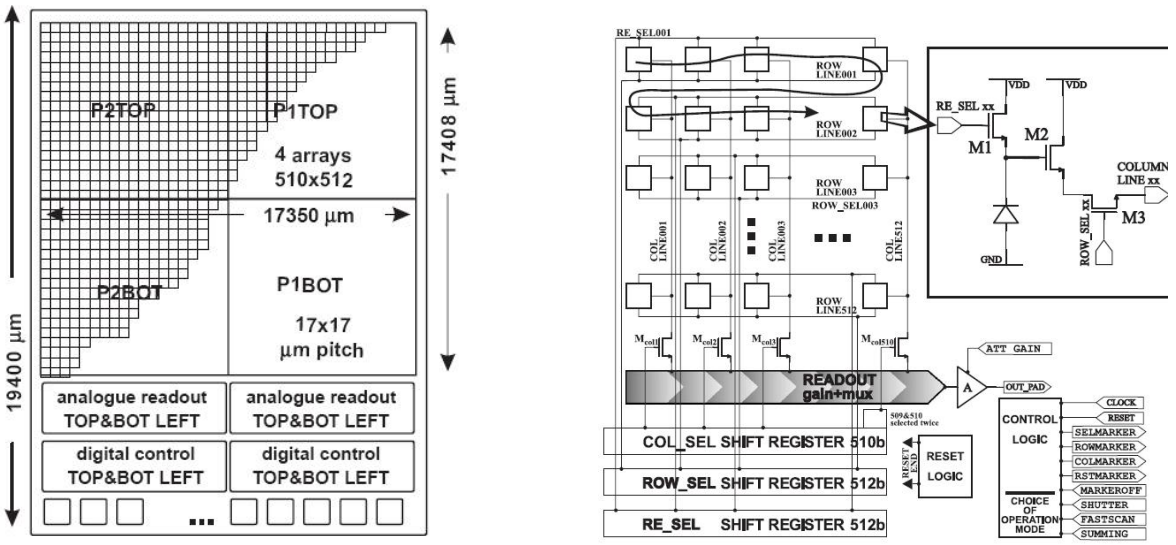

(a) (b)

Figure 2.9: Architecture of the MIMOSA-5 chip, (a) one chip composed of 4 pixel matrices of 512 × 512 pixels, (b) internal architecture of the single matrix, readout arrangement and pixel schematic diagram [28].

Readout architecture The readout of the chip is based on sequential addressing of pixels, through column and row selection shift registers. The rows are consecutively selected and pixels in whole rows are reset. Each readout sequence must be preceded by a reset phase to restore the reverse bias of the charge collecting diodes. The reset phase introduces a slight dead time to the detector operation. The result signal is calculated as a difference of two consecutive frames, by

the off-line CDS data processing.

Back-removal processing For the neutron dosimetric application, we have to detect low-energy protons and α-particles which would be partially absorbed by the SiO_2 layer. Therefore, the back-removal processing (see § 2.2.5.2) had been performed to construct a back illuminated device. After the post-processing, the epitaxial layer has a residual thickness of 10-12 µm and is covered by a passivation layer of about 160 nm SiO_2. In the experiments, the incident particles impinge on the epitaxial layer through the thin SiO_2 entrance window. The thinned-sensor is bonded on the test board, as shown in Fig. 2.11.

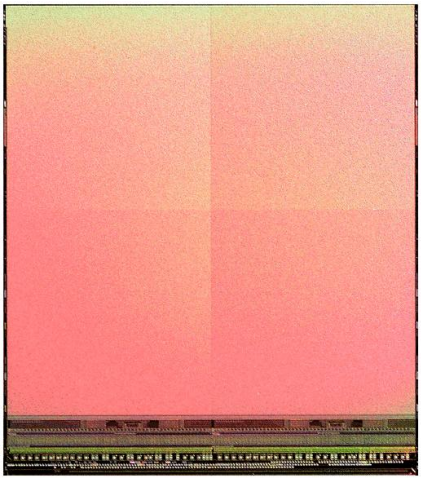

Figure 2.10: Photo of the MIMOSA-5 chip

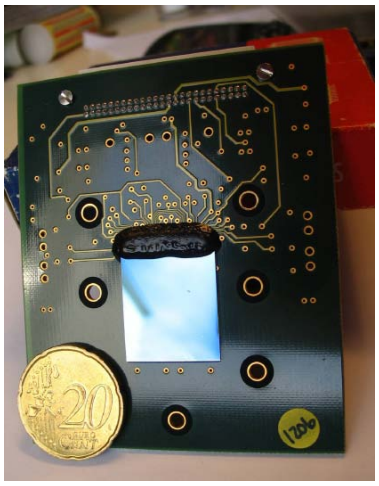

Figure 2.11: Photo of the bonded MIMOSA-5

2.3.1.2 Acquisition system

The acquisition system is composed of three parts:

- An auxiliary PCB, on which the CMOS sensor is bonded. It receives polarization signals and delivers four analog outputs (one for each matrix).
- A PC with a digital acquisition board (National Instruments PCI-6534).
- A mother-board that interfaces between the PC and the sensor. It includes a four-channel (one channel per matrix) 10-bit ADC (Analog to Digital Converter) and a FPGA (Field Programmable Gate Array) Xilinx Spartan-II XC2S100, which distributes the different signals.

Reading instructions are sent by the PC to the mother-board, which sends the reading signals to the sensor, gets the raw data back, processes it and returns it to the PC. In this application, a single matrix of MIMOSA-5 chip is used, resulting in a sensitive area of 0.75 cm^2. With a reading frequency of 5 MHz, the readout time of one frame (512×512 pixels) is 50 ms. Knowing that each frame is coded on 512 kB, this leads to a data flow of 10 MB/s (one CD per min). The latter is a stringent constraint for the measurements with low activity sources. Indeed, some

experiments require a high exposure time (more than 1 hour) to obtain a acceptable statistics for analysis.

2.3.1.3 Converters

As CMOS sensors detect charged particles, a converter must be added in front of the detector for neutron detection. Neutrons can generate charged particles through various elastic or inelastic processes, and the choice of the converters depends on the energy of the incident neutrons. In the experiments with MIMOSA-5 sensor, the polyethylene and boron are used for the detection of fast neutrons and thermal neutrons, respectively.

Polyethylene converter Polyethylene is one of the simplest polymers and the cheapest. The $(CH_2)_n$ converter was used for the detection of fast neutrons in order to benefit from the high cross-section ($>$ 1 barn below 10 MeV) of the elastic scattering of fast neutrons with hydrogen (n,p). Elastic scattering of neutrons with hydrogen nuclei produces recoil protons detected by the CMOS sensor. However, one should be aware that other reactions may occur in the converter and produce other detectable charged particles or photons by radiative process. These reactions cause pollution for the fast neutrons. There are obviously many other possible parasitic reactions, particularly with the environment (sensor-bonded PCB, acquisition hardware, etc.).

There is an optimal thickness of polyethylene for which the number of recoil protons emerging from the converters becomes constant for all energies and results in "proton" equilibrium. The conversion efficiency as a function of the converter thickness has been obtained by MCNPX (Monte Carlo N-Particles eXtended) simulation [32]. Figure 2.12 gives the proton equilibrium curves for both ^{241}AmBe and ^{252}Cf neutron sources. The proton equilibriums are reached around 900 µm and 600 µm for the AmBe and Cf sources respectively. This state leads to the conversion efficiency of 1.21×10^{-3} for AmBe and 5.72×10^{-4} for Cf. It is important to choose a thickness for which the response is flat, in order to on the one hand have a high conversion efficiency, and on the other hand limit the uncertainty. In fact, for thicknesses less than the optimum thickness, the number of protons out of the detector varies greatly, which indicates a high uncertainty on the number of recoil protons if the thickness of the converter is not precisely known. In the experiments with MIMOSA-5, the thickness of the converter was chosen as 1 mm.

Boron converter Thanks to the high cross-section of the ^{10}B(n,α)^{7}Li reaction for low energy neutrons ($E_n<$ 100 keV), boron material can be used as a thermal neutron converter. This reaction produces 94% of 1.47 MeV α-particles and 0.84 MeV ^{7}Li, as well as 6% of 1.78 MeV α-particles and 1.0 MeV ^{7}Li. Both α-particles and ^{7}Li can be detected by the CMOS sensor. For the ^{7}Li particles, because of their very short ranges in matter, only the portion created on the edge of the converter can be detected.

The cross section of neutron reactions with boron depends strongly on the isotope. In the

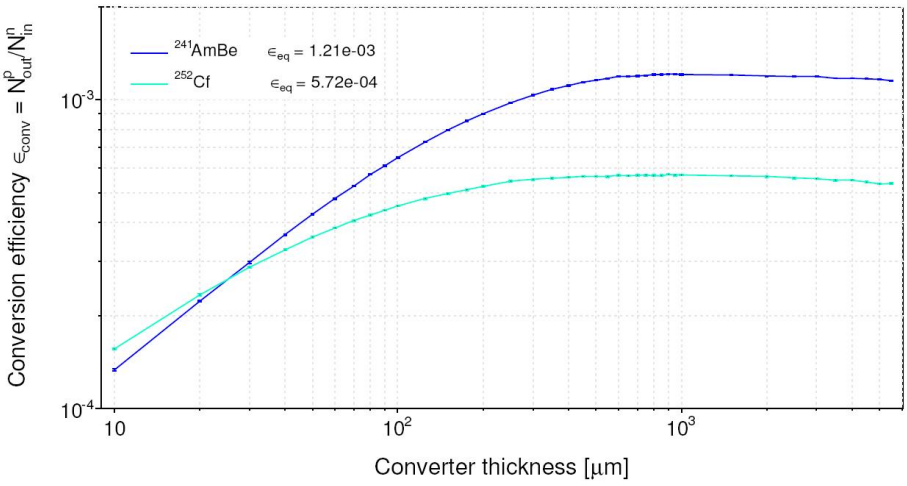

Figure 2.12: Simulated conversion efficiency as a function of the polyethylene converter thickness for the AmBe and the Cf sources [32].

thermal neutron detection with MIMOSA-5, two types of converters have been used: the first one named BN1, is made of natural boron (comprising 19.9% of ^{10}B and 80% of ^{11}B), and the other one called BE10 is composed of only 99% pure ^{10}B [33]. Both of them are provided by the company DOSIRAD [34]. Each one is composed of three layers:

1. A PET (polyethylene terephthalate, $C_{10}H_8O_4$) support layer of 100 µm-thick;
2. An adhesion layer of 2 µm-thick composed of SARAN F-310 (Polyvinyl Dichloride), MEC (Methyl ethyl ketone, C_4H_8O) and MIBK (Methyl isobutyl ketone, $C_6H_{12}O$);
3. An active layer of 92% of boron powder (BN1 or BE10 depending on the type of conveter) and 8% of an organic binder (70% of MEC, 25% of methyl esters, 5% of cyclohexane) of 40 µm-thick.

Since these converters are transparent to visible light, an opaque material is required to cover them in the detection of thermal neutrons. In practice, graphite is preferred because it is composed exclusively of carbon, which interacts only with fast neutrons.

As for fast neutrons, parasitic reactions take place between neutrons and the converter ^{10}B (or ^{11}B). In this case, the cross sections of these processes are well below those of the reaction ^{10}B(n,α)^{7}Li.

2.3.2 Response to MeV photons

The sensitive layer of the MIMOSA-5 sensor is very thin (∼10 µm). Its sensitivity to photons is expected to be low, which is just the interesting feature of this technology. However, attention must be paid to the polyethylene converter, which is also a source of photoelectrons. It is therefore important to quantify this potential contamination.

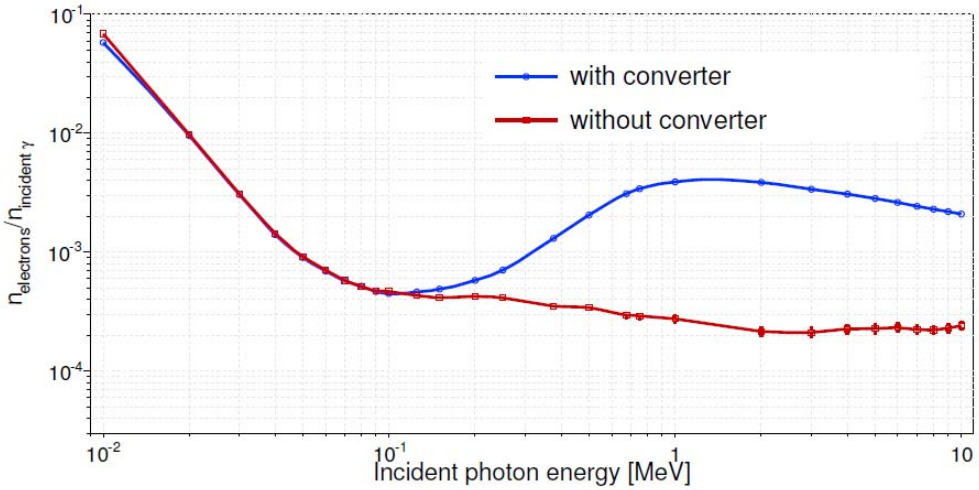

Figure 2.13: Photo response of the MIMOSA-5 with and without the $(CH_2)_n$ converter from MCNPX simulations [32].

Figure 2.13 shows the simulated sensitivity of the MIMOSA-5 to monoenergetic photons with and without converter. For an energy less than 100 keV, the presence of converter has no influence on the sensor response. When the photon energy is larger than 100 keV, Compton electrons start to dominate the photoelectric effect. The difference of the sensor response between the two cases (with and without converter) is particularly significant for 1 MeV photons. To determine the response of the sensor to MeV photons, measurements had been performed with a ^{60}Co source, emitting two γ rays of 1.17 MeV and 1.33 MeV.

Source configuration	R_γ Experiment	R_γ Simulation (all E_{dep})	R_γ Simulation ($E_{dep} > 15$ keV)
^{60}Co	$(0.28 \pm 0.02) \times 10^{-3}$	$(0.65 \pm 0.02) \times 10^{-3}$	$(0.30 \pm 0.02) \times 10^{-3}$
^{60}Co + $(CH_2)_n$	$(0.26 \pm 0.01) \times 10^{-3}$	$(8.03 \pm 0.01) \times 10^{-3}$	$(0.25 \pm 0.01) \times 10^{-3}$

Table 2.1: Measured and simulated γ-response for the MIMOSA-5 to ^{60}Co source (the response R_γ is defined as the ration of $\gamma_{detected}$ on $\gamma_{incident}$, while E_{dep} represents the deposited energy). Uncertainties are statistical [32].

Table 2.1 summarizes the simulated and measured γ-response with and without converter. The measured results are almost identical in the two cases. This behavior is in contradiction with the simulation, which predicts a large relative difference of 92% (8.03×10^{-3} with converter, 0.65×10^{-3} without converter). According to the simulated deposited energy distributions of the two γ-rays from the ^{60}Co source, the mean deposited energy by photoelectrons is 5 keV, which is well below the detection threshold (between 15 keV and 20 keV, see [32]). Therefore, a large part of photoelectrons can not be detected, which is exactly the observed result.

As a result, due to the high detection threshold, the influence of the $(CH_2)_n$ converter is

negligible for the present threshold used with this acquisition system of MIMOSA-5.

2.3.3 Response to a mixed n/γ source

To demonstrate that the recoil proton signals of a fast neutron source can be discriminated from photon signals, the MIMOSA-5 sensor had been exposed to a n/γ source ^{241}AmBe. The neutron flux is (2.24 $\pm$ 0.10)$\times$ 10^6 s^{-1}, determined by Bonner Sphere Spectrometry. It emits also γ-rays of 4.438 MeV with a γ/n ratio of 0.57 [35].

2.3.3.1 MCNPX simulations

The MCNPX (*Monte-Carlo N-Particles*) simulations show that the AmBe source generates two distinct populations in the sensor, corresponding to the two secondary particles generated by neutrons and photons: a population of electrons at low energy and a much higher energy of recoil protons coming from the interaction of fast neutron with polyethylene. Figure 2.14 presents the simulation result.

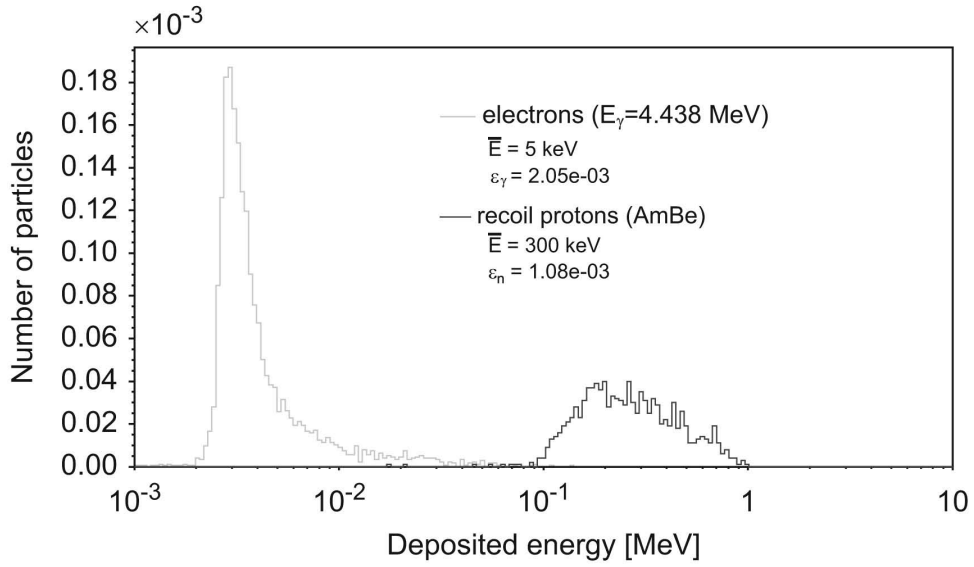

Figure 2.14: Deposited energy distributions (normalized) simulated with MCNPX for the AmBe mixed n/γ source ($n_\gamma/n_{neutrons}$ ratio of 0.57) [36].

2.3.3.2 Experimental results

The measured charge distribution in the constructed pixel clusters for a 90-min exposure at 15 cm from the source is shown in Fig. 2.15. One can see again two populations as it has been shown in the simulation: one peaked at low charge and one at a higher value. The discrimination of the two signals is more complicated than in the simulation. The proton signal slightly overlaps the electron distribution. To estimate the amount of overlap, the two populations had been fitted

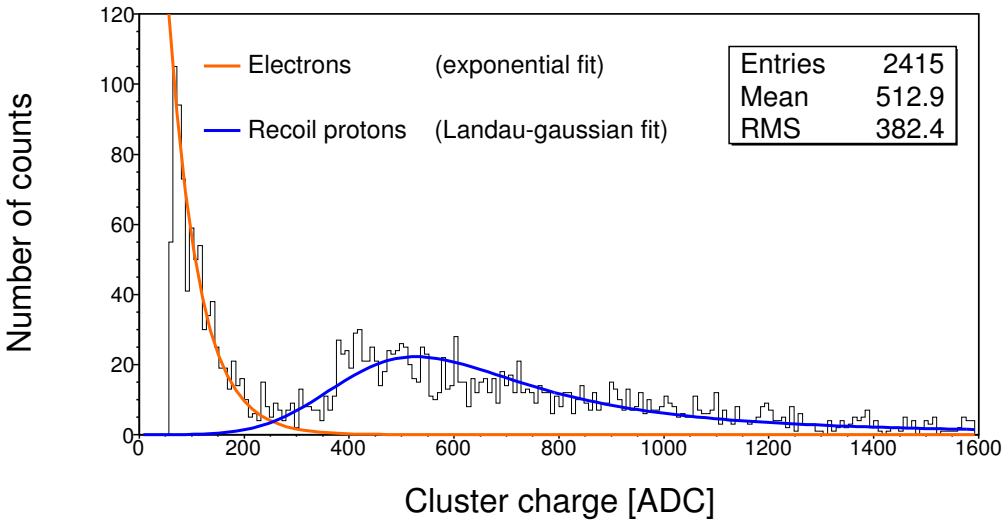

Figure 2.15: Measured cluster charge distribution (in ADC) with a 90-min exposure at 15 cm from the AmBe source. The exponential and Landau-gaussian fits are respectively for the electron and the proton components [32].

by two functions separately. A Landau convoluted with Gaussian fit has been performed on the charge distribution of protons. An exponential function is used for fitting the photoelectron component.

Several cuts in ADC charge or in multiplicity (defined as the number of hit pixels in a cluster) on the signal have been applied to achieve n/γ discrimination. Figure 2.16 illustrates the relative efficiency and the purity of signal as functions of charge and multiplicity cuts. The relative efficiency is defined as $\varepsilon_{rel} = \frac{n_c}{n_p}$, where n_c is the total number of counts obtained with the chosen threshold and n_p is the total number of recoil protons. The purity of the proton signal is defined as $p = 1 - (n_{e^-}/n_c)$, where n_{e^-} is the number of photoelectrons above the threshold. We observe that the multiplicity cuts cannot give good results with regard to n/γ discrimination. By comparing the simulated distribution of protons with the experimental one, a conversion factor around 0.4 keV/ADC results in the superposition of experimental and simulated distributions. This factor includes the effects of charge collection and is only valid for this acquisition chain. In this case, the threshold of 250 ADC corresponds to 100 keV for which the sensor can be considered as γ-transparent.

This study shows that setting only a charge threshold is sufficient to remove the photon contamination. The pixelation of the sensor is therefore unnecessary for n/γ discrimination.

The intrinsic efficiency of the sensor can be calculated by $\varepsilon = n_p/n_n$, where n_n is the number of incident neutrons on the sensor. According to this overlap study, the intrinsic efficiency is calculated as $\varepsilon_{exp} = (1.02 \pm 0.05) \times 10^{-3}$ for AmBe neutrons, which is in good agreement with

the MCNPX simulation value $\varepsilon_{mcnpx} = (1.08 \pm 0.05) \times 10^{-3}$.

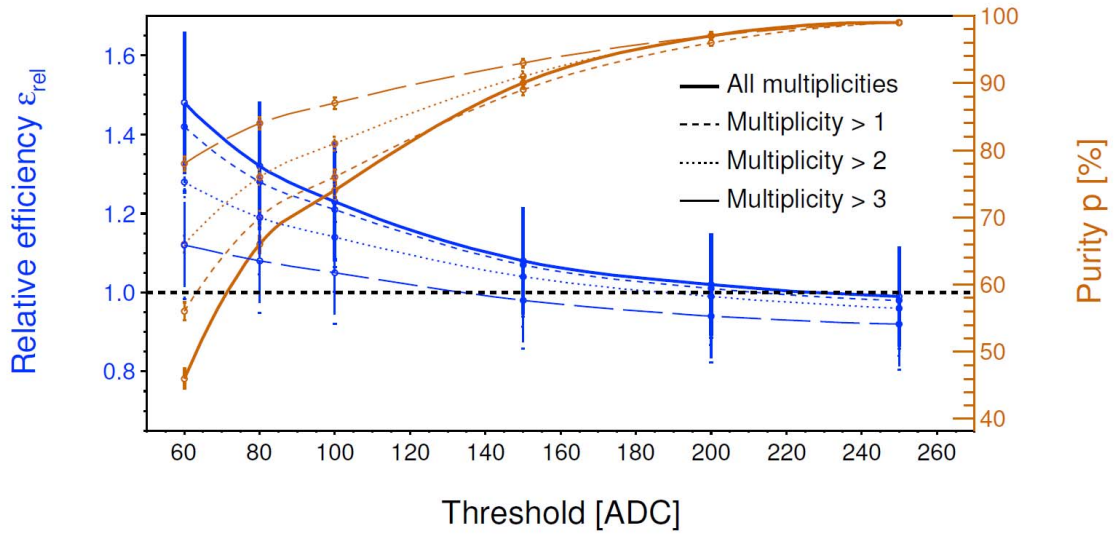

Figure 2.16: The relative efficiency and the purity of signal as functions of charge and multiplicity cuts [32].

2.3.4 Detection of thermal neutrons

To test the sensibility of the MIMOSA-5 to thermal neutrons, experiments had been performed with a californium source moderated with heavy water (^{252}Cf+D_2O) sphere on the Van Gogh irradiator [33] at the LMDN (Laboratoire de Métrologie des neutrons), IRSN, Cadarache, France. A cadmium shell of 0.8 mm-thick can be added to remove the component of the thermal neutrons of the moderated neutron spectrum. In the tests, the sensor was placed at 40 cm from the sources.

2.3.4.1 GEANT4 simulations

Simulations were performed with GEANT4 (*GEometry ANd Tracking*). The simulated deposited energy for MIMOSA-5 with BE10 and BN1 converters exposed to ^{252}Cf+D_2O and (^{252}Cf+D_2O)/Cd are exhibited in Fig. 2.17. A charge threshold of 250 ADC was applied to achieve the γ-transparent characteristic as mentioned in the previous subsection. This threshold implies a significant loss of signal, respectively 30% for the α-particles and 72% for the ^{7}Li. The contribution of thermal neutrons can be calculated by subtracting the signal coming from the (^{252}Cf+D_2O)/Cd source from the one coming from ^{252}Cf+D_2O source. The BN1 is normally less efficient than the BE10 converter since its ^{10}B concentration decreases.

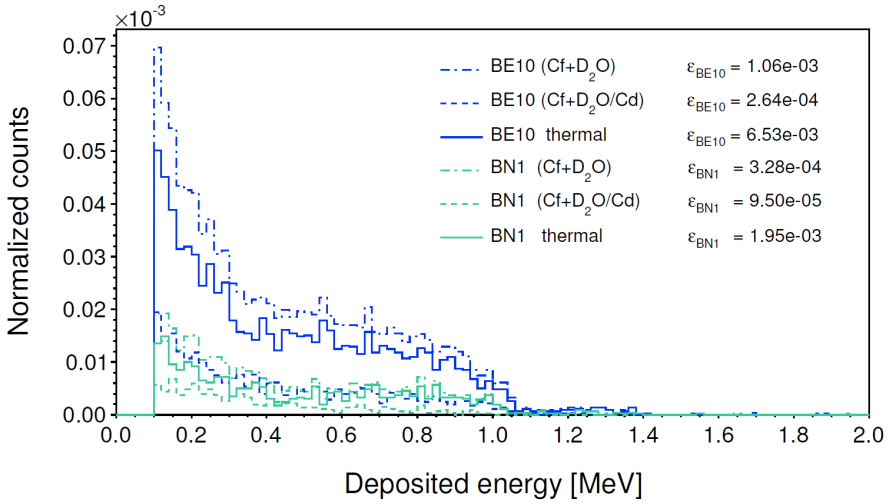

Figure 2.17: Simulated deposited energy for the MIMOSA-5 with BE10 and BN1 converters exposed to the ^{252}Cf+D_2O and the (^{252}Cf+D_2O)/Cd sources. The solid lines represent the contributions of the pure thermal neutrons [33].

	Configuration	ε_{sim}	ε_{exp}
BE10	(^{252}Cf+D_2O)	$(1.06 \pm 0.05) \times 10^{-3}$	$(1.08 \pm 0.05) \times 10^{-3}$
	(^{252}Cf+D_2O)/Cd	$(0.26 \pm 0.02) \times 10^{-3}$	$(0.29 \pm 0.02) \times 10^{-3}$
BN1	(^{252}Cf+D_2O)	$(0.33 \pm 0.02) \times 10^{-3}$	$(0.37 \pm 0.02) \times 10^{-3}$
	(^{252}Cf+D_2O)/Cd	$(0.09 \pm 0.01) \times 10^{-3}$	$(0.12 \pm 0.02) \times 10^{-3}$
BE10	Thermal neutrons	$(6.53 \pm 0.30) \times 10^{-3}$	$(6.46 \pm 0.29) \times 10^{-3}$
BN1		$(1.95 \pm 0.10) \times 10^{-3}$	$(2.08 \pm 0.11) \times 10^{-3}$

Table 2.2: Measured and simulated detection efficiencies with the MIMOSA-5 to ^{252}Cf+D_2O and (^{252}Cf+D_2O)/Cd sources using two types of converters [32].

2.3.4.2 Experimental results

For the same charge threshold (250 ADCs), the measured charge distributions (Fig. 2.18) show the same shape than the simulated ones (Fig. 2.17). The simulated and measured intrinsic efficiencies of the sensor are summarized in Table 2.2. All the experimental results coincide with the simulations. For the first rows of the table, the efficiencies are calculated on the entire spectra, including the fast neutron component. The last two rows give the detection efficiencies on the thermal neutrons. With the BE10 converter, the experimental efficiency is $\varepsilon_{exp} = (6.46 \pm 0.29) \times 10^{-3}$, and the simulated one is $\varepsilon_{sim} = (6.53 \pm 0.30) \times 10^{-3}$. In the case of BN1 converter, the efficiency is still high as $\varepsilon_{exp} = (2.08 \pm 0.11) \times 10^{-3}$. The GEANT4 simulations had demonstrated that these efficiencies are obtained together with a purity of signal as high as 98%.

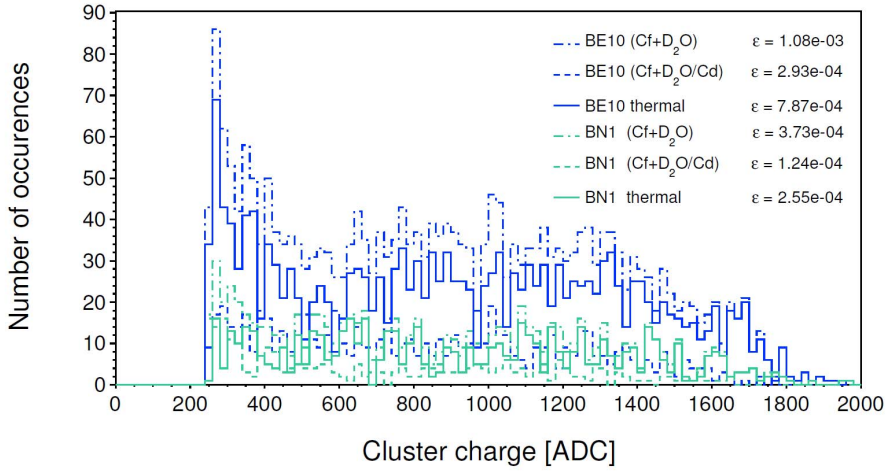

Figure 2.18: Measured deposited energy for the MIMOSA-5 with BE10 and BN1 converters exposed to ^{252}Cf+D_2O and (^{252}Cf+D_2O)/Cd sources. The solid lines represent the contributions of pure thermal neutrons [33].

2.4 Conclusion

CMOS sensors offer theoretically promising characteristics for neutron detection and their application on dosimetry. Among the important features required for a neutron dosemeter, we can mention:

- the ability to detect neutrons over a wide energy range with high sensitivity;
- low sensitivity to photons;
- the constant detection efficiency as a function of the sensor-source distance;
- an isodirectional angular response.

At the same time, the sensor should also offer a sufficient neutron detection efficiency. To intend to be a good candidate for neutron dosimetry, CMOS technology must meet these criteria.

Extensive tests with the thinned MIMOSA-5 sensor have demonstrated the feasibility of developing an APD for neutrons based on CMOS technology. Both of the measured detection efficiencies for fast and thermal neutrons are of the same order of 10^{-3}, which are encouraging to obtain a constant sensitivity response to the energy of the incident neutrons. However, the MIMOSA-5, despite fulfilling many criteria for its use as a neutron detector, has a major drawback: the pixelation makes the data stream too large to develop a portable integrated system, where the data will be directly processed into the system. Therefore, it is necessary to design a dedicated sensor for a future dosemeter, which is the main target of this thesis. The design and tests of new CMOS sensors (AlphaRad family) dedicated on the dosimetry application will be discussed in the following chapters.

Bibliography

[1] M. Trocme, S. Higueret, D. Husson, A. Nourreddine, and T. Le, "A new compact device for efficient neutron counting using a CMOS active pixel sensor," *Radiation Measurements*, vol. 43, no. 2-6, pp. 1100–1103, 2008, proceedings of the 15th Solid State Dosimetry (SSD15).

[2] G. Deptuch, "New generation of monolithic active pixel sensors for charged particle detection," Ph.D. dissertation, Université Louis Pasteur, Strasbourg, France, 2002.

[3] W. Shockley, "Currents to conductors induced by a moving point charge," *Journal of Applied Physics*, vol. 9, no. 10, pp. 635–636, 1938.

[4] S. Ramo, "Currents induced by electron motion," *Proceedings of the IRE*, vol. 27, no. 9, pp. 584–585, sept. 1939.

[5] E. Fossum, "CMOS image sensors: electronic camera-on-a-chip," *Electron Devices, IEEE Transactions on*, vol. 44, no. 10, pp. 1689–1698, oct 1997.

[6] R. Turchetta, J. Berst, B. Casadei, G. Claus, C. Colledani, W. Dulinski, Y. Hu, D. Husson, J. L. Normand, J. Riester, G. Deptuch, U. Goerlach, S. Higueret, and M. Winter, "A monolithic active pixel sensor for charged particle tracking and imaging using standard VLSI CMOS technology," *Nuclear Instruments and Methods in Physics Research Section A: Accelerators, Spectrometers, Detectors and Associated Equipment*, vol. 458, no. 3, pp. 677–689, 2001. [Online]. Available: http://www.sciencedirect.com/science/article/pii/S0168900200008937

[7] M. Szelezniak, "Development of pixel detectors with integrated microcircuits for the vertex detector in the STAR experiment at the RHIC collider," Ph.D. dissertation, Université Louis Pasteur, Strasbourg, France, 2008.

[8] N. Ricquier and B. Dierickx, "Pixel structure with logarithmic response for intelligent and flexible imager architectures," in *Solid State Device Research Conference, 1992. ESSDERC '92. 22nd European*, Sept. 1992, pp. 631–634.

[9] G. Deptuch, W. Dulinski, Y. Gornushkin, C. Hu-Guo, and I. Valin, "Monolithic active pixel sensors with on-pixel amplification and double sampling operation," *Nuclear Instruments and Methods in Physics Research Section A: Accelerators, Spectrometers, Detectors and Associated Equipment*, vol. 512, no. 1-2, pp. 299–309, 2003, proceedings of the 9th European Symposium on Semiconductor Detectors: New Developments on Radiation Detectors. [Online]. Available: http://www.sciencedirect.com/science/article/pii/S0168900203019077

[10] A. Dorokhov, "Optimization of amplifiers for monolithic active pixel sensors," in *Topical Workshop on Electronics for Particle Physics*, Prague, Czech Republic, Sep. 2007, pp. 423–427.

[11] M. Winter, "Achievements and perspectives of CMOS pixel sensors for charged particle tracking," *Nuclear Instruments and Methods in Physics Research Section A: Accelerators,*

Spectrometers, Detectors and Associated Equipment, vol. 623, no. 1, pp. 192–194, 2010, 1st International Conference on Technology and Instrumentation in Particle Physics.

[12] M. Deveaux, "Development of fast and radiation hard monolithic active pixel sensors (MAPS) optimized for open charm meson detection with the CBM - vertex detector," Ph.D. dissertation, Frankfurt University, Frankfurt , Germany & Université Louis Pasteur, Strasbourg, France, 03 2008, https://www.gsi.de/documents/DOC-2008-Jun-82.html.

[13] G. Deptuch, G. Claus, C. Colledani, Y. Degerli, W. Dulinski, N. Fourches, G. Gaycken, D. Grandjean, A. Himmi, C. Hu-Guo, P. Lutz, M. Rouger, I. Valin, and M. Winter, "Monolithic active pixel sensors with in-pixel double sampling operation and column-level discrimination," *Nuclear Science, IEEE Transactions on*, vol. 51, no. 5, pp. 2313–2321, oct. 2004.

[14] Y. Degerli, G. Deptuch, N. Fourches, A. Himmi, Y. Li, P. Lutz, F. Orsini, and M. Szelezniak, "A fast monolithic active pixel sensor with pixel-level reset noise suppression and binary outputs for charged particle detection," *Nuclear Science, IEEE Transactions on*, vol. 52, no. 6, pp. 3186–3193, dec. 2005.

[15] Y. Degerli, A. Besson, G. Claus, M. Combet, A. Dorokhov, W. Dulinski, M. Goffe, A. Himmi, Y. Li, and F. Orsini, "Development of Binary Readout CMOS Monolithic Sensors for MIP Tracking," *Nuclear Science, IEEE Transactions on*, vol. 56, no. 1, pp. 354–363, feb. 2009.

[16] C. Hu-guo, J. Baudot, G. BertoloneI, A. BessonI, B. A. *et al.*, "Design and characterisation of a fast architecture providing zero suppressed digital output integrated in a high resolution CMOS pixel sensor for the STAR vertex detector and the EUDET beam telescope," in *Topical Workshop on Electronics for Particle Physics, TWEPP08*, Naxos, Greece, Sep 2008, pp. 80–84.

[17] "Eudet: Detector r&d towards the international linear collider," European Union. [Online]. Available: http://www.eudet.org/

[18] A. Himmi, G. Doziere, C. Hu-Gio, and M. Winter, "JRA-1 Milestone SDC Prototype 2 ready," 2007. [Online]. Available: http://www.eudet.org/e26/e28/e182/e591/eudet-memo-2007-55.pdf

[19] I. Valin, C. Hu-Guo, J. Baudot, G. Bertolone, A. Besson, C. Colledani, G. Claus, A. Dorokhov, G. Doziere, W. Dulinski, M. Gelin, M. Goffe, A. Himmi, K. Jaaskelainen, F. Morel, H. Pham, C. Santos, S. Senyukov, M. Specht, G. Voutsinas, J. Wang, and M. Winter, "A reticle size CMOS pixel sensor dedicated to the STAR HFT," *Journal of Instrumentation*, vol. 7, no. 1, 2012. [Online]. Available: http://stacks.iop.org/1748-0221/7/i=01/a=C01102

[20] C. Hu-Guo, J. Baudot, G. Bertolone, A. Besson, A. Brogna, C. Colledani, G. Claus, R. D. Masi, Y. Degerli, A. Dorokhov, G. Doziere, W. Dulinski, X. Fang, M. Gelin, M. Goffe, F. Guilloux, A. Himmi, K. Jaaskelainen, M. Koziel, F. Morel, F. Orsini, M. Specht,

Q. Sun, O. Torheim, I. Valin, and M. Winter, "First reticule size MAPS with digital output and integrated zero suppression for the EUDET-JRA1 beam telescope," *Nuclear Instruments and Methods in Physics Research Section A: Accelerators, Spectrometers, Detectors and Associated Equipment*, vol. 623, no. 1, pp. 480–482, 2010, 1st International Conference on Technology and Instrumentation in Particle Physics. [Online]. Available: http://www.sciencedirect.com/science/article/pii/S0168900210006078

[21] M. Koziel, A. Dorokhov, J.-C. Fontaine, R. De Masi, and M. Winter, "Development of radiation tolerant monolithic active pixel sensors with fast column parallel read-out," *Nuclear Instruments and Methods in Physics Research Section A: Accelerators, Spectrometers, Detectors and Associated Equipment*, vol. 624, no. 2, pp. 437–442, Dec. 2010.

[22] M. Deveaux, S. Amar-Youcef, C. Dritsa, I. Froehlich, C. Muentz, S. Seddiki, J. Stroth, T. Tischler, and C. Trageser, "Design considerations for the Micro Vertex Detector of the Compressed Baryonic Matter experiment," in *17th International Workshop on Vertex detectors - Vertex 2008*, Island Ut o, Sweden, Jul 2008, p. 028. [Online]. Available: https://www.gsi.de/documents/DOC-2010-Jan-93.html

[23] A. Dorokhov, G. Bertolone, J. Baudot, A. Brogna, C. Colledani, G. Claus, R. D. Masi, M. Deveaux, G. DoziÃ¨re, W. Dulinski, J.-C. Fontaine, M. Goffe, A. Himmi, C. Hu-Guo, K. Jaaskelainen, M. Koziel, F. Morel, C. Santos, M. Specht, I. Valin, G. Voutsinas, F. Wagner, and M. Winter, "Improved radiation tolerance of MAPS using a depleted epitaxial layer," *Nuclear Instruments and Methods in Physics Research Section A: Accelerators, Spectrometers, Detectors and Associated Equipment*, vol. 624, no. 2, pp. 432–436, 2010, proceedings of the 11th European Symposium on Semiconductor Detectors. [Online]. Available: http://www.sciencedirect.com/science/article/pii/S0168900210007072

[24] M. Deveaux, J. Baudot, N. Chon-Sen, G. Claus, C. Colledani, R. D. Masi, D. Doering, A. Dorokhov, G. Doziere, W. Dulinski, I. Fr ohlich, M. Gélin, M. Goffe, A. Himmi, C. Hu-Guo, K. Jaaskelainen, M. Koziel, F. Morel, C. M untz, C. Santos, C. Schrader, M. Specht, J. Stroth, C. Trageser, I. Valin, F. M. Wagner, and M. Winter, "Radiation tolerance of a column parallel CMOS sensor with high resistivity epitaxial layer," *Journal of Instrumentation*, vol. 6, no. 02, p. C02004, 2011. [Online]. Available: http://stacks.iop.org/1748-0221/6/i=02/a=C02004

[25] A. Gay, G. Claus, C. Colledani, G. Deptuch, M. Deveaux, W. Dulinski, Y. Gornushkin, D. GrandJean, A. Himmi, C. Hu, I. Valin, and M. Winter, "High-resolution CMOS sensors for a vertex detector at the linear collider," *Nuclear Instruments and Methods in Physics Research Section A: Accelerators, Spectrometers, Detectors and Associated Equipment*, vol. 549, no. 1-3, pp. 99–102, 2005, proceedings of the 12th International Workshop on Vertex Detectors (VERTEX 2003).

[26] M. Battaglia, D. Contarato, P. Giubilato, L. Greiner, L. Glesener, and B. Hooberman, "A study of monolithic CMOS pixel sensors back-thinning and their application for a pixel beam telescope," *Nuclear Instruments and Methods in Physics Research Section A: Accelerators,*

Spectrometers, Detectors and Associated Equipment, vol. 579, no. 2, pp. 675–679, 2007, proceedings of the 6th Symposium on the Development and Application of Semiconductor Detectors.

[27] W. Dulinski, A. Braem, M. Caccia, G. Claus, G. Deptuch, D. Grandjean, C. Joram, J. Séguinot, and M. Winter, "Tests of a backside illuminated monolithic CMOS pixel sensor in an HPD set-up," *Nuclear Instruments and Methods in Physics Research Section A: Accelerators, Spectrometers, Detectors and Associated Equipment*, vol. 546, no. 1-2, pp. 274–280, 2005, proceedings of the 6th International Workshop on Radiation Imaging Detectors.

[28] G. Deptuch, "Tritium autoradiography with thinned and back-side illuminated monolithic active pixel sensor device," *Nuclear Instruments and Methods in Physics Research Section A: Accelerators, Spectrometers, Detectors and Associated Equipment*, vol. 543, no. 2-3, pp. 537–548, 2005.

[29] G. Deptuch, W. Dulinski, M. Caccia, and M. Winter, "High-resolution, back-side illuminated monolithic active pixel sensor for low-energy electron imaging," *Nuclear Science, IEEE Transactions on*, vol. 52, no. 5, pp. 1745–1754, oct. 2005.

[30] L. Badano, O. Ferrando, T. Klatka, M. Koziel, G. Molinari, and M. Pezzetta, "Secondary emission monitor for low-interception monitoring (slim): an innovative nondestructive beam monitor for the extraction lines of a hadrontherapy center," *Nuclear Science, IEEE Transactions on*, vol. 51, no. 6, pp. 2990–2998, dec. 2004.

[31] A.-C. Milazzo, P. Leblanc, F. Duttweiler, L. Jin, J. C. Bouwer, S. Peltier, M. Ellisman, F. Bieser, H. S. Matis, H. Wieman, P. Denes, S. Kleinfelder, and N.-H. Xuong, "Active pixel sensor array as a detector for electron microscopy," *Ultramicroscopy*, vol. 104, no. 2, pp. 152–159, 2005. [Online]. Available: http://www.sciencedirect.com/science/article/pii/S0304399105000513

[32] M. Vanstalle, "Dosimétrie électronique et métrologie neutrons par capteur CMOS a pixels actifs," Ph.D. dissertation, Université de Strasbourg, Strasbourg, France, 2011.

[33] M. Vanstalle, D. Husson, S. Higueret, T. Lê, and A. Nourreddine, "Detection of thermal neutrons with a CMOS pixel sensor for a future dosemeter," in *In ANIMMA Congress, Advancements in Nuclear Instrumentation Measurement Methods and their Applications*, Ghent, Belguim, June 6-9, 2011.

[34] F. Sarradin and F. Boudet, Dosirad lab, 15 Rue du GARDON, 26700 PIERRELATTE, FRANCE, 2010. [Online]. Available: http://dosirad.pagespro-orange.fr/soc_a.htm

[35] Z. Liu, J. Chen, P. Zhu, Y. Li, and G. Zhang, "The 4.438 mev gamma to neutron ratio for the am-be neutron source," *Applied Radiation and Isotopes*, vol. 65, no. 12, pp. 1318–1321, 2007. [Online]. Available: http://www.sciencedirect.com/science/article/pii/S0969804307001200

[36] M. Vanstalle, D. Husson, S. Higueret, M. Trocmé, T. Lê, and A. Nourreddine, "Demonstrating the γ-transparency of a CMOS pixel detector for a future neutron dosimeter," *Nuclear Instruments and Methods in Physics Research Section A: Accelerators,*

Spectrometers, Detectors and Associated Equipment, vol. 662, no. 1, pp. 45–48, 2012. [Online]. Available: http://www.sciencedirect.com/science/article/pii/S0168900211018481

Chapter 3

Simulation of charge collection in micro-diodes and readout electronics study

3.1 Introduction

The promising features of CMOS technology in neutron dosimetry have been demonstrated with a pixelated CMOS sensor, leading to the development of dedicated chip. As already explained in the previous chapter, a true pixel readout is unnecessary for n/γ separation. Moreover, no spatial resolution is required in our case. Therefore, the pixelation will be replaced by a "mono-pixel". A standard CMOS technology provides micro-diode structures for charge collection, providing a solution for integration of a large detecting surface ($\sim$cm^2) with low capacitance and low leakage current. Typically, the capacitance of a 3 µm×3 µm n-well/p-epi (p-epitaxial layer) diode (5 V inverse biased) is around 3 fF: this allows connecting several hundreds of diodes in parallel with still a limited capacitance. Furthermore, the segmentation of a large junction of cm^2 size into a finite number of small diodes allows to benefit from a large area with moderate leakage current. Due to the built-in potential at the interface of p-epi and p-substrate, the excess carriers created in the epitaxial layer do not escape to the substrate during diffusion. In a standard CMOS technology, the junction capacitance of a single diode C_d is modeled by

$$C_d = \frac{WLC_j}{\left(1+\frac{V_d}{V_{bi}}\right)^{M_j}} + \frac{2(W+L)C_{jsw}}{\left(1+\frac{V_d}{V_{bi}}\right)^{M_{jsw}}} \tag{3.1}$$

where W, L are the dimensions of the diode implantation area, C_j is the junction capacitance per drawn area (in fF/µm^2), C_{jsw} is the junction capacitance per drawn perimeter (in fF/µm), M_j and M_{jsw} are the area and sidewall junction grading coefficients, respectively, V_{bi} is the junction potential and V_d is the reverse bias potential of the diode. The diode array has no active pixel

addressing system, and all the diodes are just connected in parallel through standard aluminum lines running on the oxide layer. The other contribution to the total capacitance C_{det} of the diode array comes from the connection metal lines C_{con}, which is dependent on the inter-diode distance p. For a grid structure of N diodes, we have $C_{det} = N \cdot C_d + C_{con}$.

In a pixelated sensor for low ionizing particles (i.e. MIPs), the typical distance between diodes (pitch size) is ∼20 µm (see Chapter 2, § 2.2). In the case of neutrons, the charge signal generated by their secondary charged particles is hundreds times the one of MIPs. This larger linear energy transfer allows a larger inter-diode distance, however within the diffusion length condition.

Low energy neutrons can generate α-particles through a boron-rich converter. In a first stage, our group designed the first prototype, AlphaRad-1, to study the feasibility of fast α counting on a large area without individual pixel readout circuit. The AlphaRad-1 chip is designed and fabricated in the AMS (Austria Micro Systems) 0.6 µm technology with a 14 µm thick epitaxial layer on a standard silicon substrate, allowing detection of charged particles able to cross the SiO_2 layer (∼6 µm thick). In the AlphaRad-1 chip, the inter-diode distance of $p = 80$ µm, and one full array of 32×64 diodes occupies a total sensitive area of 2.56×5.12 mm^2. As a result, with $N = 2048$, $V_d = 2.5$ V and the parameters $\{C_j, M_j, C_{jsw}, M_{jsw}, V_{bi}\}$ of this technology, the total capacitance of the detector C_{det} is about 40.9 pF, comparing to a unique diode covering the same surface with an enormous capacitance of 282 pF. However, this value (40.9 pF) is by no means negligible in the integrated circuit, and it causes severe constraints on the reset transistor and on the noise figure of the signal processing circuits. For a given surface, larger inter-diode distance results in a lower total capacitance, but more charge combination before the charge collection thus a lower signal. Additionally, as the generated charge are shared in the neighboring collecting diode (a cluster), larger diode-distance cause a longer charge collection time of the cluster. Clearly, we have to make a trade-off between an efficient charge collection and a low sensor capacitance. The first part of this chapter presents the charge collection properties in the diode-array with different geometries according to the physical level simulations. In the second part, two different signal processing architectures (the voltage mode and the current mode) for the diode-array will be discussed. The voltage mode architecture used in the AlphaRad-1 chip has been redesigned in a 0.35 µm CMOS process. The current mode architecture has been proposed in this study and designed in the same process. Detailed design considerations and noise analyses will be presented.

3.2 Simulations of charge collection in micro-diodes

In the application of neutron counting, energy measurement is not required. The first prototype AlphaRad-1 has demonstrated that fast counting on a large surface can be achieved without pixellization. In the AlphaRad-2 chip 32×32 micro-diodes in the reverse bias mode are connected in parallel to construct a sensitive part with a single output to the signal processing electronics. This configuration offers at the same time a wide sensitive area, a low leakage

current, a small capacitance and a very simple signal processing scheme. The dimensions of the diodes and the inter-diode distance should be chosen according to the compromise between the collecting response and the total capacitance of the detector.

In order to study the charge collection mechanism and its time properties in diode matrices, and to estimate the charge collection efficiency and its time properties, device physics simulations have been carried out by means of the Sentaurus-TCAD commercial package [1]. Several authors had performed device simulations for monolithic active pixel sensors [2–4], concerning the charge collection in the pixel structure with small pixel pitch (∼20 µm). In this work, we address the charge collection in the diode array with a significantly larger inter-diode distance (∼80 µm).

3.2.1 Simulation tool

The Sentaurus-TCAD of Synopsys, is the newest generation of Technology Computer-Aided Design (TCAD) software, taking the place of previous ISE-TCAD of the Integrated Systems Engineering (ISE). The Sentaurus-TCAD package allows 3-dimensional modeling of the simulated device and a detailed description of the detector geometry and physical parameters. This software provides a comprehensive suite of tools, and three of them are used in this work: Sentaurus Structure Editor (SSE) for creating geometric structures and mesh grids, Sentaurus Device (SD) for simulating semiconductor device performance, and Tecplot SV for visualizing the results.

3.2.2 Models of physics

3.2.2.1 Electrical models

In all semiconductor devices, mobile charges (electrons and holes) and immobile charges (ionized dopants or traps) determine the electrostatic potential ψ, and in turn, these charges are themselves affected by the electrostatic potential. The electrostatic potential is the solution of the Poisson equation, which is

$$\nabla^2\psi = -\frac{q}{\varepsilon_0\varepsilon_{Si}}(p - n + N_D - N_A) \tag{3.2}$$

where ε_0 and ε_{Si} are the electrical permittivity of vacuum and the dielectric constant of silicon, n and p are the electron and hole densities, and N_D, N_A are the concentration of ionized donors and acceptors, respectively. In common CMOS processes, phosphorus and boron atoms are usually used as donors and acceptors. Their impurity levels in silicon are sufficiently shallow to justify the assumption of complete ionization at room temperature. The density of mean and local charge created in any part of the detector by an impinging particle is negligible compared to the density of ionized dopants at room temperature. Therefore, the potential distribution in the detector volume can be calculated by taking into account only the distributions of thermally generated charges and ionized dopants, and the external voltages applied to the contact electrodes. Then, the important hypothesis of constant electric field can be assumed for the charge transport [3].

Electron and hole densities can be computed from the electron and hole quasi-Fermi potentials, and vice versa. If Boltzmann statistics is assumed, the formulas are given by

$$n = N_C \exp\left(\frac{-q\Phi_n - E_C}{kT}\right) \qquad \text{and} \qquad p = N_V \exp\left(\frac{E_V + q\Phi_p}{kT}\right) \tag{3.3}$$

where E_C and E_V are conduction and valence band edges, and Φ_n, Φ_p are electron and hole quasi-Fermi potentials, respectively. N_C and N_V are the effective density-of-states in the conduction and the valence band, respectively, and defined as

$$N_C = 2\left(\frac{2\pi m_e kT}{h^2}\right)^{3/2} \qquad \text{and} \qquad N_V = 2\left(\frac{2\pi m_h kT}{h^2}\right)^{3/2} \tag{3.4}$$

where m_e and m_h are the effective mass of electrons and holes, respectively, and h is Planck's constant. The quasi-Fermi potentials are given by

$$\Phi_n = \psi - \frac{kT}{q}\ln\left(\frac{n}{n_{i,eff}}\right) \qquad \text{and} \qquad \Phi_p = \psi + \frac{kT}{q}\ln\left(\frac{p}{n_{i,eff}}\right) \tag{3.5}$$

where $n_{i,eff}$ is the effective intrinsic carrier density accounting for the bandgap narrowing effect, defined as

$$n_{i,eff} = n_i \exp\left(\frac{-E_{bgn}}{2kT}\right) \qquad \text{with} \qquad n_i(T) = \sqrt{N_C(T)N_V(T)}\exp\left(\frac{E_g(T)}{2kT}\right) \tag{3.6}$$

where E_g is the bandgap energy, and E_{bng} stands for the bandgap narrowing effect. [1]

The drift-diffusion transport model in Sentaurus Device was selected to study the carrier transport. The drift current densities for electrons and holes are given by

$$\overrightarrow{J_{n,diff}} = qD_e\nabla n \qquad \text{and} \qquad \overrightarrow{J_{p,diff}} = -qD_h\nabla p \tag{3.7}$$

where D_e, D_h are the diffusion constants, and ∇n, ∇p are the gradients of the carriers concentrations. The mobility constants $\mu_{e,h}$ and the diffusion constants $D_{e,h}$ are related by the Einstein equations

$$D_{e,h} = \frac{kT}{q}\mu_{e,h}. \tag{3.8}$$

By taking the gradient of Eq. (3.3) and using Eq. (3.8), the correspondence of Eq. (3.7) for electron and hole continuity equations is written

$$\overrightarrow{J_n} = -nq\mu_e\nabla\overrightarrow{\Phi_n} \qquad \text{and} \qquad \overrightarrow{J_p} = -pq\mu_h\nabla\overrightarrow{\Phi_p}. \tag{3.9}$$

1. The detailed description of the band gap value dependence on doping and temperature are discussed in the following paragraph.

3.2.2.2 Carriers mobility

In doped semiconductors, scattering of the carriers by charged impurity ions leads to degradation of the mobility. In the simulations, the Masetti model [5] was chosen to simulate doping-dependent mobility in silicon. In this model, the carrier mobility is given by

$$\mu_{dop} = \mu_{min1} \exp\left(-\frac{P_c}{N_A + N_D}\right) + \frac{\mu_{const} - \mu_{min2}}{1 + \left(\frac{N_A+N_D}{C_r}\right)^{\alpha}} - \frac{\mu_1}{1 + \left(\frac{C_s}{N_A+N_D}\right)^{\beta}} \tag{3.10}$$

where μ_{min1}, μ_{min2}, and μ_1 are the reference mobilities, and P_c, C_r, C_s are reference doping concentrations. [2] The low-doping reference mobility μ_{const} is determined by the constant mobility model [6], which accounts for phonon scattering and, therefore, it is dependent only on the lattice temperature

$$\mu_{const} = \mu_L \left(\frac{T}{300K}\right)^{-\xi} \tag{3.11}$$

where μ_L is the mobility due to bulk phonon scattering. The default values of μ_L are 1417 and 470.5 $\mathrm{cm}^2/\mathrm{V{\cdot}s}$ for electrons and holes, respectively. The exponent ξ is 2.5 for electrons and 2.2 for holes.

3.2.2.3 Carriers recombination

For the charge carriers recombination rate, only the contribution due to recombination via deep levels in the band gap, usually labeled Schockley-Read-Hall (SRH) recombination [7], was taken into account. In Sentaurus Device, the following formula is implemented

$$R_{SRH} = \frac{np - n_{i,eff}^2}{\tau_p(n + n_1) + \tau_n(p + p_1)} \tag{3.12}$$

with

$$n_1 = n_{i,eff} \exp\left(\frac{E_{trap}}{kT}\right) \qquad \text{and} \qquad p_1 = n_{i,eff} \exp\left(-\frac{E_{trap}}{kT}\right) \tag{3.13}$$

where E_{trap} is the difference between the defect level and intrinsic level. Since correct values of the defect level are poorly known, a default value of $E_{trap} = 0$ was assumed in the simulations, possibly overestimating the values of carrier lifetimes.

The minority lifetimes τ_n and τ_p are also dependent of the doping and modeled with the Scharfetter relation [1]

$$\tau_{dop}(N_A + N_D) = \tau_{min} + \frac{\tau_{max} - \tau_{min}}{1 + \left(\frac{N_A+N_D}{N_{ref}}\right)^{\gamma}} \tag{3.14}$$

where τ_{min}, τ_{max} are the reference carrier lifetimes, and N_{ref} is the reference concentration of ionized impurities. The default values of τ_{min} is 0 both for electrons and holes. τ_{max} are 10 µs and 3 µs for electrons and holes, respectively. The exponent $\gamma = 1$, and $N_{ref} = 1 \times 10^{16}$ cm^{-3}.

2. The default coefficients used in the simulations are omitted for simplicity, and can be found in [1].

The electron and hole diffusion lengths L_e and L_h are related to the electron and hole lifetimes, τ_e and τ_h, and the electron and hole mobilities μ_e and μ_h, through the following equation

$$L_e = \sqrt{\frac{kT}{q}\mu_e\tau_e} \qquad \text{and} \qquad L_h = \sqrt{\frac{kT}{q}\mu_h\tau_h} \tag{3.15}$$

The band-to-band Auger recombination, which is a typically important at high carrier densities, is activated in the simulation. The rate of band-to-band recombination rate R^A_{net} is given by

$$R^A_{net} = (C_n n + C_p p)(np - n^2_{i,eff}) \tag{3.16}$$

with temperature-dependent Auger coefficients [8–10]

$$C_n(T) = \left(A_{A,n} + B_{A,n}\left(\frac{T}{T_0}\right) + C_{A,n}\left(\frac{T}{T_0}\right)^2\right)\left[1 + H_n \exp\left(-\frac{n}{N_{0,n}}\right)\right] \tag{3.17}$$

$$C_p(T) = \left(A_{A,p} + B_{A,p}\left(\frac{T}{T_0}\right) + C_{A,p}\left(\frac{T}{T_0}\right)^2\right)\left[1 + H_p \exp\left(-\frac{p}{N_{0,p}}\right)\right] \tag{3.18}$$

where $T_0 = 300$ K. The default values of coefficients $A_{A,n,p}$, $B_{A,n,p}$, $C_{A,n,p}$, H, and N_0 [1] were used in simulations.

3.2.2.4 Bandgap model

The value of the band gap depends on the concentration of impurities as well as on the lattice temperature. The lattice temperature-dependence of the band gap is modeled by

$$E_g(T) = E_g(0) - \frac{\alpha T^2}{T + \beta} \tag{3.19}$$

where $\alpha = 4.73 \times 10^{-4}$ eV/K and $\beta = 636$ K, and $E_g(0)$ is the bandgap energy at 0 K (differs for different bandgap models). The effective band gap results form the band gap reduced by bandgap narrowing

$$E_{g,eff}(T) = E_g(T) - E_{bgn} \tag{3.20}$$

where E_{bgn} is determined by the particular bandgap narrowing model used. The Bennett-Wilson model [11] was used, and E_{bgn} is given by the following formula

$$E_{bgn} = \begin{cases} E_{ref}\left[\ln\left(\frac{N_{tot}}{N_{ref}}\right)\right]^2 & \text{if } N_{tot} \geq N_{ref} \\ 0 & \text{otherwise} \end{cases} \tag{3.21}$$

where $E_{ref} = 6.84 \times 10^{-3}$ eV, $N_{ref} = 3.16 \times 10^{18}\text{cm}^{-3}$ and $N_{tot} = N_{D,0} + N_{A,0}$ is the total doping concentration. For the Bennett-Wilson model, the bandgap energy at 0 K $E_g(0) = 1.1696$ eV.

3.2.2.5 Charge generation model

When high-energy particles penetrate a semiconductor device, they deposit their energy by the generation of excess carriers (electron-hole pairs). The interaction of a charged particle with the device is simulated by the excess charge distribution, which is declared at the beginning of each transient simulation. The impact position is defined as a point on the device surface and the distribution of the generated charge density is specified along the particle track. The *Heavy Ion Model* [1] was used to describe the excess carriers in the sensitive volume due to the passage of a single proton. In the *Heavy Ion Model*, the track of impact particle is defined by a length and the transverse spatial influence is assumed to be symmetric about the track axis, and the generation rate is computed by

$$G(l, w, t) = G_{LET}(l)R(w, l)T(t) \tag{3.22}$$

where l and w are the length and the radius of the track, respectively. $R(w)$ and $T(t)$ are functions describing the spatial and temporal variations of the generation rate. $G_{LET}(l)$ is the linear energy transfer (LET) density and its unit is pairs/cm^3. $T(t)$ is defined as a Gaussian function in the model. The spatial distribution, $R(w, l)$ can be defined as an exponential or a Gaussian function. [3] A Gaussian spatial distribution was assumed with a constant width of 1 µm along the particle track. In the simulations, the length of the track was parameterized, and the LET generation density $G_{LET}(l)$ was modified correspondingly to generate 50 000 electron-hole pairs. The amount of generated charge was chosen according to the required threshold for which the sensor can be considered as γ-transparent (see Chapter 2, § 2.3.3.2).

3.2.3 Simulated structure

The simulated structure is described by means of boundaries inside which the desired mesh granularity and doping profiles are specified. The doping profiles used in this work refer to a twin-tub CMOS 0.35 µm process. Fig. 3.1(a) presents the doping files used in the simulated structure for an epitaxial layer (epi-layer) of 14 µm. The black, solid line represents the profile along an axis passing through the center of the collecting n-well/p-epi diode, while the blue, dashed line refers to the profile along an axis passing through the complementary p-well. It can be seen that there are four orders of magnitude difference between the doping of the epi-layer (3×10^{15} cm^{-3}) and the doping of the substrate (1×10^{19} cm^{-3}), and two orders of magnitude between the doping of the epi-layer and the p-well (1×10^{17} cm^{-3}). These doping differences result in potential barriers at the boundaries of the epi-layer. As a consequence, the excess electrons remain inside the epitaxial layer, where they diffuse randomly until they are collected by the n-wells. The transition region between the epi-layer and the substrate has in reality a doping gradient, because of the dopants diffusing from the substrate during the process of the epitaxial

3. The detailed descriptions of $T(t)$ and $R(w, l)$ with default values parameters used in simulations are omitted for simplicity, and can be found in [1].

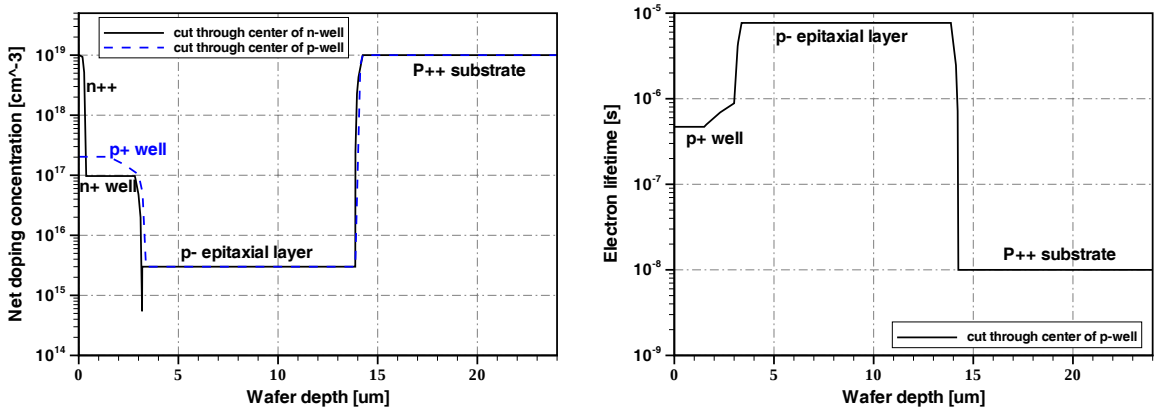

(a) (b)

Figure 3.1: (a) Doping profiles used in the device simulations, as a function of wafer depth, (b) Electron lifetime profile resulting from the doping dependence.

layer growth. Due to lack of any data on the form of this zone, the simply abrupt junction was used in the simulations.

The excess carrier lifetime in the different parts of the device is a crucial parameter for the charge collection process. The carrier lifetime at a certain temperature depends on doping concentration and on the material quality (i.e. bulk defects, traps). The latter is poorly known and was not taken into account in the simulations. The electron lifetime resulting from doping dependence is determined according to the Scharfetter relation Eq. (3.14), as shown in Fig. 3.1(b). Taking the really large electron lifetime of 7.69 µs estimated in the epi-layer, the corresponding electron diffusion length according to Eqs. (3.10) and (3.15) is calculated to be 165 µm. To simplify the simulated model, we consider the charge collection within one diffusion length from the point where the minority carriers are generated as a close approximation of the total collected charge by the whole diode array (which typically consists of thousand of diodes). Thus the dimension of the simulated structure surface was chosen to be 320×320 µm^2. The size of the simulated structure was mainly limited by the computing power of the workstation used for the simulations. Considering an epitaxial layer of 14 µm thick and a reduced substrate layer, the maximum simulated volume was 320×320×34 µm^3. In the Sentaurus Device, the outer boundaries of the simulated structure without contact are treated with the reflective boundary conditions, which potentially leads to the an overestimation of the collected charge. [4] In the real detector, charge carriers diffusing out of the simulated volume are either collected by other diodes or recombined in the detector volume. In order to simulate non-reflective boundary condition, the same boundary conditions as in [3], have been applied.

4. Reflective (or ideal Neumann) boundary conditions can be expressed as: $\overrightarrow{E} \cdot \widehat{n} = 0$, $\overrightarrow{J_n} \cdot \widehat{n} = 0$, $\overrightarrow{J_p} \cdot \widehat{n} = 0$, where $\overrightarrow{E}$ is the electric field vector, $\overrightarrow{J_n}$ and $\overrightarrow{J_p}$ are electron and hole current densities, respectively, and $\widehat{n}$ is a unity-length normal vector on the boundary surface. In this case, the charge carriers which would reach the boundaries would then be reflected backwards.

The mesh refinement was adjusted in different parts of the simulated volume in order to be optimized in terms of computation speed and the required precision of analyses. The finest size, ∼0.25 µm was used around the collecting diodes and along the path of the traversing particle. A mesh size of ∼1 µm was used in the volume of n-wells and p-wells and in the regions with high gradients of doping concentration, i.e, the interface of epitaxial and substrate layer. The mesh size was increased to 4-6 µm in the other parts.

3.2.4 Simulation procedure

Based on the selected models for state physics and meshed structures, the terminal currents, voltages and charges can be computed by the solver. The Sentauraus Device provides a series of solve modes for different applications. The Quasistationary mode is used to evaluate the DC characteristics. It can ramp a device from one solution to another through the modification of its boundary conditions (i.e. ramping the voltage at a contact or parameter values). The transient mode is used to perform a transient time simulation and it is essential for the *Heavy Ion Model*. This mode must start with a device that has already been solved, a static solution of the Poisson equation is required. Using this solution as a starting point, a static solution of the coupled Poisson and continuity equations is obtained. Then the real transient simulation starts: the crossing of a impinging charged particle on the detector structure is simulated and the relaxation process of the excess charge towards an equilibrium condition is followed in time; the current thus induced at the collecting diode electrodes is calculated and plotted.

3.2.5 Simulation results

In order to study the charge collection characteristics, i.e. the charge collection efficiency and the collection time, as functions of the design parameters, the simulations are carried out in two steps: firstly, we perform several transient simulations for a fixed simulated volume with different geometric parameters, i.e. diode size, inter-diode distance; secondly, we perform transient simulations on a given diode cluster configuration, with the substrate layer thickness as a parameter, to study the contribution of the substrate layer.

3.2.5.1 Effect of the diode array parameters

Based on the parameters of the micro-diode array in the AlphaRad-1, five sets of geometric parameters are selected to compare the collection properties using the same doping profiles as in Fig. 3.1(a). Concerning only the effect of the geometric parameters to the charge collection in a fixed sensitive volume, the substrate layer was, in a first approximation, not included in the simulated model. The simulated volume is chosen to be 320×320×14 µm^3, in which the epitaxial layer (∼14 µm-thick) and a ∼0.3 µm strongly doped p++ diffusion (10^{19} cm^{-3}) is included to simulate the interface of epitaxial layer and substrate. For the given simulation

volume, different number of diodes are inserted into the structure owing to different inter-diode distance, i.e. (3×3), (4×4) and (6×6) diodes corresponding with the distance of 100, 80 and 50 µm, respectively. In each set, a transient simulation is performed with a single event of a charged particle at a given impact point. According to the simulation of the charge collection dependence on the hit position in [3], the charge collected on the central pixel (collecting diode) depends strongly on the hit position, while this dependence is much weaker for clusters of 2×2 or 3×3 pixels. In our case, concerning only the total collected charge in the whole diode array, we neglected the influence of the impact position and intended to make a rough estimation of the expected signals.

In the simulations, the impinging particle is always passing through on diagonal side from the center of the central diode and perpendicular to the detector surface (as show in Fig. 3.2). The distance between the hit point and the center of the central diode is chosen to be $\frac{\sqrt{2}}{4}p$, where p is the inter-diode distance. For instance, the impact position is located in a distance of 28 µm on diagonal side from the center of the seed diode. All the simulations in this step are carried out at the temperature 293 K.

In all simulated structures, the collecting diodes are reverse biased at the constant potential $V_R = 1.6$ V. Figure 3.2 presents the selected transient simulation results with the same time at which the particle impacts (t=1 ns). They are obtained for the structures with a fixed diode size of 5×5 µm^2. The plots in Fig. 3.2(a) and Fig. 3.2(b) show the current in every collecting diode as a function of time, for the structure with the inter-diode distance of 80 µm and 100 µm, respectively. The charge collected in every collecting diode is calculated at the end of the transient simulation by integrating the current. The total collected charge of the simulated structure is the sum of the charge collected by every diode.

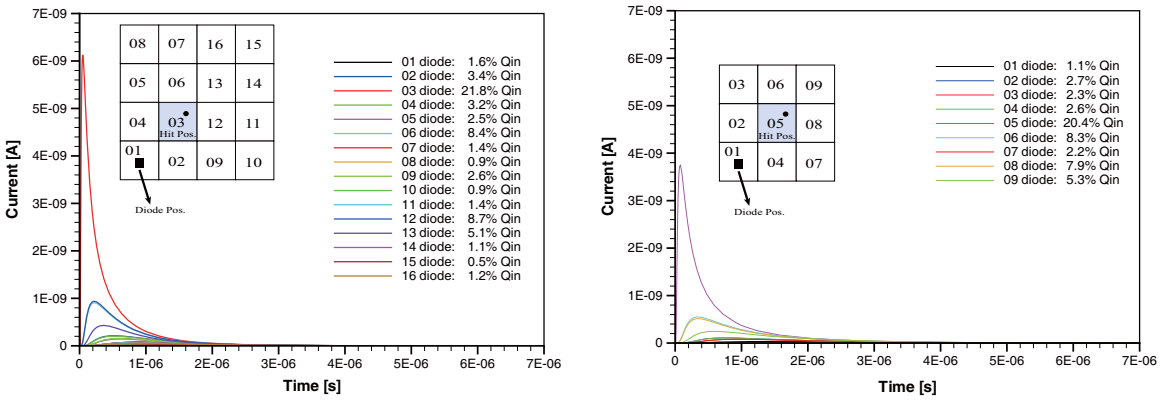

(a) (b)

Figure 3.2: Transient simulation results of the two simulated structures for an given input charge of 50 000 e-h pairs, with the inter-diode distance of (a) 80 µm, (b) 100 µm. The size of the collecting diode is of 5×5 µm^2 in the two cases.

We observed that the contribution of the diode at the edge of the simulated structure is

Diode size (μm^2)	Inter-diode distance (µm)	Collection efficiency (%)	Collection time (µs)	Total capacitance for 6.55 mm^2 (pF)
5 × 5	80	64.6	1.83	13.1
3 × 3	80	57.5	2.58	9.8
5 × 5	100	52.8	2.70	9.2
5 × 5	50	88.5	0.99	29.5
1.7 × 1.7	50	68.4	1.80	14.4

Table 3.1: Charge collection properties in the given simulated volume (320×320×14 μm^3) with different geometric parameters [12]. The collection time is defined as the time after which 90% of the total charges is collected.

about 1% in both cases. This proves that it is reasonable to neglect the collected charge outside the simulated surface (320×320 μm^2). As expected, the total collected charge increases with the size of cluster, i.e. the number of the collecting diodes in a fixed volume. Nevertheless, the total detector capacitance increases with the number of diodes. In practice, this results in a degraded SNR for the same amount of collected charge.

The collection time is commonly defined as the time after which 90% of the total charge is collected [3, 4]. The total charge is estimated from the charge collected within 7 µs after the impact, which is considered as a long enough time interval for the charge collection process to finish. Besides, it is close to the ideal electron lifetime in the epitaxial layer.

Table 3.1 summarizes the charge collection properties and the total capacitance of the detector which corresponds to the diode junction capacitances plus inter-connection line capacitances for a sensitive area of 6.55 mm^2. Since the signal processing circuit noise increases with the detector capacitance, the first set of parameters is chosen for the AlphaRad-2 by a trade-off between the collection performance (collection efficiency, collection time) and the detector capacitance. With this configuration, about 64.6% charges (without considering the substrate contribution) can be collected in the diode array of 32×32 micro-diodes, which generates a total input capacitance of 13 pF for the signal processing circuit, much lower than the 41 pF of the AlphaRad-1 prototype. A complementary discussion is proposed in the next subsection.

3.2.5.2 Effect of the substrate layer

In order to estimate more precisely the contribution of the substrate and the charge spreading properties, a set of simulations was performed for a structure with 4×4 diodes (inter-diode distance of 80 µs), and a fixed diode size of 5×5 μm^2. The impact position is the same as in the previous simulation. The thickness of the epitaxial layer is fixed as 14 µm. The thickness of the substrate used in the simulation is taken as a parameter. As already stated, the recombination

velocity is larger and the electron mobility is lower in the highly doped substrate layer than in the epitaxial layer. This effect can be seen in Fig. 3.3, which illustrates the electron concentrations in four transient simulation steps, i.e. at the impact time, 24 ns later, 299 ns later, and 999 ns later. The charge spreading is much larger in the epitaxial layer than in the substrate. Nevertheless, the electrons inside the first several micrometers of the substrate layer are much more probably to be collected by the collecting diodes through thermal diffusion. The electrons in the substrate undergo a much faster recombination, vanishing rapidly, as shown in Fig. 3.3(c). Compared to the pixel sensors with small pitch typically of ∼20 µm (the collection time is less than 100 ns), the charge collection process in our case is at least 10 times slower (see Fig. 3.3(d)), due to the fact that the charge collection mainly results from the carrier diffusion and the random walk at thermal velocity.

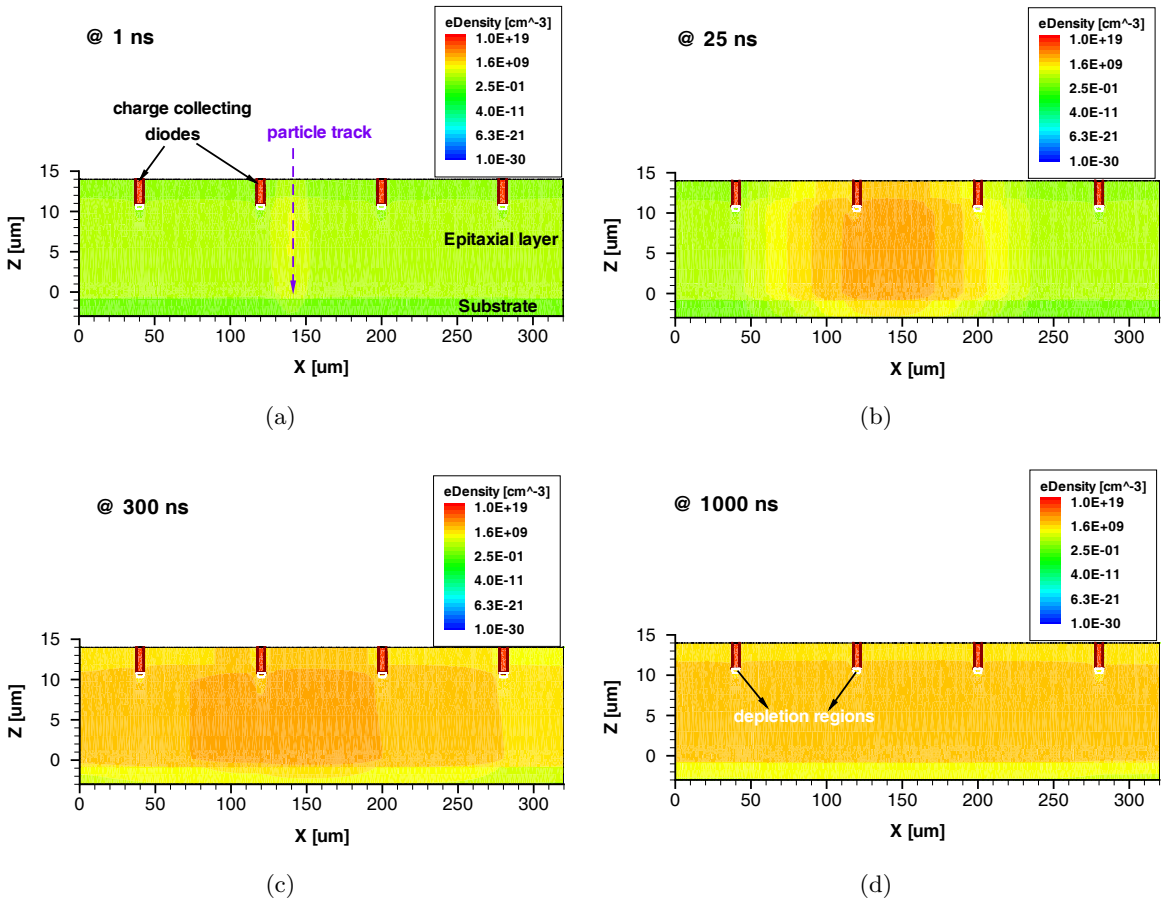

Figure 3.3: Electron concentrations for one example of the simulated structure – with a substrate layer of 3 µm (a) at the impact time, (b) after 25 ns, (c) after 300 ns, and (d) after 1000 ns.

As shown in Fig. 3.4, only about 5 µm of the substrate contributes significantly to the collected charge. This effect is consistent with the low value of the electron lifetime (∼10 ns) in the substrate layer. The distance of 5 µm corresponds to three diffusion lengths in the substrate and

is much shorter than the inter-diode distance. In our sensor (AlphaRad-2), the actual thickness of the substrate is around 700 µm before the post-processing. Considering the contribution of the substrate, we can reevaluate the estimated amount of the collected charge in each geometric set reported in Table 3.1 by a factor of 1.35.

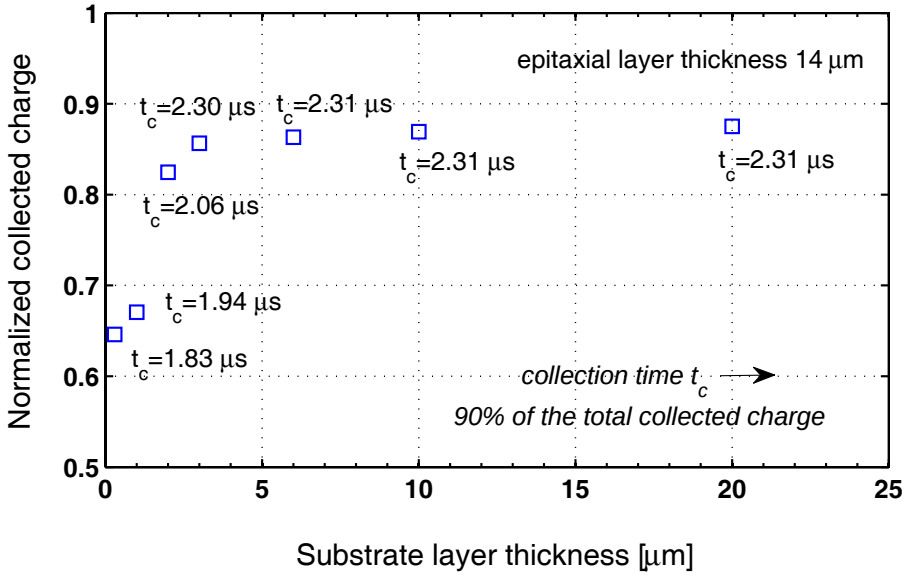

Figure 3.4: Substrate contribution to the total collected charge.

3.2.6 Discussion of simulations

The simulations have allowed us to study the behavior of our micro-diode array for efficient charged particle detection. As we are concerned by the total collected charge by the diode cluster, requiring no spatial resolution, the simulated structure with large inter-diode distances up to 100 µm have been studied. The collection time is less than 3 µs in the diode array for all the simulated configurations. Depending on the geometric parameters, the whole diode array collects between 50% and 90% of the total generated charge. With the chosen configuration for the diode array in the AlphaRad-2, the charge collection efficiency is estimated to be between 64% and 86% (depending on the thickness of the substrate layer), and the typical collection time is about 2.3 µs.

3.3 Signal processing architecture studies

The charge signal collected in the diode-array will be read out and processed by the following signal processing circuits. For a micro-diode array with thousand of diodes, the total sensor capacitance is in the order of several tens of picofarad, resulting in severe constraints on the noise figure of the signal processing circuitry. According to the study with the MIMOSA-5 and

an AmBe source, a threshold of 27000 electrons (∼100 keV) will lead to an efficiency ratio of 0.9 together with a high signal purity of 99% (n/γ ratio) (see Chapter 2, § 2.3.3.2). If we consider the conservative estimation of the charge collection efficiency (64.6%) in the previous section, the ENC at the input of the signal processing circuits should be less than 3000 e^- to guarantee a Signal to Noise Ratio (SNR) larger than 5 (at 100 keV).[5] Keeping in mind the application to a future personal dosemeter, a low power consumption chip is definitely required. The main challenge for the signal processing circuit is to achieve the noise performance with a very low power dissipation (< 1 mW). Consequently, a trade-off between low noise and low power consumption has to be made in the circuit design. Generally, the signal processing functionality can operate in voltage mode or current mode. The signal processing circuit in the AlphaRad-1 chip will be studied as an example of voltage mode, with a detailed analysis of the noise performance.

3.3.1 Voltage mode signal processing

Figure 3.5 shows the functional schematic of AlphaRad-1 chip, which was designed in 2003. The signal of the diode array is handled by a single electronic processing made of amplification discrimination and offset compensation.

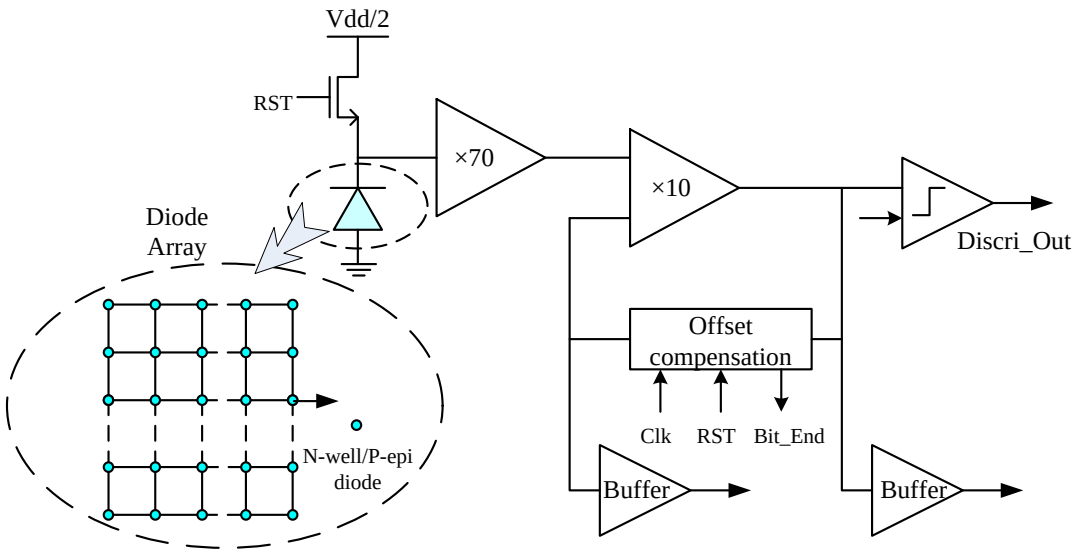

Figure 3.5: Architecture of the AlphaRad-1 chip, consisting of a diode array and a single signal processing functionality accomplished by two stages of amplification, discrimination, and offset compensation [13].

The charge collection diodes are slightly inverse-biased (Vdd = 5 V), hence the tiny depleted zone around the n-well is less than 0.5 µm thick, with a leakage current density of typically

5. In order to be able to detect thermal neutrons through (n,α), the substrate layer of the sensor needs to be removed. In this case, all the collected charge are generated only by the epitaxial layer.

$J_s = 10^{-17}$ A/µm^2. A large area diode of the size of one full matrix (13.1 mm^2) would generate a leakage current of around 134 pA, but with our choice of the diode segmentation, the total leakage current of the sensor is only $I_{leak} = 5.1$ pA. This value, even small, is continuously flowing to the sampling transistor which has to be recharged periodically. On the other hand, the reset operation is needed to periodically remove the collected charge before saturation. The reset time is to be considered as the dead time for the detector.

The amplification is performed in a two stage approach: a first amplifier of gain 70 is followed by the second one of gain 10. In the AlphaRad-1 prototype, a conventional OTA (Operational Transconductance Amplifier) is used in the two amplification stages as well as in the offset compensation block and comparator. A well known drawback of operational amplifier is the slow drift around its bias point. Therefore, an offset compensation is performed with the second amplifier. The offset compensation is carried out at 1 MHz frequency, taking 8 µs for a complete compensating operation. These additional 8 µs are another component part of dead time of the system. Typically, the RST signal is delivered at a frequency of 10 kHz, and in this interval, several α particles (up to 3) can be detected before saturation. While the compensation block has its internal reset at a much lower frequency (typically 10 Hz).

3.3.1.1 Noise during reset

The mean-square reset noise power can be calculated by means of the commonly known expression describing thermodynamic fluctuations

$$\overline{V_{rst}^2} = \frac{kT}{C_{det}} \tag{3.23}$$

where k is the Boltzmann's constant, T is the temperature in Kelvin, and C_{det} is the detector capacitance. Numerically, the root mean square (rms) reset noise is 10 µV.

3.3.1.2 Noise of the diode array

The dominant noise contribution of the collecting diode array is the shot noise due to the leakage current I_{leak}. The mean-square value of the shot noise sampled on the equivalent detector capacitance C_{det} during the integration time t_{int} is given by

$$\overline{V_{int}^2} = \frac{qI_{leak}}{C_{det}^2} t_{int}. \tag{3.24}$$

At room temperature the mean value of the leakage current in the Alpharad-1 chip is in the order of several picoamperes, and the related noise contribution is not significant for a integration time up to a few microseconds. Numerically, with an integration time as long as $t_{int} = 10$ µs, the shot noise is calculated to be of less than 0.1 µV (rms value).

3.3.1.3 Noise of the analog functionality

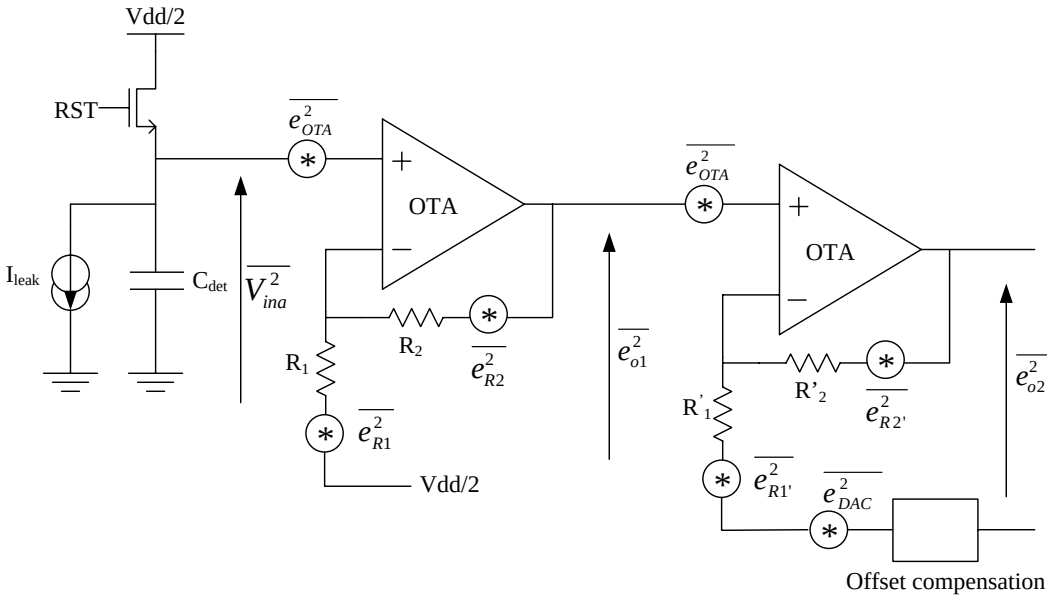

Figure 3.6: Simplified noise model of the analog functionality of the AlphaRad-1 chip.

To well understand the influence of the noise of the signal processing circuits, we analyze the total input-referred root mean square (rms) noise in the working bandwidth by calculating separately the noise contribution of the different parts. Figure 3.6 presents the noise model of the analog part of the signal processing, showing the different points considered in the noise analysis. The other noise contributors are the reset transistor and the leakage current of the diode-array.

Before doing noise analysis, we give the formula to calculate the noise of a MOS transistor. The equivalent input-voltage-noise spectral density of a transistor is defined as

$$e_n^2 = \frac{8kT}{3g_m} + \frac{K_F I_D}{g_m^2 C_{ox} L^2 f} \tag{3.25}$$

where K_F is the flicker noise coefficient, C_{ox} is the capacitance per unit area of the gate oxide, g_m is the transconductance, I_D is the drain current, L is the channel length of the transistor. The first and second term in Eq. (3.25) represent the thermal noise and flicker noise respectively.

As stressed above, the OTA is a reusable element in the signal processing circuits. Figure 3.7 shows the noise model of this OTA, ignoring the noise contribution of the dc current source (I_A). The equivalent input-voltage-noise spectral density can be approximately expressed as

$$\overline{e^2_{OTA}} \approx 2e^2_{n1,2}\left[1 + \left(\frac{g_{m3,4}}{g_{m1,2}}\right)^2 \left(\frac{e^2_{n3,4}}{e^2_{n1,2}}\right)\right] \tag{3.26}$$

where $g_{m1,2}$ is the transconductance of M_1 and M_2, $g_{m3,4}$ is the transconductance of M_3 and M_4. e^2_{ni} represents the noise source of transistor M_i. Substituting Eq. (3.25) into Eq. (3.26) gives

$$\overline{e^2_{OTA}} = \frac{16}{3}\frac{kT}{g_{m1,2}}\Big(1+\frac{g_{m3,4}}{g_{m1,2}}\Big) + \frac{I_A}{g^2_{m1,2}C_{ox}f}\Big(\frac{K_{Fp}}{L^2_{1,2}}+\frac{K_{Fn}}{L^2_{3,4}}\Big) \tag{3.27}$$

where K_{Fp} and K_{Fn} are the the flicker noise coefficients for PMOS and NMOS transistor, respectively, $L_{1,2}$ is the channel length of M_1 and M_2, and I_A is the current source of the OTA (as shown in Fig. 3.7) .

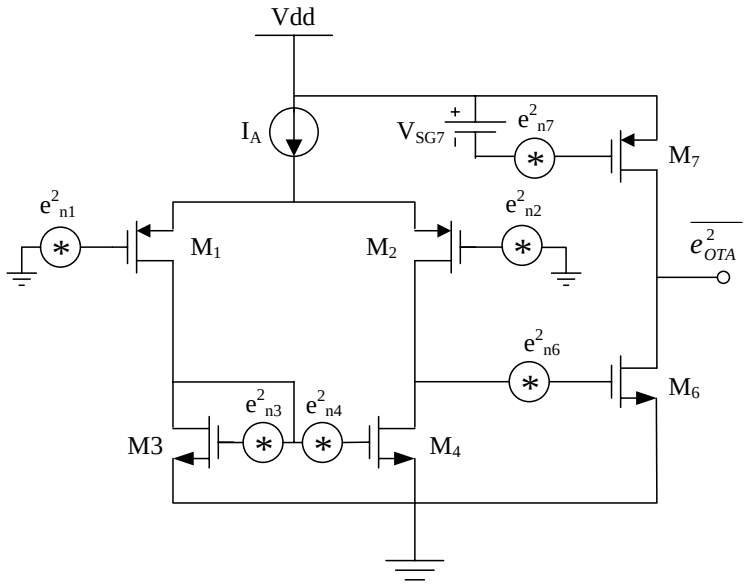

Figure 3.7: Simplified noise model of the operational amplifier used in the AlphaRad-1 chip.

Noise of the first amplification stage The total input-voltage-noise of the analog functionality can be obtained by successively calculating the noise contribution of each part. Firstly, we consider the total noise of the amplification stage with a gain of 70. $\overline{e^2_{OTA}}$ is the equivalent input-voltage-noise spectral density. $\overline{e^2_{R1}} = 4kTR_1$ and $\overline{e^2_{R2}} = 4kTR_2$ are the thermal noise of R_1 and R_2 respectively. The total output-voltage-noise spectral density, $\overline{e^2_{o1}}$, is given by the following equation

$$\overline{e^2_{o1}} = \Big(1+\frac{R_2}{R_1}\Big)\left[\overline{e^2_{OTA}}\Big(1+\frac{R_2}{R_1}\Big)+4kTR_2\right]. \tag{3.28}$$

Noise of the second amplification stage Considering the output-noise as a noise source at the input of the second amplifier together with the noise sources in the second stage (see Fig. 3.6), we can calculate its total noise. The total output-voltage-noise spectral density, e^2_{o2}, can be

calculated with the equation below

$$\overline{e_{o2}^2} = \left(1+\frac{R_2'}{R_1'}\right)^2\left[\overline{e_{o1}^2}+\overline{e_{OTA}^2}+4kT\left(\frac{R_2'R_1'}{R_2'+R_1'}\right)\right]+\overline{e_{DAC}^2}\left(\frac{R_2'}{R_1'}\right) \tag{3.29}$$

where e_{DAC}^2 is the equivalent noise sepctral density of the DAC used in the offset-compensation block. This DAC consists of an R-2R ladder and two amplifiers (the same OTA as used in the readout amplification). To analyze the noise contributed by the DAC, we use a simplified noise model as shown in Fig. 3.8, where the equivalent noise of the R-2R ladder is represented by a equivalent noise source of $\overline{e_R^2}$ in series with a resistance R (equivalent resistance of the R-2R ladder). The total output-voltage-noise spectral density of the DAC, $\overline{e_{DAC}^2}$, is given by

$$\begin{aligned}\overline{e_{DAC}^2} &= \overline{e_{OTA}^2}\left[4+\left(1+\frac{R'}{R}\right)^2\right]+4kTR\left[2+\frac{R'}{R}\left(1+\frac{R'}{R}\right)\right] \\ &= \alpha\times\overline{e_{OTA}^2}+\beta\times 4kTR.\end{aligned} \tag{3.30}$$

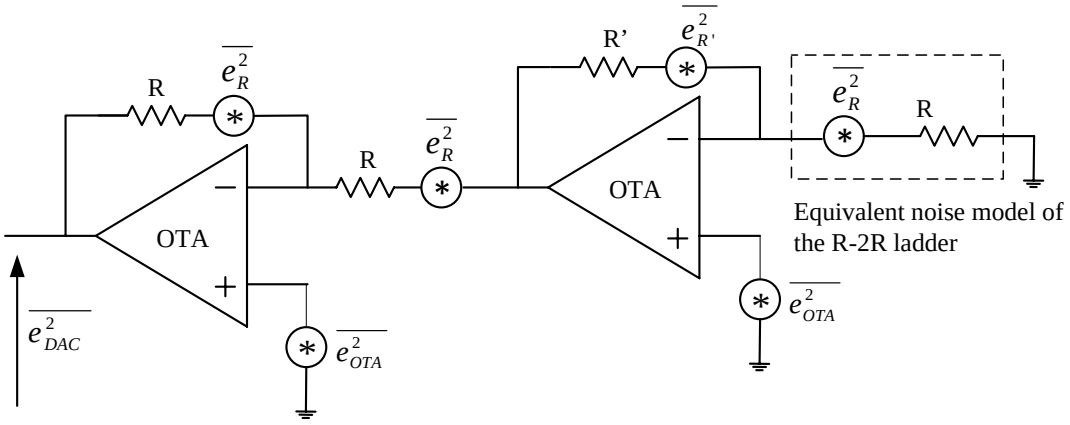

Figure 3.8: Simplified noise model of the DAC in the offset-compensation system.

3.3.1.4 Noise analysis summary

The equivalent input-voltage-noise spectral density of the amplification chain can be found by dividing Eq. (3.29) by the square gain of the signal processing chain to get

$$\overline{e_{ina}^2} = \frac{\overline{e_{o2}^2}}{\left(1+\frac{R_2}{R_1}\right)^2\left(1+\frac{R_2'}{R_1'}\right)^2}. \tag{3.31}$$

Substituting Eqs. (3.28), (3.29) and (3.30) into Eq. (3.31) gives

$$\begin{aligned}\overline{e_{ina}^2} &= \left[1+\frac{\left(1+\frac{R_2'}{R_1'}\right)^2+\alpha\left(\frac{R_2'}{R_1'}\right)^2}{\left(1+\frac{R_2}{R_1}\right)^2\left(1+\frac{R_2'}{R_1'}\right)^2}\right]\overline{e_{OTA}^2}+4kT\frac{R_1R_2}{R_1+R_2}\\ &+4kT\frac{\left(\frac{R_1'R_2'}{R_1'+R_2'}\right)^2}{\left(1+\frac{R_2}{R_1}\right)^2}+4kT\beta\frac{\left(\frac{R_2'}{R_1'}\right)^2}{\left(1+\frac{R_2}{R_1}\right)^2\left(1+\frac{R_2'}{R_1'}\right)^2}\\ &\approx \overline{e_{OTA}^2}+4kTR_1+\frac{kT}{1225}\left(\frac{R_1'R_2'}{R_1'+R_2'}\right)^2 \quad \text{for the case: } 1+\frac{R_2}{R_1}=70 \text{ and } 1+\frac{R_2'}{R_1'}=10\end{aligned} \tag{3.32}$$

where $\overline{e_{OTA}^2}$ is given in Eq. (3.26). The mean-square input-voltage noise of the amplification chain can be calculated by integrating Eq. (3.32) on the full frequency band and given in Eq. (3.33). The contribution of the OTA dominates the total noise of the amplification chain. As an approximation, performing integration in the bandwidth from 0.1 Hz to 250 kHz gives Eq. (3.33). The lower limit is very conservative as the compensation cycle is rather of ∼0.1 s. The higher limit is the -3 dB bandwidth of the amplifier.

$$\begin{aligned}\overline{V_{ina}^2} &\approx \int_{0.1}^{250{,}000}\overline{e_{ina}^2}df\\ &=\frac{1.33\times10^6kT}{g_{m1,2}}\left(1+\frac{g_{m3,4}}{g_{m1,2}}\right)+\frac{14.7I_A}{g_{m1,2}^2C_{ox}}\left(\frac{K_{Fp}}{L_{1,2}^2}+\frac{K_{Fn}}{L_{3,4}^2}\right)\\ &+2.5\times10^5\left[4kTR_1+\frac{kT}{1225}\left(\frac{R_1'R_2'}{R_1'+R_2'}\right)^2\right].\end{aligned} \tag{3.33}$$

The total equivalent rms noise of the full chain is the root square of the sum of the mean-square noise in Eq. (3.23), (3.24), and (3.33) and given by:

$$\overline{V_{n,eq}^2}=\overline{V_{rst}^2}+\overline{V_{int}^2}+\overline{V_{ina}^2}\approx\overline{V_{rst}^2}+\overline{V_{ina}^2}. \tag{3.34}$$

This equation shows the dominant contributions are kTC noise and the OTA's noise. Numerically, the kTC noise of 10 µV in this case contributes 20% to the total noise. It is well known that, kTC noise can be removed by applying the CDS technique, but with the price of an increase of the white noise contribution. To minimize the noise of OTA, Eq. (3.26) must be minimized. Choosing the product of W_1 and L_1 large can minimize the value of $e_{n1,2}^2$. And selecting the ratio of L_1 to L_3 to be less than one will reduce the contribution of $M_3, 4$. Furthermore, the noise of the amplification chain can be decreased by the reduction of the bandwidth with appropriate filters, commonly referred to as "shapers" [14]. Therefore, the signal processing consisting of a preamplifier and a "semi-Gaussian" shaper is adopted in the design of AlphaRad-2 prototype.

3.3.2 Current mode signal processing

A micro-diode array with thousand of diodes introduce a total capacitance of several tens of picofarad at the input of the signal processing chain. To reduce the input capacitance, the diode array can be segmentalized and processed by several readout blocks in parallel. And then the signals of different blocks can be added to a total output signal. Figure 3.9 presents a current mode signal processing architecture. [6] The main idea of this architecture is to isolate the detector and parasitic capacitance from the bandwidth determination and also to remove the noisy RST transistor. The charge signals are read in current mode, as current is easy to be operated such as add and subtract. As shown in Fig. 3.9, each row is composed of one 'Row-diodes' and a current readout block. The input capacitance of each row is 466 fF. A differential pair is used to separate the input capacitance from the main pole of the readout circuit. The impinging particle produces excess carriers in the epitaxial layer. The carriers are collected by the 'Row-diodes', which create a current signal. The current signal is handled by a differential pair, which can implement the current signal into a uniform amplitude and inverse current. The entire current signals generated by different diodes are summated and the total current is converted to a voltage. A common source amplifier is followed for a larger output voltage.

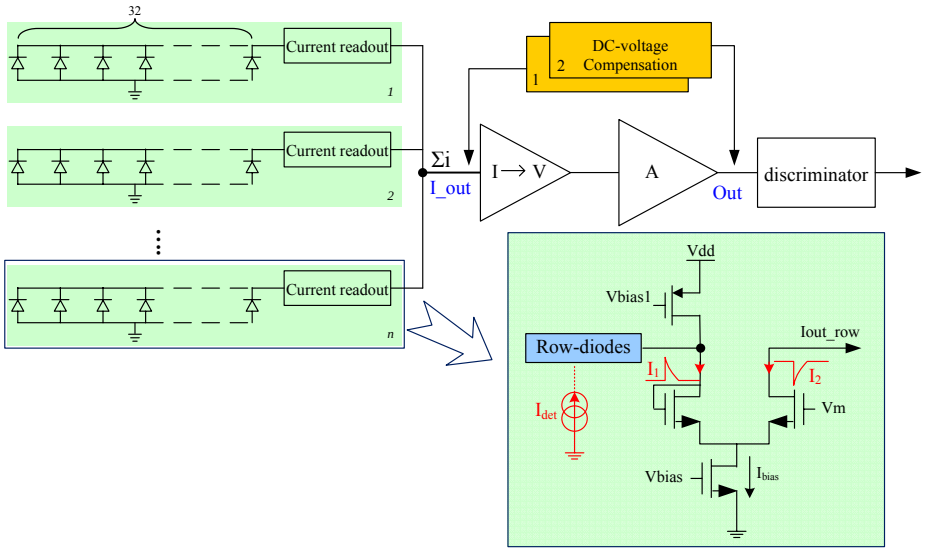

Figure 3.9: Schematic diagram of the current mode signal processing architecture.

3.3.2.1 DC voltage compensation systems

Since the front-end amplifiers (I→V, and V→V) work in open loop, their operating point voltages at the outputs present significant variations due to the process variation and mismatch.

6. This architecture was proposed initially by Anthony BOZIER in the laboratory InESS (*Institut d'Electronique du Solide et des Systèmes, UMR 7163*). It has been designed in a 0.35 µm CMOS process in this thesis.

We can analyze how the circuit works with the variation of process and mismatch through Monte-Carlo simulations. Figure 3.10 shows the statistical analysis results of the node *I_out* and *Out*. We observed that large standard deviations (326 mV or 1.5 V) exist around the mean value of their static voltage. Therefore, compensations are required to keep their DC-voltage in a limited range, which ensures the transistors are polarized in the working region and guarantees a sufficient dynamic range.

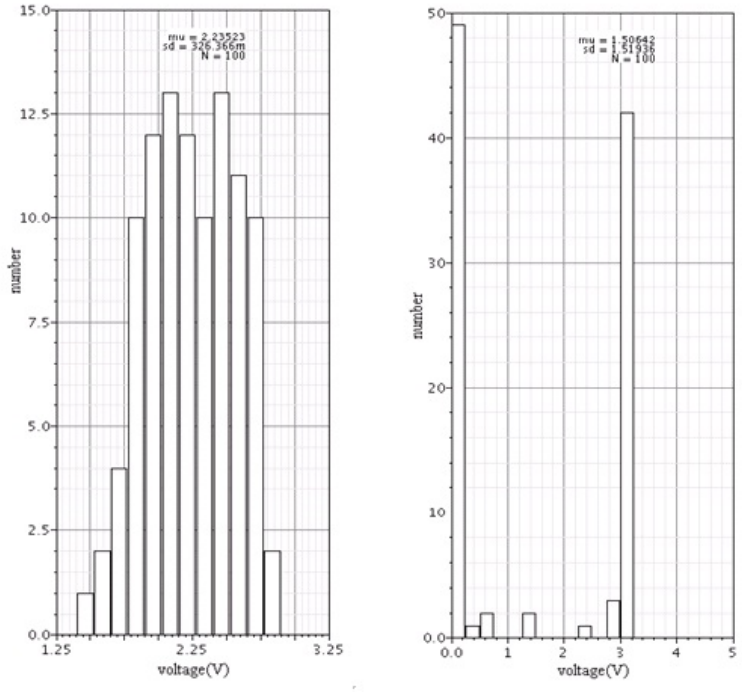

(a) (b)

Figure 3.10: DC-voltage distributions of the nodes (a) *I_out* and (b) *Out* shown in Fig. 3.9.

Figure 3.11 presents the compensation system for the node *I_out*. It is composed of an n-bit current-source DAC, a digital control block and a comparator. In order to remove the input-offset, an autozeroed comparator is used here. The comparator is used to decide if the voltage is lower or higher than the expected value. According to the comparison results, the digital block controls the n-bit current source DAC to send or shut off current. The digital block operates with a dichotomous algorithm. By adding a current source, it is only possible to increase the current flowing to the node thus to raise the node potential. Therefore, it is obligatory to keep the start voltage in a range that is always lower than the desired value. Aiming to control the voltage of the node *I_out* to be in the range of 2.25 V $\pm$ 50 mV, the initial value of this node must be lower than 2.25 V. The simulated result in Fig. 3.10 does not meet this requirement. This condition can be achieved by adjusting the dimension of the transistor M_{p1}. Then a Monte Carlo analysis allows to verify that the DC-voltage of the node *I_out* is below 2.5 V without the compensation (Fig. 3.14(a)). When the node voltage is lower than the correct value regarding

to the specifications, the control logic tries successively all bits starting with the MSB (Most Significant Bit). If the comparator does not change its state the bit is preserved, otherwise it is disabled and go to the next lower bit. Thus the compensation stops if all the n bits are tested. The value of n is chosen to be 8 according to the minimum and maximum compensating current.

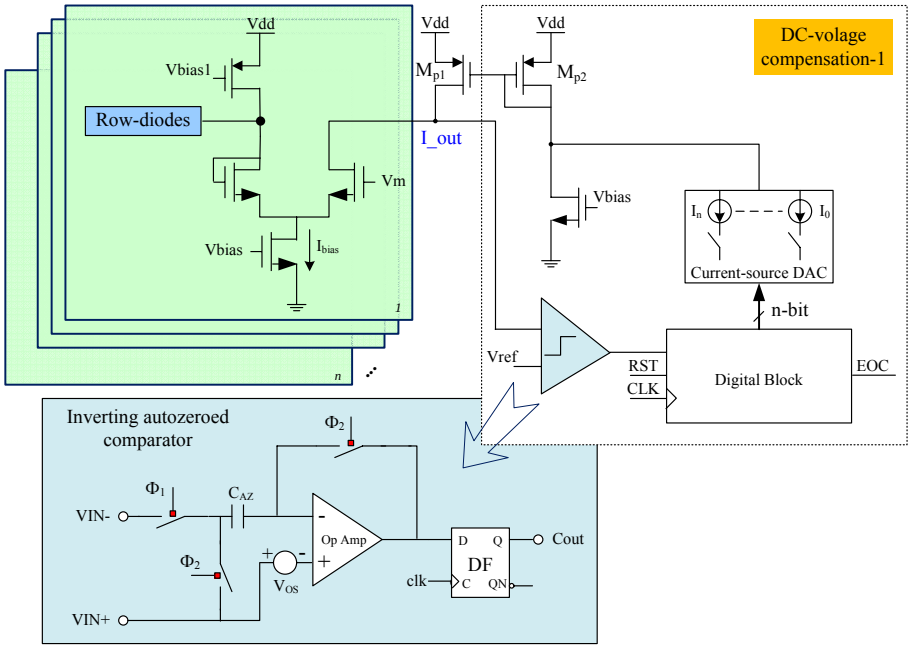

Figure 3.11: DC-voltage compensation system for the node *I_out*.

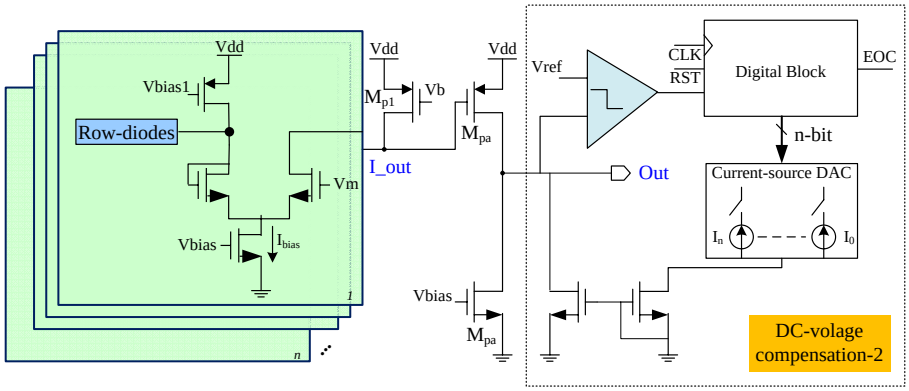

Figure 3.12: DC-voltage compensation system for the node *Out*.

At the end of compensation for the node *I_out*, a signal 'EOC' will be sent to start the second compensation system for the node *Out*. The compensation system for this node works in the same way, as shown in Fig. 3.12, but a 10-bit current source DAC is needed here, and it is only

possible to decrease the voltage of the node *Out* by adding a current source. Thus the node voltage had been adjusted to be lower than the desired value. Figure 3.13 shows the transient response of the two compensation blocks with a clock of 500 kHz.

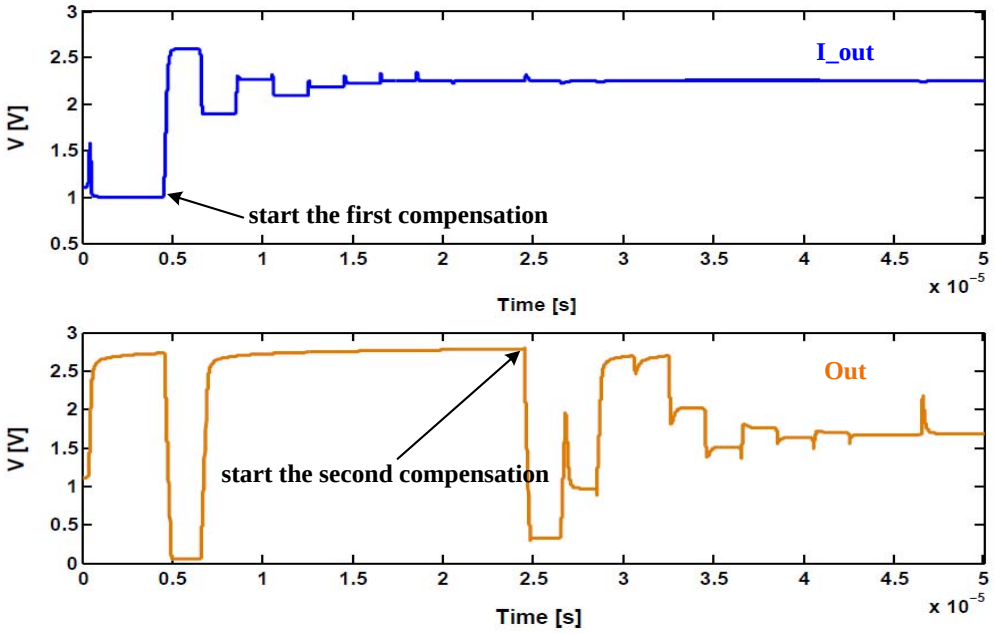

Figure 3.13: Transient response of the compensation systems for the node *I_out* (upper) and *Out* (lower) with a clock of 500 kHz.

The statistical analysis verifies that with the compensation systems, the DC voltage distributions of the two sensitive nodes can be effectively controlled, as shown in Fig. 3.14 and Fig. 3.15. We notice that with the compensation, the deviations of voltage distribution are quite small. These results meet very well the requirements.

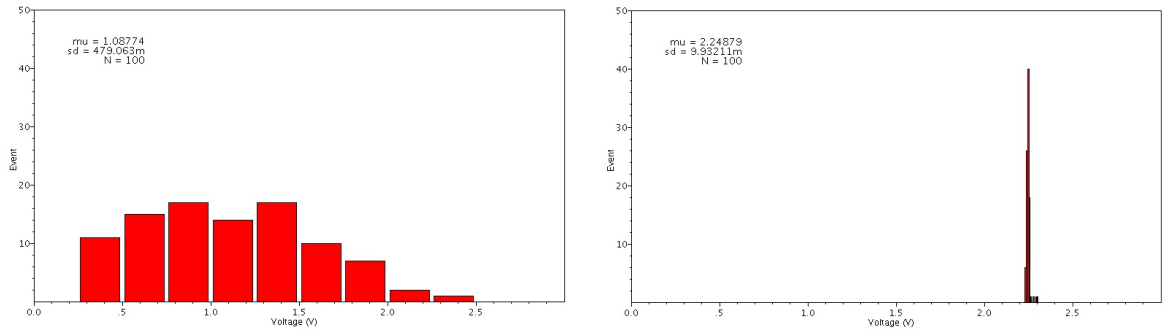

(a) (b)

Figure 3.14: DC-voltage distributions of the node *I_out*, (a) without compensation, (b) with compensation.

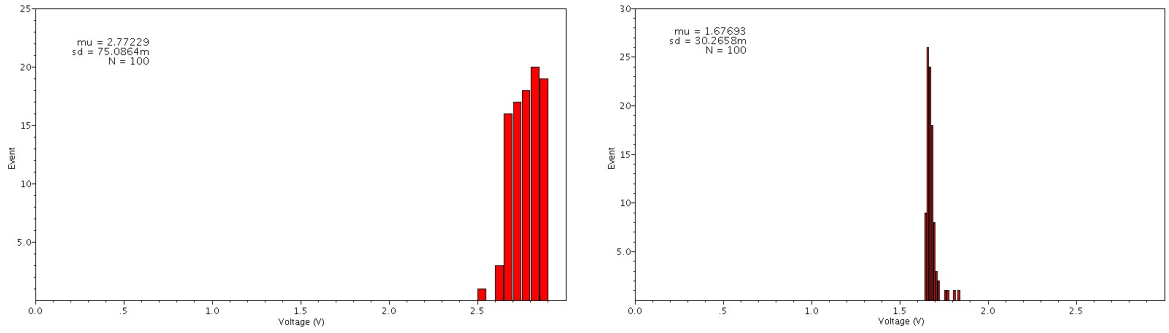

(a) (b)

Figure 3.15: DC-voltage distributions of the node *Out*, (a) without compensation, (b) with compensation.

3.3.2.2 Noise analyses of the current mode signal processing

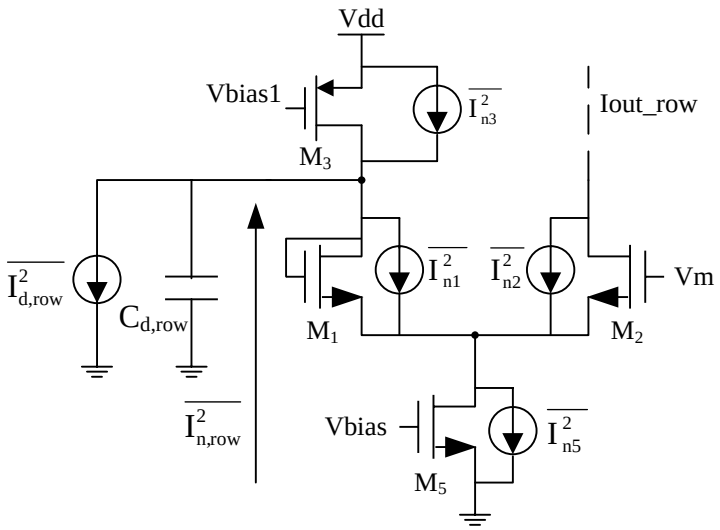

Figure 3.16: Noise model of the current readout stage for each row.

The same way than for the voltage mode architecture, we have to understand and minimize the electronic noise of the current mode architecture. Figure 3.16 presents the noise model of the 'Current readout' block for each row in Fig. 3.9. $\overline{I^2_{d,row}}$ and $C_{d,row}$ are the total shot noise [15] and the total capacitance of diodes in one row. I^2_{ni} represents the mean square current-noise spectral density of the transistor M_i and is given by

$$\overline{I^2_{ni}} = \frac{8kTg_m}{3} + \frac{K_F I_D}{fC_{ox}L^2} \tag{3.35}$$

where K_F is the flicker noise coefficient, C_{ox} is the capacitance per unit area of the gate oxide, g_m is the transconductance, I_D is the drain current, L is the channel length of the transistor.

The total output-current-noise spectrum density of the current readout stage for each row can be calculated with Eq. (3.36).

$$\overline{I_{n,row}^2} \approx \overline{I_{d,row}^2} + \overline{I_{n3}^2} + \overline{I_{n5}^2} = 64qI_{leak} + \overline{I_{n3}^2} + \overline{I_{n5}^2} \tag{3.36}$$

where I_{leak} represents the leakage current of one diode. Hence, the total noise contribution of all the current readout for the full matrix is then calculated as the product of the number of rows N_r and the noise given in Eq. (3.36).

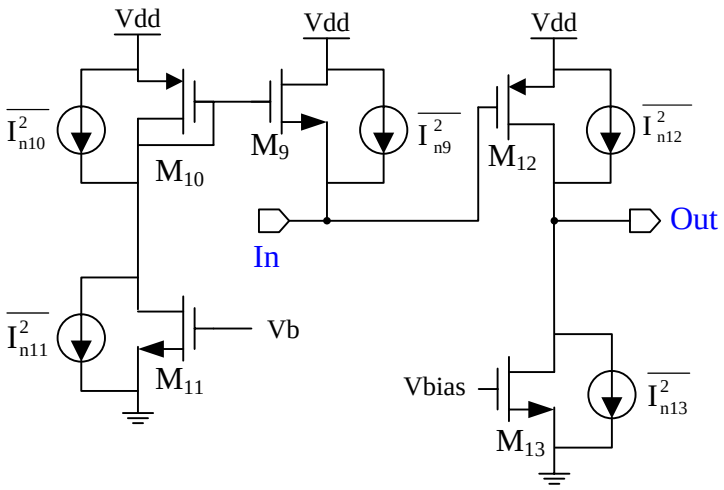

Figure 3.17: Noise model of the current-to-voltage stage and the voltage amplifier for the full matrix.

The second part of the signal processing chain is used for the full matrix, including a current-to-voltage stage and a voltage amplifier, whose noise model is presented in Fig. 3.17. The total output-voltage-noise spectral density, $\overline{V_{IIo}^2}$ is given in Eq. (3.37), where we have defined that the small-signal channel resistance of the transistor M_i is r_{0i}.

$$\overline{V_{IIo}^2} = \left[\overline{I_{n9}^2} + \frac{g_{m9}^2}{g_{m10}^2}(\overline{I_{n10}^2} + \overline{I_{n11}^2})\right] r_{09}^2 g_{m12}^2 (r_{012} \parallel r_{012})^2 + (\overline{I_{n12}^2} + \overline{I_{n13}^2})(r_{012} \parallel r_{012})^2. \tag{3.37}$$

The equivalent input-current-noise spectral density of the second readout stage shown in Fig. 3.17 can be found by dividing Eq. (3.38) by the total current-to-voltage gain $r_{09}g_{m12}\cdot(r_{012} \parallel r_{012})$ to get

$$\overline{I_{IIo}^2} = \overline{I_{n9}^2} + \frac{g_{m9}^2}{g_{m10}^2}(\overline{I_{n10}^2} + \overline{I_{n11}^2}) + \frac{1}{r_{09}^2 g_{m12}^2}(\overline{I_{n12}^2} + \overline{I_{n13}^2}). \tag{3.38}$$

As the current gain in the first stage is 1, the equivalent input-current-noise spectral density

($\overline{I_{eq}^2}$) of the full signal processing chain is given by

$$\begin{aligned}\overline{I_{eq}^2} &= N_r\overline{I_{n,row}^2} + \overline{I_{IIo}^2} \\ &= N_r(64qI_{leak} + \overline{I_{n3}^2} + \overline{I_{n5}^2}) + \overline{I_{n9}^2} + \frac{g_{m9}^2}{g_{m10}^2}(\overline{I_{n10}^2} + \overline{I_{n11}^2}) + \frac{1}{r_{09}^2 g_{m12}^2}(\overline{I_{n12}^2} + \overline{I_{n13}^2})\end{aligned} \tag{3.39}$$

where the mean square current-noise spectral density of the transistor is given by (3.35). The drain current of M_9, I_{D9} is the sum of drain current of M_2 in each row. Hence, M_9 is one of the dominant noise sources. I_{D9} increases with the matrix size (number of rows). It means the noise contributions of M_9, M_{10}, M_{11} depend on the matrix. The shot noise of diode-array also increase with the matrix size, however its contribution to the total noise is insignificant due to the low leakage current ($\sim 10^{-15}$ A/diode) of the micro-diode.

3.3.3 Comparison of the signal processing architectures

To compare the voltage mode (Fig. 3.5, was in a 0.6 µm process) and current mode (Fig. 3.9) signal processing architecture in terms of noise performance, we redesign the voltage mode architecture in the AMS 0.35 µm CMOS technology with a 3.3 V power supply. The voltage amplification chain designed performs a gain of 700, a bandwidth of 2 MHz, an RMS noise voltage of 17 µV, and a power consumption of 1.6 mW.

To be simple, the noise contribution of the offset-compensation in the voltage mode and the DC-voltage compensation in the current mode are not taken into account in the noise performance comparison. In both architectures (current mode and voltage mode), the diode size and inter-diode distance are 5×5 µm^2, and 80 µm, respectively. We analyze now the noise in terms of signal-to-noise ratio (SNR), considering the minimum input charge is as much as the signal threshold (50 000 e$^-$). The corresponding input current signal is the sum of the currents in Fig. 3.2(a). Each row of the diode matrix consists of 32 diodes, and the number of the rows is taken as a variable.

The results of the SNR dependence on the diode matrix size for the two architectures are illustrated in Fig. 3.18. The matrix size increases with the number of rows, which means increasing only the number of 'Row-diodes' (32 diodes/row) in the voltage mode, while means increasing both the 'Row-diodes' number and the number of 'Current readout' in the current mode. In both cases, the detector capacitance increases with the matrix size, resulting in the degradation of the SNR. The simulation result indicates that current mode architecture has worse noise performance than the voltage mode architecture in all the range of input capacitance. In the voltage mode, increasing the matrix size translates into the increase of the leakage current and the detector capacitance. Compared to the voltage mode, a larger matrix size accompanies with not only a larger leakage current and a larger capacitance but also more noise introduced by 'Current readout' in the current mode. With one row detector (i.e. number of rows = 1), the current mode architecture performs a charge-to-current gain of 0.4 pA/e- and an

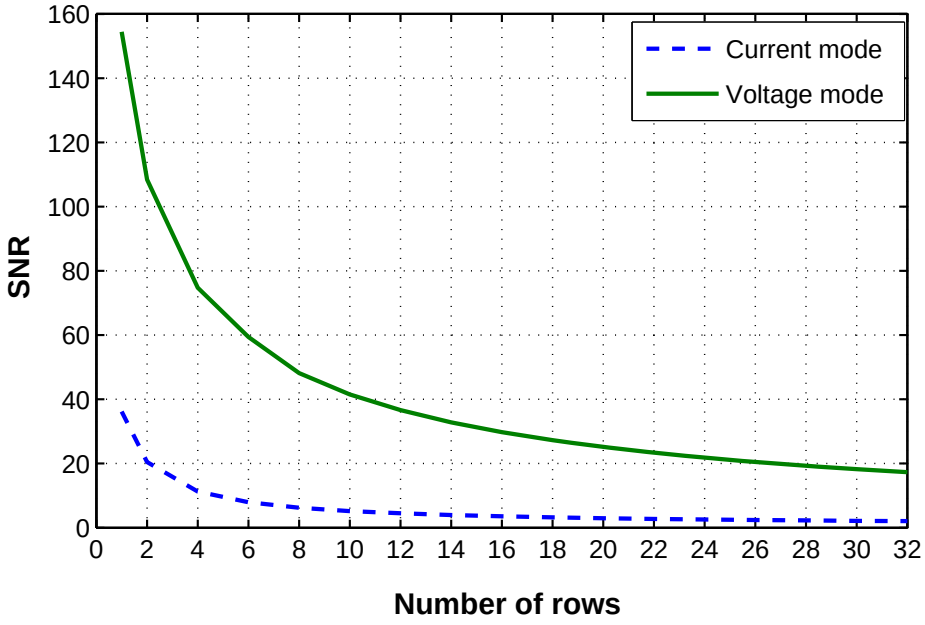

Figure 3.18: SNR dependence on the diode matrix size for the voltage mode (solid line) and current mode (dashed line) signal processing architectures.

RMS noise current of 320 pA, which corresponds to an ENC of 800 e^-. The problem is that the charge-to-current gain of 'Current readout' is very small relative to the induced noise current. Using one row detector in the voltage mode, a charge-to-voltage gain of 0.32 $\mu V/e^-$ and an RMS noise voltage of 69 µV lead to an ENC of 216 e^-. With a 32 rows detector, the voltage mode architecture performs more than eight times as much SNR as the current mode architecture. Therefore, we decided to implement the signal processing chain in a voltage mode. However, the architecture shown in Fig. 3.5 (which was used in the AlphaRad-1 chip) needs a compensation system to control the static voltage of the open loop amplification chain. In order to simplify the structure, we propose a new architecture to improve the noise performance and reduce the power consumption. This will be done in Chapter 4.

Bibliography

[1] *Sentaurus Device User Guide*, Synopsys Inc., 2010, version D-2010-3.

[2] D. Husson, "Device simulation of a CMOS pixel detector for MIP tracking," *Nuclear Instruments and Methods in Physics Research Section A: Accelerators, Spectrometers, Detectors and Associated Equipment*, vol. 461, no. 1-3, pp. 511–513, 2001, 8th Pisa Meeting on Advanced Detectors. [Online]. Available: http://www.sciencedirect.com/science/article/pii/S0168900200012869

[3] G. Deptuch, "New generation of monolithic active pixel sensors for charged particle detection," Ph.D. dissertation, Université Louis Pasteur, Strasbourg, France, 2002.

[4] D. Contarato, "Silicon Detectors for Particle Tracking at Future High-Energy Physics Experiments," Ph.D. dissertation, Universit at Hamburg, Hamburg, Germany, 2005.

[5] G. Masetti, M. Severi, and S. Solmi, "Modeling of carrier mobility against carrier concentration in arsenic-, phosphorus-, and boron-doped silicon," *Electron Devices, IEEE Transactions on*, vol. 30, no. 7, pp. 764–769, jul 1983.

[6] C. Lombardi, S. Manzini, A. Saporito, and M. Vanzi, "A physically based mobility model for numerical simulation of nonplanar devices," *Computer-Aided Design of Integrated Circuits and Systems, IEEE Transactions on*, vol. 7, no. 11, pp. 1164 –1171, nov 1988.

[7] W. Shockley and W. T. Read, "Statistics of the recombinations of holes and electrons," *Phys. Rev.*, vol. 87, pp. 835–842, Sep 1952. [Online]. Available: http://link.aps.org/doi/10.1103/PhysRev.87.835

[8] L. Huldt, N. G. Nilsson, and K. G. Svantesson, "The temperature dependence of band-to-band Auger recombination in silicons," *Applied Physics Letters*, vol. 35, no. 10, pp. 776–777, nov 1979.

[9] W. Lochmann and A. Haug, "Phonon-assisted Auger recombination in Si with direct calculation of the overlap integrals," *Solid State Communications*, vol. 35, no. 7, pp. 553–556, 1980. [Online]. Available: http://www.sciencedirect.com/science/article/pii/0038109880908960

[10] R. Hacker and A. Hangleiter, "Intrinsic upper limits of the carrier lifetime in silicon," *Journal of Applied Physics*, vol. 75, no. 11, pp. 7570–7572, jun 1994.

[11] H. S. Bennett and C. L. Wilson, "Statistical comparisons of data on band-gap narrowing in heavily doped silicon: Electrical and optical measurements," *Journal of Applied Physics*, vol. 55, no. 10, pp. 3582–3587, 1984. [Online]. Available: http://link.aip.org/link/?JAPIAU/63/425/1

[12] Y. Zhang, C. Hu-Guo, D. Husson, and Y. Hu, "Design of an ultra low power cmos pixel sensor for a future neutron personal dosimeter," in *Advancements in Nuclear Instrumentation Measurement Methods and their Applications (ANIMMA), 2011 2nd International Conference on*, june 2011, pp. 1–7.

[13] D. Husson, A. Bozier, S. Higueret, T. D. Lê, and A. M. Nourreddine, "AlphaRad, a new integrated CMOS System-on-Chip for high efficiency alpha particles counting," *Nucl. Instr. and Meth. A*, vol. 569, no. 3, pp. 845–852, 2006.

[14] L. Rossi, P. Fischer, T. Rohe, and N. Wermes, *Pixel Detectors: From Fundamentals To Applications*. Springer, 2010.

[15] B. Schneider and M. Strutt, "Theory and Experiments on Shot Noise in Silicon P-N Junction Diodes and Transistors," *Proceedings of the IRE*, vol. 47, no. 4, pp. 546–554, april 1959.

Chapter 4

Design of the AlphaRad-2 chip

4.1 Proposition of a new architecture

Figure 4.1 shows the proposed architecture for a new compact neutron dosimetry device based on CMOS sensors. Neutrons can generate charged particles through various reactions with matter, and the choice of the converter depends on the energy of incident neutrons. In particularly, we use a polyethylene radiator to benefit from the high (n, p) elastic scattering cross-section for fast neutrons (100 keV to 10 MeV), as well as B/Li converters for thermal neutrons (1 meV to 1 eV) through (n, α) reactions. Charged particles are detected by a dedicated CMOS sensor, AlphaRad-2 chip, which consists of the sensing part and the signal processing electronics on the same substrate. It has a binary output connected with a counter to register a single incident neutron. For the detection of neutrons in a large energy range, the future dosemeter will comprise 2 to 4 chips, and each one with its own converter and threshold. Then an additional block will be used to convert the counting rates into doses. The first step of the new device development is the implementation of the AlphaRad-2 chip, which is the key component to achieve the high sensitivity for neutrons.

The AlphaRad-2 chip is a dedicated CMOS sensor for efficient neutron counting. Aiming at a miniaturized system, we proposed a simple configuration, as shown in Fig. 4.1. The sensing part of the AlphaRad-2 chip consists of a micro-diode matrix of 32×32 diodes. Each diode is an n-well/p-epi (epitaxial layer) diode with an area of 5×5 µm^2. All the diodes connected in parallel through standard aluminum lines are handled with a single output. With an inter-diode distance of 80 µm, the full sensing part covers an area of 2.56×2.56 mm^2. The dimension of the diode and the inter-diode distance have been chosen based on the charge collection study (see Chapter 3, § 3.2). This approach provides a large detecting surface with a moderate capacitance ($\sim$13 pF) and at the same time a very low leakage current ($<$ 1 pA), which strongly affects the radiation tolerance.

For neutron sensitive electronic personal dosemeters, general requirements concern not only good detection performance, such as low detection level of 10 µSv (10 µSv/h, in ratemeter

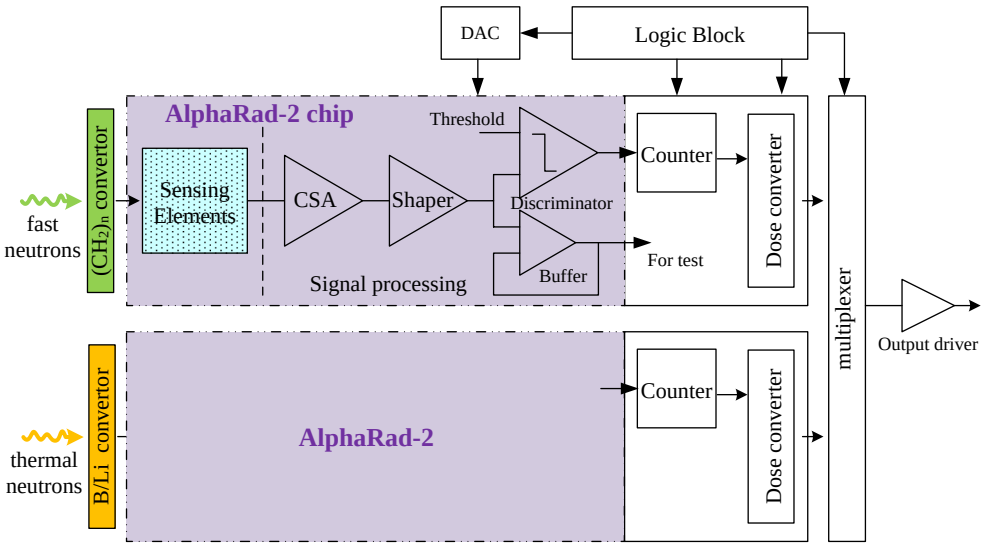

Figure 4.1: Architecture of the proposed compact device based on CMOS sensors for operational neutron dosimetry.

mode), but also the characteristics for portability, i.e. battery charge allowing 100 h continuous use and weight below 200 g [1]. Targeting on these requirements, we have tried to simplify the signal processing architecture to achieve a compact device with low noise (which ensures a low detection level) and an ultra low power dissipation ($<$ 1 mW). In the AlphaRad-2, a Charge Sensitive Amplifier (CSA) is used to amplify the input charge signals. The CSA followed by a pulse shaper implements the low noise analog signal processing, which integrates and transfers the charge signal of the sensing element into a voltage signal. A hysteresis comparator provides a binary output. In this chapter, the design details of the signal processing as well as the electrical test results of the AlphaRad-2 chip will be presented.

4.2 Design considerations

The impact particles produce an input charge that is a function of the particle energy. For this reason, the detector preamplifier should produce an output that is proportional to the collected charges. In the AlphaRad-1 prototype, voltage preamplifiers were used. However, in that case, the signal voltage in the input of the preamplifier is not only proportional to the collected charge, but also inversely proportional to the input capacitance. Because the detector capacitance is usually a weak function of the temperature, temperature changes cause drifts in the preamplifier gain. In the AlphaRad-2 chip, a charge sensitive amplifier is utilized, which has a gain equal to the inverse of the feedback capacitance, and independent of the input capacitance.

In this section, we give the theoretical analysis of the choice of the architecture and the main parameters of the CSA by modeling the detector signal and the CSA.

4.2.1 Modeling the signal from the diode array

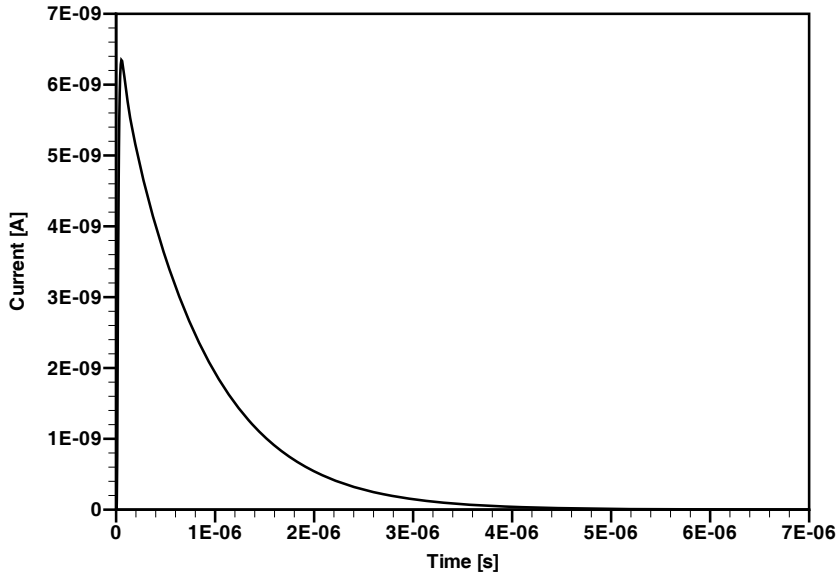

Figure 4.2: Total output current of a 4 × 4 diode cluster, with the diode size of 5×5 µm^2 and an inter-diode distance of 80 µm.

As already stated, neutrons can generate secondary charged particles through various elastic or inelastic processes in the appropriate converters, and the charged particles create electron/hole pairs when they impinge on the CMOS sensor. The excess carriers constitute a current under the influence of the external electric field. This current signal will be sensed and processed by the following electronics. In the case of AlphaRad-2 chip, the total current of the whole diode matrix is the input signal to the processing circuit. Concerning the recoil protons from fast neutrons, a charge threshold of 50 000 e-h pairs was chosen according to the study with the MIMOSA-5. Taking this value as an input charge, we have presented the current signal contributed by each collecting diode in a 4×4 cluster (see Chapter 3, Fig. 3.2(a)). The total current of the diode array can be estimated by summing up the output current of all diodes, as shown in Fig. 4.2.

In order to use this current signal in the circuit design, we have modeled it by two exponential functions. Figure 4.3 gives the modeled signal, showing a good agreement with the raw data from the device simulation. [1] Thus an exponential current source was used in the circuit simulations to evaluate the circuit response. The time-domain equation of the input current is given by Eq. 4.1.

$$i(t) = \begin{cases} i_p\left[1 - \exp\left(-\frac{t-t_{dr}}{\tau_r}\right)\right] & \text{for} \quad t_{dr} < t < t_{df} \\ i_p \cdot \exp\left(-\frac{t-t_{df}}{\tau_f}\right) & \text{for} \quad t \geq t_{df} \end{cases} \tag{4.1}$$

where i_p is maximum current, t_{dr} is rise time delay, t_{df} is fall time delay, τ_r is rise time constant, and τ_f is fall time constant. The charged particles impinging on the sensor at $t = 1$ ns, and the

1. For readability, only the first 3 µs of the current is shown.

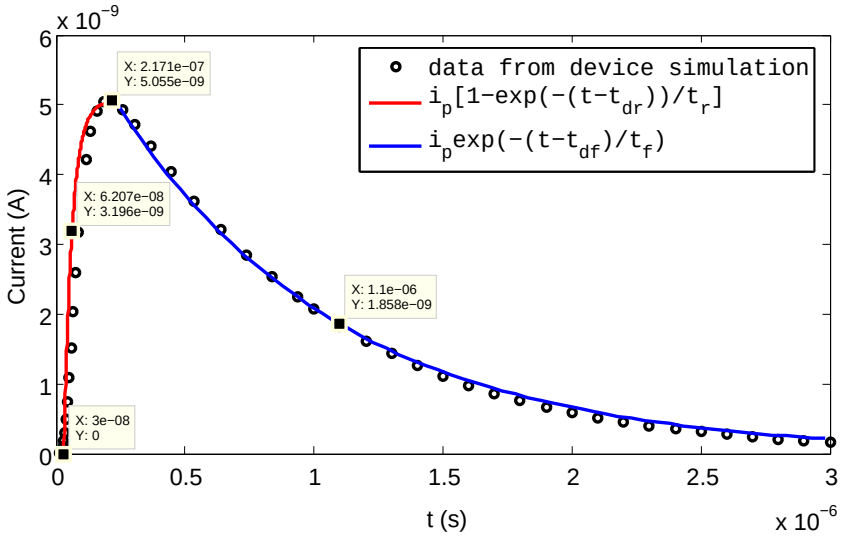

Figure 4.3: Total output current of a 4 × 4 diode cluster, with simulated points, and our exponential model. The corresponding collected charge is about 5.83 fC.

initial current is zero. At the time of t_{dr}, the current increases fast until i_p and then at $t = t_{df}$ decays slowly with the time constant τ_f. Taking the Laplace transform of Eq. (4.1), we can get its frequency-domain equation expressed as

$$I(s) = \begin{cases} i_p \left[\frac{1}{s} - \frac{\tau_r \exp\left(\frac{t_{dr}}{\tau_r}\right)}{1+s\tau_r} \right] & \text{for} \quad \frac{1}{t_{df}} < s < \frac{1}{t_{dr}} \\ i_p \cdot \frac{\tau_f \exp(\frac{t_{df}}{\tau_f})}{1+s\tau_f} & \text{for} \quad s \leq \frac{1}{t_{df}}. \end{cases} \tag{4.2}$$

The total collected charge Q_e is easily calculated by integrating the current, given as

$$\begin{aligned} Q_e &= \int_0^\infty i(t)\,dt = \int_{t_{dr}}^{t_{df}} i_p \left[1 - \exp\left(-\frac{t - t_{dr}}{\tau_r} \right) \right] dt + \int_{t_{df}}^{\infty} i_p \cdot \exp\left(-\frac{t - t_{df}}{\tau_f} \right) dt \\ &= i_p(t_{df} - t_{dr}) + i_p\tau_r \left[1 - \exp\left(-\frac{t_{df} - t_{dr}}{\tau_r} \right) \right] + i_p\tau_f \\ &\approx i_p(t_{df} + \tau_f) \qquad (\text{in our case} \quad \tau_f > t_{df} \gg t_{dr}, \text{ and } t_{dr} \approx \tau_r). \end{aligned} \tag{4.3}$$

Finally, the current signal of the micro-diodes can be normalized in charge, defined as

$$I_n(s) = I(s)/Q_e. \tag{4.4}$$

4.2.2 Choice of the integration time

As already stated, we use a charge sensitive amplifier (CSA) as the detector preamplifier. This kind of preamplifier is widely used in detectors where the energy measurement of individual ionizing events is of interest. Its principle schematic is illustrated in Fig. 4.4(a). The CSA

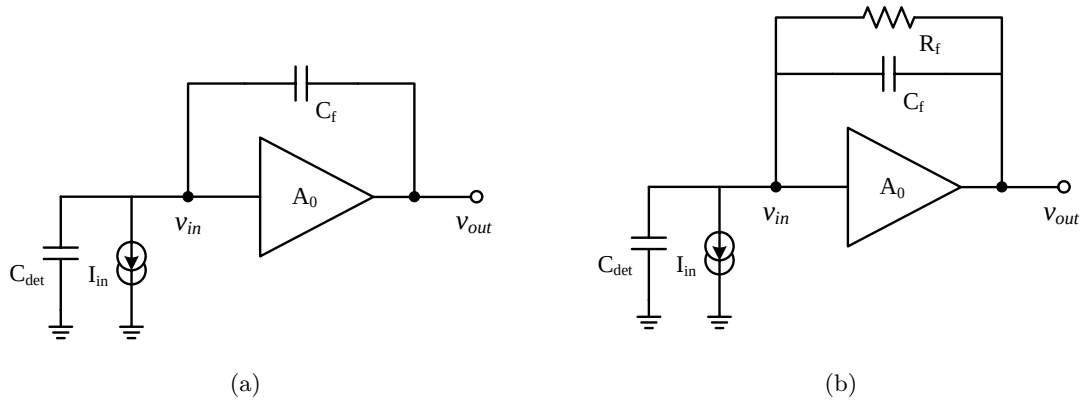

(a) (b)

Figure 4.4: Principle schematic of the charge sensitive amplifiers with (a) an infinite, and (b) a finite integration time.

integrates the input charge and produces an output voltage step proportional to this charge. The effective input capacitance C_{eff} of the CSA is given by

$$C_{eff} = C_f(A_0 - 1) \qquad \text{if} \quad Z_{in} \to \infty \tag{4.5}$$

where C_f is the feedback capacitance, A_0 is the DC gain of the amplifier, and Z_{in} is the impedance of the amplifier. C_{eff} acts in parallel to C_{in}, which is the sum of the detector capacitance C_{det}, the preamplifier input capacitance C_{amp}, and the parasitic contributions C_{stray}.

The charge-to-voltage gain A_Q of the CSA is calculated as

$$A_Q = \frac{v_{out}}{Q_{int}} = \frac{A_0 v_{in}}{C_{eff} v_{in}} = \frac{A_0}{C_f(A_0 - 1)}, \tag{4.6a}$$

for $A_0 \gg 1$, we obtain:

$$A_Q \approx \frac{1}{C_f} \tag{4.6b}$$

where Q_{int} represents the integrated charge by the CSA. With a finite gain A_0, only a fraction of the charge generated Q_{gen} by the impact particle is collected by C_{det}, C_{amp}, and C_{stray}, resulting in a charge integration error, defined as

$$\varepsilon_{int} = 1 - \frac{Q_{int}}{Q_{gen}} = 1 - \frac{1}{1 + \frac{C_{det}+C_{amp}+C_{stray}}{A_0 C_f}} = 1 - \frac{1}{1 + \frac{C_{in}}{A_0 C_f}}. \tag{4.7}$$

A significant fraction of the signal is lost when C_{in} approaches $A_0 C_f$. It is therefore usually required that the effective input capacitance to be significantly larger than the detector capacitance.

A feedback circuit is needed to define the DC-operation point of the CSA shown in Fig. 4.4(a) and to remove input charges from the feedback capacitor C_f after the dynamic response

of the amplifier so that the CSA output voltage returns to its initial value. The discharge can be realized periodically by a clock controlled switch connected in parallel to C_f. This method is an efficient solution for applications where a continuous reset is not needed. However, the arrival time of a charged particle is completely random in our case, therefore we use a parallel feedback resistance R_f to discharge continually the capacitance C_f, as shown in Fig. 4.4(b). The charge integration duration is determined by the integration time defined as $\tau_i = R_f C_f$. A finite integration time leads to a decreased charge-to-voltage gain as compared to the ideal one $1/C_f$ (this effect is commonly referred as to *ballistic deficit*). The choice of the integration time is motivated on one side by the need of preventing from pile-up problem, on the other side by the goal of ensuring a sufficient integrated charge.

Making the frequency-domain analysis will allow us to calculate easily the output signal in the time-domain. The frequency-domain transfer function of the CSA (shown in Fig. 4.4(b)) can be expressed as

$$F(s) = \frac{R_f}{1 + sR_fC_f}. \tag{4.8}$$

Normalizing this function by the ideal charge-to-voltage of $1/C_f$ gives

$$F_n(s) = \frac{F(s)}{1/C_f} = \frac{R_fC_f}{1 + sR_fC_f} = \frac{\tau_i}{1 + s\tau_i}. \tag{4.9}$$

By combining Eqs. (4.2), (4.3), (4.4) and (4.9), we obtain the normalized output signal of the CSA:

$$V_{o,n}(s) = I_n(s)F_n(s) = \begin{cases} \frac{\tau_i}{\tau_f + t_{df}} \cdot \left[\frac{1}{s(1+s\tau_i)} - \frac{\tau_r \exp(t_{dr}/\tau_r)}{(1+s\tau_r)(1+s\tau_i)}\right] & \text{for} \quad \frac{1}{t_{df}} < s < \frac{1}{t_{dr}} \\ \frac{\tau_f \exp(t_{df}/\tau_f)}{(\tau_f + t_{df})} \cdot \frac{\tau_i}{(1+s\tau_f)(1+s\tau_i)} & \text{for} \quad s \leq \frac{1}{t_{df}}. \end{cases} \tag{4.10}$$

Taking the inverse Laplace transformation of $V_{o,n}$ gives the time-domain equation as

$$V_{o,n}(t) = \begin{cases} \frac{\tau_i\tau_r \exp(t_{dr}/\tau_r)}{(\tau_f + t_{df})(\tau_r - \tau_i)}\left[\exp(-\frac{t}{\tau_i}) - \exp(-\frac{t}{\tau_r})\right] + \frac{\tau_i}{\tau_f + t_{df}}\left[1 - \exp(-\frac{t}{\tau_i})\right] & \text{for} \quad t_{dr} < t < t_{df} \\ \frac{\tau_f\tau_i \exp(t_{df}/\tau_f)}{(\tau_f + t_{df})(\tau_f - \tau_i)}\left[\exp(-\frac{t}{\tau_f}) - \exp(-\frac{t}{\tau_i})\right] & \text{for} \quad t \geq t_{df}. \end{cases} \tag{4.11}$$

The current related parameters: i_p, t_{dr}, t_{df}, τ_r, and τ_f are mainly dependent on the impact position for a given geometry. Fig. 4.3 presents their values for a fixed impact position. Substituting those values in Eq. (4.11), we can obtain the normalized output pulse of the CSA with different integration times. Figure 4.5 presents the fraction of the recovered charges with different integration times. The longer the integration time, the more charges are collected, thus a higher signal, but the time of returning to the baseline is also longer, leading to a lower counting rate. Finally, an integration time of 12 µs was chosen as a compromise between the high count rate and the high recovered charge. C_f of 100 fF is chosen as a trade-off between the matching and a reasonable gain. To obtain 12 µs, a feedback resistance R_f of 120 MΩ is required. Such

a large resistor cannot be implemented as a passive device (leading to an enormous area), and the associated capacitive parasitics would be prohibitive. We chose the simplest solution of a transistor operated in the linear region as the feedback resistor. A well known weakness of this solution is that it results in a very limited linear region. Nevertheless, it will not pose problem for a counting mode system (where the energy resolution is not required).

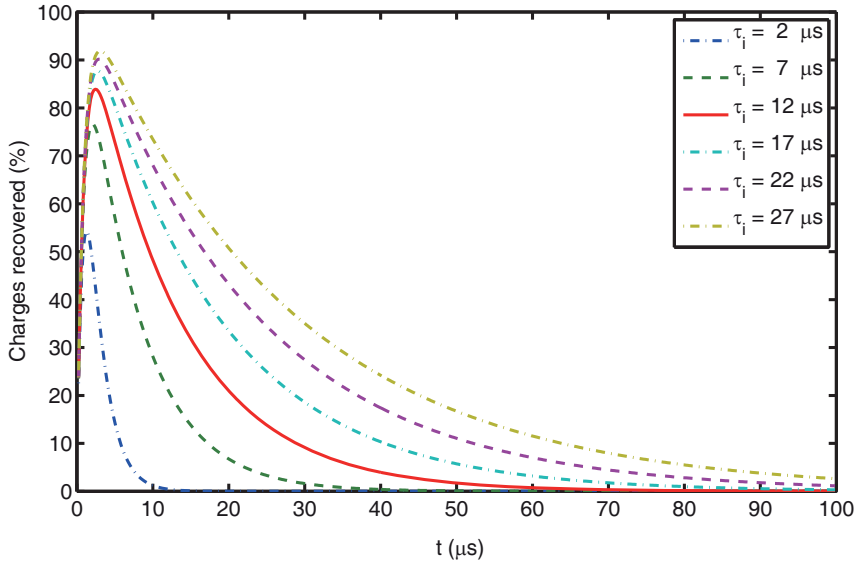

Figure 4.5: Normalized CSA output pulses for an unit input charge with different integration time. The later choice (12 µs) is depicted by a solid line.

4.3 Circuit implementations

In our application, the main constraint on the signal processing originates from the realization of the low noise figure under an ultra low power consumption (< 1 mW). In order to limit the power dissipation, the electronics is designed in a 2.5 V single power supply.

4.3.1 Charge Sensitive Amplifier

The preamplifier is one of the most crucial parts in the signal processing. Its design followed several different considerations. It must provide a gain of above 7000 to ensure a charge lost of less than 2% as demonstrated by Eq. (4.7). Moreover, its power consumption must be kept very low. As the noise of the preamplifier is a crucial factor for the performance of the sensor, both the white noise as well as the $1/f$ noise must be minimized for the relative large detector capacitance ($\sim$13 pF). The input transistor usually generates the dominant noise and therefore its type, size and the biasing condition must be chosen carefully.

A simple single-ended cascode amplifier is used extensively in processing the signals from

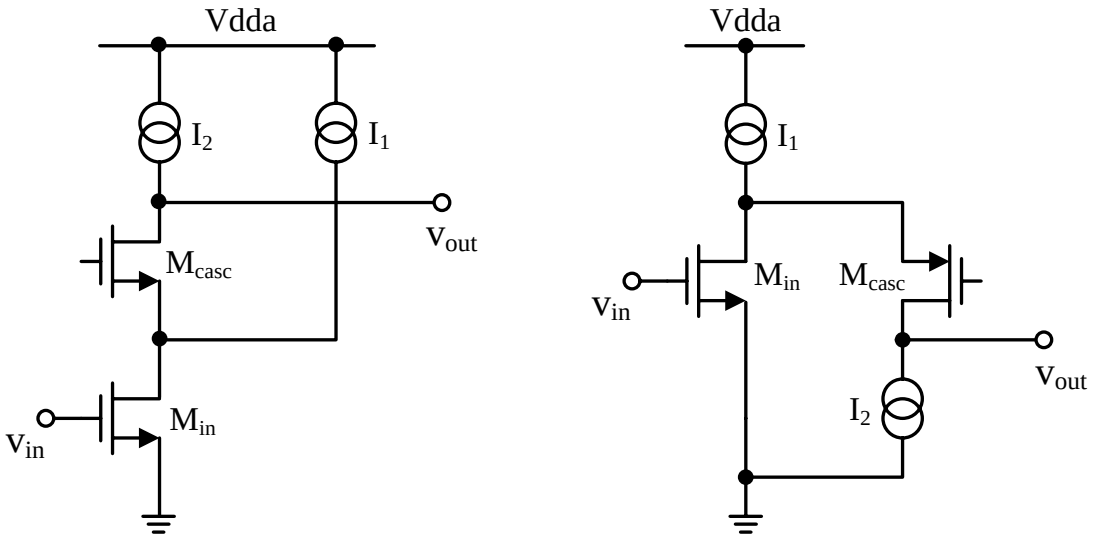

Figure 4.6: The commonly used single-ended amplifier configurations: (a) the "direct" cascode, (b) the "folded" cascode.

capacitive sensors such as particle silicon detectors [2], PET (Positron Emission Tomography) detectors [3,4], and X-ray detectors [5]. Its basic configurations include the "direct" (or "straight") cascode (Fig. 4.6(a)) and the "folded" cascode (Fig. 4.6(b)). In this work, we propose a modified structure as shown in Fig. 4.7. This structure offers a simple and current efficient solution. The input transistor M_0 is mainly biased by the current I_1. The smaller current I_2 in the other branch makes it easier to achieve a high DC-gain, which guarantees that most of the input charges are integrated by C_f. The cascode transistor M_2 keeps the drain of M_0 at a constant potential so that the signal current flows to the node V_2 where it generates a voltage signal. As in [4], the input is also cascoded (M_1) in order to minimize the Miller effect. A source follower is added to reduce the capacitive loading of the dominant node in order to increase the bandwidth. For the input transistor, NMOS is usually favored due to the higher transconductance compared to a PMOS. However, in our case, a PMOS makes it easier to achieve a higher DC potential at the input of the preamplifier. Since the preamplifier is DC coupled with the diode array, the higher DC potential of the preamplifier input node, the larger inverse bias voltage for the diodes, thus the lower diode junction capacitance and the better charge collection efficiency can be obtained in the process with high resistivity epitaxial layer. Hence, a PMOS transistor has been chosen as the input device. In order to have a sufficient high gain and limited power consumption, a current of 30 µA has been chosen for the drain current (I_0) of the input transistor M_0, and $I_1 =$ 25 µA, $I_2 = 5$ µA are used.

It is well known that the noise performance of a charge amplifier is not only determined by its intrinsic noise but also by the optimal matching condition [5]. Both optimal noise matching

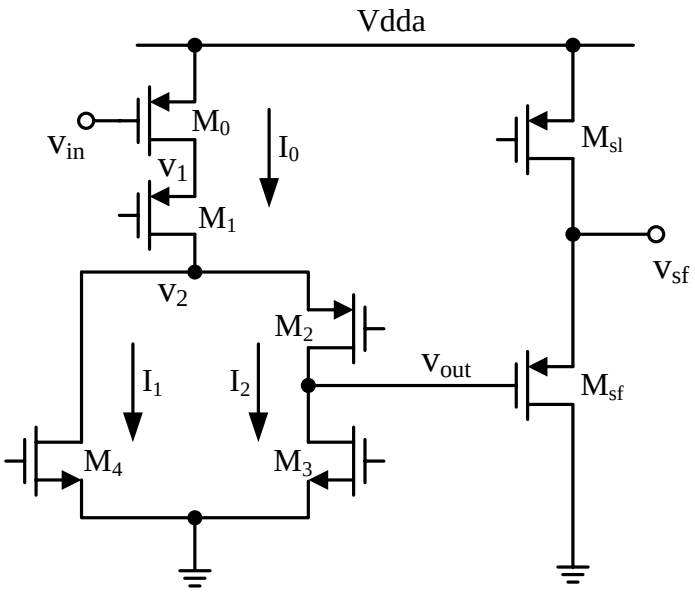

Figure 4.7: Schematic of the single-ended input split-leg cascode amplifier, where the voltage follower used to decouple the amplifier from the following circuits is also indicated.

condition and total noise contribution of the CSA are mainly constrained by the input transistor (the condition of the input transistor dominating the total noise contribution will be explained later). To maximize the g_m/I_D ratio (which gives a more power-efficient circuit) and dynamic range, the input transistor has been designed to operate in the moderate inversion region and at low drain-source voltage. The noise performance of the device is also generally better in the moderate inversion region [6]. The minimum channel length maximizes the transconductance to capacitance ratio of the input transistor. In order to reduce the process mismatch, a channel length of 0.5 µm (the minimum length is 0.35 µm in this technology) is used. The width of the input transistor M_0 is determined to optimize the noise. According to [7], for the transistor operating in the moderate inversion region, a new capacitive matching rule is valid. The optimal gate capacitance is given in Eq. (4.12).

$$C_{g,opt} = \frac{L_{min}^2 I_D}{2\mu(nV_t)^2} \tag{4.12}$$

where L_{min} is the minimum channel length, I_D is the drain current, μ is the carrier mobility, n is the subthreshold slope factor and $V_t = kT/Q$ is the thermal voltage. However, this rule has only considered the white series noise. As addressed in [8], $1/f$ noise is minimized when the input capacitance is equal to that of the detector. Therefore, considering both the thermal noise and $1/f$ noise, the optimum gate capacitance lies between the value given in Eq. (4.12) and the detector capacitance C_{det}. As a result, the width of the input transistor is chosen to be 340 µm.

4.3.1.1 Gain and noise analyses

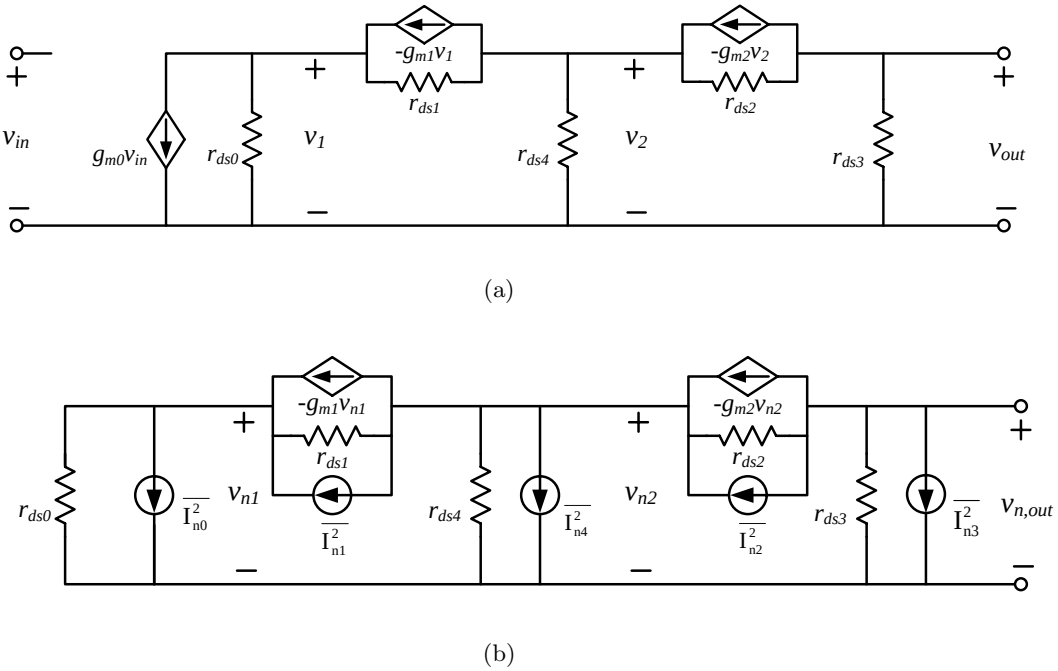

Figure 4.8: Small-signal model of Fig. 4.7 for (a) gain analysis, and for (b) noise analysis, where the source follower and the bulk effect on M_1 and M_2 are neglected

The choices of the dimensions of other transistors in the preamplifier are mainly governed by the goals of a sufficient gain and minimized noise contribution. The gain and total noise of the preamplifier can be calculated through the small-signal analyses. The small-signal performance of the preamplifier of Fig. 4.7 can be analyzed with the assistance of the following model (ignoring body effect) shown in Fig. 4.8(a). Using model analysis, we may write

$$\begin{cases} g_{m0}v_{in} + v_1 g_{ds0} = -g_{m1}v_1 + (v_2 - v_1)g_{ds1} \\ -g_{m1}v_1 + (v_2 - v_1)g_{ds1} + v_2 g_{ds4} = -g_{m2}v_2 + (v_{out} - v_2)g_{ds2} \\ -g_{m2}v_2 + (v_{out} - v_2)g_{ds2} + v_{out}g_{ds3} = 0. \end{cases} \tag{4.13}$$

Solving for the voltage gain, v_{out}/v_{in} yields

$$A_0 = \frac{v_{out}}{v_{in}} \approx -\frac{g_{m0}}{g_{ds3} + \frac{g_{ds2}}{g_{m2}}\left(g_{ds4} + \frac{g_{ds0}g_{ds1}}{g_{m1}}\right)} \tag{4.14}$$

where g_{m0} and g_{m1} are the transconductances of M_0 and M_1 respectively, and g_{dsi} is the channel conductances of the transistor M_i ($r_{dsi} = 1/g_{dsi}$ is shown in Fig. 4.8(a)).

Fig. 4.8(b) present the small-signal model of the preamplifier for noise analysis, where $\overline{I_{ni}^2}$ represents the sum of the thermal noise and flicker noise of the transistor M_i. The mean-square

current-noise power spectra of the NMOS ($\overline{I_{n,N}^2}$) and the PMOS ($\overline{I_{n,P}^2}$) in the AMS 0.35 µm process are defined in Eqs. (4.15) and (4.16) respectively.

$$\overline{I_{n,N}^2} = \frac{8}{3}kTg_m + \frac{K_{Fn}I_d^{AF_n}}{C_{ox}L^2f} \tag{4.15}$$

$$\overline{I_{n,P}^2} = \frac{8}{3}kTg_m + \frac{K_{Fp}I_d^{AF_p}}{C_{ox}WLf} \tag{4.16}$$

where k is the Boltzmann's constant, T is the temperature in Kelvin, C_{ox} is the capacitance per unit area of the gate oxide, and I_D is the drain current. W and L are the channel width and length respectively. $K_{Fn} = 2.170 \times 10^{-26}$ and $AF_n = 1.507$ are the flicker noise coefficients for NMOS. $K_{Fp} = 1.191 \times 10^{-26}$ and $AF_p = 1.461$ are the flicker noise coefficients for PMOS.

Using the model of Fig. 4.8(b), we can write

$$\begin{cases} I_{n0} + v_{n1}g_{ds0} = -g_{m1}v_{n1} + (v_{n2} - v_{n1})g_{ds1} + I_{n1} \\ -g_{m1}v_{n1} + (v_{n2} - v_{n1})g_{ds1} + I_{n1} + v_{n2}g_{ds4} + I_{n4} = -g_{m2}v_{n2} + (v_{n,out} - v_{n2})g_{ds2} + I_{n2} \\ -g_{m2}v_{n2} + (v_{n,out} - v_{n2})g_{ds2} + I_{n2} + v_{n,out}g_{ds3} + I_{n3} = 0. \end{cases} \tag{4.17}$$

Solving the equations we can obtain the total mean-square output-voltage-noise spectral density, $\overline{v_{n,out}^2}$ as given in Eq. (4.18). This equation indicates that the noise contribution of M_1 and M_2 are negligible.

$$\begin{aligned} \overline{v_{n,out}^2} &= \frac{\overline{I_{n0}^2} + \overline{I_{n3}^2} + \overline{I_{n4}^2} + \overline{I_{n1}^2}(\frac{g_{ds0}}{g_{m1}})^2 + \overline{I_{n2}^2}(\frac{g_{ds0}+g_{ds4}}{g_{m2}})^2}{\left[g_{ds3} + \frac{g_{ds2}}{g_{m2}}\left(g_{ds4} + \frac{g_{ds0}g_{ds1}}{g_{m1}}\right)\right]^2} \\ &\approx \frac{\overline{I_{n0}^2} + \overline{I_{n3}^2} + \overline{I_{n4}^2}}{\left[g_{ds3} + \frac{g_{ds2}}{g_{m2}}\left(g_{ds4} + \frac{g_{ds0}g_{ds1}}{g_{m1}}\right)\right]^2} \end{aligned} \tag{4.18}$$

The equivalent input-voltage-noise spectral density can be found by dividing Eq. (4.18) by Eq. (4.14) to get:

$$\overline{v_{n,in}^2} \approx \frac{1}{g_{m0}^2}(\overline{I_{n0}^2} + \overline{I_{n3}^2} + \overline{I_{n4}^2}). \tag{4.19}$$

Substituting Eqs. (4.15) and (4.16) into Eq. (4.19) gives

$$\overline{v_{n,in}^2} = \frac{8}{3}kT\frac{1}{g_{m0}}(1 + \frac{g_{m3}}{g_{m0}} + \frac{g_{m4}}{g_{m0}}) + \frac{1}{g_{m0}^2}(\frac{K_{Fp}I_0^{AF_p}}{C_{ox}W_0L_0f} + \frac{K_{Fn}I_2^{AF_n}}{C_{ox}L_3^2f} + \frac{K_{Fn}I_1^{AF_n}}{C_{ox}L_4^2f}). \tag{4.20}$$

In terms of device parameters this equivalent input-noise can be expressed as

$$\overline{v_{n,in}^2} = \frac{8}{3}kT\frac{1}{g_{m0}}(1+\frac{\sqrt{2K_{Pn}\frac{W_3}{L_3}I_2}}{I_0/nV_t}+\frac{\sqrt{2K_{Pn}\frac{W_4}{L_4}I_1}}{I_0/nV_t})+\frac{1}{g_{m0}^2}(\frac{K_{Fp}I_0^{AF_p}}{C_{ox}W_0L_0f}+\frac{K_{Fn}I_2^{AF_n}}{C_{ox}L_3^2f}+\frac{K_{Fn}I_1^{AF_n}}{C_{ox}L_4^2f}) \tag{4.21}$$

where n is the subthreshold slope factor and $V_t = kT/Q$ is the thermal voltage, and $K_{Pn} = 170$ µA/V^2 is the process transconductance parameters for NMOS. We remind that, M_0 works in the moderate inversion region, whereas the current sources M_3 and M_4 are operated in the strong inversion region. $I_2 = 5$ µA has been chosen to ensure a high output resistance, thus a sufficient high gain A_0. Equation 4.21 indicates that the current source is a secondary source of noise. To minimize this contribution the aspect ratio W/L of the current source transistor must be minimized while staying in the saturation region. In our design, $\frac{W_3}{L_3} = \frac{3.9}{15.6}$ and $\frac{W_4}{L_4} = \frac{19.5}{15.6}$ have been chosen so that the noise of the current sources contributes less than 15% to the overall CSA noise.

4.3.1.2 Effect of the leakage currents

In this work, the CSA is DC coupled to the diode matrix. The leakage current of one 5×5 µm^2 n-well/ p-epi diode is around 0.7 fA at room temperature, therefore the total leakage current of the whole diode matrix is less than 1 pA. This value produces a negligible DC voltage drop across the feedback resistor of less than 100 µV. Considering the presence of ionizing radiation, the leakage current may be ten times larger, translating into a DC voltage drop of 1 mV. This value is still insignificant.

4.3.2 Shaper

The noise at the output of the CSA can be decreased by the reduction of the bandwidth with appropriate filters, commonly referred to as shapers [9]. Considering the low power consumption, a semi-gaussian shaper based on the CR-RC principle is used in this work. In the frequency domain, this kind of shaper can be considered as an active band-pass filter. The detail of the shaper is shown in Fig. 4.9. A linearized degenerated differential pair is used as the active feedback for the shaper. This structure provides an area-efficient solution for the long shaping time. Moreover, the output DC level of this structure is controlled by the input DC voltage V_{dc}, and therefore it is possible to tune different DC levels for different secondary charged particles generated by neutrons. The transconductance of the feedback circuit depends on the transconductances of M_1, M_2 and the conductance g_{ds} of M_3, M_4 connected in parallel [10], [11], as calculated by

$$g_{mf} = \frac{4\beta_2\sqrt{\beta 1}}{\beta_1+4\beta_2}\sqrt{\frac{I_f}{2}} \tag{4.22}$$

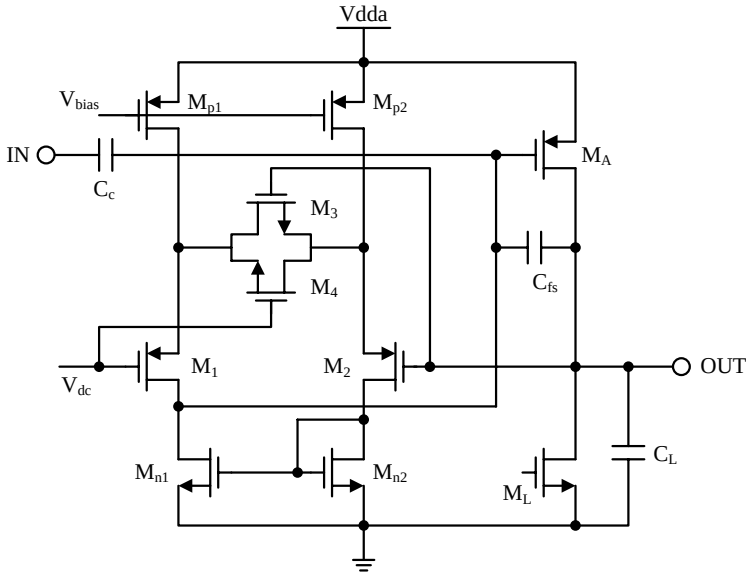

Figure 4.9: Schematic of the shaper with the active feedback.

where $\beta_1 = K_p \frac{W_{1,2}}{L_{1,2}}$, $\beta_2 = K_p \frac{W_{3,4}}{L_{3,4}}$, K_p is the process transconductance parameter for PMOS, $W_{1,2}$ and $L_{1,2}$, $W_{3,4}$ and $L_{3,4}$ are the dimensions of the transistors, I_f is the bias current. The transconductance of the feedback varies with the change of their bias current, so the shaping time can be adjusted by changing the bias. In order to achieve microsecond level peaking time, the differential pair of M_1 and M_2 constructs a very low transconductance amplifier, which consumes only several tens of nA. Compared with the conventional shaper with a passive feedback resistor, this solution is much easier to implement in a compact readout circuit. The noise contribution from the active feedback depends mainly on the bias current (I_f) and the transconductance of M_{n1} ($g_{m,n1}$). In order to reduce the noise of the shaper, I_f and $g_{m,n1}$ have to be minimized [10].

As the simplest way to meet the specification of very long peaking time, a PMOS inverter is used as the amplifier stage in the shaper. The coupling capacitance (C_c), the feedback capacitance (C_{fs}), and the load capacitance (C_L) are 6 pF, 0.6 pF and 1.2 pF, respectively.

The transfer function of the shaper is expressed as

$$H(s) = \frac{s g_{mA} C_c}{\xi s^2 + (C_{ts}/R_{fs} + g_{mA} C_{fs}) s + g_{mA} R_{fs}} \tag{4.23}$$

where g_{mA} and C_{gsA} are the transconductance and input capacitance of the input transistor (M_A), respectively, $C_{ts} = C_c + C_{gsA} + C_L$, $C_{os} = C_L + C_{fs}$, $\xi = C_c C_{os} + C_{gsA} C_{os} + C_{fs} C_L$, and R_{fs} represents the feedback resistance given by the reciprocal of the g_{mf} in Eq. (4.22). A double real pole appears if the feedback resistance is exactly equal to

$$R_{fs} = \frac{1}{g_{mA} C_{fs}^2} \left[2\xi - C_{fs} C_{ts} + 2\sqrt{\xi(\xi - C_{fs} C_{ts})} \right] \tag{4.24}$$

The pole is located at frequency ω_s expressed in Eq. 4.25.

$$\omega_s = \frac{1}{\tau_s} = \frac{2g_{mA}}{C_{os} + R_{fs}C_{fs}g_{mA}} \tag{4.25}$$

where τ_s represents the filter time constant. The gain of the shaper, A_s, becomes

$$A_s = R_{fs}C_c\omega_s. \tag{4.26}$$

The time constant of the shaper τ_s was chosen in order to optimize the total noise of the CSA and the shaper. The detailed analysis will be presented in the following sub-section.

4.3.3 Optimization of the total noise

The noise equivalent model for the CSA and the shaper is depicted in Fig. 4.10, where C_{det} represents the detector capacitance (∼13 pF), and C_{pre} is the capacitance of the input transistor. The noise of the CSA is modeled by a serial noise voltage source e_n^2, and a parallel noise current source i_n^2 at its input. These noise contributions are expressed as:

$$d\langle e_n^2(f)\rangle = V_d + V_f f^{-1} = \frac{8}{3}\frac{kT}{g_{m0}} + \frac{K_f}{C_{ox}WLf}, \tag{4.27}$$

$$d\langle i_n^2(f)\rangle = I_d = 2qI_{leak} + \frac{4kT}{R_f} \tag{4.28}$$

where V_d and V_f represent the white noise and the $1/f$ noise of the input transistor of the CSA, respectively. g_{m0} is the transconductance of the input transistor (M_0), and C_{ox} is the oxide capacitance per unit area. W and L are the dimensions of the input transistor, I_{leak} is the total leakage current of the diode array, K_f is the coefficient for the $1/f$ noise, and R_f is the feedback resistance. Compared to the feedback resistor, the noise contribution of the leakage current is negligible.

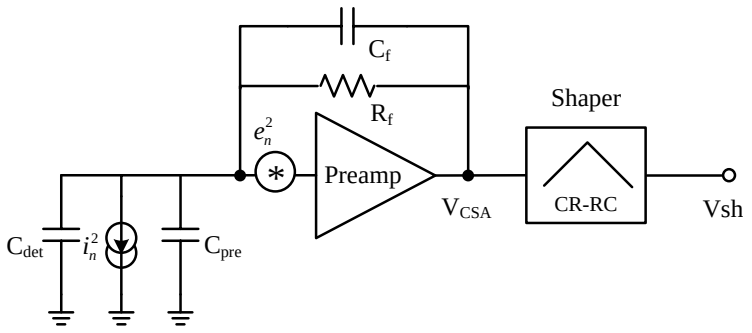

Figure 4.10: Noise equivalent model for the CSA and the shaper with the detector capacitance input load.

Since the two noise sources are uncorrelated, the effect of them on the CSA output voltage

can be calculated separately. At the output of the CSA, the total noise voltage can be described by

$$d\langle V_{n,CSA}^2(\omega)\rangle = \sum_{k=-2}^{0} c_k \omega^2, \tag{4.29}$$

with

$$c_{-2} = \frac{I_d}{2\pi C_f^2}, \quad c_{-1} = \frac{K_f}{C_{ox} W L}\frac{C_{in}^2}{C_f^2}, \quad c_0 = \frac{8}{3}\frac{kT}{g_{m0}}\frac{C_{in}^2}{2\pi C_f^2} \tag{4.30}$$

where the spectrum has been expressed as a function of the angular frequency $\omega = 2\pi f$. The sum $C_{in} = C_{det} + C_{pre} + C_{par}$ represents the total capacitance at the input of CSA, and C_{par} represents the parasitic capacitance.

The squared transfer function of the shaper is given by

$$H_{sh}^2(\omega) = \left[A_s \frac{\omega/\omega_s}{(1+\omega/\omega_s)^2}\right]^2. \tag{4.31}$$

With Eqs. (4.29) and (4.31), we obtain the total squared noise-voltage at the output of shaper calculated by Eq. (4.32).

$$\begin{aligned} V_{n,sh}^2 &= \int_0^{+\infty} H_{sh}^2(\omega)\, d\langle V_{n,CSA}^2(\omega)\rangle \\ &= \frac{A_s^2}{2}\frac{1}{\Gamma(2)}\sum_{k=-2}^{0} c_k \omega_s^{k+1}\Gamma\left(1+\frac{k+1}{2}\right)\Gamma\left(1-\frac{k+1}{2}\right) \\ &= A_s^2\frac{\pi}{4}\left(\frac{c_{-2}}{\omega_s} + \frac{2}{\pi}c_{-1} + \omega_s c_0\right), \end{aligned} \tag{4.32}$$

where Γ is the gamma function with $\Gamma(x+1) = x\Gamma(x)$, $\Gamma(1) = 1$ and $\Gamma(1/2) = \sqrt{\pi}$ [9].

In order to calculate the total gain of the CSA and the shaper, we assume an input charge of a single electron ($Q_{in} = q$). With the ideal gain of the CSA of $1/C_f$ and the transfer function of the shaper $H_{sh}(s)$, the signal at the output of the shaper in the frequency domain is given by

$$v_{os}(s) = \frac{q}{sC_f}H_{sh}(s) = \frac{q}{sC_f}\cdot\frac{A_s s\tau_s}{(1+s\tau_s)^2} \tag{4.33}$$

where C_f is the feedback capacitance of the CSA, and τ_s is the time constant of the shaper. Taking the inverse Laplace transformation of Eq. (4.33) gives the output signal in the time domain as

$$v_{os}(t) = \frac{A_s q t^2}{2C_f\tau_s^2}e^{-\frac{t}{\tau_s}}. \tag{4.34}$$

The ideal total electron-to-voltage gain (A_e) equals to the maximum amplitude of the $v_{os}(t)$, given by:

$$A_e = \frac{A_s q}{eC_f}. \tag{4.35}$$

Accordingly, the total ENC referred back to the input of the CSA becomes

$$ENC_t^2 = \frac{V_{n,sh}^2}{A_e^2} = \frac{e^2}{4q^2}(\frac{1}{2}\tau_s I_d + \frac{1}{2\tau_s}C_{in}^2 V_d + 2C_{in}^2 V_f) \tag{4.36}$$

where τ_s is the time constant of the shaper expressed in Eq. (4.25), and I_d, V_d, V_f are defined in Eqs. (4.27) and (4.28). To minimize the input ENC in Eq. (4.36), the optimal shaper time constant, $\tau_{s,opt}$, is given by

$$\tau_{s,opt} = \sqrt{\frac{C_{in}^2 V_d}{I_d}}. \tag{4.37}$$

In the ideal case (where the signal at the output of the CSA is an ideal step voltage), with the chosen dimension of the input transistor (M_0) (W/L=340 µm/0.5 µm), $C_{in} \approx 13\ pF$, I_{leak} = 720 fA, R_f = 120 MΩ, and T = 300 K, the optimal shaper time constant is calculated to be about 2.1 µs. The design parameters, R_{fs}, and g_{mA}, were chosen to achieve τ_s = 2.1 µs and a reasonable gain.

4.3.4 Discriminator

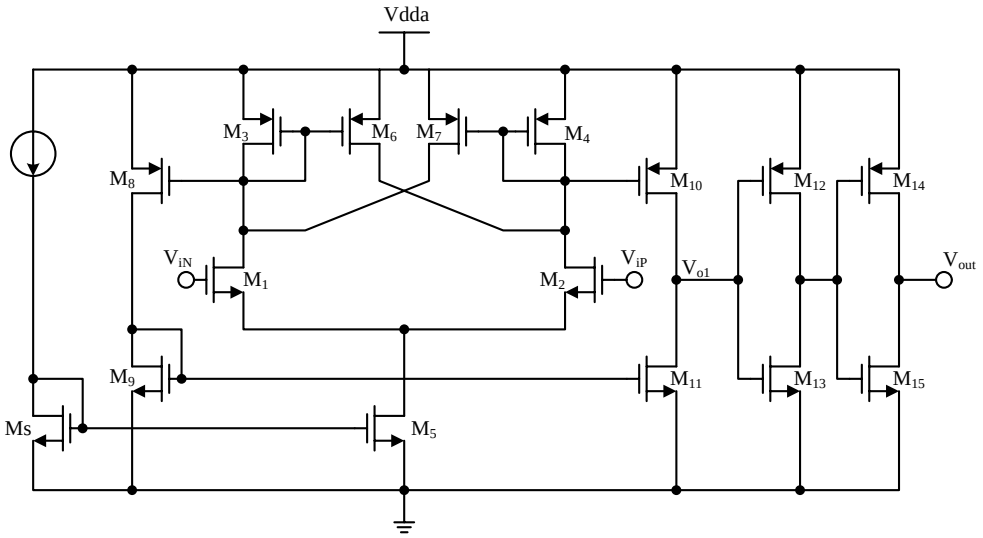

Figure 4.11: Schematic of the hysteresis comparator using the internal positive feedback.

A direct readout is required in an electronic personal dosemeter. Therefore, in the AlphaRad-2 chip, a discriminator is used to detect the shaper output signals above a given threshold providing one-bit binary output. The implementation of the discriminator in this design is a hysteresis comparator, which is desirable in the noisy environment. Figure 4.11 presents the comparator using internal positive feedback in the input stage of a high-gain, open loop comparator to perform the hysteresis. In this structure, there are two paths of feedback: a negative-feedback path and a positive-feedback path. The negative one is the current-series feedback through the

common source node of transistors M_1 and M_2. The positive one is the voltage-shunt feedback through the gate-drain connections of transistors M_6 and M_7. Only if the positive-feedback factor is greater than the negative-feedback factor (i.e. $\frac{(W/L)_6}{(W/L)_3} > 1$), the overall feedback will be positive, resulting in hysteresis in the voltage-transfer curve [12]. A hysteresis comparator has a *bistable* characteristic. When the input voltage $V_{iP} - V_{iN}$ starts negative and goes positive, the output does not change until it reaches the positive trip point, V_{TRP}^{+}. When the input returns in the negative direction, the output keeps its state until the input reaches the negative trip point, V_{TRP}^{+}. In the circuit of Fig. 4.11, the positive trip point is given by Eqs. (4.38) and (4.39).

$$V_{TRP}^{+} = \sqrt{\frac{2i_1}{\beta_1}} + V_{T1} - \sqrt{\frac{2i_2}{\beta_2}} - V_{T2}, \tag{4.38}$$

with

$$i_1 = \frac{i_5}{1 + [(W/L)_6/(W/L)_3]}, \qquad i_2 = i_5 - i_1 \tag{4.39}$$

where i_k, is the drain currents of the transistor M_k, V_{Tk} is the threshold voltage of M_k, $(W/L)_k$ and $(W/L)_6$ are the dimension ratio of M_k, and β is the transconductance parameter defined as $\beta = K_{Pn}\frac{W}{L}$. While the negative trip point, V_{TRP}^{-}, can be found in a similar manner and given by Eqs. (4.40) and (4.41)

$$V_{TRP}^{-} = \sqrt{\frac{2i_1}{\beta_1}} + V_{T1} - \sqrt{\frac{2i_2}{\beta_2}} - V_{T2}, \tag{4.40}$$

with

$$i_2 = \frac{i_5}{1 + [(W/L)_7/(W/L)_4]}, \qquad i_1 = i_5 - i_2. \tag{4.41}$$

The positive and negative trip points are designed to be identical in this work. As the rms noise at the output of the shaper is about 2 mV, we chose a trip point voltage of 18 mV to ensure the hysteresis higher than the largest expected noise amplitude.

The output stage (M_8 – M_{11}) in Fig. 4.11 is used to accomplish the differential-to-single-ended conversion and to provide a Class AB type of driving capability. The last two push-pull inverters are added to drive a large value capacitive load. Figure 4.12 shows the simulated transfer curve of the comparator with a 10 pF load.

4.3.5 Testability

The readout chain of the diode-matrix works in the count mode in the presence of charged particles. However, in the test mode, analog output signals are required in order to characterize the CSA and the shaper. Therefore, a low noise analog buffer has been designed. A conventional two-stage Miller operational amplifier is employed. The shunt down mode is kept in the buffer, allowing to measure the power consumption of the readout chain. The observation of analog

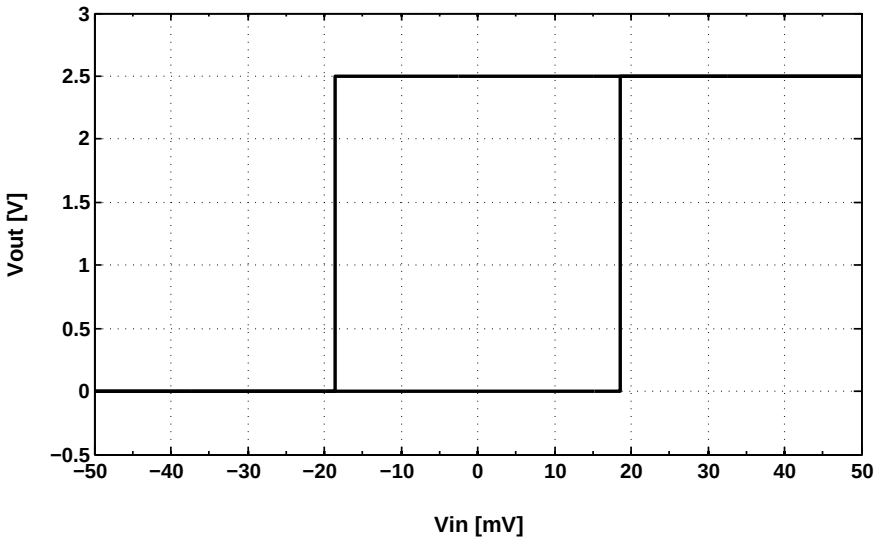

Figure 4.12: Simulated transfer curve of the hysteresis comparator with a 10 pF load.

waveforms can be accomplished by selected switches connected to the CSA and the shaper. The characteristics of this amplifier has been verified in the simulation. The DC gain is 88 dB and the unity-gain bandwidth is 8 MHz. The phase margin is equal to 67 °. The rms noise is about 19 µV.

In order to test the chip with electrical signals, an injection capacitor in serial with the readout chain is integrated on the chip. The injection capacitor controlled by a select switch will be disconnected to the readout during the test with radiation sources.

4.4 Simulation results and layout

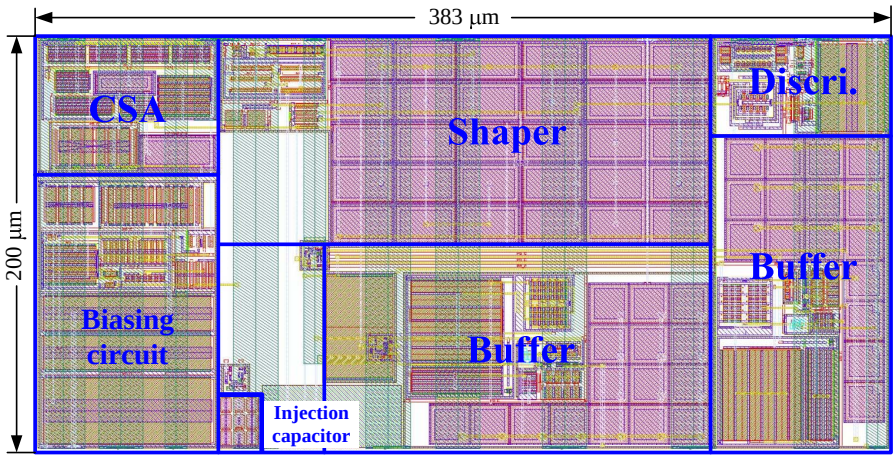

Figure 4.13: Layout of the readout circuit, containing CSA, shaper, discriminator and analog buffers.

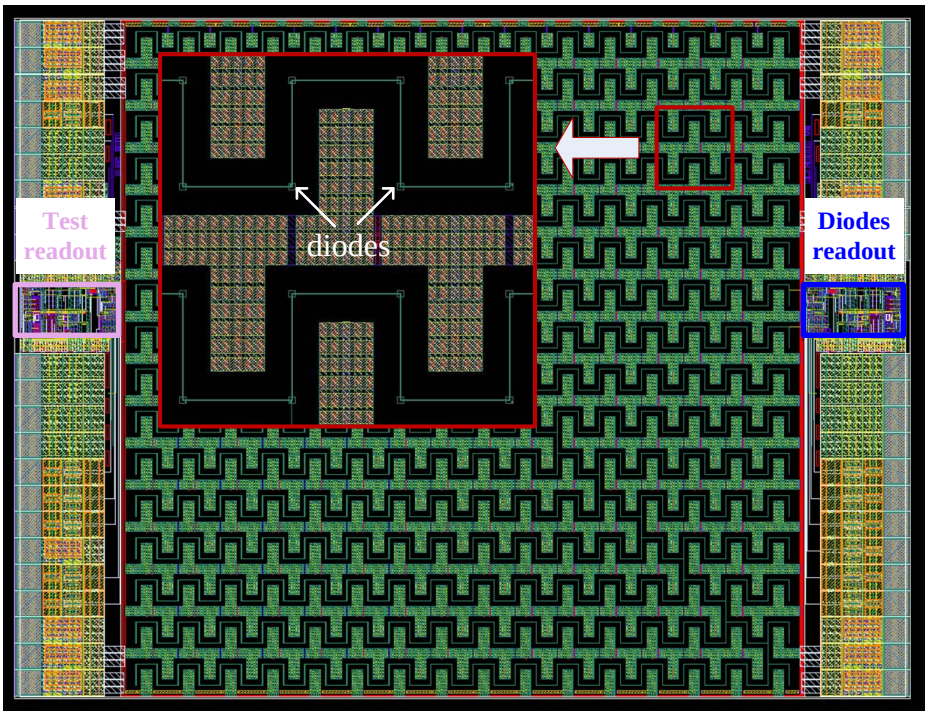

Figure 4.14: Layout of the AlphaRad-2 chip.

The AlphaRad-2 chip has been implemented in the AMS (Austria Micro Systems International GmbH) 0.35 µm CMOS OPTO process (with an epitaxial layer of ∼14 µm). The diode-array readout chain contains a CSA, a shaper, a discriminator, the biasing circuit, an injection capacitor, and two output buffers. The dimension of the readout chain is 200 µm × 383 µm (Fig. 4.13). The micro-diode array occupies 2.56×2.56 mm^2 as the active area. Figure 4.14 presents the layout of the AlphaRad-2 chip. The die area is 2.58×3.4 mm^2. The sensing part (6.55 mm^2) occupies more than 75% of the total area. An improvement in the detector layout is that the straight lines are replaced by poly lines for the diodes connections. Moreover, small segments of filling (comprising four metal layers and a poly layer for the metal and poly density requirement) with vias between layers and contacts to the substrate are used. These two improvements are chosen because in such a large diode matrix, a long straight line may increase the possibility of open via due to the mechanical stress. The diode-array readout chain is connected to the matrix on the right side. On the left of the diode-array, the 'test readout' as a duplicate of the matrix readout is separated from the pixel array. The IO pads are located above and below the readout chain.

Using the modeled current signal in Fig. 4.3 as the input signal, the transient response of the preamplifier, shaper, and discriminator from the post simulation are presented in Fig. 4.15.

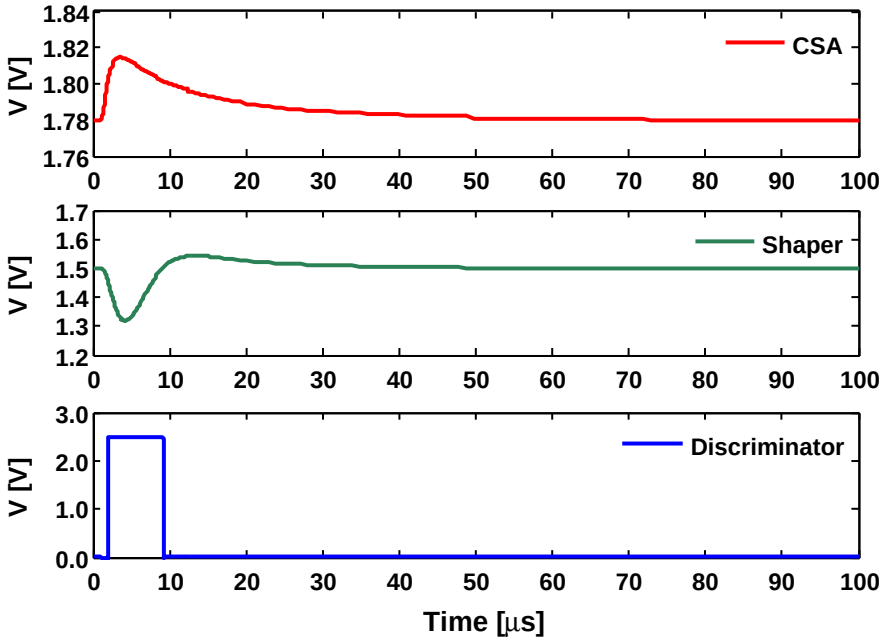

Figure 4.15: Transient response of the chip to the input signal (charge of 5.83 fC) in Fig. 4.3 from the post-simulation.

4.5 Electrical test results

When slow neutrons are converted to α particles, irradiation from the front side (through the oxide layer) is no more possible. In order to be suitable for backside-illumination, the chips are wirebonded to the daughter boards, which can be plugged into the test board. Figure 4.16 shows a photograph of the bonded sensor. Figure 4.17 shows the test board for the electrical test of AlphaRad-2 chip. [2]

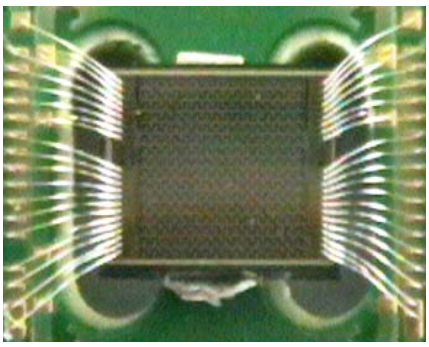

Figure 4.16: Photo of the wire bonded AlphaRad-2 chip

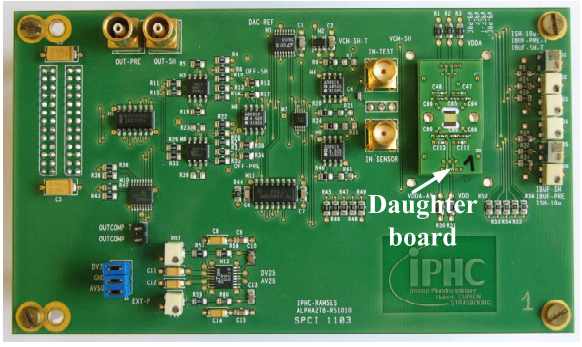

Figure 4.17: Photo of the test board

2. The test board design is not part of this thesis. The schematic of the test board can be found in Appendix A.

4.5.1 Charge response and noise performance

The response of the chip and the noise measurements have been performed with electrical signals. We inject voltage pulse signals through an injection capacitor. We can also adjust the level and frequency of the input signal. Figure 4.18 shows the response of CSA, shaper and discriminator to the injected charge of 5.83 fC (which is equal to the input charge in Fig. 4.15). It is in good agreement with the simulation. Figure 4.19 exhibits the simulated and measured peak values of the shaper output at shaping time as a function of the injected charges. The response of the readout chain is linear in the range of below 17 fC, with a charge to voltage gain of about 30.9 mV/fC (32.4 mV/fC in the simulation). The good agreement with the simulated value is an important point to assess all our calculations. The vertical error bars are corresponding to the statistic error, while the horizontal error bars are due to the capacitance parameter dispersion of the AMS process. The signal to noise ratio is larger than 80 at the signal threshold (32 000 e^-). The electrical test results indicate that the AlphaRad-2 has a very low noise of less than 400 electrons, a very low power consumption of 314 µW, and a count rate of 20 kHz. This readout frequency seems to be much lower compared to the AlphaRad-1 but we will show later that it is adequate for the application.

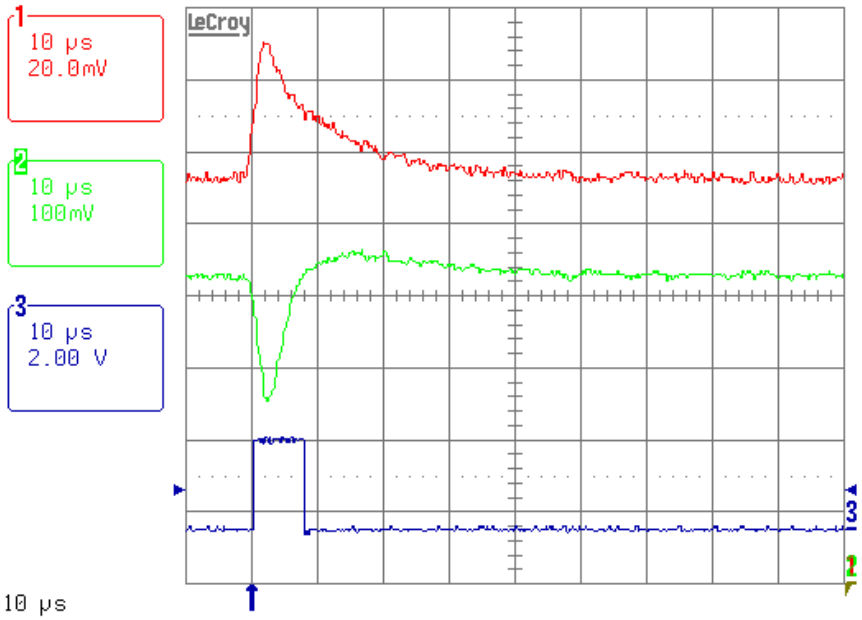

Figure 4.18: Measured waveform of the chip's response to an injected charge of 5.83 fC: at the output of CSA (upper curve), shaper (middle curve), and discriminator (lowest curve).

The measured characteristics of the two AlphaRad prototypes are summarized in Table 4.1. Compared to our previous design AlphaRad-1 [13], the new prototype is able to detect recoil protons and α-particles at the single particle level thanks to its low noise. Moreover, the power consumption is reduced significantly.

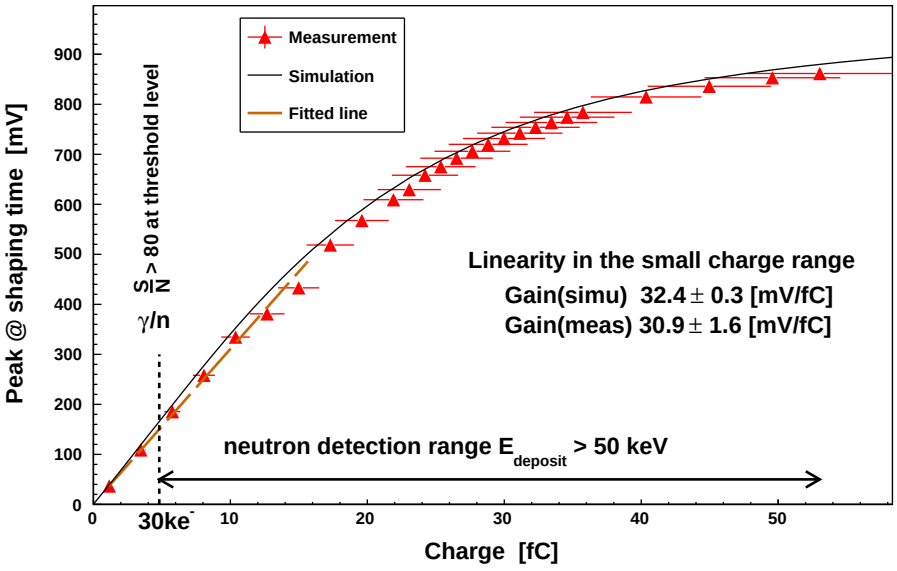

Figure 4.19: Measured versus simulated signal amplitudes at the output of shaper with different input charges. (The vertical uncertainties for the measurement are in the level of some millivolts so that they are invisible due to the scale).

Prototype	AlphaRad-1 [13]	AlphaRad-2
Technology	AMS 0.6 µm	AMS 0.35 µm
Sensitive area (mm^2)	2.56 × 5.12	2.56 × 2.56
Sensor capacitance	∼ 40.9 pF	∼ 13 pF
Readout chain Config.	V-Amp + discr. + Compens.	CSA + Shaper + discr.
ENC	≈ 14000 e^-	390 ± 2 e^-
Detected particles	1 meV-100 keV neutrons & α	1 meV-10 MeV neutrons (→p, α)
Counting rate	≈ 300 kHz	≈ 20 kHz
Power consumption	≈ 10 mW	≈ 314 µW

Table 4.1: The performance comparison of the two AlphaRad chips.

4.5.2 A remark on safety level

The actual readout frequency of the AlphaRad-2 was chosen for electronic performance optimization. But for our neutron dosimetric application, the present counting rate ensures a very good safety level. The maximal dose allowed (per year) for workers is 20 mSv. Assuming in an accidental case, the dosemeter must be able to handle even catastrophic dose rates. Taking the conversion factor of 600 pSv·cm^2 (for fast neutrons), this upper limit corresponds to a fluence of 3×10^7 cm^{-2}. With our sensor (active area of 6.55 mm^2, counting rate of 20 kHz), this means that even if this enormous radiation level is accidentally delivered in 2 minutes, our system will be able to measure it and to call for alarm. The AlphaRad-1 was designed to handle also direct alpha irradiation.

4.6 Conclusion

This chapter presents the dedicated chip, AlphaRad-2, for efficient neutron counting through proton and alpha detection. Targeting on a miniaturized system, we proposed a monolithic configuration that integrates the sensing elements and the signal processing electronics on the same silicon substrate. The 1024 micro-diodes connected in parallel are used for charge collection, leading to a large detecting surface (6.5 mm^2) with a relative low capacitance ($\sim$13 pF) and at the same time a very low leakage current ($<$ 1 pA). A critical constraint for the proposed chip is the low power consumption. With the constraints of the detector capacitor and the low-power, we have optimized the noise feature of the signal processing functionality to provide a sufficient sensitivity with a very low power consumption (300 µW). The electrical tests have demonstrated that the proposed chip satisfies well the requirements. Thanks to the natural low sensitivity to γ-rays and the very low noise readout ($<$ 400 e$^-$), this prototype is expected to provide efficient monitoring of fast and slow neutrons. Sensor development for a future dosemeter needs to be completed with extensive measurements to radioactive sources. The experimental results for its response to several sources (α, γ, X, n) will be presented in Chapter 5.

Bibliography

[1] F. d'Errico, M. Luszik-Bhadra, and T. Lahaye, "State of the art of electronic personal dosimeters for neutrons," *Nucl. Instr. and Meth. A*, vol. 505, no. 1-2, pp. 411–414, 2003.

[2] A. Codino, "Gallium arsenide telescope for measuring the time of flight of ionizing particles," *Nuclear Instruments and Methods in Physics Research Section A: Accelerators, Spectrometers, Detectors and Associated Equipment*, vol. 410, no. 1, pp. 12–18, 1998, Proceedings of the Fifth International Workshop on GaAs Detectors and Related Compounds. [Online]. Available: http://www.sciencedirect.com/science/article/pii/S0168900298000953

[3] M. Paulus, J. Rochelle, M. Andreaco, and D. Binkley, "A low-noise, wide-band CMOS charge-sensitive preamplifier for use with APD/LSO PET detectors," *Nuclear Science, IEEE Transactions on*, vol. 43, no. 3, pp. 1666 –1671, jun 1996.

[4] M. Weng, E. Mandelli, W. Moses, and S. Derenzo, "A high-speed low-noise CMOS 16-channel charge-sensitive preamplifier ASIC for APD-based PET detectors," *Nuclear Science, IEEE Transactions on*, vol. 50, no. 4, pp. 898 – 902, aug. 2003.

[5] Y. Hu, J. D. Berst, and M. Schaeffer, "A Very Low Power Consumption, Low Noise Analog Readout Chip for Capacitive Detectors with a Power Supply of 3.3 V," *Analog Integr. Circ. and Sig. Process.*, vol. 17, pp. 249–260, 1998.

[6] G. Anelli, K. Borer, L. Casagrande, M. Despeisse, P. Jarron, N. Pelloux, and S. Saramad, "A high-speed low-noise transimpedance amplifier in a 0.25 μm CMOS technology," *Nucl. Instr. and Meth. A*, vol. 512, no. 1-2, pp. 117–128, 2003.

[7] P. O'Connor and G. D. Geronimo, "Prospects for charge sensitive amplifiers in scaled CMOS," *Nucl. Instr. and Meth. A*, vol. 480, no. 2-3, pp. 713–725, 2002.

[8] W. M. C. Sansen and Z. Y. Chang, "Limits of low noise performance of detector readout front ends in CMOS technology," *IEEE Trans. Circuits and Systems*, vol. 37, no. 11, pp. 1375–1382, 1990.

[9] L. Rossi, P. Fischer, T. Rohe, and N. Wermes, *Pixel Detectors: From Fundamentals To Applications*. Springer, 2010.

[10] C. Hu-Guo, D. Bonnet, A. Brogna, J. P. Coffin, and e. a. G. Deptuch, "The HAL25 front-end chip for the ALICE silicon strip detectors," in *Proc. 7th Workshop on Electronics for LHC Experiments*, Stockholm, Sweden, Sep. 2001, pp. 76–80.

[11] F. Krummenacher and N. Joehl, "A 4-MHz CMOS continuous-time filter with on-chip automatic tuning," *Solid-State Circuits, IEEE Journal*, vol. 23, no. 3, pp. 750–758, jun 1988.

[12] P. Allen and D. Holberg, *CMOS Analog Circuit Design*. Oxford University Press, 2002.

[13] D. Husson, A. Bozier, S. Higueret, T. D. Lê, and A. M. Nourreddine, "Alpharad, a new integrated CMOS system-on-chip for high efficiency alpha particles counting," *Nucl. Instr. and Meth. A*, vol. 569, no. 3, pp. 845–852, 2006.

Chapter 5

Characterization of AlphaRad-2 with radiative sources

5.1 Acquisition system and noise

The AlphaRad-2 chip comprises an internal discriminator for a straightforward binary output, but a complete analog signal processing is also possible through the analog buffers integrated on the chip in parallel with the discriminator output. Figure 5.1 exhibits the diagram of the acquisition system for the analog signal analysis. In the present configuration, the bonded AlphaRad-2 chip (on a daughter board, see § 4.5, Fig. 4.16) is mounted on its test board (Test_Alp2_PCB), which receives polarization signals and delivers analog and digital outputs, as well as control signals. This board is coupled with a 12-bit ADC and a FPGA for signal processing. The discriminator output of AlphaRad-2 chip is sent to the FPGA, implementing a counting process. At the same time, the analog signal at the shaper output delivered by the AlphaRad-2 chip is sampled by an 12-bit ADC at a frequency of 33 MHz to digitalize the signal amplitude at the peaking time. Polarization and reading instructions are sent by the PC to the FPGA through a USB connector. The FPGA processes the sampling data and returns it to the PC.

The total acquisition noise (which is resulting from the test electronics and the AlphaRad-2 chip itself) can been obtained by running the acquisition in the absence of source. Figure 5.2 shows an example of the noise distribution (in unit of ADC) measured in the dark. The RMS value (2.6 ADC) of this distribution translates to the mean value of the total acquisition noise. Combined with the conversion factor of the acquisition, the corresponding noise-voltage is about 2.2 mV. In order to overcome the noise, a signal cut is decided to be 24 ADC ($\sim$20 mV). This value is consistent with the trip point of our hysteresis comparator and ensures a signal to noise ratio larger than 5.

This measurement allows us to determine also the baseline voltage at the output of the shaper (i.e. the mean value in Fig. 5.2). The baseline level is required later to calculate the

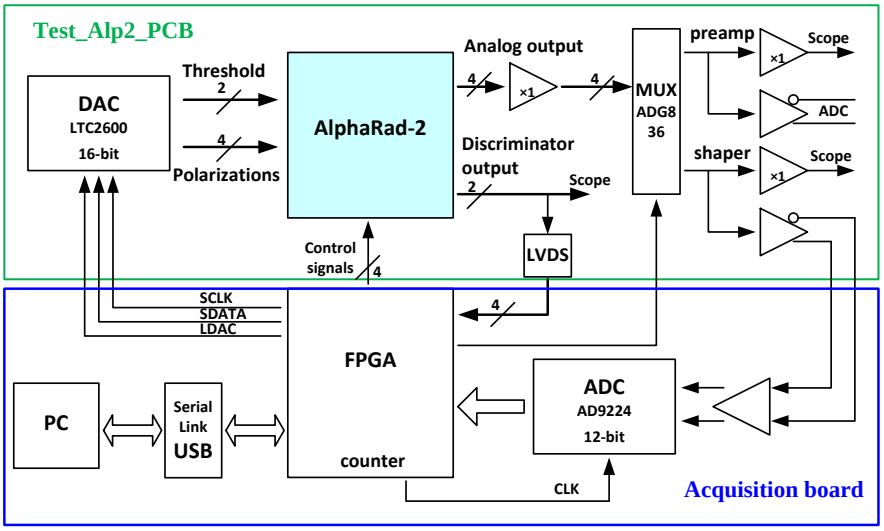

Figure 5.1: Diagram of the acquisition system for the analog signal analysis.

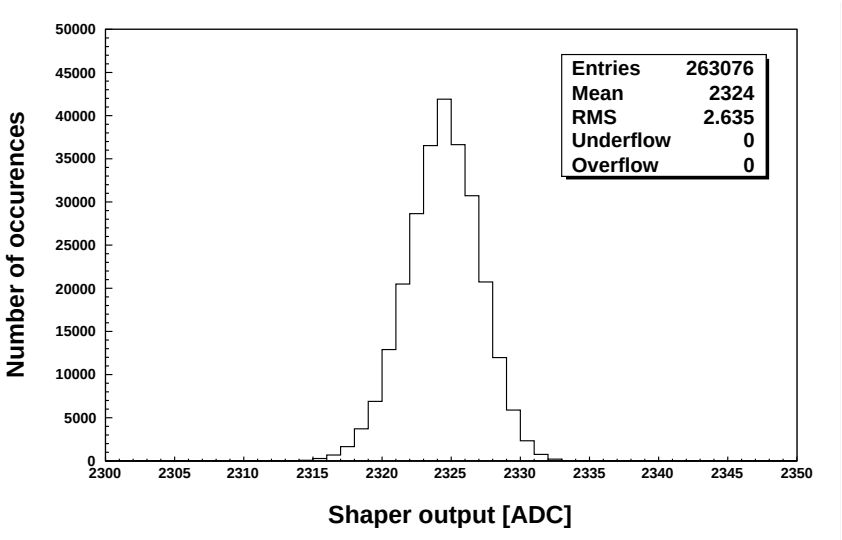

Figure 5.2: Signal distribution at the output of the shaper from the acquisition in the dark. The mean value represents the baseline, and the RMS is the total electronic noise.

signal amplitudes in the presence of a radiation source. As the sampling ADC digitalizes the absolute value of the output signal, the actual signal with respect to the detected charge equals the difference of the sampled ADC value and the baseline value.

In the following sections, we present the extensive measurements of the AlphaRad-2 to radioactive sources in detail. As the thinning down processing of our sensor was still in progress during the work in this chapter, we performed all the experiments with the standard sensors (which have an oxide layer, an epitaxial layer and a substrate layer).

5.2 Response to α-particles

Before the measurements to neutrons, we performed a series of experiments with an ^{241}Am source to calibrate the sensor in counting rate. In our experiments, the sensor is front-illuminated: the incident particles impinge onto the oxide layer.

5.2.1 Alpha source

This source with an activity of 22.3 kBq in 2π is constituted of americium powder deposited on a base of metal. It emits α-particles of energies 5388.26 keV (1.66%), 5442.86 keV (13.23%) and 5485.56 keV (84.45%). This isotope decays with a half life of 432.6 years as the following equation:

$$^{241}Am \rightarrow \alpha +^{237} Np$$

where ^{237}Np is not stable and decays into Pa, but with a much longer half life of 2.14×10^6 years. This source was chosen because its activity was well known. Moreover, it is emitting α particles ($E_\alpha \sim 5.5$ MeV), which are highly ionizing particles and therefore can be easily detected.

5.2.2 SRIM simulations

Due to the distance from the source to the sensor, the α particles loose some energy in the air before they impinge onto the sensor. After that, they have to pass through the oxide layer and then reach the epitaxial layer (sensitive volume) of the sensor. The strong absorption in the air and in the oxide layer means that the α particles enter the epitaxial layer with an energy lower than their original ones. The energy of the incident α particles entering the epitaxial layer depends on the thicknesses of the air layer (i.e. sensor-source distance) and the oxide layer. According to the AMS process (which is used in the AlphaRad-2), the oxide layer is typically 5.7±1.7 µm. To understand the travel range of α-particles in our sensor, the simulations with SRIM (The Stopping and Range of Ions in Matter) [1] have been carried out. In the simulations, a structure with a 5 µm-thick SiO_2, a 14 µm-thick epitaxial layer and a 11 µm-thick substrate was used, and the 5.5 MeV α-particles come from the front of the sensor with a 0° impact angle. Figure 5.3 shows the ranges of the incident α particles in the simulated structure with four

working distances, which are 1.0, 1.5, 2.5 and 3.0 cm. For the distance of 1 cm, the α particle entering the epitaxial layer did not lose enough energy to be completely stopped in this layer. For the last three distances, the α particles don't have enough energy to cross the epitaxial region and therefore deposit all their remaining energy there. We remind that the substrate thickness of the AlphaRad-2 is around 700 µm. This means that for any simulated distance the impact α particles cannot cross the complete sensor and will stopped inside the silicon volume. Increasing in the distance, the energy lost in the air and the oxide is certainly increased, therefore, the average deposited energy decreases. Both the energies deposited in the epitaxial layer and in the substrate contribute to the detected signals (see Chapter 3, § 3.2.5.2). We should notice that, for the distance of 3 cm, the Bragg peak of the incident α particle is located very close to the oxide layer (in the case of 5 µm oxide layer).

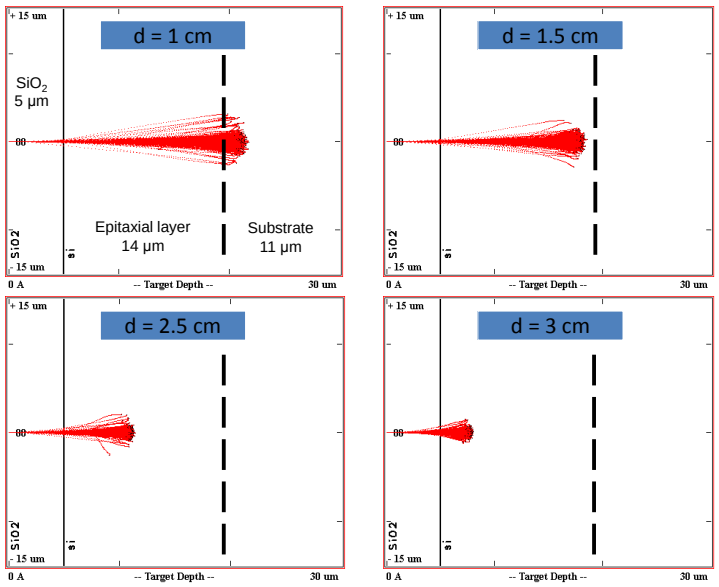

Figure 5.3: Ranges of the 5.5 MeV α-particles traveling in the CMOS sensor simulated by SRIM for four sensor-source distances.

5.2.3 Experimental setup and results

The experimental setup is shown in pictures 5.4(a) with the metal barrel which contains the ^{241}Am source and the sensor, and 5.4(b) for the base plate on which the source and the sensor are mounted, allowing adjustment of the distance with an accuracy of 0.1 cm.

The measurements have been performed at several distances from the source. Figure 5.5 shows the distributions of the detected charge (in ADC) obtained for an exposure of 2 minutes at the selected working distances: 1.0, 1.5, 2.5, and 2.8 cm. We observe that the average detected charge (which is proportional to the average deposited energy) decreases with the distance. This

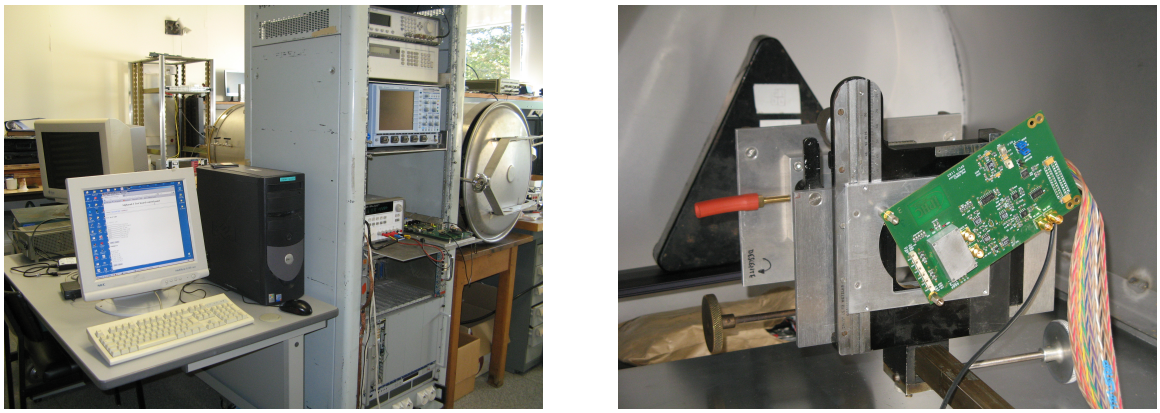

(a) (b)

Figure 5.4: Photos of the experimental setup: (a) overall view of the setup, showing the barrel containing the source and the sensor, mother-board, power supply and controlled computer; (b) inside of the barrel, showing the base plate holding the source and the AlphaRad-2 test board.

is in good agreement with the simulation results. The simulation shows that for the distance of 3 cm some energy is deposited in the first 3 µm of the epi-layer (where the charge signal is generated). However, we found no observed counts in the experiment at this distance of 3 cm. We attribute this phenomenon to the edge effect of the detector and an oxide layer which is in fact thicker than 5 µm (the value used in the simulation).

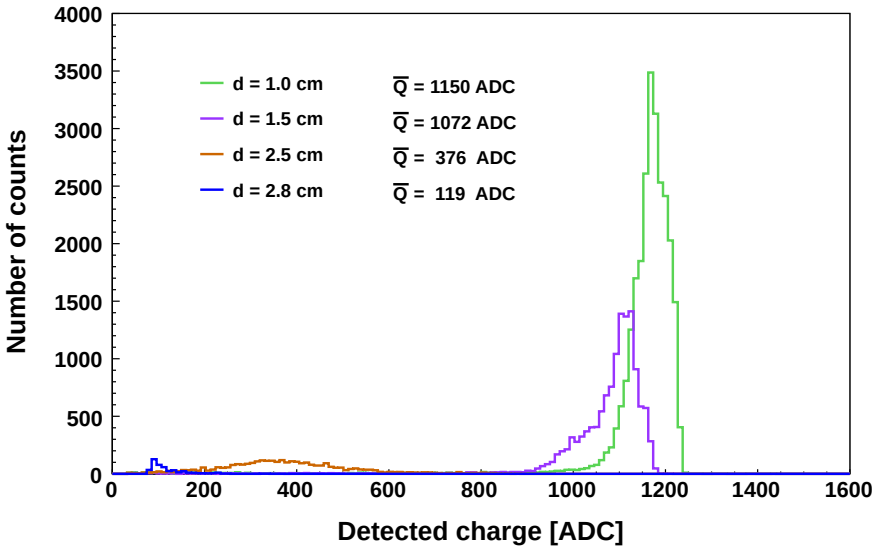

Figure 5.5: Distributions of the detected charge obtained for an exposure of 2 minutes with the ^{241}Am source at the four working distances.

Figure 5.6 illustrates the measured counting rate versus geometric calculation as a function of the source-sensor distances. The vertical error bars correspond to the statistical uncertainty,

while the horizontal error bars are due to the uncertainty of the distance. The solid angle of detection can be defined as

$$\Delta\Omega = \frac{S}{d^2} \tag{5.1}$$

where S is the sensitive area, and d is the sensor-source distance. The fluence of incident particles being proportional to the solid angle, the number of detected events will also be proportional to $1/\mathrm{d}^2$. Figure 5.6 indicates that the measurement result coincides with the calculation for distances less than 2.5 cm. The deviation in the longest distances ($d > 2.5$ cm) is probably due to the oxide layer of the sensor larger than 5 µm. In this case, the Bragg peak of the impact alpha particle may be located in the oxide layer. The effect of the SiO^2 layer on the protons will be seen too (in § 5.4.2.3).

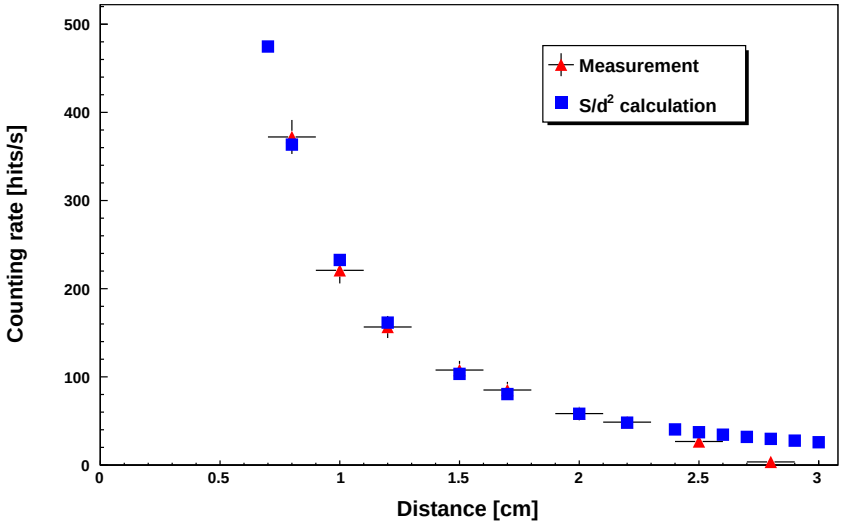

Figure 5.6: Counting rate of the ^{241}Am α-measurements versus geometric calculation as a function of the source-sensor distances [2].

5.3 Response to 622 keV photons

In the next paragraph, the AlphaRad-2 chip will be exposed to a mixed n/γ source. In order to test our device in a pure photon field, we used a ^{137}Cs source of 163 kBq activity, which was checked at the RaMsEs group with less than 3% uncertainty. The measurement was performed at fixed distance (d = 1 cm), in the dark, adding or removing an aluminium screen to shield against X ray background.

The 662 keV energy photons is important for us, because these photoelectrons are more impinging than the ones generated by 4.4 MeV photons (see § 5.4.2.2) and therefore, these electrons represent the most critical background for the protons we aim to detect. Moreover, the direct conversion of 600 keV photons in 10 µm silicon (epitaxial layer) happens with an

efficiency of 2×10^{-4} [3]. Even worse, we have a photoelectron conversion efficiency of 5×10^{-3} in a 500 µm-thick polyethylene, which is to be compared directly to the conversion rate of (n,p).

Figure 5.7 gives the detected charge distributions for the two configurations (with and without the aluminium foil). The charge difference is clearly visible, with the drastic decrease in the number of counted photons. At 1 cm distance, we detected 0.234 hits/s with the aluminium shielded sensor. With this counting rate, the detection efficiency to photons is calculated to be $(2.75 \pm 0.05) \times 10^{-4}$.

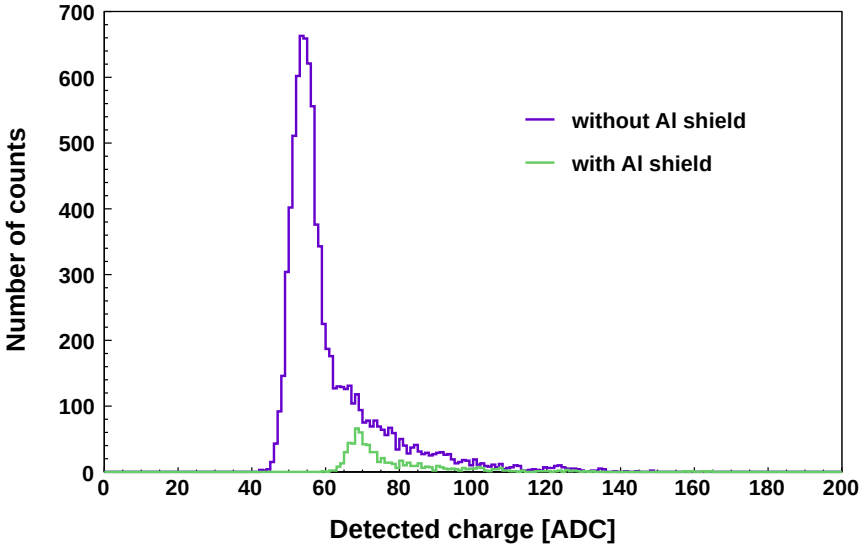

Figure 5.7: Measured charge distributions with and without the aluminium shield for a 50 minutes exposure at 1 cm from the ^{137}Cs source.

This test allows us to locate the distributions of photoelectrons relative to those of protons. We can see that the working cut (determined in the next section § 5.4), will be extremely efficient to remove most of this photon background.

5.4 Measurements with mixed n/γ fields

We study in this section the most important feature of the device, its sensitivity to mixed n/γ fields, aiming at determining a threshold for γ-rejection. In this work, two ^{241}AmBe sources (one is provided by the IPHC, Strasbourg, and the other is in the LMDN/IRSN, Cadarache) for fast neutrons have been used. As already stated, our sensor needs to be thinned down in order to detect thermal neutrons. The post-processing (thinning down) of AlphaRad-2 is under way, and the experiments with thermal neutrons will be performed in the future with the californium source moderated with heavy water (Cf+D_2O) on the Van Gogh irradiator at the IRSN. The spectra of the fast and thermal neutron sources are given in Fig. 5.8.

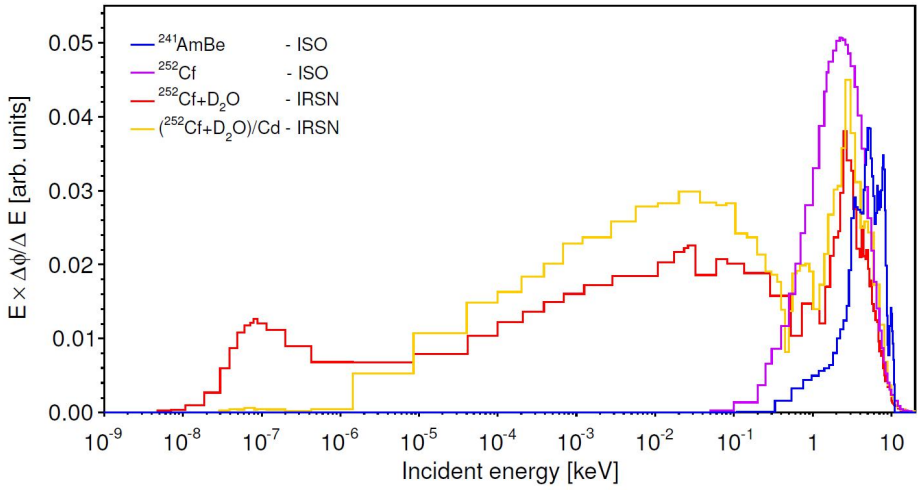

Figure 5.8: Spectra of the neutron sources at the IRSN.

5.4.1 Converter

In the study with MIMOSA-5, the polyethylene $(CH_2)_n$ converter (1 mm thick) was used for the detection of fast neutrons in order to benefit from the high (n,p) elastic scattering cross-section ($>$ 1 b below 10 MeV). The MCNPX simulations had indicated that the proton equilibrium is reached around 900 µm for the AmBe (see Chapter 2, § 2.3.1.3), but the optimal thickness had not been proved by experiments in the case of MIMOSA-5. In this work, we have done the experiments with 5 different thicknesses (from 0.2 mm to 3.0 mm) of the converter.

5.4.2 Measurements with ^{241}AmBe on the Van Gogh irradiator

5.4.2.1 Van Gogh irradiator

The irradiator Van Gogh of the IRSN (Cadarache), as shown in Fig. 5.9, uses two types of neutron sources: a ^{241}AmBe source and a ^{252}Cf source. When they are not used they are kept in a polyethylene container at the bottom of the irradiator. The sources are located at a height of 3.2 m to limit the background noise due to neutron scattering by the ground. The sources are brought into position for irradiation by compressed air in a guide tube. A motorized calibration setup allows to place the instruments at different distances from the source. We have performed experiments at two different distances: 75 cm and 20 cm. The latter is chosen to achieve usable statistics during a short irradiation time (around 6 hours). The ^{241}AmBe source activity is 10 Ci (370 GBq) and the fluence rate is 528 cm^{-2}s^{-1} with an uncertainty of 4.2% at the distance of 75 cm (the distance recommended by the IRSN is 75 cm, where we have the first numbers, with metrological certification).

Figure 5.9: Photo of the Van Gogh irradiator [4].

5.4.2.2 Response to MeV photons

It is well known that AmBe sources emit also γ-rays of 4.438 MeV with a γ/n ratio of 0.57. To check the response of the AlphaRad-2 to the pure photons, we have performed measurements with aluminium shielding for a 310-min exposure at 20 cm from the source. Figure 5.10 shows the charge distributions for the two thicknesses of the aluminium foils (without polyethylene converter). We observe a single population of particles peaked at low charge. It demonstrates that the Compton electrons are generated by MeV photons inside the aluminium, without attenuation for a 2.0 mm thick screen. These spectra fit very well to the pure photon signal obtained previously with the ^{137}Cs source.

5.4.2.3 Response to the mixed n/γ

To detect fast neutrons, we need a hydrogen-rich polyethylene converter to generate recoil protons. We performed a measurement with a 500 µm $(CH_2)_n$ at 20 cm from the source. Figure 5.11 shows the charge distribution measured with a 140-min exposure. Like for the measurement with MIMOSA-5 (see Chapter 2, Fig. 2.15), we observe again two populations of particles: one peaked at low charge and the other at higher values. The lower population corresponding to electrons generated by 4.438 MeV γ-rays has the same peaked value as the photoelectrons in Fig. 5.10. The higher population coming from the recoil protons from the converter has a large spreading. This spread is due to the fact that the charge transport mechanism in our sensor results in incomplete charge collection. The measurement with MIMOSA-5 was performed with a thinned down sensor in the back-illuminated way: the incident particles impinge on the epi-layer through the very thin (∼160 nm) SiO_2 layer. While in the case of AlphaRad-2, the experiments

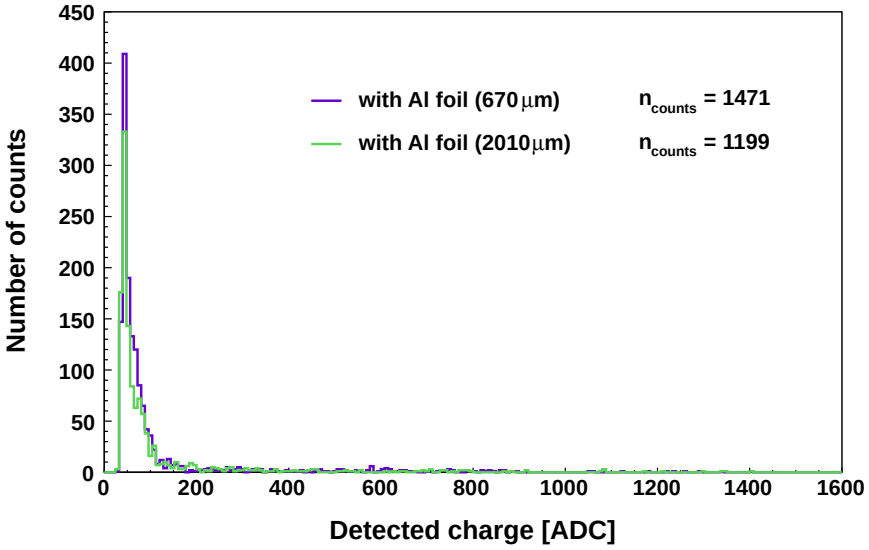

Figure 5.10: Distributions of the detected charge for a 310-min exposure at 20 cm from the ^{241}AmBe source with two aluminium foils (670 and 2010 µm thick).

are performed with a standard sensor in the front-illuminated way: the recoil protons have to cross the much thicker (> 5 µm) SiO_2 layer and four metal layers before they create the charge signal in the sensor. As they loose part of their energy in the oxide layer, the deposited energy of the protons in the epitaxial and the substrate layer may be reduced, and therefore the population of recoil protons shifts to a lower charge. Whereas the photoelectron component does not shift because the photons loose their energy in a single event (photo conversion). This explains the observed differences in signal overlap of the two sensor: compared to the n/γ response with MIMOSA-5, the result with AlphaRad-2 shows a larger overlap.

Material	Weight (mg)	% N	% C	% H	% S	% O
Graphite	1.0673	1.92	91.08	2.45	0.00	4.55
	1.0130	1.93	91.23	2.48	0.00	4.36
Polyethylene	0.9790	0.00	85.66	14.56	0.00	0.00
	0.9363	0.00	85.71	14.59	0.00	0.00

Table 5.1: Elemental analysis results of the graphite and polyethylene converters.

Effect of the $(CH_2)_n$ converter We should notice that the polyethylene converter is the source of photoelectrons. To verify the effect of the $(CH_2)_n$ converter, we have carried out an experiment with a graphite foil. The graphite is ideal because it partially equivalent to polyethylene. The comparison of the experiments for the 310-min exposure at 20 cm from source with a 670 µm graphite foil and with a 500 µm polyethylene converter is illustrated in Fig. 5.12. It indicates that the carbon generates some photoelectrons (the polyethylene will also generate).

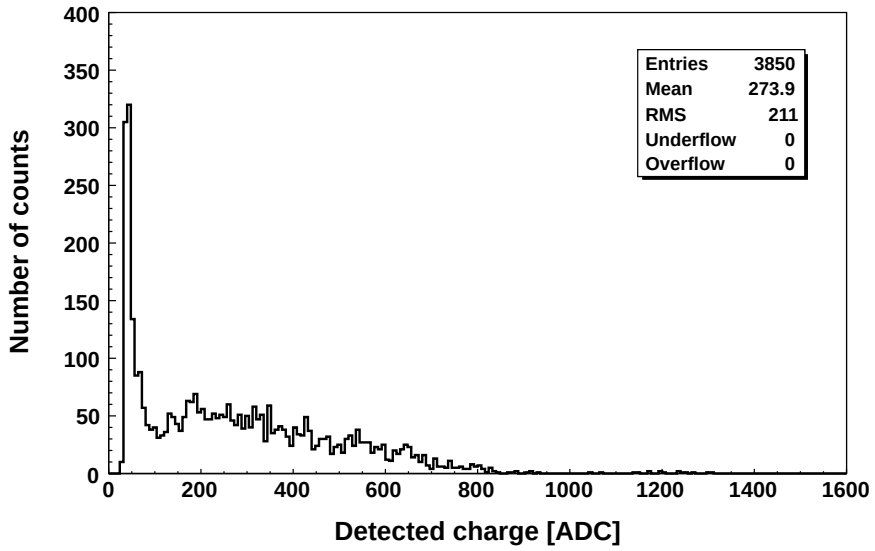

Figure 5.11: Measured charge distribution for a 140-min exposure at 20 cm from the ^{241}AmBe source.

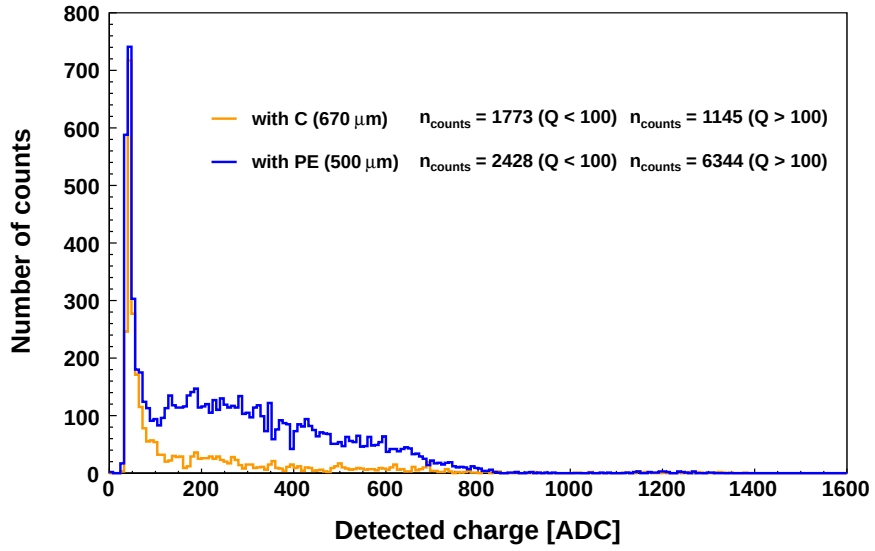

Figure 5.12: Distributions of the detected charge for a 310-min exposure at 20 cm from the ^{241}AmBe source with two converters: a graphite foil (C) and a polyethylene (PE) converter.

More unexpected, we observe some proton signals in higher charge. This may be explained by the fact that our graphite foil seems to contain some hydrogen according to IR absorption surface binding analysis. To qualify our graphite and polyethylene converters, we ordered an elemental analysis (for elements: Carbon, Hydrogen, Oxygen, Nitrogen and Sulfur) in the ICS (Institut Charles Sadron) research center. For each material two samples had been analyzed. The analysis results are presented in Table 5.1. We found that the graphite foil contains indeed some hydrogen, which generates recoil protons. In order to compare the proton signals associated with the graphite and the polyethylene converters, we applied a charge cut at 100 ADC to remove the electron noise (the purity of signal will be discussed in the following subsection). As shown in Fig. 5.12, the numbers of protons in the case of graphite and polyethylene converters are 1145 and 6344 respectively, resulting a ratio of 0.18. This value is consistent with the ratio of hydrogen in the two converters of 0.17.

Fitting of the distribution As the photoelectron signal overlaps the proton distribution, we have to choose an ADC threshold to remove γ-background, but this will also remove a part of the protons. To evaluate the amount of the overlap, we fitted the two populations with the same method used in the MIMOSA-5 study. A Landau convoluted with Gaussian fit has been performed on the charge distribution of protons. The Landau part describes the fluctuations in the energy loss of a charged particle passing through a thin layer of matter, and the Gaussian part describes the additional stochastic phenomena, i.e. incident energy of the neutron, initial position and emission angle of the recoil protons, as well as carrier diffusion inside the silicon. Each recoil proton has a different energy and is emitted with different direction. Therefore, they deposit different amount of energy in the sensor when they pass through. For the population of photoelectrons, an exponential function is used to fit the upper part of the distribution. The two fits have been performed with determined start parameters and with maximum likelihood estimation. Figure 5.13 presents the fitting results, and the fit parameters are given in Table 5.2.

Model	Parameter	Description	Value
Gaussian	N_L	Normalization constant	$(7.12 \pm 0.08).10^4$
	σ_g	Width (sigma) of convoluted Gaussian	40.0 ± 12.6
Landau	MPV	Most probable value	197.2 ± 4.4
	σ_l	Width (scale) of Landau density	99.5 ± 2.0
Exponential	N_{exp}	Normalization constant	8.2 ± 0.1
	a	Fall factor	$(4.4 \pm 0.2).10^{-2}$

Table 5.2: Fitting parameters for the charge distribution with the AmBe source (Fig. 5.13).

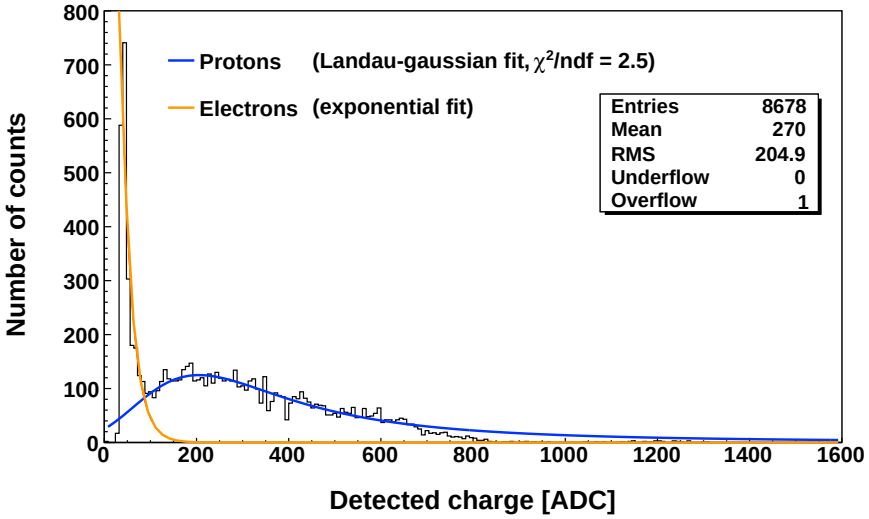

Figure 5.13: Distributions of the detected charge for a 310-min exposure at 20 cm from the ^{241}AmBe source. The two fitting functions are presented: the Landau-gaussian (in blue) for proton distribution and the exponential (in orange) for electron distribution.

ADC threshold	Q > 40	Q > 60	Q > 80	Q > 90	Q > 100	Q > 120	Q > 150
ε_{rel}	1.25	1.08	0.98	0.95	0.94	0.89	0.84
Purity	78%	89%	96%	97%	98%	99%	100%

Table 5.3: The relative efficiencies and signal purities for different applied ADC charge cuts.

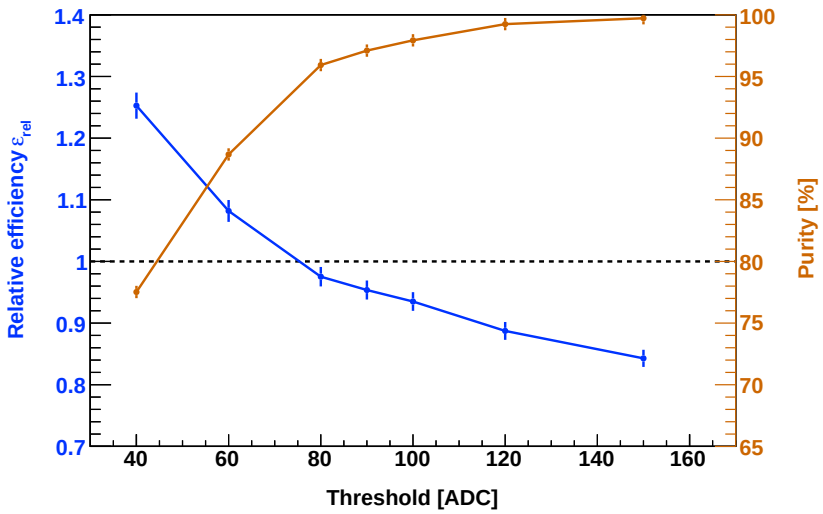

Figure 5.14: The relative efficiency and the purity of signal as a function of charge cut (only statistical uncertainty is included in the error bars).

Signal purity analysis Ideally, a simple cut on the distribution could maximize the number of real protons by suppressing the photo-background. Several cuts in ADC charge on the signal have been applied to achieve n/γ discrimination. For each cut, the number of lost protons and the number of electrons which contaminate the proton signal are determined by extrapolation from the two fitting functions. The relative detection efficiency of the sensor is defined as $\varepsilon_{rel} = n_c/n_p$, where n_c is the number of counts for a given threshold, and n_p is the total number of recoil protons. We define the unknown number of protons as $n_p = (n_c - n_e) + n_{p,lost}$, where n_e is the number of photoelectrons above the threshold, and $n_{p,lost}$ is the number of lost protons due to the cut applied. This definition of ε_{rel} means that apparent values above 100% are possible. In the calculations, the numbers of detected protons (or electrons) is the integral of the corresponding fit. Clearly, a low threshold will maximize the signal but alow higher contamination from photoelectrons. The purity of signal is defined as $p = 1 - (n_e/n_c)$. Table 5.3 summarizes the values of relative efficiency and purity of signal for each cut, and they are illustrated in Fig. 5.14. Values of ε_{rel} above 1 imply a certain contamination inside the proton distribution, whereas those below 1 correspond to a loss of proton signal. On the other hand, the threshold must be increased to obtain a purity close to 100%, resulting in a relative detection efficiency less than 1.

The overlap study allows us to determine the best threshold for the n/γ discrimination: a good compromise is to chose the cut at 80 ADC, which gives a high relative efficiency of 0.98 together with a good signal purity ($> 95\%$). The obtained discrimination is slightly worse than for the MIMOSA-5 study (see Chapter 2, § 2.3.3.2), essentially because of edge effects (the AlphaRad-2 sensor is in effect ten times smaller than the MIMOSA-5). One should notice that the chosen threshold of 80 ADC is not an absolute value but obtained for the mixed field with γ/n ration of 0.57.

The intrinsic detection efficiency The intrinsic detection efficiency of the sensor is defined as $\varepsilon_{int} = n_p/n_{int}$ where n_p is the number of counted recoil protons and n_{int} is the number of the incident neutrons impinging on the sensor. This efficiency is independent of the solid angle. Using the threshold of 80 ADC, the intrinsic efficiency of the AlphaRad-2 at the working distance of 20 cm is $\varepsilon_{int,d20} = (7.23 \pm 0.32) \times 10^{-4}$. This efficiency is independent of incident neutrons on the detector. The uncertainty includes the statistical uncertainty and the systematic uncertainty on the activity of the source (the detailed calculation of detection efficiency and its uncertainty are in Appendix B).

We have also exposed our sensor to the AmBe source at the recommended distance of 75 cm. The measured result has been analyzed in the same way (distribution fitting and purity analysis) as used for the measurement at 20 cm. In order to compare the charge distribution at the two distances (20 and 75 cm), the two spectra are normalized by the associated exposure time. We scale the distribution for 75 cm by a factor of $(\frac{75}{20})^2$ (solid angle law), and the two distributions are very close, as shown in Fig. 5.15. Using again the charge cut of 80 ADC to remove photoelectrons,

we obtain the intrinsic detection efficiency $\varepsilon_{int,d75} = (7.18 \pm 0.35) \times 10^{-4}$, being in a good agreement with the efficiency at 20 cm. For point like sources, a dosemeter should provide a constant detection efficiency for different source-sensor distances (converted from the $1/d^2$ effect) for point like sources. More measurements will be performed to verify this feature in the following subsection with the AmBe source at IPHC (see § 5.4.4).

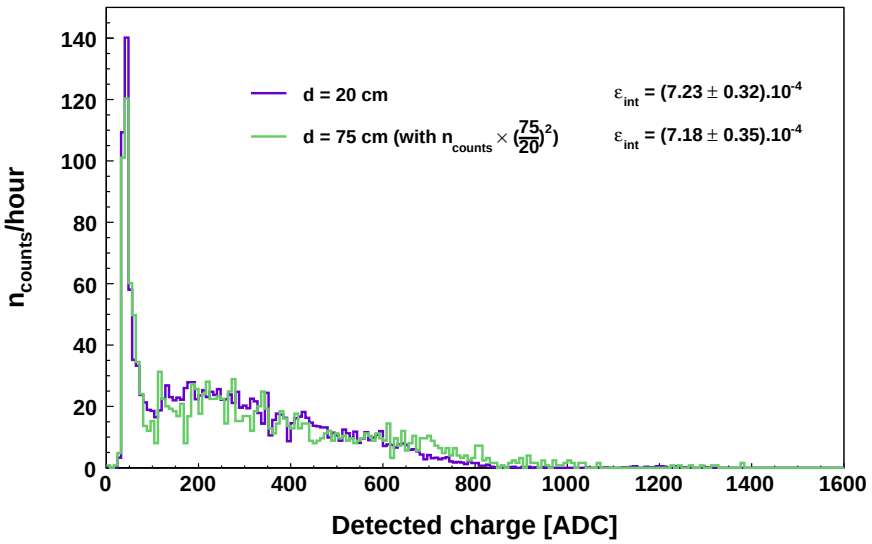

Figure 5.15: Normalized charge distributions measured at the distance of 20 cm and 75 cm from the AmBe source on the Van Gogh irradiator.

The linearity One of the other essential properties of a dosemeter is the linear response. We exposed our device at 20 cm from the IRSN AmBe source for 5.7 hours. We divide the maximum exposure time into ten equidistant points corresponding to different number of incident neutrons, and for each point we calculate the number of detected neutrons by applying the predetermined cutoff at 80 ADC. The fluence-dose relationship for neutrons is defined by international conventions. In the 1 MeV region, it is of about 416 pSv·cm^2 for both the ambient dose equivalent $H^*(10)$ and the personal dose equivalent $H_p(10, 0°)$, following the ICRP report 74 [5]. The number of detected neutrons as a function of dose is illustrated in Fig. 5.16, showing a good linearity and no saturation to be observed until a cumulated dose of 70 mSv (10^7 incident neutrons).

5.4.3 Measurements with ^{241}AmBe at IPHC

We have also performed experiments with the ^{241}AmBe source at IPHC. This source was used for the MIMOSA-5 (see Chapter 2, § 2.3.3). Its neutron flux is $(2.24 \pm 0.10) \times 10^6$ s^{-1}. This source is located in an AmBe local irradiation (calibrator) that contains a system for automatic control of the release and retraction of the remote source (without risk of unnecessary exposure to the user). When not used it is stored in a polyethylene cube, which absorbs all the neutron

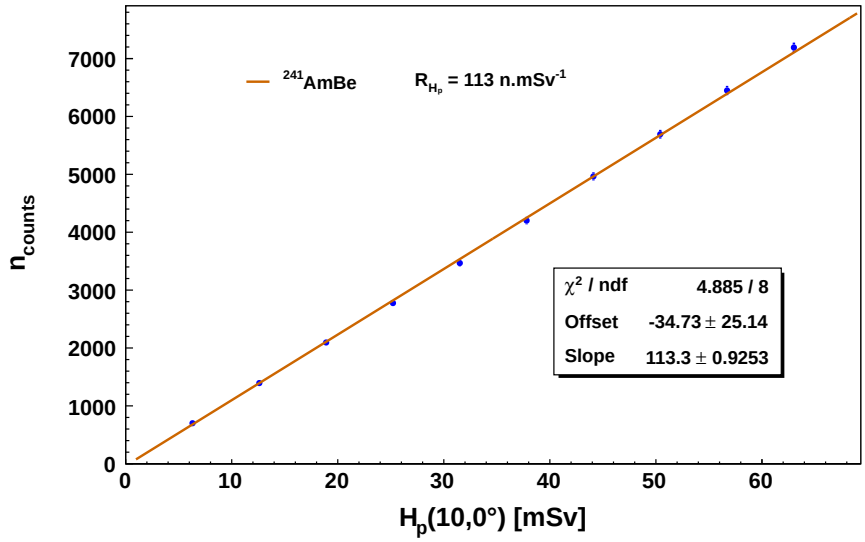

Figure 5.16: Dose response function of AlphaRad-2 measured with the AmBe source at the IRSN (10 Ci activity).

radiation. Its geometry and dimensions are given in Fig. 5.17.

The americium dioxide powder is sealed in a lead cup which absorbs the low energy γ-rays from ^{241}Am (up to 59 keV) and the α particles produced by this same americium. The thickness of lead (about 3 mm) is not sufficient to absorb the γ-rays of 4.438 MeV emitted from the excitation of ^{13}C. This AmBe source is therefore a mixed n/γ source, which can be used to test the sensitivity to photons of the AlphaRad-2 and its ability to discriminate the two radiations.

The measurements at IPHC allow us to compare our results obtained with the Van Gogh irradiator. Moreover, the tests at different working distances have been carried out to verify that the detection efficiency is constant with distance. The influence of the thickness of the converter has also been measured with this source. The experimental setup is presented in Fig. 5.18.

5.4.3.1 Influence of the converter thickness on the detection efficiency

The conversion efficiency as a function of the converter thickness had been simulated in the study of MIMOSA-5. In this work, we have performed tests concerning the influence of the converter thickness on the detection efficiency. The measurements during 21 hours were carried out with the AmBe source of IPHC for the five thicknesses: 0.2, 0.5, 1.0, 1.5 and 3.0 mm. A short distance of 8.2 cm was chosen due to the ten times lower activity of the IPHC source (1 Ci) than the source on the Van Gogh irradiator. The normalized charge distributions for the five cases are presented in Fig. 5.19.

Figure 5.20 shows the dependance of the detection efficiency to the polyethylene converter thickness. For the converter thickness less than 1 mm, the detection efficiency increases with the thickness. The response becomes approximately constant at 1 mm, which indicates that the

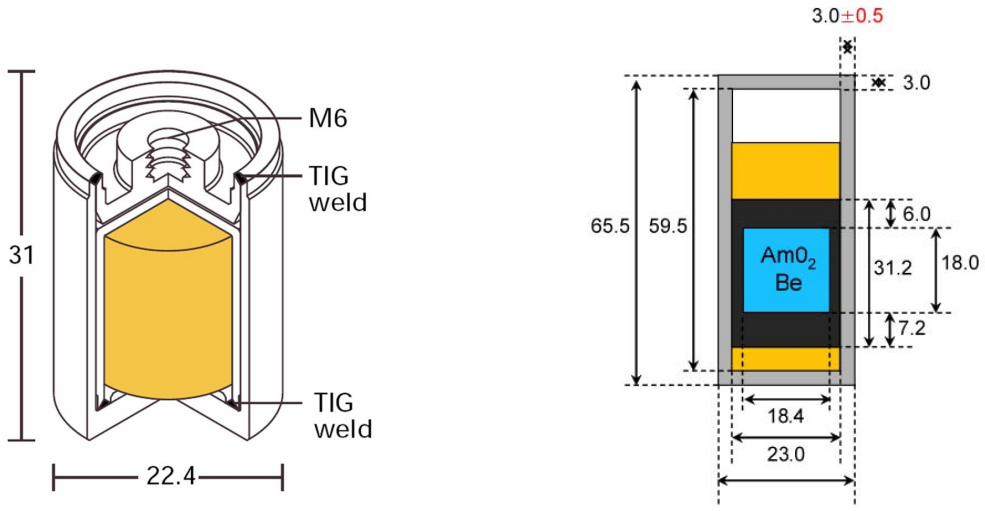

(a) (b)

Figure 5.17: Schematics of the ^{241}AmBe source at IPHC, showing (a) geometry, (b) dimensions of the source (the values are given in mm) [3].

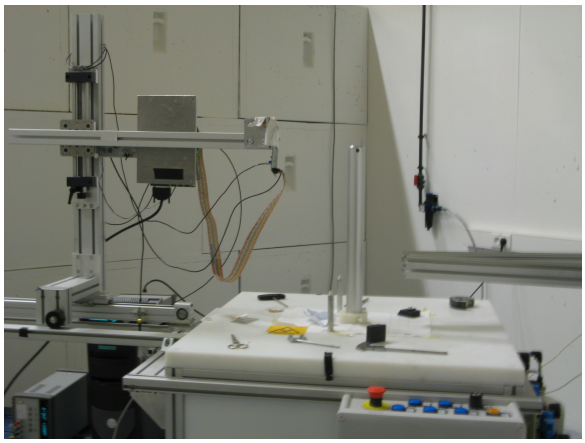

Figure 5.18: Photo of the experimental setup for the measurements with the AmBe source at IPHC.

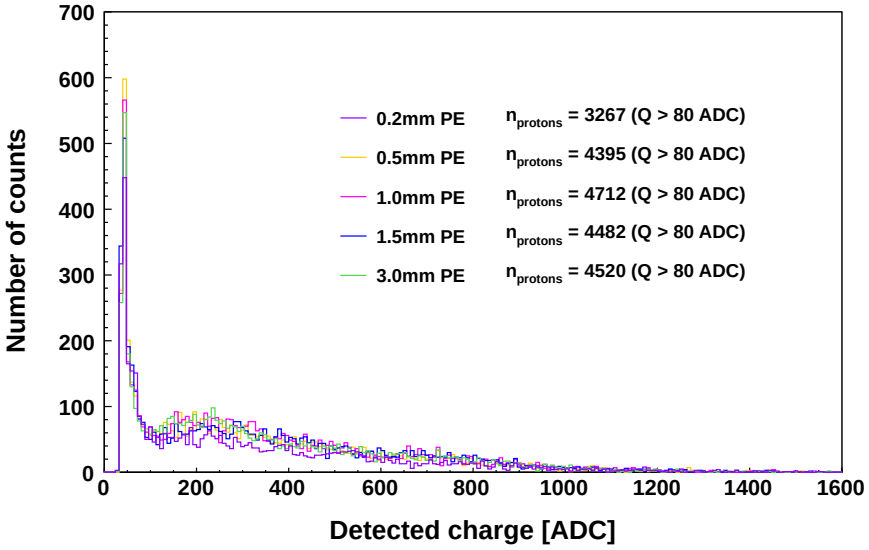

Figure 5.19: Measured charge distributions for different polyethylene converter thicknesses during the 21 hours exposure at 8.2 cm from the AmBe source at IPHC.

proton equilibrium is reached. This result is consistent with what we observed in the simulation result of the previous study (see Chapter 2, Fig. 2.12). On Fig. 5.20, we didn't represent the quite large uncertainty on the thickness of the polyethylene foil (large dispersions of 20% indicated by the manufacturer).

5.4.4 Efficiency versus the distance

For a future dosemeter, as a worker rarely remains motionless, it is important to have a system with a constant intrinsic detection efficiency (converted from the solid angle law) as a function of distance from the point like source. We performed a set of measurements with the AmBe source at IPHC. According to the converter thickness study in the previous subsection, a 1 mm-thick polyethylene converter was used in the experiments to benefit from the proton equilibrium. Figure 5.21 presents the charge distributions for the five distances. The five spectra were normalized by their respective exposure time in order to be readable.

Applying again the 80 ADC charge cut for the γ-rejection, we calculate the normalized detection efficiencies for each distance, as shown in Fig. 5.22. It demonstrates that the response of the AlphaRad-2 remains constant with the distance.

5.5 Discussion of the sensitivity

The last discussion of the quality of the dosemeter addresses the sensitivity. As the maximal allowed dose for workers is of 20 mSv a year, any type of dosemeter has to be sensitive to very low doses, at the level of fractions of mSv. On the other hand, the linearity of the device has

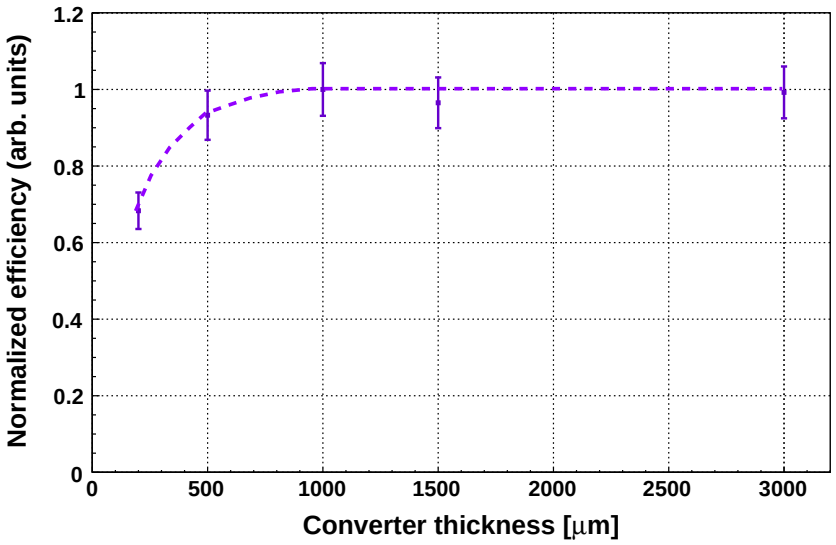

Figure 5.20: Dependance of the detection efficiency to the polyethylene converter thickness measured at 8.2 cm from the IPHC AmBe source.

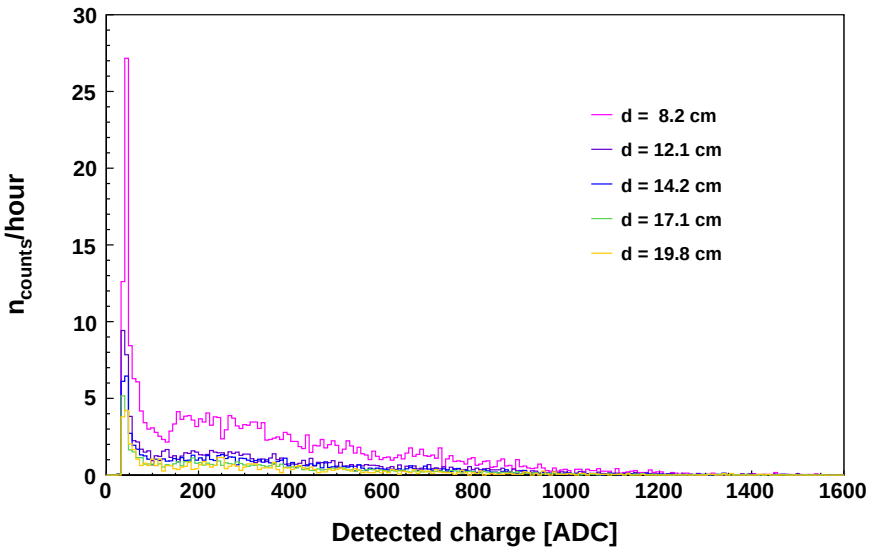

Figure 5.21: Measured charge distributions (normalized by their respective exposure time) for different distances from the AmBe source at IPHC.

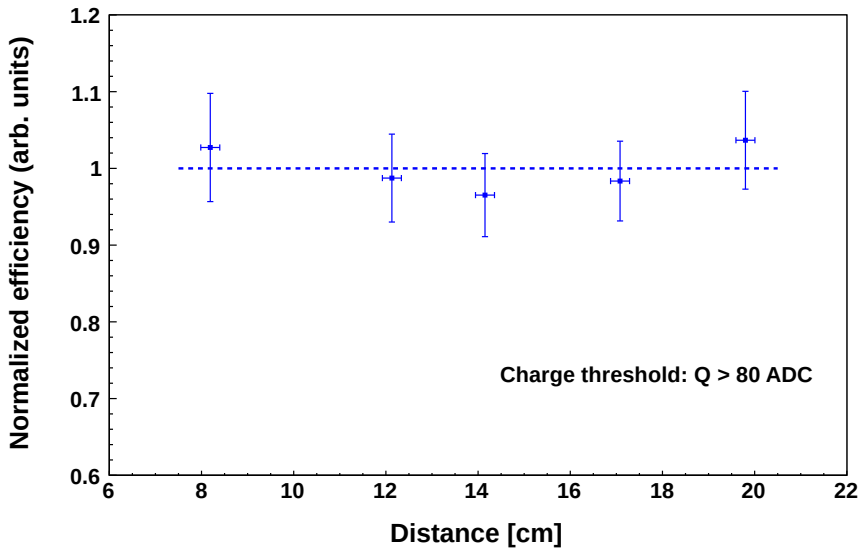

Figure 5.22: Distance dependance of the intrinsic detection efficiency measured with the AmBe source at IPHC.

to extend over the highest possible dynamic range, up to a maximal recordable dose before saturation, this upper level ideally being much higher than the 20 mSv limit. In this section, we discuss the sensitivity of AlphaRad-2 concerning its lower and upper limits.

5.5.1 Lower limits

The minimal sensitivity of conventional dosemeters is often related to parasitic hits (radon or gamma background, physical "fog", parasitic electrical mode shots...). The AlphaRad-2 chip is poorly sensitive to radon, being shielded by the neutron converter, and also free of gamma contamination, both by construction (i.e. thin sensitive layer) and by an adjustable electronic cut. We can focus this discussion on fast neutrons (which have been effectively measured by our device) but the same line of reasoning is valid for slow neutrons.

Our device has a detecting sensitivity at the level of one single secondary charged particle (proton or alpha), which is a firm starting point. However, a reasonable definition for a valid measurement should rely on, at least, 10 recorded hits (protons), allowing a statistical dispersion of about 30%. Taking our detection efficiency of 7.24×10^{-4}, these 10 recordings correspond to 1.38×10^{4} neutrons unambiguously detected in a single chip (of 6.55 mm^2 sensitive area). Converted into $H^*(10)$ or $H_p(10, 0°)$ (with the same method described in § 5.4.2.3), the minimal sensitivity is then of 90 µSv (with 30% uncertainty) for fast neutrons. As the sensor is small, one can easily equip a dosemeter with several independent chips. Using N chips in the dosemeter would lead to a resulting sensitivity (30% dispersion) of $90/N$ µSv.

For slow neutrons, we foresee a neutron-to-alpha conversion efficiency between 2 and 6 times higher, and because of a dose-fluence correspondence 50 times smaller in the 1 eV region, the

minimal sensitivity should be below 0.9 µSv (at 30%, and for $N = 1$).

As the device works on a counting mode, with no need of pre-processing or resetting, there is absolutely no concern about a minimal dose rate.

5.5.2 Upper limits

On the upper edge of the response function, any dosemeter faces limitations in maximal dose or maximal dose rate (or both). The maximal dose is often related to saturation phenomena due to the physics of the process of conversion.

Highest cumulated dose For electronic counters, there is, at first view, no highest limit on the measurable cumulated dose. The only existing limit is then the breakout of the device, if exposed to really damaging levels of radiation. For this technology, the damaging levels are in the range of some 10^{10} cm^{-2} and, for charged particles, more than 10 kGy. Obviously these numbers are such far above the allowed doses to human beings that, in practice, the question of highest measurable cumulative dose of this device, in the field of radioprotection for man, is irrelevant.

Highest dose rate Every type of electronic counter is defined by a count rate (typical or maximum), which is limited by construction or by dead time. Starting from the physical characteristic times for carriers dynamics and signal formation in a CMOS sensor, the AlphaRad-2 readout chain has been designed (for both noise and power optimization) with a readout cycle of 20 kHz. This important parameter sets the limit on dose rate, or the minimal time interval before significant pile-ups. As we already discussed in the previous chapter (see Chapter 4, § 4.5.2), if a sudden irradiation of 20 mSv occurs, our system will be able to measure it and to call for alarm in 2 minutes (in this case, the irradiated person has to stop working with radiations a full year after the accident). Clearly any type of passive dosemeter is unable to handle properly such an accident.

From this discussion, we conclude that an electronic device is really mandatory, and for our device, that the chosen readout frequency ensures a very good safety level for nuclear workers.

Bibliography

[1] J. F. Ziegler, J. P. Biersack, and M. D. Ziegler, *SRIM - The Stopping and Range of Ions in Matter*, SRIM-2008.04 ed., 2008. [Online]. Available: http://www.srim.org

[2] Y. Zhang, C. Hu-Guo, D. Husson, T.-D. Le, S. Higueret, and Y. Hu, "A High-Sensitivity Low-Power CMOS Sensor for a Future Neutron Personal Dosimeter," *Nuclear Science, IEEE Transactions on*, vol. 59, no. 4, pp. 1465 –1471, aug. 2012.

[3] M. Vanstalle, "Dosimétrie électronique et métrologie neutrons par capteur CMOS a pixels actifs," Ph.D. dissertation, Université de Strasbourg, Strasbourg, France, 2011.

[4] V. Gressier, "Les installations de l'IRSN dédiées à la métrologie des neutrons." IRSN/LMDN, Tech. Rep., 2005.

[5] ICRP, "ICRP publication 74: Conversion coefficients for use in radiological protection against external radiation," ICRP, International Commission on Radiological Protection, Technical Report Annals of the ICRP Volume 26 (3-4), 1996, Oxford, Pergamon Press.

Conclusions and perspectives

General conclusions

CMOS sensors offer theoretically promising characteristics for neutron detection and their applications to dosimetry. The RaMsEs group in IPHC is working on the development of a new compact device based on CMOS technology for operational neutron dosimetry. A previous study in our group had demonstrated that the CMOS technology is a promising candidate for future use in neutron dosimetry. The aim of this thesis was to develop a dedicated CMOS sensor for a future neutron electronic personal dosemeter.

Targeting on a portable integrated system, we proposed the AlphaRad-2 chip, which works on a counting mode providing a direct binary output. The AlphaRad-2 chip integrates the sensing part and the signal processing micro-circuit on the same silicon substrate. The sensing part is made of a micro-diode array of 32×32 n-well/p-epi diodes, with an inter-diode distance of 80 µm, leading to a sensitive area of 6.55 mm^2. The thousand diodes are connected in parallel with a single output for the whole matrix. This is motivated on one side by the aim to benefit from a large area with a moderate detector capacitance (∼pF) and low leakage current (< 1 pA), on the other side by the facts that the pixellization is unnecessary for n/γ separation and no spatial resolution is required in our application. In order to study the charge collection mechanism in diode matrices, and to optimize the collection efficiency and its time properties, we have performed device simulations through the Sentaurus-TCAD commercial package. The dimension of diodes and the inter-diode distance were chosen according to the compromise between the collection response and the total capacitance of the detector.

To fulfill the general requirements for APDs including high sensitivity, low power consumption, real-time readout, light weight, etc, we have tried to simplify the signal processing architecture to implement a compact device with low noise (which ensures a low detection level) and a very low power dissipation (< 1 mW). The AlphaRad-2 chip has been designed and fabricated in the AMS 0.35 µm CMOS OPTO process (with an epitaxial layer of ∼14 µm). The detector capacitance is of about 13 pF. Its readout circuit is composed of a CSA, a shaper, and a hysteresis comparator. This configuration allows us to maximize the SNR, and thus to increase the detecting sensitivity. By optimizing the component parameters, i.e. the input transistor of the CSA, the integration time, the shaping time, we demonstrate a SNR of about 80 (corresponding

to an ENC of 390 e^-) at the energy threshold of 100 keV. The counting rate of AlphaRad-2 is up to 20 kHz with a power consumption of 314 µW.

Our device has a detecting sensitivity at the level of one single secondary charge particle (proton or α). The experiments with the ^{241}Am source indicates a detection efficiency of close to 100%. Detector sensitivity to photons is also tested by exposing it to the ^{241}AmBe source on the Van Gogh irradiator in Cadarache. The detection of fast neutron (between 100 keV and 10 MeV) is possible by combining the AlphaRad-2 chip with polyethylene converters. The results are promising with a detection efficiency to fast neutrons of $\varepsilon_{exp} = (7.23 \pm 0.32) \times 10^{-4}$ obtained with a good purity of signal (the recoil protons produced by elastic scattering of neutrons on hydrogen nuclei take 95% of the total signal) by applying an appropriate cut-off. With this threshold, our device is able to discriminate neutrons from photons, and therefore is useful in a mixed n/γ field. To detect thermal neutrons, the AlphaRad-2 requires to be thinned down (for substrate removing), which is under way. We should note that the high cost of the thinning process and its complexity make the production of a sensitive detector to thermal neutrons complicated. This problem has to be resolved in order to develop a final dosemeter for both fast and thermal neutrons.

The effect of the thickness of the polyethylene converters on the proton equilibrium has also been studied. The experimental results indicate that a constant detection efficiency reaches at around 1 mm, which is in a good agreement with the MCNPX simulation. Moreover, experimental results have demonstrated that the intrinsic detection efficiency of our system remains constant with the distance to point like sources, which is another important feature for a future dosemeter.

Our device shows a good linearity and no saturation response up to a cumulated value of 70 mSv neutron dose. For the AlphaRad-2 chip, the counting rate of 20 kHz ensures a very good safety level for nuclear workers. For instance, if a sudden catastrophic irradiation at 20 mSv happens, our device is able to measure it and call for alarm within 2 minutes. The minimal sensitivity of our device is about 90 µSv (with 30% uncertainty) for fast neutrons.

Perspectives

The AlphaRad-2 chip, dedicated for a future personal neutron dosemeter, have demonstrated the feasibility to construct a portable device using CMOS technology. The simple configuration of the chip has been confirmed to be suitable for our application. Moreover, the first experiments with radiative sources, including fast neutrons, show promising results, leading to the design of an update version, AlphaRad-3 chip. The new prototype has been designed in spring of 2012 with the same architecture as AlphaRad-2 by our group in a specialized process (XO035 technology, X-FAB) for optoelectronic applications. The XO035 process provides optimized PIN (photo) diodes, which are interesting for neutron detection. The PIN diodes are constructed by the n-well and quasi p-well, but using lower doped epitaxial (10^{13} cm^{-3} compared to the 10^{15} cm^{-3} for

standard epitaxial layer) wafers. This results in a very fast charge collection. The most attractive feature for us is its open window above the PIN diodes, which allows the direct impinging of the secondary charged particle on the sensitive layer. It means no post-processing (thinning) needed to be able to detect thermal neutrons.

The AlphaRad-3 chip is under manufacturing and will be tested in the near future. At this stage, we assessed the designed properties of the core of a complete device. The future complete dosemeter will be made of four chips, on the same board (PCB) each one with its own converter, in order to cover the complete spectrum of neutron energies. This complete device has to be commissioned carefully, the remaining work including:

- simulations for the full device, including the chip, PCB, converters, phantoms, etc.;
- measurements in realistic neutron fields and tests with pure photons sources;
- various tests (angle, temperature, etc.).

Appendix A

Schematic of the test board for AlphaRad-2 chip

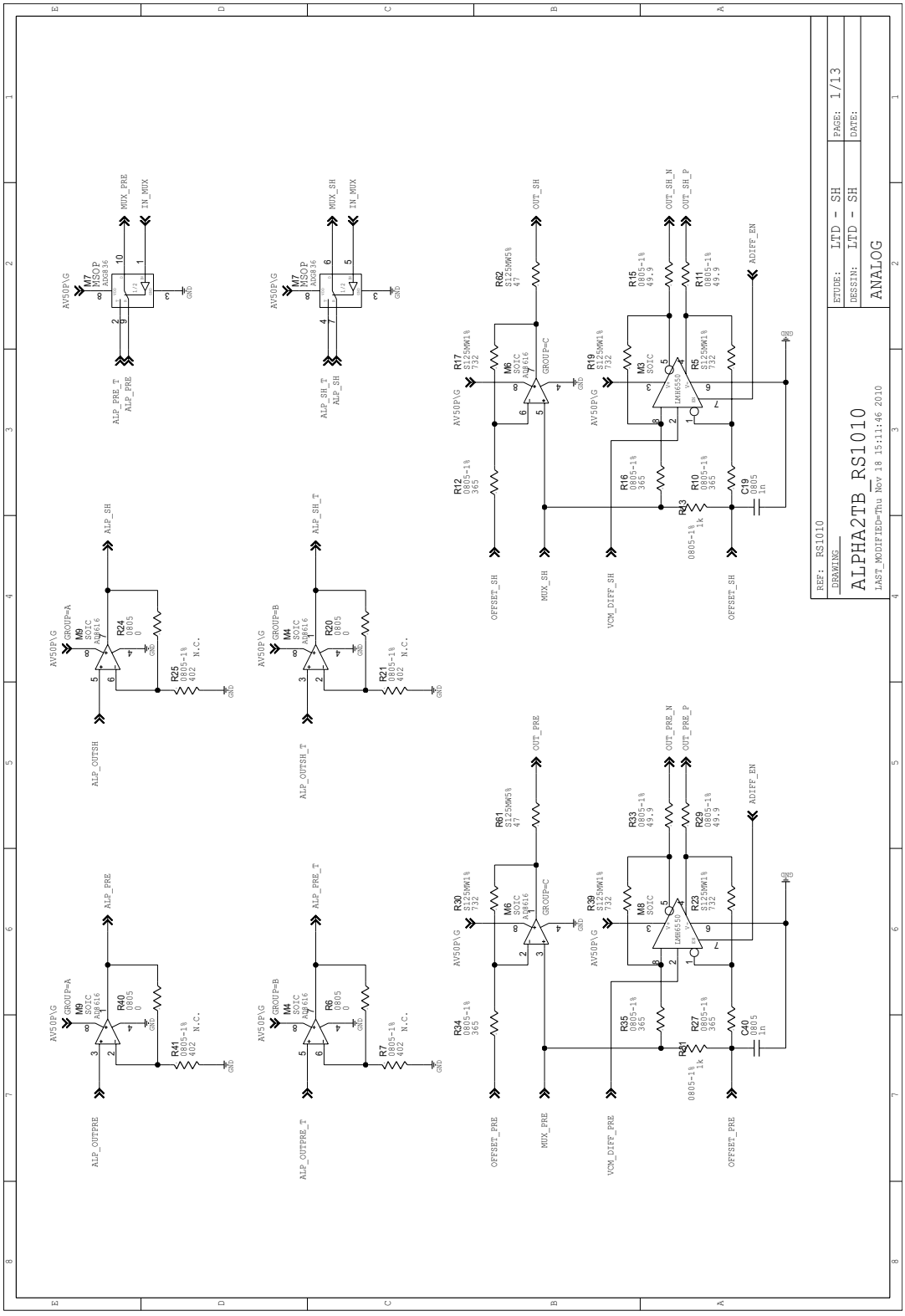

Figure A.1: First page of the schematic of the AlphaRad-2 test board.

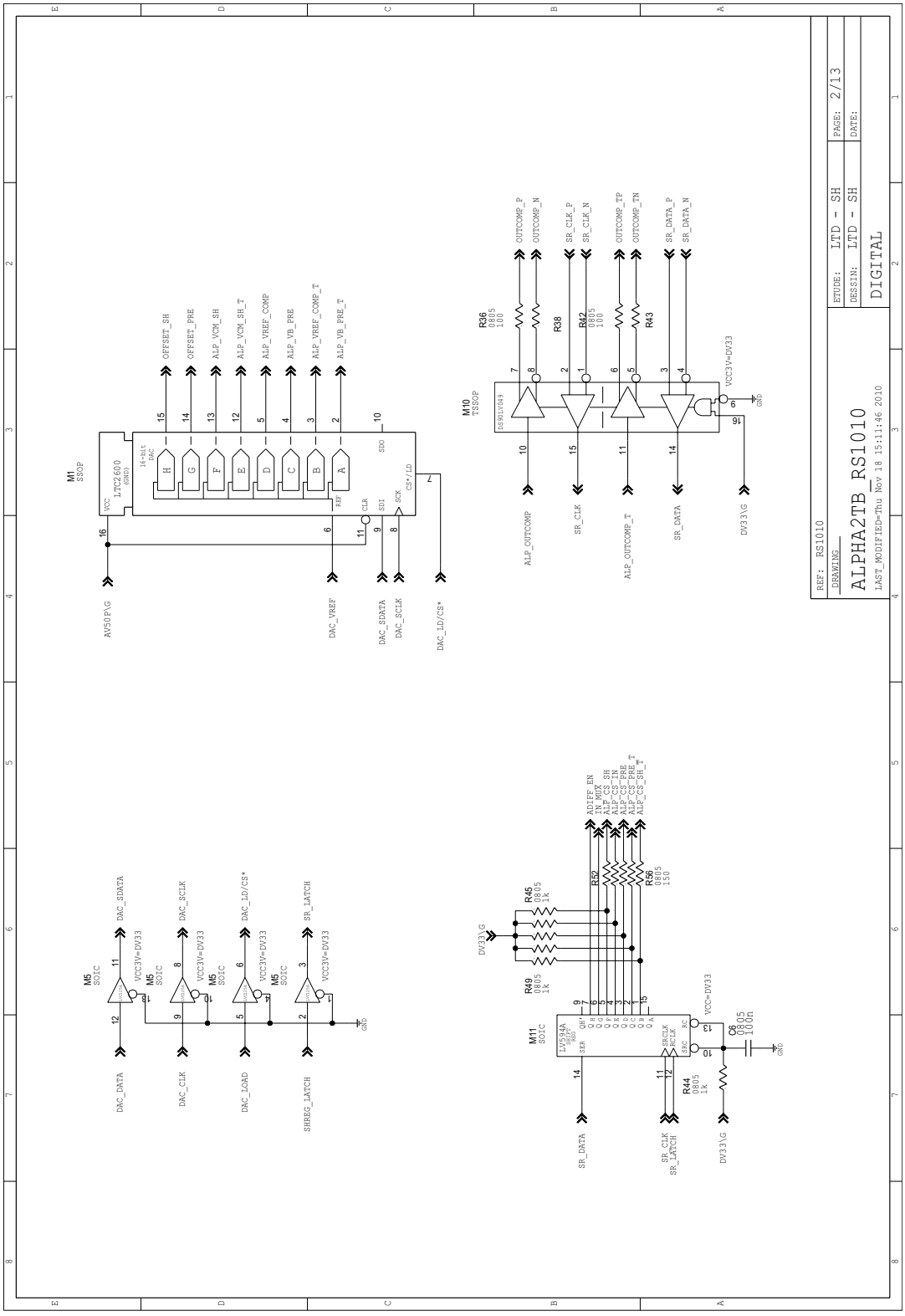

Figure A.2: Second page of the schematic of the AlphaRad-2 test board.

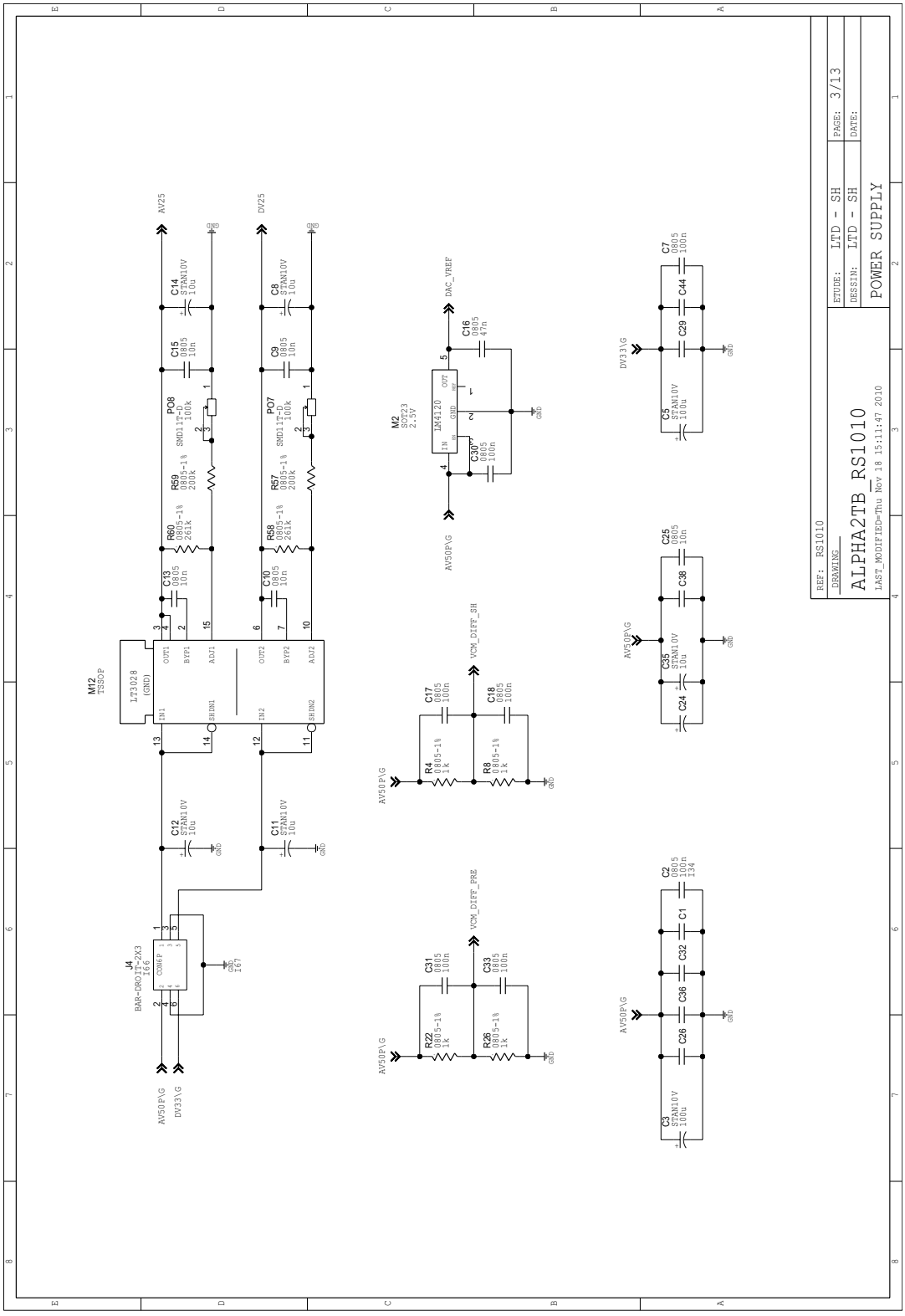

Figure A.3: Third page of the schematic of the AlphaRad-2 test board.

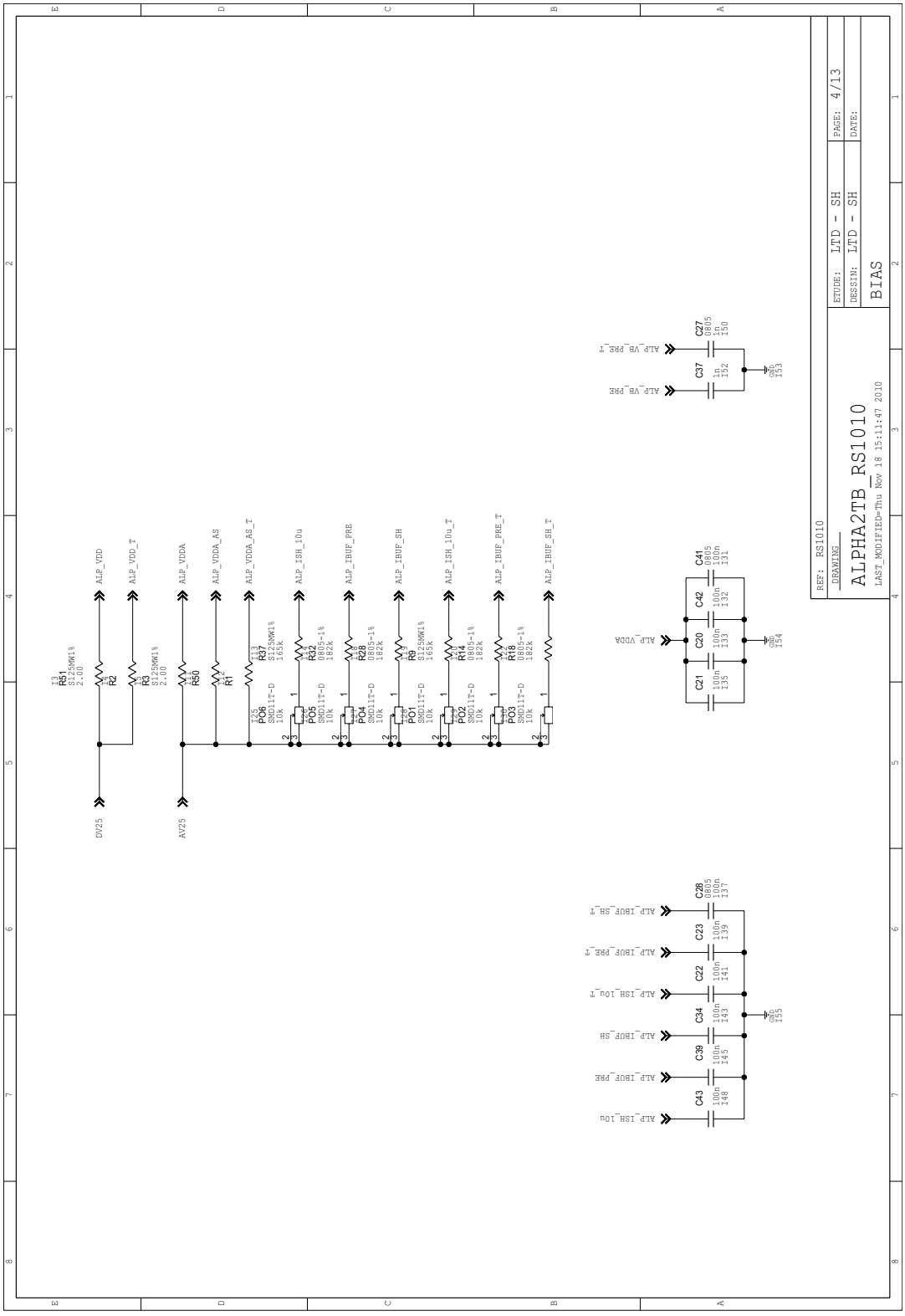

Figure A.4: Forth page of the schematic of the AlphaRad-2 test board.

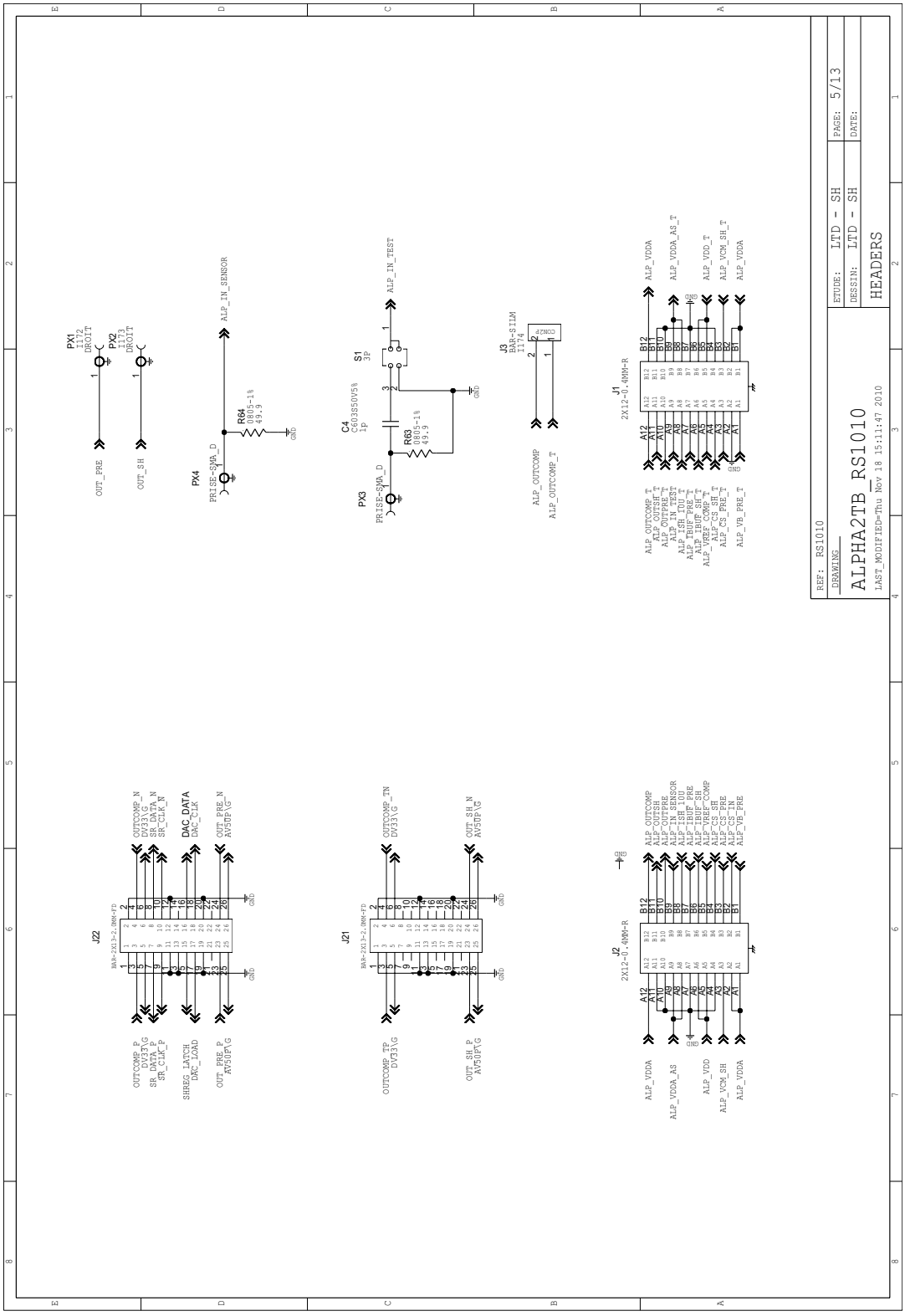

Figure A.5: Fifth page of the schematic of the AlphaRad-2 test board.

Appendix B

Calculation of detection efficiency

B.1 Detection efficiency

We can define two types of detection efficiency: absolute efficiency (ε_{abs}) and intrinsic efficiency (ε_{int}). The former is defined as

$$\varepsilon_{abs} = \frac{n_c}{n_{emit}}$$

where n_c is the number of measured counts and n_{emit} is the number of primary particles emitted by the source. This efficiency is dependent not only on the properties of the detector but also on the geometry (including the distance between source and detector).

The intrinsic efficiency is given by

$$\varepsilon_{int} = \frac{n_c}{n_{int}}$$

where n_{int} is the number of neutrons impinging on the detector. The intrinsic efficiency is dependent on the detection solid angle, and therefore dose not vary with distance. The tow efficiencies are linked by the following relation

$$\varepsilon_{int} = \varepsilon_{abs} \cdot \frac{4\pi}{\Omega}$$

where Ω is the detection solid angle.

For our application, we have calculated the intrinsic efficiency of our sensor. This depends primarily on the detection material, the radiation energy and the thickness of the material passed through.

B.2 Determination of the fluence at a distance d

To determine the value of detection efficiency, it is necessary to know the fluence of incident particles arriving on the detector. In most experiments in this work, the flux at working distances were calculated from the total activity of the source according to the equation:

$$\phi = A_0 \frac{S}{4\pi d^2}$$

where A_0 is the activity for 4π sphere of the source, S is the detection surface (0.0655 cm^2 for the AlphaRad-2), and d is the distance from the source. In some cases it may be more convenient to extrapolate the fluence value at a distance d_1 from the known fluence at a distance d_2 using the formula

$$\frac{\phi_1}{\phi_2} = \frac{d_2^2}{d_1^2}.$$

However, these two relations can be used only in cases where the source-sensor distance is large (if $d \gg \sqrt{S}$). Then the source can be considered as point source.

B.3 Uncertainty of detection efficiency

We recall the detection efficiency is given by

$$\varepsilon_{det} = \frac{n_c}{n_n}$$

where n_c is the number of detected particles and n_n is the number of incoming neutrons. We define σ_c and σ_n as the corresponding uncertainties. Knowing that the covariance term is zero, the uncertainty σ_ε on the detection efficiency is given by error propagation

$$\begin{aligned} \sigma_\varepsilon^2 &= \left(\frac{\partial \varepsilon}{\partial n_c}\right)^2 \sigma_c^2 + \left(\frac{\partial \varepsilon}{\partial n_n}\right)^2 \sigma_n^2 \\ &= \frac{1}{n_n^2}\sigma_c^2 + \left(\frac{n_c}{n_n^2}\right)^2 \sigma_n^2 \\ &= \frac{1}{n_n^2}\left(\sigma_c^2 + \varepsilon^2 \sigma_n^2\right). \end{aligned} \tag{B.1}$$

Publications

1. **Y. ZHANG**, C. Hu-Guo, D. Husson, T. D. Lê, S. Higueret, and Y. Hu, "A High-sensitivity Low-power CMOS Sensor for a Future Neutron Personal Dosimeter," *Nuclear Science, IEEE Transactions*, vol. 59, no. 4, pp. 1465-1471, August 2012.
2. **Y. ZHANG**, C. Hu-Guo, D. Husson, S. Higueret, T. D. Lê, and Y. Hu, "Design of a Monolithic CMOS Sensor for High Efficiency Neutron Counting," *Microelectronics Journal*, vol. 43, no. 11, pp. 730-736, November 2012.

Communications

1. **Y. ZHANG**, D. Husson, T. D. Lê, S. Higueret, C. Hu-Guo, and Y. Hu, "Development of an integrated CMOS sensor for efficient neutron counting," in Proceedings *Nuclear Science Symposium and Medical Imaging Conference (NSS/MIC), 2011 IEEE*, Valencia, Spain, 23-29 October 2011, pp. 409-415.
2. **Y. ZHANG**, C. Hu-Guo, D. Husson, and Y. Hu, "Design of an ultra low power CMOS pixel sensor for a future neutron personal dosimeter," *Advancements in Nuclear Instrumentation Measurement Methods and their Applications (ANIMMA), 2011 2nd International Conference*, Ghent, Belgium, 6-9 June 2011.

ABSTRACT

This thesis presents the development of CMOS sensors for a future neutron sensitive electronic individual dosemeter. Active dosemeters, exist but do not yet give results as satisfactory as passive devices, being however, mandatory for workers in addition to the passive dosimetry since 1995 (IEC 1323). The RaMsEs group in the laboratory IPHC is exploring a new compact device based on CMOS sensors for operational neutron dosimetry. In this thesis, a dedicated sensor, AlphaRad-2, with low noise and very low power consumption (314 µW), has been implemented in a commercial CMOS technology. The AlphaRad-2 integrates the sensing part made of a micro-diode array of 32×32 n-well/p-epi diodes on a sensitive area of 6.55 mm^2 and the signal processing electronics on the same silicon substrate. Device physics simulations have been performed to study the charge collection mechanism in diode matrices, and to optimize the collection efficiency and its time properties. The sensor geometry is a compromise between the collection performance and the total capacitance of the detector. A charge sensitive amplifier (CSA), a shaper, and a discriminator are employed in the readout circuit. We present its theoretical analysis, circuit design, and electrical tests. Our device has a sensitivity at the level of one single secondary charge particle (proton or α) thanks to its excellent noise performance. Extensive measurements to radioactive sources of α-particles, photons, and fast neutrons, have demonstrated good detection efficiency to fast neutrons and excellent γ-rejection through applying an appropriate electronic threshold.

Keywords: Neutron dosimetry, Electronic Personal Dosemeters (EPD), CMOS sensors, Application Specific Integrated Circuit (ASIC), Low noise, Low power consumption.

RÉSUMÉ

La thèse présente le développement de capteurs CMOS pour un futur dosimètre électronique neutrons. A côté des systèmes passifs largement répandus, les dosimètres actifs existants ne donnent pas satisfaction, alors qu'ils sont fermement recommandés par une directive européenne (IEC 1323). Le groupe RaMsEs de l'IPHC développe un nouveau concept de dosimètre électronique personnel neutrons à base de capteurs CMOS. Au cours de cette thèse, le circuit intégré AlphaRad2, à très bas bruit et très faible consommation électrique, a été implémenté dans une technologie commerciale. Il intègre un réseau de micro-diodes sur une surface sensible de 6.55 cm^2 avec sa chaîne de traitement sur le même substrat de silicium. Des simulations physiques ont permis d'étudier le processus de collection de charge et d'optimiser l'efficacité de collection. La géométrie du capteur est un compromis entre la collection des électrons secondaires et de la capacité totale du détecteur. Le circuit de lecture comprend un amplificateur de charge (CSA), un circuit de mise en forme (shaper) et un discriminateur pour une réponse digitale. Nous présentons une analyse théorique complète du circuit, les paramètres de dessin, ainsi que des tests électriques et des tests en sources de rayonnement. La sensibilité effective du système est au niveau de la particule unique (proton ou alpha), grâce à un très bon rapport signal à bruit. Une série complète de mesures en sources de photons, de neutrons et de particules chargées a permis de démontrer une bonne efficacité aux neutrons rapides et surtout une excellente réjection gamma grâce à l'application d'un seuil électronique approprié.

Mots-clés : Dosimétrie neutrons, EPD (Electronic Personal Dosemeters), CMOS capteurs, ASIC (Application Specific Integrated Circuit), Bas bruit, Faible consommation électrique.